WOOD RESEARCH
66 (1): 2021
01-14
doi.org/10.37763/wr.1336-4561/66.1.0114

WOOD SPECIES IDENTIFICATION BASED ON AN ENSEMBLE OF DEEP CONVOLUTION NEURAL NETWORKS

Tao He[1], Shibiao Mu[2], Houkui Zhou[1], Junguo Hu[1]
[1]Zhejiang A&F University
China
[2]Yiwu Industrial & Commercial College
China

(Received March 2020)

ABSTRACT

Our paper proposed an ensemble framework of combining three deep convolution neural networks (CNN). This method was inspired by network in network. Transfer learning used to accelerate training and deeper layers of network. Nine different CNN architectures were trained and evaluated in two wood macroscopic images datasets. After two times of 30 epochs training, our proposed network obtained 100% test rate in our dataset, which including 8 kinds of wood species and 918 images. The proposed method achieved 98.81% test recognition rate after three times training with 30 epochs in other dataset, which including 41 kinds of wood species and 11,984 images. Results showed that magnification macroscopic images can be instead of microscopic images in wood species identification, and our proposed ensemble of deep CNN can be used for wood species identification.

KEYWORDS: Wood identification, deep convolution neural networks, ensemble framework, macroscopic images.

INTRODUCTION

Wood is regarded as a renewable and environmental material (Yasar 2019). Different kinds of wood species are far from each other in use and price (Barmpoutis et al. 2018). It is important to develop a quick and accurate method to identify wood species, which not only leads to the proper utilization of woods, but also to the prevention of wood smuggling and the protection of several endangered tree species.

Wood researches focus on microstructure or macroscopic of the wood (Gong et al. 2019). So microscopic images and macroscopic images are used to identify wood species in machine

learning. Microscopic images have two disadvantages: (1) For obtaining wood anatomical features (Al-Mefarrej and Suansa 2019), acquisition method is destructive, because wood samples must be sliced or flattened to expose three different planes: the transverse, radial, and tangential sections (Kobayashi et al. 2019). (2) The process is quite complex and laborious. Since the wood samples must be boiled to make it softer at first, then cut with a sliding microtone to a thickness, colored with (acridine red, chrysoidine, or astra blue), dehydrated in an ascending alcohol series and finally acquired the image from sheets of wood using a microscope (Filho et al. 2014). The complexity of the make procedure of wood slices used in the microscopic approach does not make it suitable for the use in the field, where one needs less expensive and more robust hardware. To overcome this problem some authors (Barmpoutis et al. 2018, Hu et al. 2016, Filho et al. 2014) have investigated the use of macroscopic images to identify forest species. Compared to the microscopic image, macroscopic image presents some significant loss of information related to specific features of the forest species, but it is easy to obtain and enough to distinguish wood species.

With the rapid development of information technology, image processing technology and machine learning technology have been widely used in wood classification. Traditional machine learning algorithms used in wood identification, which contain Linear discriminant analysis, Binary tree classification, Logical linear regression, K-order nearest neighbor classification, Bayesian classification, Support vector machine (Mallik et al. 2011). These above algorithms are based on image preprocessing and image feature extraction. In addition, most of the current computer automatic recognition systems of wood categories are based on the microstructure image of wood slices (Filho et al. 2014, Maruyama et al. 2018).

Deep learning as a branch of artificial intelligence has made a great progress in recently years. Convolutional neural network (CNN), as a technical direction of deep learning, has successfully made a great breakthrough in image classification (Krizhevsky et al. 2012). In this paper, an ensemble of deep CNN is applied to classification and recognition of wood species. Compared to the traditional wood recognition method, it has two advantages: (1) Traditional wood recognition technologies need to extract various features of wood, such as (heartwood and sapwood) color, axial parenchyma, wood ray, ring, conduit and wood texture (Sundaram et al. 2015, Baas et al. 2004). The quality of features extraction will influence the accuracy of wood recognition. There are many disadvantages in these methods, such as large amount of data operation, large amount of work and require domain experience in feature extraction and feature selection. However, deep CNN does not need features extraction by human. It requires very little engineering by hand, just inputting the original data directly, it can extract feature by itself, which avoid human operational bias will improve recognition accuracy. (2) Wood images are not completely normalized. Because environmental factors such as distance, height, angle and illumination often cause image scaling, rotation, blur and other changes, which increases the difficulty of recognition. Deep CNN insensitive to large irrelevant variations such as the background, pose, lighting and surrounding objects (Lecun et al. 2015), which reduce the external interference factors of wood image effectively.

One contribution of our work is proposed an effective ensemble of deep learning methodology, which is used to identification wood species. The deeper layers of network, the higher accuracy the model achieve in the same dataset (Szegedy et al. 2015, Simonyan and Zisserman 2015). Transfer learning is easy to build a deep layers model and leverage the feature extracting capability of the trained layers (Pan 2014). Transfer learning is used in our method, models are downloaded from Tensorflow (Abadi et al. 2016), which are pre-trained with ImageNet (Russakovsky et al. 2015). Inspired by network in network (Lin et al. 2014). A framework in framework is proposed in our method, the same network training three times as a small framework and sum of each prediction

probability, three different frameworks are integrated as a framework, which add probability of each framework, finally sum all the predict probability to identification the wood species.

Nine kinds of popular deep learning models based on CNN for wood identification to compare test rate by transfer learning (Leonardo et al. 2019), including VGG16, Inception v3, ResNet50 v2, ResNet101 v2, ResNet152 v2, InceptionResNet v2, DenseNet121, DenseNet169, and DenseNet201. Three highest test accuracy models in the above models are selected and used in our ensemble framework, which are DenseNet121, DenseNet201 and InceptionResNet v2. The identification algorithms are trained, validated and tested in two wood datasets. One dataset contains 8 wood species consisting 918 macroscopic images created by our lab called Stereogram Wood Dataset (SWD), the other one called Forest Species Database–Macroscopic (FSD-M) ,which includes 41 kinds of wood species and 35,952 wood images (Filho et al. 2014). The ensemble algorithm gets higher accuracy than a single deep CNN in both datasets. The ensemble method achieves 100% test accuracy in SWD after two times of 30 epochs training, and 98.81% in FSD-M after three times of 30 epochs training which 1.04% higher than the best method proposed by Filho et al. 2014.

MATERIAL AND METHODS

Datasets description

Stereogram-wood images were acquired by stereo microscope connected with a computer. The stereo microscope using an Olympus DP70 connected with MD50 model which was manufactured by Guangzhou Mingmei, the microscope has 16 times maximum magnification. Eight kinds of wood species images were obtained in 8 times magnification. After obtaining the large cross-section of the sample wood images, cutting the images into small images with 224 x 224 pixels 24 bit RGB. Tab. 1 describes the eight wood species in the dataset, and selected sample images with 8 times magnification are shown as Fig. 1.

Tab. 1: Description of SWD.

ID	Species	Images
1	*Quercus acutissima* Carr.	108
2	*Quercus variabilis* Bl.	108
3	*Celtis biondii* Bl.	108
4	*Ulmus parvifolia* Jacq.	108
5	*Sassafras tzumu* (Hemsl.)Hemsl.	108
6	*Euodia rutaecarpa* (Juss.)Benth	162
7	*Ailanthus altissima* (Mill.)Swingle	108
8	*Meliosma angustifolia* Franch.	108

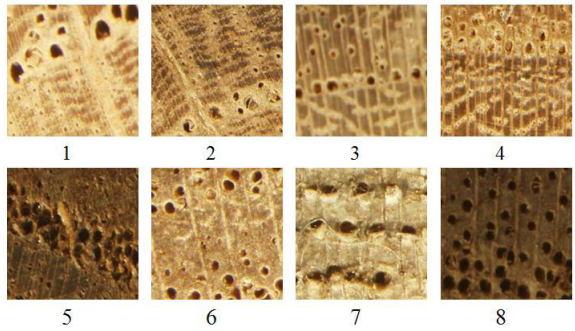

Fig. 1: Selected cross section of wood stereogram images (as described in Tab.1).

The wood macroscopic images dataset was collected using a Sony DSC T20 with the macro function activated. The resulting images were then saved in JPG format with no compression and a resolution of 3,264 × 2,448 pixels. In total 2,942 macroscopic images had been acquired and carefully labeled by experts in wood anatomy. To enlarge the dataset, every image was clipped to 4 images, with 1120 × 1120 pixels. Tab. 2 describes the 41 wood species in the database, and sample images are shown as Fig. 2.

Tab. 2: Description of FSD-M.

ID	Species	Images	ID	Species	Images
1	*Aspidosperma polyneuron*	212	22	*Cariniana estrellensis*	396
2	*Araucaria angustifolia*	252	23	*Couratari sp.*	256
3	*Tabebuia* sp.	172	24	*Carapa guianensis*	328
4	*Cordia goeldiana*	396	25	*Cedrela fissili*	220
5	*Cordia* sp.	252	26	*Melia azedarach*	184
6	*Hura crepitans*	164	27	*Swietenia macrophylla*	348
7	*Acrocarpus fraxinifolius*	192	28	*Brosimum paraense*	368
8	*Hymenaea* sp.	300	29	*Bagassa guianensis*	384
9	*Peltogyne* sp.	288	30	*Virola surinamensis*	204
10	*Hymenolobium petraeum*	392	31	*Eucalyptus sp.*	380
11	*Myroxylon balsamum*	144	32	*Pinus sp.*	396
12	*Dipteryx* sp.	396	33	*Podocarpus lambertii*	172
13	*Machaerium* sp.	224	34	*Grevilea robusta*	316
14	*Bowdichia* sp.	268	35	*Balfourodendron riedelianum*	248
15	*Mimosa scabrella*	204	36	*Euxylophora paraensis*	236
16	*Cedrelinga catenaeformis*	312	37	*Micropholis venulosa*	232
17	*Goupia glabra*	396	38	*Pouteria pachycarpa*	396
18	*Ocotea porosa*	212	39	*Manilkara huberi*	232
19	*Mezilaurus itauba*	376	40	*Erisma uncinatum*	248
20	*Laurus nobilis*	344	41	*Vochysia sp.*	552
21	*Bertholethia excelsa*	392	**Total**		**11,984**

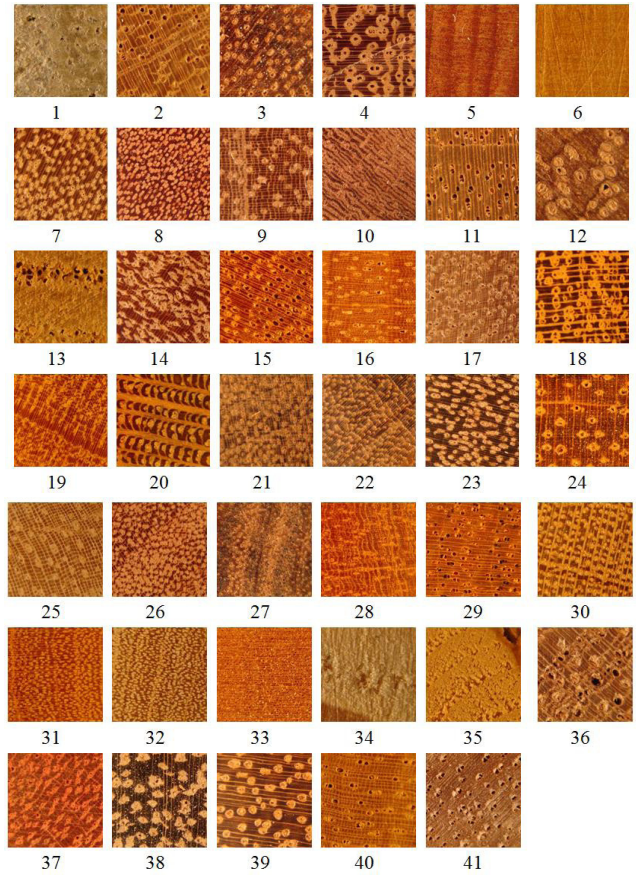

Fig. 2: Selected samples of FSD-M of 41 different kinds of wood (as described in Tab. 2).

Experimental environment and data preprocess

The experimental computer environment was 3.5GHz i7-7800X CPU, 32GB memory, 2 NVIDIA Geforce GTX 1080 Ti , windows 10 operating system. Python 3.7 and CUDA 10.2 were installed. Attribute to highly modular neural network library, Tensorflow 2.1.0-gpu was installed, which is a newest version of Tensorflow supporting GPU to accelerate computation.

Deep learning requires thousands of samples, so random augmentations were applied to compensate for lacking of insufficient training samples. A sequence of augmentation steps were defined in the augmentation process (Jalali et al. 2020). Data preprocess included resize image to the input size of the model, up and down flip, random crop of images, normalization the images to 0~1, finally change each image to a tensor. The labels of images were turned to one-hot coding. Both datasets were applied the same strategy: 60% of images were shuffled random for training, 20 % of images were for validation, and 20% of images were for testing.

Methodology

Transfer learning

Transfer learning methods have been widely adopted in image classification and other fields due to their little sample sizes. Higher layers of representation amplify aspects of the input, which are important for discrimination and suppress irrelevant variations to classification (Lecun et al. 2015). Because layers of net are crucial to CNN, transfer learning was applied to deeper layers in our paper. Transfer learning retrained deep learning models and the wood species identification tasks were evaluated in terms of accuracy and efficiency.

Pre-trained models which had trained in other datasets, such as ImageNet (Deng et al. 2009) dropping its final classification layer as fixed feature extractor can learn complex features of the wood macroscopic images. All these learned layers were connected to a fully connected layer, a batch normal layer and a dropout layer, final layer with a dense to classify wood species.

Models were used to train on both wood macroscopic images datasets using transfer learning to compare with our proposed method. Nine kinds of popular deep learning models based on CNN for wood identification by transfer learning (Leonardo et al. 2019), including VGG16, Inception v3, ResNet50 v2, ResNet101 v2, ResNet152 v2, InceptionResNet v2, DenseNet121, DenseNet169, and DenseNet201. Information extracted from images by ResNet equal to extracted by Inception (McNeely-White et al. 2020). The use of residual connections seems to improve the training speed greatly, which is alone a great argument for their use (Szegedy et al. 2017). So, InceptionResNet was used in our network. Guo used two different layers of Resnet as a framework to train datasets, achieved a result of 0.917 on the test set, which is 0.046 higher than a single ResNet (Guo and Yang 2018). Doing to above conclusions, our proposed method integrated with InceptionResNet v2, DenseNet121, and DenseNet169 to identification wood species. Our method contains different layers of network and different networks.

VGG

VGG net is a CNN model proposed by Simonyan and Zisserman, which holds an architecture with very small (3 × 3) convolution filter to achieved the depth to 16-19 weight layers. Max pooling handles reducing the size of the volume (down-sampling). Additionally, two fully connected layers each with 4096 nodes and a softmax classifier as shown in their work (Simonyan et al. 2015). VGG16 has a depth of 16 layers, which is adopted in our test.

GoogLeNet Inception and InceptionResNet

The "Inception" concept was first introduced in the GoogLeNet architecture by Szegedy et al. (2017). Now the latest version is Inception V4. This architecture combines the Inception architecture with residual connections, which aim being to accelerate the training of Inception networks.

The Inception module is made up of a pooling layer and convolution layers stacked together. The convolutions are of varied sizes of 1×1, 3×3 and 5×5. Another salient feature of the Inception module is the use of bottleneck layer which is a 1×1 convolution. The bottleneck layer helps in reduction of computation requirements. Additionally, there is pooling layer is used for dimension reduction within the module. InceptionResNet is a costlier hybrid Inception version, which combined with ResNet has significantly improved recognition performance (Szegedy et al. 2017). GoogLeNet Inception v3 and InceptionResNet v2 by using pre-trained weights from Tensorflow were performed in experiment.

ResNet

ResNet model was first introduced by He et al. (He et al. 2016), which was a basis of their proposed model in ILSVRC 2015 and COCO 2015 classification challenge. Their model won the 1st place with error rate of 3.57% in the ImageNet classification. ResNet is a network-in-network architecture that relies on many stacked residual units. These residual units are the set of building blocks used to construct the network. A collection of residual unit's forms building blocks that leads to the ResNet architecture (He et al. 2016). The residual units are composed of convolution, pooling layers. The architecture is similar to the VGG net (Simonyan et al. 2015) consisting of 3×3 filters but ResNet, is about 8 times deeper than VGG network. This is attributed due to the usage of global average pooling rather than fully-connected layers. A further update of ResNet (He et al. 2016) was done to obtain more accuracy by updating the residual module to use identity mappings. ResNet50, ResNet101, ResNet152 with 50,101,152 layers downloaded with pre-trained weights from Tensorflow are used in our paper.

DenseNet

Huang et al. introduced a densely connected convolutional network architecture (Huang et al. 2017). To ensure maximum information flow between layers in the network, all layers are connected directly with each other in a feed-forward manner. For each layer, the feature maps of all preceding layers are used as inputs and its own feature maps are used as inputs into all subsequent layers. DenseNet alleviates the problem of the vanishing gradient problem and has substantially reduced number of parameters (Huang et al. 2016). For this task of wood species recognition, DenseNet models with 121, 169, 201 layers were used. The models were downloaded with pre-trained weights from Tensorflow.

Our proposed ensemble framework of deep CNN model

Deep CNN is currently one of the most popular models and has exhibited their great performance on many image classification problems (Kamilaris et al. 2018). The deeper layers of network will achieve higher accuracy to the same dataset (Szegedy et al. 2017), and combing different networks also get higher identification accuracy than single network (Guo et al. 2018). So, an effective deep CNN model for the identification of wood species is proposed in our paper, which is also inspired by network in network(Lin et al. 2014). Because of Resnet can deeper network easily, InceptionResNet combining the advantages of Inception and ResNet, and different layers of network also improve the identification accuracy. The ensemble model integrated InceptionResNet v2, ResNet121, and ResNet201. Fig. 3 presents the framework of our proposed model.

Images in both wood macroscopic datasets were reshaped to the size of 224 × 224 (wide and height) in this experiment. The above nine pre-trained models were downloaded from Tensorflow, which had pre-trained with ImageNet. By dropping the final classification layer as fixed feature extractor to learn complex features from wood images training dataset. All these learned layers were connected to a fully connected layer with ReLU (Rectified linear unit, ReLU) activation, then added a batch normal layer which can increase the speed of learning and the overall classification accuracy, and sequenced with a dropout layer to avoid over-fitting, finally with a dense layer to identify wood species. Inspired by network in network (Lin et al. 2014). A framework in framework was proposed in our method, the same network training three times as a small framework and summed each prediction probability, three different frameworks were integrated as a framework, which added probability of each framework, finally summed all the predict probability to identification the wood species.

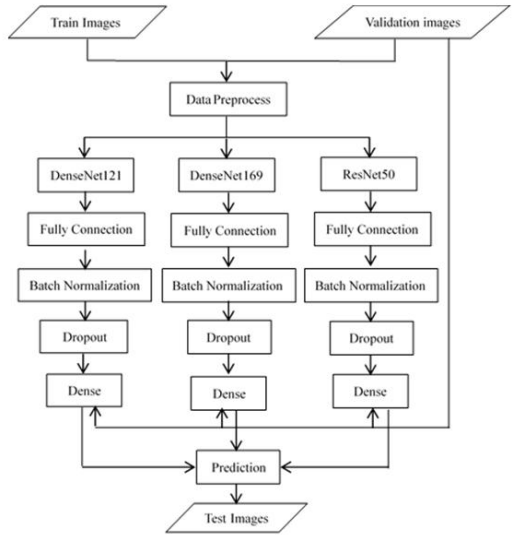

Fig. 3: Ensemble framework of deep CNN method.

Validation dataset was used to adjust parameters of network adjusted when training. The model evaluated based on cross-entropy loss and accuracy on the test dataset. Test dataset was used to evaluate the models identification accuracy. After training and validating with above nine kinds of CNN, used the network models to predict the probability labels of test images, adding three kind of CNN's predict labels, finally got the total probability labels, the maximum probability label as the identification label.

Following definitions of the recognition rate was used. Let B be a test set with N_B images, Acc_{Rec} represents as test accuracy of identification. If the recognition system classifies correctly N_{Rec} , then

$$Acc_{Rec} = \frac{N_{Rec}}{N_B} \times 100\% \quad (1)$$

RESULTS AND DISCUSSION

Training

For every experiment, accuracy metric was adopted for evaluation of the models. The hyper-parameters were standardized on all the networks. All the network models were trained using Stochastic Gradient Descent (SGD), which runs faster and converges easily (He et al. 2016). Batch Normalization technique and ReLU activation function (Glorot et al. 2011) were applied in all the experiments. Because of GPU memory constraints, batch size of 16 was used. The learning rate was set to 0.001 for all networks. In order to relieve the problem of little data, data augmentations were done to all networks including up and down flip, random crop of images. Nine different kinds of CNN were trained in the both dataset, and saved the model weight parameters.

Results of the experiments

In our study, an assessment of the appropriateness of state-of-the-art deep CNN for the task of wood species identification using images was done. VGG16, Inception v3, ResNet50 v2, ResNet101 v2, ResNet152 v2, InceptionResNet v2, DenseNet121, DenseNet169, and DenseNet201 and our proposed ensemble deep convolutional neural network were trained and tested. In our paper, all models were trained 1 to 5 times, and trained for 30 epochs every time in both datasets. The average test identification accuracy of different train times of each models are shown in Tab. 3 and Tab. 4.

Tab. 3: Test recognition rates of various deep CNN learning algorithms in SWD.

Model	Train times (%)				
	1	2	3	4	5
VG16	13.59	37.23	22.28	54.76	60.22
Inception v3	86.96	91.85	91.85	93.21	95.33
ResNet50 v2	86.96	85.05	88.41	91.30	85.54
ResNet101 v2	70.65	14.67	19.57	91.85	47.07
ResNet152 v2	80.43	14.95	19.57	82.07	79.67
InceptionResNet v2	96.20	97.55	91.85	84.92	96.09
DenseNet121	98.37	97.01	90.94	90.22	90.76
DenseNet169	97.28	71.11	75.56	87.78	75.56
DenseNet201	94.02	75.82	94.38	94.57	94.35
Ensemble of Deep CNN	98.91	100.00	100.00	100.00	100.00

Tab. 4: Test recognition rates of various deep CNN learning algorithms in FSD-M.

Model	Train times (%)				
	1	2	3	4	5
VG16	53.81	53.81	81.50	77.48	87.07
Inception v3	95.17	95.17	73.56	93.06	93.10
ResNet50 v2	84.79	84.79	88.24	89.98	90.26
ResNet101 v2	70.26	70.26	66.37	67.14	79.71
ResNet152 v2	45.34	45.34	57.82	74.26	65.40
InceptionResNet v2	95.81	95.81	96.67	95.60	98.19
DenseNet121	92.60	76.21	86.57	95.19	95.48
DenseNet169	92.94	88.49	89.40	89.90	93.78
DenseNet201	90.38	93.47	92.52	92.76	93.64
Ensemble of Deep CNN	96.98	97.66	98.81	98.85	99.46

Tab. 3 and Tab. 4 have shown as follows: Our proposed ensemble of deep CNN obtained the highest test accuracy among the different networks. The accuracy achieved 100.00% in our dataset. After three times train, test accuracy got 98.81%, which was 1.04% higher than the proposed method by Filho (Filho et al. 2014), and a confusion matrix is presented in Tab. 5 for each wood species in FSD-M.

Tab. 5: Confusion matrix for FSD-M (numbers in brackets is mistaken predict label).

ID	Number of test images		ID	Number of test images	
	Classification	Misclassification		Classification	Misclassification
1	53	0	22	68	2(23)
2	77	1(17)	23	37	0
3	22	1(22)	24	4	0
4	1	1(37)	25	65	3(26)
5	42	0	26	73	0
6	56	0	27	26	0
7	45	1(27)	28	67	1(37)
8	73	0	29	5	0
9	77	9(37)	30	39	1(7)
10	42	0	31	54	0
11	93	0	32	73	0
12	52	0	33	33	0
13	74	0	34	76	0
14	7	0	35	47	0
15	84	1(14)	36	55	1(37),2(38)
16	49	0	37	38	1(28)
17	59	1(3),1(33)	38	2	1(29)
18	46	0	39	47	1(40)
19	41	0	40	47	0
20	67	3(15),1(28)	41	7	0
21	76	0	**Total**	**1999**	**27**

As indicated by the Tab. 5, nine test images misclassification of wood species happened in the same family, and 27 test images misclassification in 2,026 test images. It illustrates that our proposed method is able to deal with the great intra-class variability presented by the forest species.

CONCLUSIONS

In this paper, an ensemble framework of deep CNN spired by network in network is introduced into the field of wood recognition, and a framework of wood feature extraction and recognition is constructed by deep CNN. The deep CNN has two advantages in the processing of wood macroscopic images: (1) Because there is no feature extraction step, the two-dimensional images are read directly into the network, which reduces the difficulty of image preprocessing; (2) local field and weight sharing technology greatly reduces the amount of parameters and the complexity of the algorithm. Traditional wood recognition technology has many problems, such as large number of images, more training data, time-consuming, etc., while deep CNN can better overcome the above shortcomings, and avoid the process of image extraction and classification, reducing the demand of artificial expertise.

From our experiment, some conclusions are obtained as follow: The ensemble of deep CNN integrates the advantages of various models which inspired by network in network and makes it achieve higher accuracy than single model. Mixed many times of train model parameters weight

improve the identification accuracy. The transfer learning makes the data train more easily.

Compared to the microscopic image, macroscopic image presents some significant loss of information related to specific features of the forest species, but it is easy to obtain and enough to distinguish wood species by our proposed ensemble of deep CNN. The performance of our method in SWD is better than in FSD-M. Macroscopic images are captured in eight times magnification in SWD, but we do not know which times magnification in FSD-M. If the images are captured by less than eight times magnification, then we can get follow inclusion: higher magnification of the wood macroscopic images will improve wood species recognition, because more details help our proposed ensemble of deep CNN to identify the wood species.

The wood recognition system constructed in this paper has a high recognition rate for wood cross-section stereo images, and the proposed ensemble of deep CNN recognition rate of 8 kind of wood species in eight times magnification macroscopic image reaches 100%, which are trained more than two times, and trained 30 iterations every time. Even though the performance of the architecture is good, further research needs to be done to improve on the computational time, and which magnification images is best for wood identification is also to be considered.

ACKNOWLEDGMENTS

This work was supported in part by the National Natural Science Foundation of China under Grant 31971493, Zhejiang Provincial Natural Science Foundation of China under Grant LY19F020048 and Zhejiang Provincial Key Laboratory of Forestry Intelligent Monitoring and Information Technology. The authors have no conflict of interest to declare.

REFERENCES

1. Abadi, M., Barham, P., Chen, J., Chen, Z., Davis, A., Dean, J., Devin, M., Ghemawat, S., Irving, G., Isard, M., Kudlur, M., Levenberg, J., Monga, R., Moore, S., Murray, D.G., Steiner, B., Tucker, P., Vasudevan, V., Warden, P. , Wicke ,M., Yu,Y., Zheng, X., 2016: Tensor flow: A system for large-scale machine learning. Proceedings of the 12th USENIX Symposium on operating systems design and implementation, OSDI,16, Pp 265-283.
2. Al-Mefarrej, H.A., Suansa, N.I., 2019: Trait-based ecology using conduits comparison approach. Wood Research 64(6): 1055-1064.
3. Baas, P., Blokhina, N., Fujii, T., Gasson, P.E., Grosser, D., Heinz, I., Ilic, J., Xiaomei, J., Miller, R., Newsom, L.A., Noshiro, S., Richter, H.G., Suzuki, M., Terrazas, T., Wheeler, E., Wiedenhoeft, A., 2004: IAWA List of microscopic features for softwood identification. IAWA Journal 25(1): 1-70.
4. Barmpoutis, P., Dimitropoulos, K., Barboutis, I., Grammalidis, N., Lefakis, P., 2018: Wood species recognition through multidimensional texture analysis. Computers and Electronics in Agriculture 144: 241-248.
5. Deng, J., Dong, W., Socher, R., Li, L. jia, Li, K., Fei-fei, L., 2009: ImageNet: a large-scale hierarchical image database. IEEE Computer society conference on computer vision and pattern recognition (CVPR 2009): 20-25.
6. Filho, P.L.P., Oliveira, L.S.,Nisgoski, S., Britto, A.S., 2014: Forest species recognition using macroscopic images. Machine Vision and Applications 25: 1019-1031.
7. Gong, L., Zhang, Q., Liang, H., Ren, S., Wang, J., 2019: Mechanical properties and microstructure of *Zabelia biflora*. Wood Research 64(3): 423-436.

8. Guo, S., Yang, Z., 2018: Multi-Channel-ResNet: An integration framework towards skin lesion analysis. Informatics in Medicine Unlocked 12: 67-74.
9. He, K., Zhang, X., Ren, S., Sun, J., 2016: Deep residual learning for image recognition. Proceedings of the IEEE Computer society conference on computer vision and pattern recognition 2016 Dec: 770-778.
10. Hu, S., Li, K., Bao, X., 2016: Wood species recognition based on SIFT keypoint histogram. In: Proceedings 8th International congress on image and signal processing (CISP), Pp 702-706.
11. Huang, G., Liu, Z., Van Der Maaten, L., Weinberger, K.Q., 2017: Densely connected convolutional networks. Proceedings - 30th IEEE Conference on computer vision and pattern recognition, CVPR, Pp 4700-4708.
12. Jalali, A., Lee, M., 2020: High cursive traditional Asian character recognition using integrated adaptive constraints in ensemble of DenseNet and Inception models. Pattern Recognition Letters 131: 172-177.
13. Kamilaris, A., Prenafeta-Boldú, F. X., 2018: Deep learning in agriculture: A survey. Computers and Electronics in Agriculture 147(1): 70-90.
14. Kobayashi, K., Hwang, S. W., Okochi, T., Lee, W. H., Sugiyama, J., 2019: Non-destructive method for wood identification using conventional X-ray computed tomography data. Journal of Cultural Heritage 38: 88-93.
15. Krizhevsky, A., Sutskever, I., Hinton, G.E., 2012: ImageNet classification with deep convolutional neural networks. Advances in Neural Information Processing Systems 25(2): 1-9.
16. Lecun, Y., Bengio, Y., Hinton, G., 2015: Deep learning. Nature 521: 436-444.
17. Leonardo, M.M., Carvalho, T.J., Rezende, E., Zucchi, R., Faria, F.A., 2019: Deep feature-based classifiers for fruit fly identification (*Diptera: Tephritidae*). Proceedings - 31st Conference on graphics, patterns and images, SIBGRAPI 2018: 41-47.
18. Lin, M., Chen, Q., Yan, S., 2014: Network in network. 2nd International conference on learning representations (ICLR). Conference track proceedings, 10 pp.
19. Mallik, A., Tarrío-Saavedra, J., Francisco-Fernández, M., Naya, S., 2011: Classification of wood micrographs by image segmentation. Chemometrics and Intelligent Laboratory Systems 107(2): 351-362.
20. Maruyama, T. M.,Oliveira, L. S.,Britto, A. S.,Nisgoski, S., 2018: Automatic classification of native wood charcoal. Ecological Informatics 46: 1–7.
21. McNeely-White, D., Beveridge, J.R., Draper, B.A., 2020: Inception and ResNet features are (almost) equivalent. Cognitive Systems Research 59: 312-318.
22. Pan, S.J., 2014: Transfer learning. Data classification: Algorithms and applications ,IBM T. J. Watson Research Center Yorktown Heights, New York, USAIBM T. J. Watson Research CenterYorktown Heights, New York, USA, Pp 537-570.
23. Russakovsky, O., Deng, J., Su, H., Krause, J., Satheesh, S., Ma, S., Huang, Z., Karpathy, A., Khosla, A., Bernstein, M., Berg, A.C., Fei-Fei, L., 2015: ImageNet large scale visual recognition challenge. International Journal of Computer Vision 115(3): 211-252.
24. Simonyan, K., Zisserman, A., 2015: Very deep convolutional networks for large-scale image recognition. 3rd International conference on learning representations (ICLR). Conference track proceedings, Cornel University 14 pp.
25. Sundaram, M., Abitha, J., Mal Mathan Raj, R., Ramar, K., 2015: Wood species classification based on local edge distributions. Optik 126: 2884-2890.

26. Szegedy, C., Ioffe, S., Vanhoucke, V., Alemi, A.A., 2017: Inception-v4, inception-ResNet and the impact of residual connections on learning. 31st AAAI Conference on artificial intelligence, AAAI 2017: Pp 4278-4284.
27. Szegedy, C., Liu, W., Jia, Y., Sermanet, P., Reed, S., Anguelov, D., Erhan, D., Vanhoucke, V., Rabinovich, A., 2015: Going deeper with convolutions. Proceedings of the IEEE Computer society conference on computer vision and pattern recognition, Pp 1-9.
28. Yasar, S.S., 2019: Effects of wood preservatives on the combustion process and combustion quality of wood. Wood Research 64(1): 59-71.

Tao He, Houkui Zhou*, Junguo Hu*
School of Information Engineer
Zhejiang A&F University
Lin'an, Zhejiang 311300
China
*Corresponding authors: zhouhk@zju.edu.cn and hujunguo@zafu.edu.cn

Shibiao Mu
Yiwu Industrial & Commercial College
Yiwu, Zhejiang 322300
China

WOOD RESEARCH
66 (1): 2021
15-26
doi.org/10.37763/wr.1336-4561/66.1.1526

THERMOGRAVIMETRIC ANALYSIS, DIFFERENTIAL SCANNING CALORIMETRY AND TIME-TO-IGNITION OF WOOD MATERIALS TREATED WITH WATER GLASS FLAME RETARDANTS

Juraj Jancík, Linda Makovická Osvaldová
University of Zilina
Slovakia

Frank Markert
Technical University of Denmark
Denmark

(Received August 2020)

ABSTRACT

The paper investigates efficiency of silicate flame retardants on wooden fibres (used for production of medium-density fibreboards) and spruce boards. A simultaneous thermal analysis and cone calorimetry were used for the assessment. Specimens were treated with three different types of silicate water glass: sodium silicate, potassium silicate and modified silicate. Along with these, one sample of untreated fibres was tested in order to provide a baseline sample. As a result of the simultaneous thermal analysis, the ability of the treatments to increase the residual amount of biological char in samples during pyrolysis and ability of the flame retardant to be retained in these wood fibres was used to assess the efficiency of each flame retardant on the wood fibres.

KEYWORDS: Simultaneous thermal analysis, cone calorimetry, time of ignition, mass loss, fibreboard, spruce, pyrolysis.

INTRODUCTION

Wood as a thermally thick construction material is widely used in various types of buildings globally. One of the weaknesses of wooden materials are the fire resistant properties, therefore, modifications to improve these properties can be beneficial. Application of flame retardants is one of the possible material modifications that is common thanks to its efficiency (Eremina et al. 2020, Gasparik et al. 2017, Lu et al. 2019, Baysal et al. 2019).

We use water glass flame retardants for these experiments. This type of flame retardation is popular for its simple preparation and application on and into the material surface and is used not only in combination with wood materials but also with a variety of others such as coal (Fan et al. 2020) or graphite (Ustinov et al. 2017, Kasymov et al. 2019). To ensure thorough impregnation of the flame-retarding agent a vacuum/pressure impregnation is commonly used for wood materials (Lou et al. 2018, Clause et al. 2010). This was avoided in the following experiments to investigate material behavior with slender layer of flame retardant on and underneath the surface.

Testing of fire resistant properties of materials has evolved and changed through time (Makovicka Osvaldova et al. 2013, 2015) from which both rather traditional and novel methods were used, i.e. methods of cone-calorimetry and simultaneous thermal analysis (hereinafter referred to as STA). STA integrates two measurement methods, i.a. thermogravimetric analysis (hereinafter referred to as TGA) and differential scanning calorimetry (hereinafter referred to as DSC), which are widely used with wood materials (Dineff et al. 2014, Azizi et al. 2017, Grønli et al. 2002.). Results will help to assess the efficiency of silicates used as flame retardants and extend the knowledge of biochar forming in pyrolysis previously investigated by Kloss et al. (2012), Haseli et al. (2012) and Qi et al. 2016, England and Iskra (2020).

MATERIALS AND METHODS

The reaction to heat of treated hardwood and wood fibres was investigated in this paper. The density of the MDF material was about 160 $kg \cdot m^{-3}$. The STA was used to evaluate the effect of the different treatments. Water soluble silicates (water glass) flame retardants were used for treating: sodium silicate - type N37/40, potassium silicate - type K4009, and modified silicate - type K1530, all provided by a Danish company Bollerup Jensen A/S. Microscopic images of the samples in different phases of experiment are included accompanied by a brief commentary.

Sodium silicate (type N37/40) was marked as N (Danish: "Natron vandglas") for easier labelling of the samples that was also used during the experiment. Sodium silicate is made by melting the sand together with sodium carbonate which will end up as glass that is dissolved in water under high temperature and pressure resulting in the production of water glass. Its consistency is best described as a thick and clear liquid. The chemical formula of sodium silicate is $Na_2Si_3O_7$ with a pH value >12. The density was measured to be 1.27 $g \cdot ml^{-1}$.

Potassium silicate (type K4009) was marked as K (Danish: "Kali vandglas"). It is a versatile inorganic chemical produced by melting sand together with potassium carbonate, dissolved in water afterwards. Potassium silicate is also thick and clear but it is easily soluble in water. It also achieves higher temperature tolerance, however it is more expensive. Chemical formula of potassium silicate is $K_2Si_3O_7$ and its pH value is > 12 (Bollerup Jensen A/S 2016). Its density was measured at 1.24 $g \cdot ml^{-1}$.

Modified silicate (type K1530) will be marked as S (silica sol). It is a liquid with a mat opaque colour and sharp odour. Just like the previous silicates, it is soluble in water. Modified silicate is more expensive than the other treatments, however its lower pH value is favourable for wood penetration. Its pH value was between 3-5. Its density was measured at 1.12 $g \cdot ml^{-1}$.

The first of two base materials were wood fibres typically used in MDF (medium density fibreboards). These were used for the simultaneous thermal analysis. Experiments with 4 differently treated samples were conducted. One sample consisted of untreated fibres to provide the basic data for further comparison of changes with different treatments. Other three samples were treated with various types of water glass, specifically with sodium silicate (type N37/40),

potassium silicate (type K4009) and modified silicate (type K1530). Wood materials tend to produce biochars with rather basic pH values in pyrolysis as indicated by Kloss et al. (2012) on spruce and poplar specimen. All densities were measured weighing 10 ml of the treatment and scales with resolution of 0.01 g.

Cone calorimetry was used to investigate the effect of silicate water glass flame retardants on spruce board evaluating the time to ignition at different heat fluxes (20/25/30/40/50 $kW \cdot m^{-2}$) and estimating the critical heat flux for each type of treatment, including untreated specimens. The spruce board was treated with the flame retardants by soaking under atmospheric pressure which was expected to impregnate specimens creating a thin layer on and under the surface. Pressure impregnation was not incorporated in this study.

For the cone calorimetry a specimen of spruce (*Picea abies*) was used. Very important property of wood is its density as it has direct impact on the flame retardant efficiency (Makovická Osvaldová et al. 2016). Average density of the spruce board was estimated to be 560 $kg \cdot m^{-3}$ for thickness ranging from 17 to 21 mm. Specimens were standardly square-shaped with an exposed surface area to heat flux of 100 cm^{-2}. Fibres and spruce specimens were treated with all the three water glass flame retardants using the same conditions. The tests include pure (untreated) spruce specimens that undergo the same procedure for further comparison of changes.

Sample preparations

Four small bowls were prepared for all treatments (pure/N/S/K). A certain amount of MDF fibres was picked for each sample and weighed afterwards to find the real weight of basic material. One gram of the agent was diluted in approximately 5 ml of distilled water. The solution was then poured into the bowl containing fibres and stirred for approximately 5 min to achieve equal distribution of treatment into the entire sample. Afterwards, all the samples were inserted into a heating cabinet for a 24 hour drying process. A constant temperature of 100°C ± 5°C was used. Samples were cut into finer fibres and stirred again to achieve higher homogenisation. Obviously, this whole preparation process is not necessary for the pure fibres. However, the pure sample was wetted with water and dried in the heating cabinet as well, as we wanted to keep the undergoing process equal for all tested samples. The spruce board underwent the same drying process as the fibres being exposed to 100°C ± 5°C in 24 hour time span. Soaking in the water-diluted flame retardants was conducted afterwards. Specimens were soaked approximately 1 cm deep in flame retardant solution for 90 min and left for a week to dry again naturally. An optical microscope with installed camera was used to take microscopic pictures of the samples in 3 different phases of the testing, i.a. before, after STA and after furnace experiments, using the 20x magnification. The same samples were used for all phases of the microscopic photos. For the simultaneous thermal analysis, consisting of thermogravimetric analysis and differential scanning calorimetry, a STA 449 F3 Jupiter device manufactured by Netzsch was used. Samples were weighed with resolution of 1 µg. Temperature range of the measurements was set to 35-1000°C with heating rate set to 10 $K \cdot min^{-1}$. Before starting the STA temperature ramp the sample holder was evacuated. The pyrolysis atmosphere during the measurements consisted of 100% pure nitrogen. For further analysis of the results Proteus 6.1.0 software was used. Correction of TGA for phenomenon of buoyancy effect and friction force from vertically moving gas was done using TGA-BeFlat® procedure which is part of the mentioned software.

RESULTS AND DISCUSSION

First of all, the results of thermogravimetric analysis (TGA) are shown in Fig. 1, compile all samples for clear comparison of the data. The residual masses after the pyrolysis consist of biochar from the MDF fibres and the solid residues of the silicates. In order to estimate the fractions of the biochar and the silicate residues, all samples were placed in a furnace at 950°C for 2 hours in air to remove the carbonized residue (biochar) of the MDF fibres. Assuming a high heat stability of the silicates, we estimated the fraction of silicate residues and thus also the ratio between these two components after the pyrolysis.

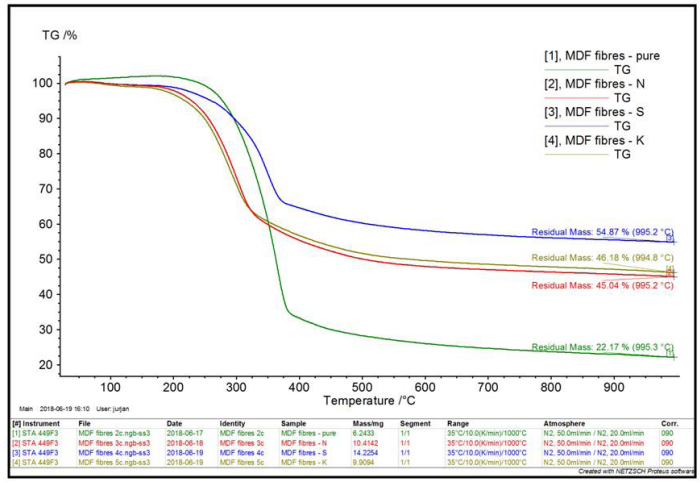

Fig. 1: Thermogravimetric analysis of the treated MDF fibres.

The results showed significant difference between treated and untreated MDF fibres as seen in Fig. 1. All the treatments (curves 2-3-4) change the pyrolysis behaviour relative to the pure MDF fibres (curve 1). Based on residual mass, modified silicate (S) achieved the best result surpassing residual mass of pure fibres by 32.7%. Sodium silicate (N) and potassium silicate (K) show a very similar progress (curves 2-4) with residual masses differing only by 1.14%. Behaviour of the sodium silicate (N) and potassium silicate (K) samples show an interesting progress during the first third of measurement interval (Fig. 1) as they seem to initiate rapid mass loss earlier (at lower temperature) than the other samples, even relative to pure fibres. The residual masses after the pyrolysis consisted of biochar from the MDF fibres and the solid residues of the silicates. In order to estimate the fraction of the biochar, all samples were exposed to 950°C in a furnace for 2 hours in air and weighed afterwards (Tab. 1).

Tab. 1: Composition of samples before and after pyrolysis.

MDF	Pure	+N	+S	+K
Fibres (mg)	6.2433	8.6909	9.2824	7.7049
Treatment (mg)	-	1.7233	4.943	2.2045
Biochar residue (mg) / (%)	1.3841 / 22.17	2.9673 / 34.14	2.8625 /30.84	2.3717 / 30.78
Biochar (%) / Treatment (%)	-	63.26 / 36.74	36.67 / 63.33	51.83 / 48.17

Biochar residue mass values are given in mg, as shown in Tab. 1, and express the mass of the biochar in the sample after pyrolysis. The additional percentage value is its fraction in the pure fibers. The respective percentages of the biochar and the treatment are given in the bottom of Tab. 1 and are based on the mass of the STA pyrolysis measurement (Fig. 1). Comparing the biochar residue (Tab. 1) we can see that sodium silicate (N) achieved the best result from all the treatments with 34.14% residue of the former mass of fibres. Modified silicate (S) and potassium silicate (K) acquired almost identical values of 30.84% and 30.78%. The increase is evident in treatments compared to biochar residue of pure MDF fibres which acquired 22.17% residue of former mass before the pyrolysis.

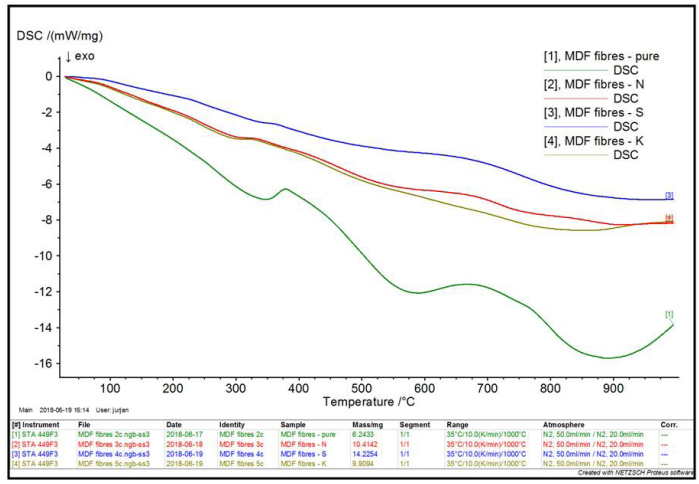

Fig. 2: Differential scanning calorimetry of the treated MDF fibres.

In addition to thermogravimetric analysis a differential scanning calorimetry (DSC) analysis was conducted and results are shown in Fig. 2. Note that the DSC results are mostly exothermic except for a signal of pure fibres where two significant parts between peaks 347.7-378.5°C and 590.9-668.7°C show the reaction is endothermic. It can be also seen at the last part of measurement on the same curve. Production of volatile by-products of the pyrolysis caused the sample to absorb energy which makes the reaction endothermic (Anca-Couce 2016). The applied treatments appear to reduce this production. Imperfection of the measuring device can influence the results as well which can be seen especially in the end of measurement on the green curve representing pure fibres. This phenomenon does not occur to such an extent in other signals where treatments moderate the progress of pyrolysis. The same samples that underwent the STA were subsequently placed in a furnace for 120 min at a constant temperature of 950°C with air atmosphere to remove the carbonized fibres (biochar) produced during the pyrolysis to find the share of biochar and treatment in sample after the STA. Microscopic images were made for the samples in 3 phases of the experiment and are shown in the Figs. 3-6. The first image was of the sample before the STA, the second image was the sample after the STA and the last one shows the sample after the furnace exposure.

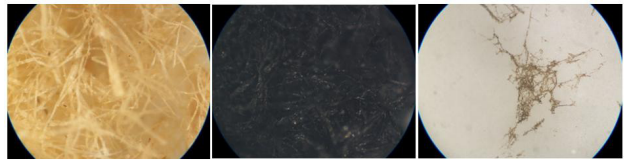

Fig. 3: Sodium silicate (N): a) original, b) after STA, c) after furnace.

As we can see in the third phase (Fig. 3), there are almost no remains of fibres after the furnace exposure, demonstrating that most of it combusted completely. The amount left is negligible.

Fig. 4: Pure fibres: a) original, b) after STA, c) after furnace.

Compared to pure fibres a difference in the first phase is visible (Figs. 3-4) as fibres are more bound and a colour shade appears to be a bit darker likely caused by the pH value of the treatment. The treatment formed a glass layer as shown at last phase of Fig. 4. There are no visible remains of fibres in the last phase.

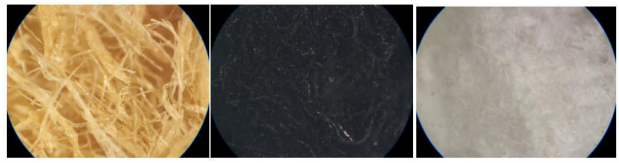

Fig. 5: Modified silicate (S): a) original, b) after STA, c) after furnace.

For the modified silicate (S) fibres in the first phase we can also see binding (Fig. 5), however the shade appears a bit brighter compared to sodium silicate (N) in Fig. 4. The third phase shows that the treatment attained a white crystalized form.

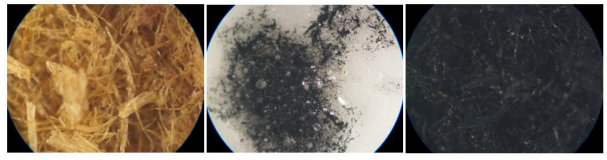

Fig. 6: Potassium silicate (K): a) original, b) after STA, c) after furnace.

At the phases of potassium silicate (K) (Fig. 6) we can see similarities with phases in Fig. 4, however in the third phase of Fig. 6 a minor remains are visibly melted into the glass formed by the treatment which we should take into account for it causes a small inaccuracy in the results. Time to ignition measurements are shown in Tab. 2. The results displayed represent average value as every measurement was done twice to achieve higher precision.

Tab. 2: Measured times of ignition of the specimens at different heat fluxes.

Specimen	Time of ignition (s)	Specimen	Time of ignition (s)	qe″(kW·m^{-2})
Pure 1	137.5	N 1	104	20
Pure 2	60	N 2	55	25
Pure 3	51	N 3	38	30
Pure 4	24.5	N 4	23.5	40
Pure 5	14	N 5	11	50
S 1	122.5	K 1	103.5	20
S 2	68	K 2	59.5	25
S 3	40	K 3	35.5	30
S 4	20	K 4	20.5	40
S 5	10.5	K 5	13	50

From the raw data we can see that untreated specimens exhibited the longest time to ignition in general, while treatments seem to reduce it. Ignition delay time 1/tig$^{1/2}$ (1/s$^{1/2}$) is calculated according to Eq. 1 for thermal thick behavior where *kpc* is thermal inertia, *qe″* is incident heat flux, *Tig* is temperature of ignition and *T0* is the ambient temperature which was measured to be 25 °C.

$$\frac{1}{\sqrt{t_{ig}}} = \frac{2}{\sqrt{\pi}\sqrt{k\rho c}} \frac{q_e^{"}}{(T_{ig} - T_0)} \tag{1}$$

These results are displayed in Fig. 7 and for a more detailed insight also in Tab. 3 with all the source data included. Along with the ignition delay time the critical heat flux q0ig" is estimated. For the description of deviation of results a standard deviation and standard error are evaluated.

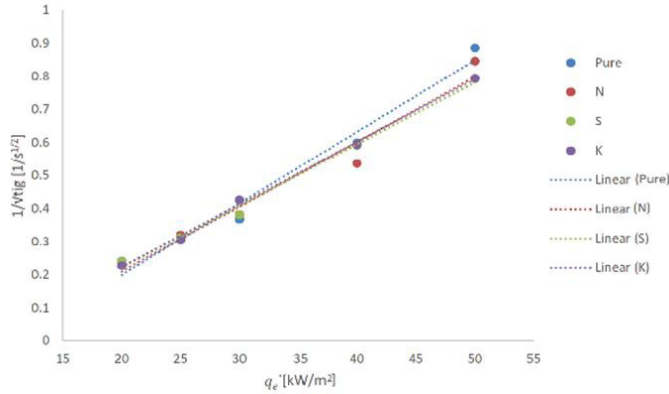

Fig. 7: Ignition delay time for different heat fluxes.

Tab. 3: Ignition delay time, critical heat flux and standard deviation of critical heat flux.

Specimen	**1/√tig (1/s$^{1/2}$)**	**Specimen**	**1/√tig (1/s1/2)**	**q_e" (kW·m^{-2})**
Pure 1	0.241	N 1	0.236	20
Pure 2	0.309	N 2	0.320	25
Pure 3	0.368	N 3	0.382	30
Pure 4	0.600	N 4	0.537	40
Pure 5	0.886	N 5	0.846	50
Slope	0.022 ±0.002	**Slope**	0.0196 ± 0.002	-
Intercept	-0.23 ± 0.07	**Intercept**	-0.18 ± 0.07	-
R^2	0.977	**R^2**	0.966	-
***q0ig*" (kW·m^{-2})**	11 ± 3	***q0ig"*(kW·m^{-2})**	9 ± 4	-
Specimen	**1/√tig (1/s$^{1/2}$)**	**Specimen**	**1/√tig (1/s$^{1/2}$)**	**q_e" (kW·m^{-2})**
S 1	0.240	K 1	0.228	20
S 2	0.313	K 2	0.305	25
S 3	0.382	K 3	0.427	30
S 4	0.591	K 4	0.594	40
S 5	0.792	K 5	0.794	50
Slope	0.0187 ± 0.0008	**Slope**	0.0189 ± 0.0005	-
Intercept	-0.15 ± 0.07	**Intercept**	-0.16 ± 0.02	-
R2	0.994	**R2**	0.998	-
q0ig" (kW·m^{-2})	8 ± 2	**q0ig" (kW·m^{-2})**	8 ± 1	-

The estimates of the critical heat flux q0ig" have shown that pure specimens achieve value of 11 ± 3 kW·m^{-2} which roughly corresponds to critical heat flux of wood in general. Different types of wood achieve values around 12 kW·m^{-2}. A decrease to 9 ± 4, 8 ± 2 and 8 ± 1 kW·m^{-2} in treated specimens seems odd as it appears to be counter-intuitive yet it matches the trending data when compared. Results of all of the measurements appear to be very similar which can be clearly seen visualized in Fig. 7. A gap of 2 – 3 kW·m^{-2} is minor, however should not be caused by error as standard deviations and standard errors of every type of treatment are almost identical, which means that no extreme values interfering data appeared or appeared equally in all measurements. Specimens were cut in half after the experiments conducted using cone calorimeter in order to investigate carbonized layer. Captures of specimens that were exposed to 50 kW·m^{-2} heat flux are shown in Fig. 8.

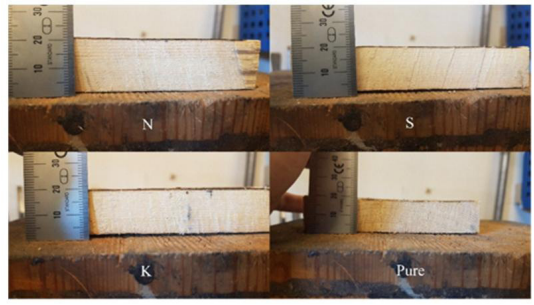

Fig. 8: Carbonized layer of spruce specimens – 50 kW·m^{-2} heat flux.

Approximately, a 0.5 mm thick carbonized layer occurred in all of the treated specimens. This, however, does not apply to the pure sample where carbonization occurred solely on the surface in significantly lesser extent. Furthermore, the pure specimen exhibited the longest time to ignition (Tab. 2a). It appears that small amount of these water glass flame retardants applied with thin impregnation layer accelerated the process of carbonization at high heat flux rates. This phenomenon did not occur in samples exposed to a lower heat flux of 20 $kW \cdot m^{-2}$, where the carbonized layer thickness occurred equally in all of the tested specimens. Increased carbonization in spruce specimens after usage of mono-ammonium phosphate flame retardant was also reported by (Hagen et al. 2009) as we as for many other flame retarding agents as reported by (Schaffer 1974) and (Nussbaum 1988). The surface temperature at ignition varied from 240 to 271°C in these specimens at 50 $kW \cdot m^{-2}$ heat flux, which is on the edge of onset temperatures range for pyrolysis of lignin (227-550°C) (Tan et al. 2006), cellulose (250-350°C) (Yeng et al. 2015) and hemicellulose (220-315°C) (Yang et al. 2007). It could also be that other organic compounds may help create the flammable mixture over the surface. So called extractives are common organic compounds found in wood, however their content in spruce wood reaches around 2% (Hillis 1971, Shebani et al. 2008). Their possible contribution to a flammable mixture creation in influential extent was therefore highly questionable and improbable. It is important to note that it was not a question of determining the course and development of the charred layer, but the final value after the end of the experiment. All measurements were in the same time interval.

CONCLUSIONS

The results of this experiment have shown the differences between tested treatments including no treatments. All of them have proved to have a significant effect on the pyrolysis of MDF fibres. According to biochar residue, sodium silicate (N) has shown the best results acquiring 34.14% of the former fibre mass of the sample. This is an interesting finding from the commercial point of view as it is the cheapest of the evaluated treatments and it improves also other properties of wood such as hardness, bending strength etc. (Ming-Li et al. 2019). Sample of MDF fibres treated with modified silicate (S) achieved the best results in thermogravimetric analysis (Fig. 1) with 54.87% of residual mass, however most of this residue (63.33%) consists of the treatment itself and biochar residue acquires the value of 30.84% of the former fibre mass (Tab. 1). Low pH value of modified silicate (S) enabled it to be retained in the MDF fibres most effectively compared to other treatments with 4.943 mg of treatment in 9.2824 mg of MDF fibres. Potassium silicate (K) acquired almost identical result of biochar residue like modified silicate (S) with value of 30.78%, however the share of treatment in the sample after pyrolysis was lower, achieving 48.17% which shows better efficiency at lower concentration compared to modified silicate (S). Both of these results are however outperformed by sodium silicate (N) having 36.74% share of treatment in the sample after pyrolysis and achieving best results in biochar residue as mentioned.

All three types of used water glass flame retardants show decrease in the onset temperature of pyrolysis which was also reported by (Hagen et al. 2009). The critical heat flux decrease from estimated 11 $kW \cdot m^{-2}$ to 9 $kW \cdot m^{-2}$ for sodium silicate (N) and 8 $kW \cdot m^{-2}$ for modified silicate (S) and potassium silicate (K) is most probably caused by application method where only thin layer of flame retardant in specimens was created. Authors that used vacuum pressure impregnation for wood materials report an increase in critical heat fluxes, see e.g. (Hagen et al. 2009). Cause of this decrease in fire resistant properties of flame retarded specimens might be that low amount of

thinly penetrated flame retardant might serve as empowering initializer of pyrolysis, as indicated before, yet failing to provide sufficient protection due to its inadequate impregnation. Another reason for the occurrence of this phenomenon might be that layer of flame retardant might obstruct the absorbed energy from cone to radiate partly back through the surface which would result in accelerated heating of the material on and under the surface accumulating heat, thus decreasing also the time to ignition. These are just hypotheses and further research is necessary in order to prove or disprove them.

ACKNOWLEDGEMENTS

The author would like to thank the Erasmus+ programme for the travelling grant enabling the stay at DTU FireLab. Also thank to the Danish company Bollerup Jensen A/S for providing the different water soluble silicates for material treatments.

This research was financially supported of the project KEGA 033ŽU-4/2019 "Integration of practical training in the study program of the rescue service".

REFERENCES

1. Anca-Couce, A., 2016: Reaction mechanisms and multi-scale modelling of lignocellulosic biomass pyrolysis. Progress in Energy and Combustion Science 53: 41-79.
2. Azizi, K., Moraveji, M.K., Najafabadi, H.A., 2017: Characteristics and kinetics study of simultaneous pyrolysis of microalgae *Chlorella vulgaris*, wood and polypropylene through TGA. Bioresource Technology 243: 481-491.
3. Baysal, E., Altay, C., Torkoglu, T., Toker, H., Peker, H., 2019: Impact of UV irradiance on selected parameters of Scots pine impregnated with some commonly used fire-retardants. Wood Research 64(2): 237-248.
4. Clausen, C.A., Green, F., Kartal, S.N., 2010: Weatherability and leach resistance of wood impregnated with nano-zinc oxide. Nanoscale Research Letters 5: 1464-1467.
5. England, P., Iskra, B., 2020: Australian building code change - eight-storey timber buildings. In: Wood & Fire Safety. Pp 219-225, Proceedings of the 9th International Conference on Wood & Fire Safety, Springer Nature Switzerland AG.
6. Eremina, T., Kuznetsova, I., Rodionova, L., 2020: The study of various factors influencing the fire retardant efficiency of wood varnish. Proceedings of the 9th International Conference on Wood & Fire Safety, Springer Nature Switzerland AG, Pp 119-113.
7. Fan, Y.J., Zhao, Y.Y., Hu, X.M., Wu, M.Y., Xue, D., 2020: A novel fire prevention and control plastogel to inhibit spontaneous combustion of coal: Its characteristics and engineering applications. Fuel 263(1): 1-9.
8. Gasparik, M., Makovicka Osvaldova, L., Cekovska, H., Potucek, D., 2017: Flammability characteristics of thermally modified oak wood treated with a fire retardant. Bioresources 12: 8451-8467.
9. Grønli, M.G., Várhegyi, G., Di Blasi, C., 2002: Thermogravimetric analysis and devolatilization kinetics of wood. Industrial & Engineering Chemistry Research 41: 4201-4208.
10. Hagen, M., Hereid, J., Delichatsios, M.A., Zhang, J., Bakirtzis, D., 2009: Flammability assessment of fire-retarded nordic spruce wood using thermogravimetric analyses and cone calorimetry. Fire Safety Journal 44(8): 1053-1066.

11. Hillis, W., 1971: Distribution, properties and formation of some wood extractives. Wood Science and Technology 5: 272-289.
12. Kloss, S., Zehetner, F., Dellantonio, A., Hamid, R., Ottner, F., Liedtke V., Schwanninger, M., Gerzabek, M.H., Soja, G., 2012: Characterization of slow pyrolysis biochars: Effects of feedstocks and pyrolysis temperature on biochar properties. Journal of Enviromental Quality 41: 990-1000.
13. Lou, Z., Han, H., Zhou, M., Han, J., Cai, J., Huang, C., Zou, J., Zhou, X., Zhou, H., Sun, Z., 2018: Synthesis of magnetic wood with excellent and tunable electromagnetic wave-absorbing properties by a facile vacuum/pressure impregnation method. ACS Sustainable Chemistry & Engineering 6(1): 1000-1008.
14. Lu, X., Li, Y.G., Zhou, X.F., Lei, F.H., Liu, Z.G., Wang, T., 2019: Degradation of wood fire retardant by UV assisted biomimetic oxidation over Cu([H4]salen) using BDE209 as a model. Wood Research 64(1): 83-96.
15. Makovicka Osvaldova, L., Osvald, A., 2013: Flame retardation of wood. Advance Materials Research (690-693): 1331-1334.
16. Makovická Osvaldová, L., Gašpercová. S., Mitrenga, P., Osvald. A., 2016: The influence of density of test specimens on the quality assessment of retarding effects of fire retardants. Wood Research 61(1): 35-42.
17. Ming-Li, L., Chun-Feng, L., Yan-Long, L., 2019: Physical and mechanical properties of modified poplar wood by heat treatment and impregnation of sodium silicate solution. Wood Research 64: 145-154.
18. Mitrenga, P., Vandlíčková, M., Dušková. M., 2016: Evaluation of the new fire retardants on wood by proposed testing method. Production management and engineering sciences. - Leiden; London: CRC Press/Balkema; Taylor & Francis Group: 481-485.
19. Nussbaum, R., 1988: The effect of low concentration fire retardant impregnations on wood charring rate and char yield. Journal of Fire Sciences 6: 290-307.
20. Qi Y., Jang, J.H., Hidayat, W., Lee, A.H., Lee, S.H., Chae, H.M., Kim, N.H., 2016: Carbonization of reaction wood from *Paulownia tomentosa* and *Pinus densiflora* branch wood. Wood Science and Technology 50: 973-987.
21. Schaffer, E., 1974: Effect of fire retardant impregnations on wood charring rate. Journal of Fire and Flammability/Fire Retardant Chemistry Supplement 1: 96-109.
22. Shebani, A.N., van Reenen, A.J., Meincken, M., 2008: The effect of wood extractives on the thermal stability of different wood species. Thermochimica Acta 471(1–2): 43-50.
23. Tan, H., Wang, S., Luo, Z.-Y., Cen, K. F., 2006: Pyrolysis behaviour of cellulose, xylan and lignin. Ranliao Huaxue Xuebao/Journal of Fuel Chemistry and Technology 34: 61-65.
24. Ustinov, A., Pitukhin, E., Pitukhin, A., 2017: Research of thermal stability and fire-resistance properties of the composite material "Water glass-graphite microparticles". Key Engineering Materials 744: 27-31.
25. Yang, H., Yan, R., Chen, H., Lee, D.H., Zheng, C., 2007: Characteristics of hemicellulose, cellulose and lignin pyrolysis. Fuel 86: 1781-1788.
26. Yeng, L.C., Wahit, M.U., Othman, N., 2015: Thermal and flexural properties of regenerated cellulose (RC)/ poly(3-hydroxybutyrate) (PHB) biocomposites. Jurnal Teknologi 75: 107-112.
27. Kasymov, D., Agafontsev, M., Perminov, V., Matrynov, P., 2019: Investigation of the ignition of wood structural materials (with and without fire retardant treatment) under the influence of a model fire of irregular intensity. The European Physical Journal Conferences 01/2019(196): 00038.

Juraj Jancík*, Linda Makovická Osvaldová
University of Žilina
Faculty of Security Engineering
Department of Fire Engineering
1. Mája 32
010 26 Žilina
Slovakia
*Corresponding author: juraj.jancik@fbi.uniza.sk

Frank Markert
Technical University of Denmark
Faculty of Civil Engineering
Department of Civil Engineering
Brovej 118
2800 Kongens Lyngby
Denmark

WOOD RESEARCH
66 (1): 2021
27-38
doi.org/10.37763/wr.1336-4561/66.1.2738

EXPERIMENTAL AND NUMERICAL STUDIES ON MECHANICAL BEHAVIORS OF BEECH WOOD UNDER COMPRESSIVE AND TENSILE STATES

Wengang Hu*, Bingrui Chen
Nanjing Forestry University
China

Tianxing Zhang
Wuyi University
China

(Received April 2020)

ABSTRACT

Effect of loading type (compression and tension) on mechanical properties, including elastic constants, yield strength and ultimate strength of beech (*Fagus orientalis*) wood were studied based on experimental and numerical methods. The mechanical behaviors of beech wood in compressive and tensile states were simulated by finite element method (FEM) using mechanical parameters measured in an experiment. The results showed that the effect of loading types on mechanical properties of beech was statistically significant. The elastic moduli measured in tension were all bigger than those in compression, but the Poisson's ratios determined in compression were bigger than those in tension. In compressive state, the yield and ultimate strengths of beech in longitudinal grain orientation were all smaller than those measured in tensile state, while the yield and ultimate strengths of beech in radial and tangential directions were higher than those of longitudinal direction. The results of the FEM in compression and tension were all well consistent with those measured by experiments respectively, and the average errors were all within 13.69%. As a result, the finite element models proposed in this study can predict the mechanical behaviors of wood in tensile and compressive states.

KEYWORDS: Beech, elastic modulus, compression, tension, loading type, FEM, *Fagus orientalis*.

INTRODUCTION

Beech (*Fagus orientalis*) wood is a main wood species naturally grown and commonly used in the forest products industry, especially in furniture industries in China. However, with the

decrease of qualified forestry resources, the wood materials should be used more scientifically and efficiently in wood products like furniture. Finite element method (FEM) has been commonly used in lots of engineering fields by the virtue of developing technologies (Liu et al. 2018, Zhou et al. 2017, Zhou et al. 2018, Hu et al. 2019, Valachova and Skotnicova 2019). Mackerle (2005) reviewed more than 300 articles published from 1995 to 2004 on using FEM in wood products and wood constructions, and the results emphasized that mechanical properties of wood were vitally important to the application of FEM in wood products.

The mechanical properties of wood are commonly divided into three stages including elasticity, plasticity and fracture. It is complicated to analyze the mechanical properties of wood with FEM by regarding it as an anisotropic material. In order to make it adjust to computer modeling, it is usually regarded as an orthotropic material. In this case, the mechanical properties of wood can be determined in longitude, radial and tangential directions by small clear wood samples.

Many studies have been investigated on elastic constants of wood through using different testing methods, such as electric resistance strain gauges (Aira et al. 2014, Adyin and Adyin 2018, Hu and Guan 2017a), non-destructive method (Tomazello et al. 2008, Xu et al. 2020), and resonant beam technique (Gerhard et al. 2020). Keunecke et al. (2008) performed tensile tests on dog-bone-shaped yew specimens and determined the three Young's moduli and six Poisson's ratios using a universal testing machine and a digital image correlation technique. Ozyhar et al. (2013) studied the influence of moisture on the elastic characteristics of beech wood by means of ultrasonic waves. Sobotka et al. (2017), also Andor and Bellovics (2020) used two methods for measurement Young´s modulus elasticity: static tensile test and three-point bend test to obtain statistical evaluation about influence of these testing methods on the final values of modulus of elasticity. Gonçalves et al. (2011) compared the elastic constants of wood determined by ultrasonic wave propagation and static compression testing, and the results showed the ultrasonic test for determining the Young's and shear moduli of wood was found to be simpler and less expensive than the static compression test, and the results were equally useful.

Elastic constant, yield and ultimate strengths are basic parameters used in FEM. If these parameters can be applied to simulating the mechanical behaviors of wood through using FEM, then mechanical properties of small wood block can be used to analyze the large structure of wood products by FEM. It will contribute to the design of wood products, and reduce costs of time and material. Tankut et al. (2014) gave a bibliographical review of the FEM applied in the analysis of furniture products construction with wood including wood as a furniture construction material and its mechanical properties. Kasal et al. (2016) studied the moment resistance, stiffness and numerical analysis of various sizes of round-end mortise and tenon joints with L-shaped and T-shaped specimens. Structure optimization design of modified wood mortise-and-tenon joint furniture using finite element method was studied by Chen and Wu (2018). Withdrawal resistance of mortise-and-tenon joint was studied by experiment and FEM based on the elastic constants measured using compressive method (Hu and Guan 2017b, Xi et al. 2020).

Previous studies confirmed that mechanical properties of wood were basic parameters needed in FEM, and FEM has been widely used in structure design of wood products and wood constructions. However, the mechanical parameters used in the FEM were usually measured in compression by regarding mechanical properties of wood measured in compression are the same with those in tension, which will decrease the accuracy of simulation based on FEM. The effect of loading type on elastic constants has rarely been studied. The aim of this paper is to study the influences of different loading types, i.e., compression and tension, on mechanical properties (elastic constants, yield strength and ultimate strength) of beech wood, and introduce how to use these parameters to simulate the wood mechanical behaviors based on FEM.

MATERIAL AND METHODS

Materials and equipment

All specimens were made with beech (*Fagus orientalis*) wood bought from local commercial supplier (Nanjing, China). The density averaged 712 kg·m^{-3}, and the moisture content of beech was conditioned to and held at 12.03% before and during tests. In addition, the temperature was controlled in 20 ± 2°C, and the relative humidity was 65 ± 3 % during the entire process of experiment. A 100 kN universal testing machine AG-IC (SHIMADZU, Japan) was applied to carry out the experiment. A static data acquisition instrument TDS-530 (TML, Japan) was applied to determine the elastic constants with electrical resistance strain gauges.

Specimen preparation

The specimens applied to determine the mechanical properties of beech in three grain orientations (longitudinal, radial, and tangential) and two loading types (compression and tension) were machined according to the GB/T 1935 (CNS 2009), GB/T 1939 (CNS 2009), GB/T 1938 (CNS 2009), GB/T 14017 (CNS 2009), respectively. The dimensions of compressive specimens in three directions were all 20 mm wide × 20 mm thick × 30 mm high. The dimensions of tensile specimens in radial (R) and tangential (T) directions were 30 mm wide × 20 mm thick × 150 mm long, and in longitudinal (L) direction was 20 mm wide × 15 mm thick × 370 mm long.

Testing methods

Fig. 1 shows dimensions, grain orientations, and positions of strain gauges of samples used to evaluate the elastic moduli (E_L, E_R, E_T), Poisson's ratios (v_{LR}, v_{LT}, v_{RT}, v_{RL}, v_{TR}, v_{TL}), and moduli of rigidity (G_{RT}, G_{RT} and G_{RT}) of beech wood. Specimens shown in Fig. 1a, b and c were applied to measure elastic moduli and Poison ratios of beech wood, and specimens presented in Figs. 1d,e,f were used to determine moduli of rigidity of beech. Ten measurements were repeated for each specimen type. In addition, compressive yield and ultimate strengths of beech wood were also determined by the same size specimens (Fig.1a,b,c) without sticking strain gauges. Fig. 2 shows dimensions and positions of strain gauges of specimens used to measure the mechanical properties of beech in tension. The specimens shown in Fig. 2a (front view) and Fig. 2b (top view) were used to determine mechanical properties of beech perpendicular to grain in tensile state. The elastic constants E_R, v_{RL}, E_T and v_{TL} were obtained, when the axial direction of specimens were radial and tangential respectively. Fig. 2c and Fig. 2d were front view and top view of specimens used to measure E_L, v_{LR} and v_{LT} with the wide direction of specimen in radial and tangential directions respectively. Each test was measured with ten replications. The moduli of rigidity in tensile state were not available in this study, since specimens used to determine them were not available. Fig. 3 shows the setups for measuring the elastic constants of beech in compression and tension.

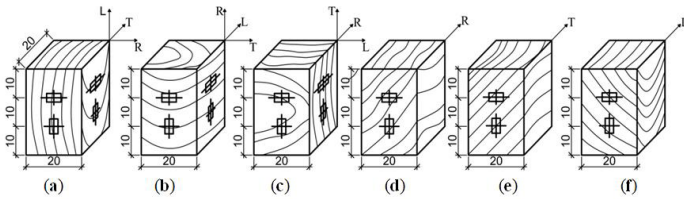

Fig. 1: Specimens used to determine elastic constants of beech in compression (units in mm).

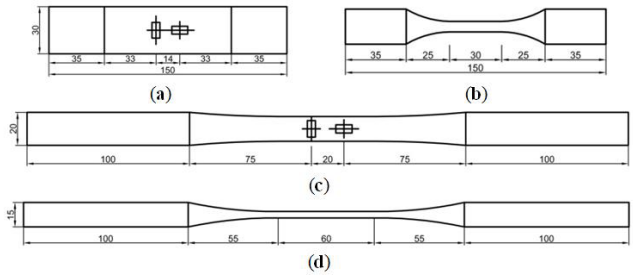

Fig. 2: Specimens used to measure the elastic constants of beech in tensile state (units in mm).

Fig. 3: Setup for measuring elastic constants of beech in compressive (a) and tensile, (b) states.

Finite element model

The finite element models were established by ABAQUS 6.14-1 software. Firstly, the geometric model of specimen was built in the same size with the beech wood specimen. It is recommended that established them in computer assistant design (CAD) software in advance and then imported them into ABAQUS.

The critical point to set up a finite element model was to specify the material properties of to model. The beech wood was regarded as an orthotropic material in this study. In the elastic stage of beech, the elastic constants were required to input as form of the elastic stiffness matrix shown in Eq. 1:

$$\begin{Bmatrix}\sigma_{11}\\ \sigma_{22}\\ \sigma_{33}\\ \sigma_{12}\\ \sigma_{13}\\ \sigma_{23}\end{Bmatrix}=\begin{bmatrix}D_{1111} & D_{1122} & D_{1133} & 0 & 0 & 0\\ \square & D_{2222} & D_{2233} & 0 & 0 & 0\\ \square & \square & D_{3333} & 0 & 0 & 0\\ \square & \square & \square & D_{1212} & 0 & 0\\ \square & \square & \square & \square & D_{1313} & 0\\ \square & \square & \square & \square & \square & D_{2323}\end{bmatrix}\begin{Bmatrix}\varepsilon_{11}\\ \varepsilon_{22}\\ \varepsilon_{33}\\ \varepsilon_{12}\\ \varepsilon_{13}\\ \varepsilon_{23}\end{Bmatrix} \quad (1)$$

where: $D_{1111} = E_L(1-\upsilon_{RT}\upsilon_{TR})\gamma$

$D_{2222} = E_R(1-\upsilon_{LT}\upsilon_{TL})\gamma$

$D_{3333} = E_T(1-\upsilon_{LR}\upsilon_{RL})\gamma$

$D_{1122} = E_L(\upsilon_{RL}+\upsilon_{TL}\upsilon_{RT})\gamma$

$D_{1133} = E_L(\upsilon_{TL}+\upsilon_{RL}\upsilon_{TR})\gamma$

$D_{2233} = E_R(\upsilon_{RT}+\upsilon_{LR}\upsilon_{TL})\gamma$

$D_{1212} = G_{LR}$

$D_{1313} = G_{LT}$

$D_{2323} = G_{RT}$

$$\gamma = \frac{1}{1-\upsilon_{LR}\upsilon_{RL}-\upsilon_{RT}\upsilon_{TR}-\upsilon_{LT}\upsilon_{RL}-2\upsilon_{RL}\upsilon_{TR}\upsilon_{LT}}$$

In plastic stage, the constitutive relationship of true stress and true strain are required. The true stress and true strain can be transported from engineering stress and strain by Eq. 2 and Eq. 3, respectively. In addition, the ultimate strength was regarded as the failure criterion of element. The elements will degrade when maximum stress exceeds the ultimate strength of wood.

$$\sigma_i = \sigma_{nom} (1 + \varepsilon_{nom}) \quad (2)$$

$$\varepsilon_i = \ln (1 + \varepsilon_{nom}) \quad (3)$$

where: σ_i - the true stress (MPa), σ_{nom} - engineering stress (MPa), ε_i - the true strain, ε_{nom} - engineering strain.

RESULTS AND DISCUSSION

Mechanical properties of beech

The elastic constants of beech in two loading types (compression and tension) were shown in Tab. 1. It suggests that the elastic moduli in tensile state were all bigger those in compressive state, while the Poison's ratios measured in tension were all smaller than those determined in compression. In addition, one-way analysis of variance (ANOVA) of the effect of the loading type on the elastic constants was conducted. The results showed the *p*-values of elastic moduli (E_L, E_R and E_T) were all smaller than 0.01 and *p*-values of Poisson's ratios were all bigger than 0.01, which indicated that the effect of loading type on elastic moduli was statistically significant, but on Poisson's ratios were not.

Tab. 1: Comparisons of elastic constants of beech measured in tensile and compressive states.

Loading type	**Elastic modulus (MPa)**			**Poisson's ratio** (dimensionless)						**Shear modulus (MPa)**		
	E_L	E_R	E_T	v_{LR}	v_{LT}	v_{RT}	v_{RL}	v_{TL}	v_{TR}	G_{LR}	G_{LT}	G_{RT}
Compression	12205	1858	774	0.500	0.710	0.530	0.078	0.038	0.370	899	595	195
Tension	13644	2024	1051	0.410	0.460	--	0.073	0.035	--	--	--	--

Note: "--" suggested that these parameters were not measured or available.

The yield strength is usually used to differentiate the elasticity and plasticity of wood (Xu and Cai 2015), and the ultimate strength is applied to judge whether the wood is destroyed or not. Tab. 2 presents the yield and ultimate strengths of beech wood in three directions measured in compression and tension indicating that the yield strengths and ultimate strengths in compression were all smaller than those in tension in L direction, while the yield strengths measured in compression in R and T directions were bigger than those measured in tension. In addition, the yield strengths and ultimate strengths of beech in L direction were all bigger than those in R and T directions, which was confirmed by previous studies (Xu and Cai 2015, Franke and Quenneville 2013). The ANOVA of effect of loading types on yield strengths and ultimate strengths were also conducted with their *p*-values all smaller than 0.01 meaning the effect of loading types on yield strengths and ultimate strengths was statistically significant.

Tab. 2: Yield and ultimate strengths of beech measured in compressive and tensile states.

States	Longitudinal (MPa)		Radial (MPa)		Tangential (MPa)	
	Yield strength	Ultimate strength	Yield strength	Ultimate strength	Yield strength	Ultimate strength
Compression	53.62(12.1)	58.21(6.5)	12.00(3.7)	23.82(12.2)	6.23(15.4)	48.88(4.7)
Tension	75.53(5.8)	168.25(8.6)	5.45(6.1)	17.13(5.4)	4.10(5.9)	9.71(6.3)

Note: The values in parentheses are coefficient of variances (COV).

The typical load-displacement curves in compression and tension were shown in Fig. 4. It suggested that failure behavior of beech in tension was similar to brittleness, while the mechanical behavior of beech in compression was not the same with that in tension, especially, in R and T directions. The load increased continuously after the plastic stage because the beech wood was compressed to denser than before, making it more solid. Therefore, in this study, the assumption was that the wood compressed within small deformation stage within 8 mm displacement.

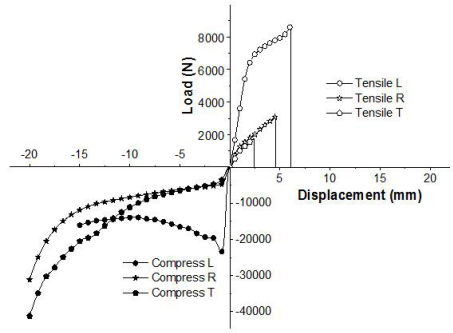

Fig. 4: Comparisons of mechanical behavior of beech measured in compressive and tensile states.

Comparisons between FEM and experiment

Fig. 5 shows the changes of stress distributions in longitudinal compression from beginning of loading (Fig. 5a) to the failure of sample (Fig. 5d). Figs. 5c,d were stress distributions during loading processes. The grain orientations of beech can be specified using local coordinates in ABAQUS. The load-displacement curves in three grain orientation were obtained by ABAQUS, which were used to compare with the results of experiments.

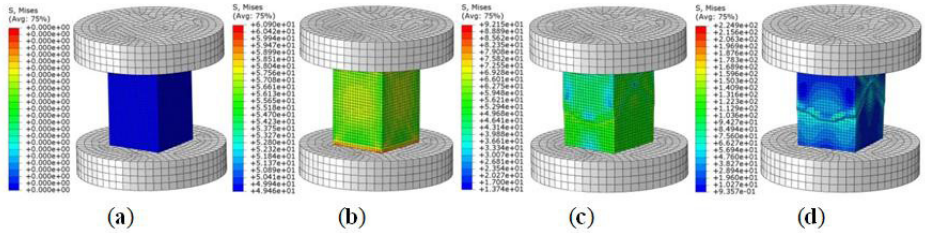

Fig. 5: Stress distributions of wood in compressive state based on FEM during loading process.

Fig. 6 shows load-displacement curves of experiments and FEMs in three grain orientations in compressive state, suggesting that the results of FEMs were well consistent with those of experiments, especially in R and T grain orientations. Furthermore, Tab. 3 shows the errors between the results of FEM and experiment compared at five certain points of displacements from 1 mm to 8 mm with 1 mm increment in R and T direction, and 0.5 mm increment in L direction. The average errors are 13.69%, 4.93% and 3.96% in L, R and T directions, respectively.

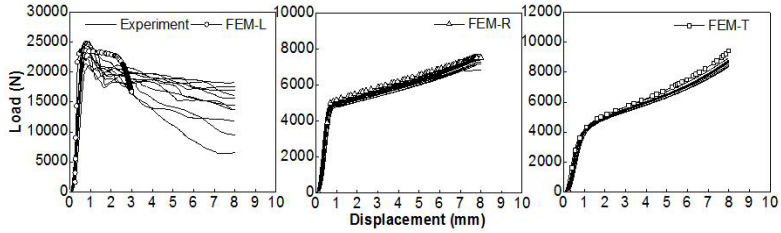

Fig. 6: Comparisons of load-displacement curves of experiment and FEM in compressive state.

Tab. 3: Comparisons of load values between FEM and experiment in compressive state at different displacement points.

Displacement	Longitudinal (N)		Error	Radial (N)		Error	Tangential (N)		Error
(mm)	Observed	FEM	(%)	Observed	FEM	(%)	Observed	FEM	(%)
0.5	18362 (14.1)	23245	28.23	4975 (2.1)	5183	4.18	4015 (3.5)	4332	7.90
1.0	23394 (6.7)	23511	0.50	5281 (2.3)	5604	6.11	4965 (1.6)	5196	4.67
1.5	20196 (5.2)	23223	14.99	5592 (2.3)	5889	5.31	5484 (1.7)	5491	0.13
2.0	19570 (5.5)	22890	16.96	5908 (2.2)	6199	4.93	5965 (1.7)	6199	3.92
2.5	19307 (5.5)	21258	10.10	6248 (2.2)	6557	4.95	6483 (1.7)	6557	1.14
3.0	18834 (7.5)	16690	11.39	6619 (2.3)	6891	4.10	7076 (1.8)	7502	6.02
Average	--	--	13.69	--	--	4.93	--	--	3.96

Note: The values in parentheses are coefficient of variances (COV).

Fig. 7 shows the stress distributions of beech in tensile state. It presents the variations of stress distributions during loading processes (Figs. 7a-d). The load-displacement curves of three grain orientations were output by ABAQUS.

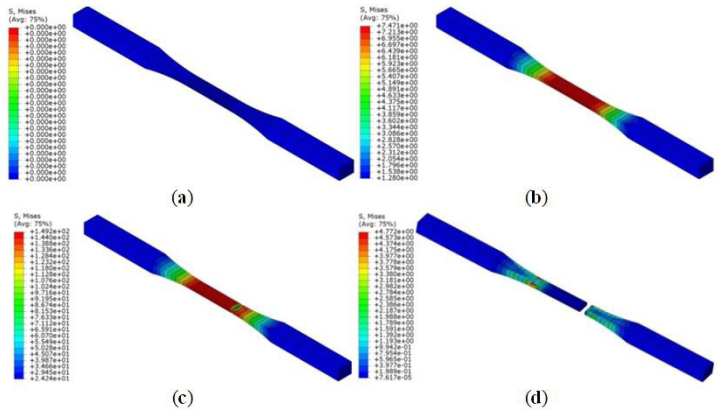

Fig. 7: Stress distributions of beech in tensile state during loading process.

Fig. 8 shows load-displacement curves of experiments and FEMs in tension, which suggests that load-displacement curves experienced the elastic, plastic and fracture stages. The results of the FEMs were in good agreement with those of experiments in three directions. In addition, errors between FEM and experiment in three directions were analyzed shown in Tab. 4 indicating that the average errors of FEMs in L, R, and T directions were 6.95%, 2.44%, and 10.92%, respectively.

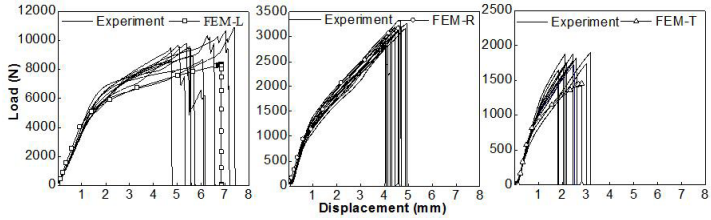

Fig. 8: Comparison of load-displacement curves between FEM and experiment in tensile state.

Tab. 4: Comparisons of load values between FEM and experiment in tensile state at different displacement points.

Displacement	Longitudinal (N)		Error	Radial (N)		Error	Tangential (N)		Error
(mm)	Observed	FEM	(%)	Observed	FEM	(%)	Observed	FEM	(%)
1	3799 (5.0)	4022	5.86	1239 (7.0)	1256	1.32	499 (4.4)	572	14.68
2	6207 (5.6)	5898	4.99	1829 (5.6)	1905	4.15	1010 (8.3)	970	3.88
3	7294 (4.9)	6737	7.63	2342 (4.6)	2395	2.29	1307 (9.7)	1146	12.34
4	8000 (5.8)	7256	9.30	2882 (3.4)	2939	1.99	1558 (9.7)	1359	12.79
Average	--	--	6.95	--	--	2.44	--	--	10.92

Note: The values in parentheses are coefficient of variances (COV).

CONCLUSIONS

In this study, the mechanical properties of beech wood in compression and tension were studied by experimental and numerical methods. Following conclusions were drawn: (1) The effect of loading type on elastic moduli were significant, but on Poisson's ratios were not. The elastic moduli measured in tensile state were all higher than those measured in compression, while the Poisson's ratios measured in compression were bigger than those in tension. (2) The results of ANOVA showed that the effect of loading types on yield and ultimate strengths were statistically significant. The yield and ultimate strengths of beech wood in L direction in compression were all smaller than those in tension. While the yield strengths of beech wood in R and T grain orientations in compression were bigger than those in tension. (3) The results of the proposed finite element model were all well consistent with those measured by experiments in compression and tension, and the errors were all within 13.69 %.

In conclusion, the finite element models created in this study were capable of predicting the mechanical behaviors of beech wood in compression and tension using the mechanical parameters measured in corresponding loading types. The methods used to obtain the mechanical properties should be considered when used in FEM. This study will contribute to promote FEM used in wood structures design and got more accurate simulations.

ACKNOWLEDGMENTS

This work was supported by a Scientific Research Foundation of Metasequoia teacher (163104060), Project from International Cooperation Joint Laboratory for Production, Education, Research and Application of Ecological Health Care on Home Furnishing.

REFERENCES

1. Aira., J.R., Arriaga., F., González, G.L., 2014: Determination of the elastic constants of scots pine (*Pinus sylvestris* L.) wood by means of compression tests. Biosystem Engineering 126: 12–22.
2. Andor, K., Bellovics, B., 2020: Analysis of modulus of elasticity of spruce beams under bending with and without fibre reinforcement. Wood Research 65(1): 101-110.
3. Aydin, Y., Aydin, M., 2018: Comparison of temperature dependent Young's modulus of oriental beech (*Fagus orientalis* L.) that determined by ultrasonic wave propagation and compression test. Turkish Journal of Forestry 19(2): 185–191.
4. Chen, Y,S., Wu, Z.H., 2018: Study on structure optimization design of modified wood furniture tenon structure based on the finite element analysis of ANSYS. Journal of Intelligent & Fuzzy Systems 34(2): 913-922.
5. CNS GB/T 1935, 2009: Method of testing in compressive strength parallel to grain of wood.
6. CNS GB/T 1939, 2009: Method of testing in compression perpendicular to grain of wood.
7. CNS GB/T 1938, 2009: Method of testing in tensile strength parallel to grain of wood.
8. CNS GB/T 14017, 2009: Method of testing in tensile strength perpendicular to grain of wood.
9. Divos, F., Tanaka, T., Nagao, H., Kato, H., 1998: Determination of shear modulus on construction size timber. Wood Science and Technology 32(6): 393-402.

10. Franke, S., Quenneville, P., 2013: Compression behavior and material parameters of radiata pine at different orientations to the grain. Journal of Materials in Civil Engineering 25(10): 1514-1523.
11. Gerhard, S., Maierhofer, J., Loidli, D., Puchegger, S., Stanzl-Tschegg, S., 2020: Elastic constants of six wood species measured with the resonant beam technique. Wood Research 65(2): 347-352.
12. Goncalves, R., Trinca, A.J., Cerri, D.G.P., 2011: Comparison of elastic constants of wood determined by ultrasonic wave propagation and static compression testing. Wood and Fiber Science 43(1): 64-75.
13. Hu, W.G., Guan, H.Y., 2017a: Study on elastic constants of beech in different stress states. Journal of Forestry Engineering 2(06): 31-36.
14. Hu, W.G., Guan, H.Y., 2017b: Investigation on withdrawal capacity of mortise and tenon joint based on friction properties. Journal of Forestry Engineering 2(04): 158-162.
15. Hu, W.G., Wan, H., and Guan, H.Y., 2019: Size effect on the elastic mechanical properties of beech and its application in finite element analysis of wood structures. Forests 10(9): 783.
16. Keunecke, D., Hering, S., Niemz, P., 2008: Three-dimensional elastic behaviour of common yew and Norway spruce. Wood Science and Technology 42(8): 633-647.
17. Kasal, A., Smardzewski, J., Kuşkun, T., Erdil, Y.Z., 2016: Numerical analyses of various sizes of mortise and tenon furniture joints. BioResources 11(3): 6836-6853.
18. Liu, J.X., Zhou, W., Li, C., 2018: Stress wave vibration characterization of cross section of log using finite element method. Journal of Forestry Engineering 3(6): 19-24.
19. Mackerle, J., 2005: Finite element analyses in wood research: a bibliography. Wood Science and Technology 39(7): 579-600.
20. Ozyhar, T., Hering, S., Sanabria, S.J., Niemz, P., 2013: Determining moisture-dependent elastic characteristics of beech wood by means of ultrasonic waves. Wood Science and Technology 47(2): 329-341.
21. Sobotka, J., Solfronk, P., Korecek, D., Kolnerova, M., 2017: Influence of testing methods on the final values of the modulus of elasticity E. MM Science Journal (05): 1942-1946.
22. Tankut, N.D., Tankut, A.N., Zor, M., 2014: Finite Element Analysis of Wood Materials. Drvna Industrija 65(2): 159-171.
23. Tomazello, M., Brazolin, S., Chagas, M.P., Oliveira, J.T.S., Ballarin, A.W., Benjamin, C.A., 2008: Application of X-ray technique in nondestructive evaluation of eucalypt wood. Maderas-Ciencia y Tecnologia 10(2): 139-149.
24. Valachova, D., Skotnicova, I., 2019: Using the finite element method to predict heat dissipation in a timber frame building construction. Wood Research 64(5): 859-870.
25. Xi, X., Yang, Y., Zhang, Z.F., 2020: Pull-out force and finite element analysis of T-type components of *Vitex negundo* L. scrimber with different node forms. Journal of Forestry Engineering 5(1): 182-187.
26. Xu, B.H., Cai, J., 2015: State-of-the-art in strength criteria for wood. China Civil Engineering Journal 48(1): 64-73.
27. Xu, W., Fang, X.Y., Han, J.T., Wu, Z.H., Zhang, J.L., 2020: Effect of coating thickness on sound absorption property of four wood species commonly used for piano soundboards. Wood and Fiber Science 52(1): 28-43.
28. Zhao, Z., Sakai, S., Wu, D., Chen, Z., Zhu, N., Huang, C., Sun, S., Zhang, M., Umemura, K., Yong, Q., 2019: Further exploration of sucrose–citric acid adhesive: investigation of optimal hot-pressing conditions for plywood and curing behavior. Polymers 11:1996.

29. Zhou, C.M., Yu, M.N., Zhou, T., 2018: Experimental study on three-dimensional shape mapping of complex furniture. EURASIP Journal on Image and Video Processing (9): 89.
30. Zhou, F.S., Li, L.J., Ouyang, Y.B., 2017: Lightweight research of mower frame based on ANSYS. Journal of Forestry Engineering 2(6): 103-109.

Wengang Hu*, Bingrui Chen
Nanjing Forestry University
Co-Innovation Center of Efficient Processing and Utilization of Forest Resources
College of Furnishings and Industrial Design
Nanjing 210037
China
*Corresponding author: hwg@njfu.edu.cn

Tianxing Zhang
Wuyi University
School of Art and Design
Jiangmen, 529020
China

WOOD RESEARCH
66 (1): 2021
39-48
doi.org/10.37763/wr.1336-4561/66.1.3948

THE CONCENTRATION OF SELECTED HEAVY METALS IN POPLAR WOOD BIOMASS AND LIQUID FRACTION OBTAINED AFTER HIGH TEMPERATURE PRETREATMENT

Donata Krutul, Jan Szadkowski, Andrzej Antczak,
Michał Drożdżek, Andrzej Radomski, Stanisław Karpiński,
Janusz Zawadzki
Warsaw University of Life Sciences
Poland

(Received May 2020)

ABSTRACT

The concentration of selected heavy metals: chromium (Cr), manganese (Mn), iron (Fe), nickel (Ni), copper (Cu) and zinc (Zn) in 5-year-old wood of *Populus trichocarpa* before and after steam explosion (SE) and liquid hot water (LHW) pretreatments was studied. The concentration of the above heavy metals in the liquid fraction obtained after pretreatments was also studied. The studied problem of heavy metals in lignocellulosic biomass is an interesting and important issue in the context of bioethanol production technology. An X-ray fluorescence spectrometer (XRF) was used to analyse the concentration of heavy metals. The change of concentration of the tested elements in wood biomass after pretreatment was small (except for iron). On the other hand, the average concentration of iron in wood biomass of a 5-year-old *Populus trichocarpa*, after SE and LHW with duration of the pretreatments 15 and 60 min, increased about 24-fold to 28-fold, comparing to its average concentration in native wood. During the pretreatment process, wood biomass absorbed the iron that at high temperatures passed from the pretreatment equipment to the solution. The average concentration of the elements under research in liquid fraction obtained during SE and LHW of wood biomass with duration of the pretreatments 15 and 60 min was at a low level.

KEYWORDS: *Populus trichocarpa*, poplar, steam explosion, liquid hot water, liquid fraction, heavy metals.

INTRODUCTION

Nowadays biomass hydrolysis is preferably performed via the enzymatic process, although acidic hydrolysis is better known. Acidic hydrolysis causes a higher negative impact on the natural

environment and that is why the application using enzymes has been focused on. Enzymatic hydrolysis is basically a well known process and has been used many times by different authors (Mansfield et al. 1999, Palonen et al. 2004, Martin et al. 2008, Kumar and Wyman 2009, Studer et al. 2011, Antczak et al. 2018, Antczak et al. 2019), but the high cost of the enzymes to be used make the process unprofitable. The content of possible enzymatic hydrolysis inhibitors in raw material is also a very important factor which should be taken in to account.

The technological process of biofuel production from wood biomass can be hindered by organic and inorganic inhibitors. Among organic substances, it is worth mentioning furan aldehydes created mostly as a result of decomposition and further transformations of hemicelluloses to furfural, 5-hydroxymethylfurfural, as well as soluble phenolic compounds appearing due to lignin degradation (Palmqvist and Hahn-Hägerdal 2000a, b, Klinke et al. 2002, Garcia-Aparicio et al. 2006, Alvira et al. 2010, Horn et al. 2011, Tomás-Pejó et al. 2011, Chandel et al. 2013, Jönsson et al. 2013).

Poplar is a known fast-growing species which can be used for biofuel production. It may be useful as a raw material further processed to biogas or liquid biofuels (Antczak et al. 2014, Antczak et al. 2018).

Inorganic inhibitors include some heavy metals which can accumulate in the trees depending on their growth environment, as well as in the wood during the process of its impregnation finish, as well as during pretreatment of lignocellulosic biomass during its preparation for biofuel production. The source of contamination with metals can be compounds and alloys used to manufacture the blades of industrial wood grinders, as well as reactors, in which the pretreatment processing takes place (Palmqvist and Hahn-Hägerdal 2000a,b). During pretreatment, high temperature and pressure can facilitate the transfer of metals from the machines into wood biomass. Metals can also pass to the liquid fraction created after pretreatment (Warzee et al. 1966). The salts of chromium, iron, nickel and copper are metal compounds considered to be inhibitors in wood biomass pretreatment processes and its fermentation (Warzee et al. 1966, Chandel et al. 2013). Moreover, some of metal ions may additionally bind to lignin, causing a change in the energy potential of the biomass leading to an increase of enzymatic hydrolysis efficiency (Liu and Zhu 2010, Akimkulova et al. 2016). The process of enzymatic hydrolysis of wood biomass leads to ions of such metals being combined with proteins, which causes their denaturation and deactivation, and as a consequence: lower efficiency of glucose production. In the available literature, there is scarce information on studies of heavy metals concentration released during pretreatment such as steam explosion and liquid hot water of poplar wood biomass.

The aim of this paper was to investigate the concentration of selected heavy metals in 5-year-old *Populus trichocarpa* wood biomass before and after SE and LHW pretreatments. The concentration of the above heavy metals in liquid fraction obtained after pretreatments was also studied.

MATERIAL AND METHODS

Material (mixed sapwood and hardwood) were obtained from the trunk of an about 5-year-old *Populus trichocarpa*. The high temperatures used in pretreatment processes of plant biomass cause the transmission of chemical compounds from the solid fraction to the liquid fraction used as reaction environment.

The measurement of heavy metal concentration in the wood was performed for such metals as Cr, Ni, Cu, Mn, Zn and Fe, after the wood was burnt and converted to ashes. On the other hand, in the liquid fraction generated after pretreatment, the measurement was conducted directly.

The heavy metal concentration was measured with an X-ray fluorescence spectrometer Spectro Midex M. The spectrometer was equipped with a 540 x 600 x 2500 mm chamber, with test bench positioning with the precision of 2.5 μm. Measurement points were set with the help of a system of two cameras controlled by the Spectrum X-labro software, permitting very precise location of the measurement points and the position of the sample in relation to the detector. Moreover, the device was equipped with an X-ray lamp cooled with air, containing a molybdenum anode. The maximum power was 30 W, and the maximum voltage, 50 kV. The heavy metal concentration was measured for wood biomass of *Populus trichocarpa* before and after SE and LHW processes.

Wood biomass was converted into ashes in a muffle furnace, which took 6 hours at 600˚C. The increase at temperature from 20˚C to 600˚C lasted for additional 2.5 hours. Samples were converted to ashes in order to concentrate them (Harju et al. 1997).

Wood biomass was subjected to steam explosion in a stainless steel autoclave. According to the technical specification (Explo Solution company), the autoclave was made of 316Ti stainless steel (complaint with the PN-EN 10088-1) characterized by the following composition: C- max. 0.080%, Mn- max. 2.00%, Si- 0.75%, P- 0.045%, S- 0.030%, Cr- 16.00 ÷ 18.00%, Ni- 10 ÷ 14.00%, Mo- 2.00 ÷ 3.20%, Ti- max. 0.70%, N- max. 0.10%. The interchangeable elements of the apparatus, in accordance with the technical specification (Explo Solution company), are made of CuZn33 brass (complaint with the PN-EN 1652), composed of: Cu- 66.0 up to 68.0%, Pb- max. 0.05%, Al- max. 0.02%, Fe- max. 0.05%, Ni- max. 0.3%, Sn- max. 0.1% and Zn- 31.5%.

The wood biomass of a 5-year-old *Populus trichocarpa* was subjected to the processes of SE and LHW. The processes were done in a stainless-steel reactor with a total volume of 250 cm^3. To each of pretreatment process about 20 g of size reduced (fraction between 0.43 and 1.02 mm) wood was used. Before the pretreatment, the wood in the reactor was supplemented with distilled water to a volume of 250 cm^3. The ratio of wood to distilled water was 1:12.5. The SE and LHW processes were conducted at temperatures of 160˚C, 175˚C and 190˚C, with duration of the pretreatments 15 and 60 min. The concentration of selected metals in the liquid fraction obtained after pretreatments was tested in drops, whose volume amounted to about 0.3 cm^3 of liquid. In addition, the concentration of heavy metals in distilled water, which was used during the pretreatment, was tested. For each processing temperature and pretreatment kind (SE and LHW) at least three drops of the same volume were tested, and one point of measurement was set in each of them. The test made use of a 2 x 2 mm shutter and time of exposure of 300 sec.

RESULTS AND DISCUSSION

The results of the concentration of selected metals in native wood (biomass before the pretreatments) of a 5-year-old *Populus trichocarpa*, in wood after high temperature pretreatments with different residential times (15 and 60 min), in distilled water and in liquid fraction are presented in Figs. 1-6. On the basis of the data presented in Fig. 1, we can conclude that the chromium concentration in wood biomass subjected to steam explosion, independently of the temperature and time of pretreatment, doubled or tripled, comparing with the concentration of this metal in native wood and in distilled water. The average concentration of chromium in liquid fraction oscillated between 26.0-29.0 ppm, independently of the steam explosion temperature and heating temperature residential time.

The data provided by Zielenkiewicz et al. (2016) indicate that the concentration of chromium in a native wood of 2.5-year-old *Populus trichocarpa* amounted to 11 ppm, which is consistent with the data obtained for a native wood of 5-year-old *Populus trichocarpa* (10.0 ppm). The average

concentration of chromium in the wood biomass of the 5-year-old *Populus trichocarpa* after the LHW process with residential times of 15 and 60 min it was similar to its concentration in wood biomass after steam explosion, and fell in the range between 17.0 ppm and 41.0 ppm (Fig. 1).

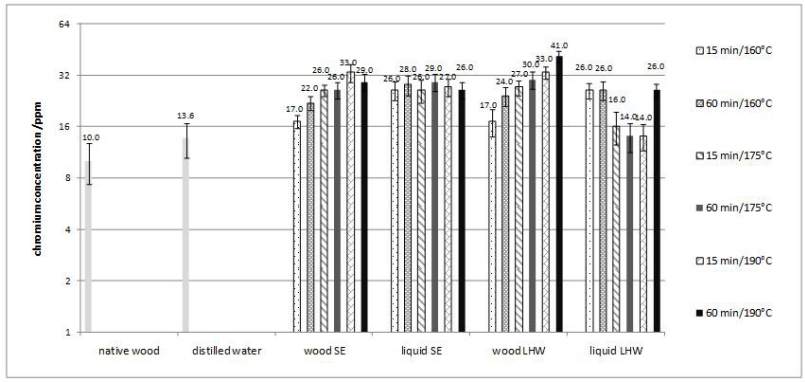

Fig. 1: Chromium concentration in native wood of a 5-year-old Populus trichocarpa, in wood after high temperature pretreatments (SE and LHW) with different residential times (15 and 60 min), in distilled water and in liquid fraction obtained after above pretreatments.

In the wood biomass of a 2.5 year-old *Populus trichocarpa* subjected to steam explosion at the temperatures of 160°C and 190°C, the concentration of chromium was 17 ppm and 32 ppm, respectively. In the wood biomass of a 5 year-old *Populus trichocarpa* subjected to steam explosion at the temperatures of 160°C, 175°C and 190°C, the average concentration of chromium was from 17.0 ppm to 33.0 ppm, in both heating times: 15 and 60 min. To sum up, it can be concluded that both native wood and wood biomass after steam explosion have a low concentration of chromium. Similarly, in the liquid fraction obtained after SE and LHW, the average concentration of this element fell in the range between 14.0 ppm and 29.0 ppm (Fig. 1).

On the basis of data presented in Fig. 2, it can be concluded that the concentration of nickel in the wood of the 5-year-old *Populus trichocarpa* and wood biomass after high temperature treatment was similar to the chromium concentration (Fig. 1). In wood biomass after steam explosion at the temperatures of 175°C and 190°C, with residential times of 15 and 60 min, the average concentration of nickel was two and three times higher than its average concentration in native wood or in distilled water, and fell in the range between 34.0 ppm and 51.0 ppm. According to Zielenkiewicz et al. (2016), in the wood biomass of a 2.5 year-old *Populus trichocarpa* subjected to steam explosion at the temperatures of 160°C and 190°C, with residential times of 15 and 60 min, the concentration of nickel amounted to 16 ppm and 40 ppm, respectively. For the liquid fraction obtained after steam explosion treatment of the wood biomass of a 5-year-old *Populus trichocarpa* at the temperatures of 160°C, 175°C and 190°C, with residential times of 15 and 60 min, the average concentration of nickel fell in the range between 38.0 ppm and 41.0 ppm (Fig. 2). Similarly to the concentration of chromium and nickel, the average concentration of copper in the native wood of a 5-year-old *Populus trichocarpa* was low and amounted to 14.0 ppm (Fig. 3).

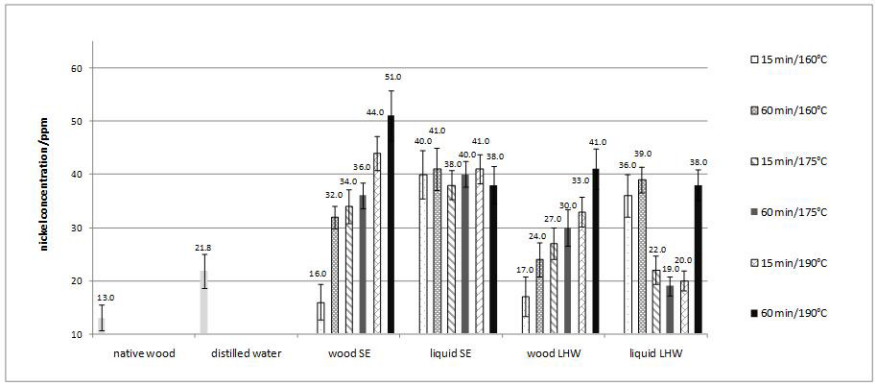

Fig. 2: Nickel concentration in native wood of a 5-year-old Populus trichocarpa, in wood after high temperature pretreatments (SE and LHW) with different residential times (15 and 60 min), in distilled water and in liquid fraction obtained after above pretreatments.

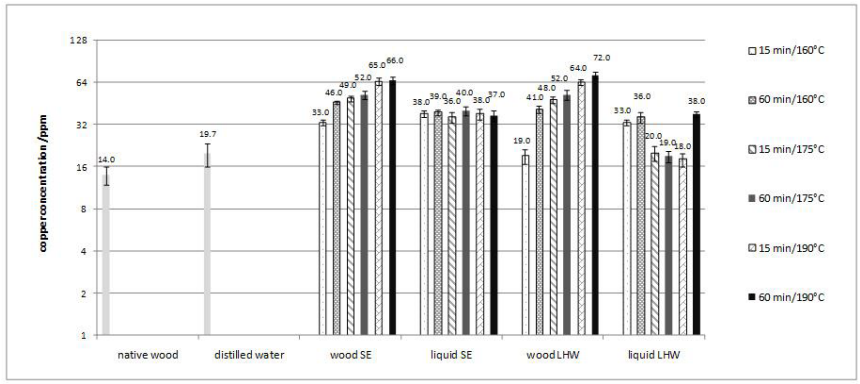

Fig. 3: Copper concentration in native wood of a 5-year-old Populus trichocarpa, in wood after high temperature pretreatments (SE and LHW) with different residential times (15 and 60 min), in distilled water and in liquid fraction obtained after above pretreatments.

Also according to Zielenkiewicz et al. (2016), the concentration of copper in the wood of a 2.5-year-old *Populus trichocarpa* amounted to 12 ppm and its concentration increased 6-fold in the biomass after steam explosion treatment at 130°C, 3-fold after the treatment at 160°C, and 5-fold after the treatment at 190°C. On the basis of data presented in Fig. 3, we can see that the copper average concentration in wood biomass subjected to pretreatment with SE and LHW, with residential times of 15 and 60 min, at the temperature of 190°C increased 4- and 5-fold comparing to its average concentration in native wood and increased 3-fold comparing to its average concentration in distilled water. The average concentration of copper in the liquid fraction changed irregularly together with the increase of process temperature and residential time during which the heating temperature was maintained.

Fig. 4 presents data concerning the concentration of manganese in the native wood of a 5-year-old *Populus trichocarpa*, in biomass after SE and LHW processes, as well as in distilled water and in the liquid fraction. The native wood of the 5-year-old *Populus trichocarpa* had

a manganese average concentration of 118.0 ppm, which was similar to its concentration in the wood of a 2.5-year-old *Populus trichocarpa*, amounting to 120 ppm (Zielenkiewicz et al. 2016). The average concentration of manganese in wood biomass after pretreatment with steam explosion, independently of the temperature and the residential time, did not change, while wood biomass after LHW contained about 10% more of manganese comparing to its average concentration in native wood. In the liquid fraction obtained after pretreatment processes of wood biomass and in distilled water, the manganese average concentration was low and fell in the range between 12.0 ppm and 31.0 ppm (Fig. 4).

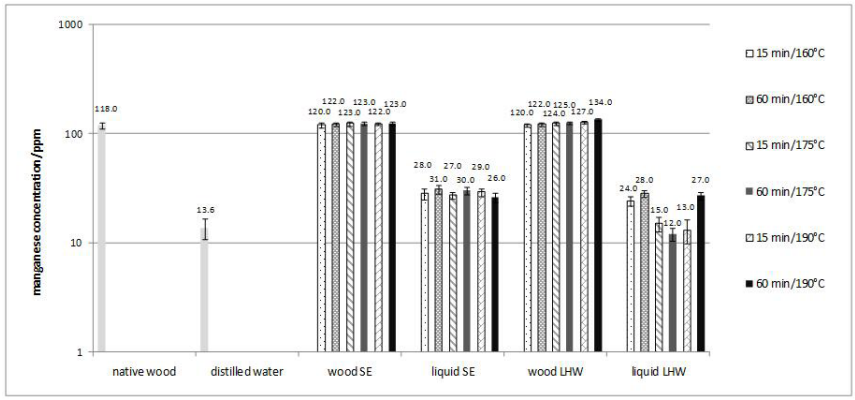

Fig. 4: Manganase concentration in native wood of a 5-year-old Populus trichocarpa, in wood after high temperature pretreatments (SE and LHW) with different residential times (15 and 60 min), in distilled water and in liquid fraction obtained after above pretreatments.

The average concentration of zinc in the native wood of a 5-year-old Populus trichocarpa amounted to 155.0 ppm (Fig. 5) and was similar to its concentration in a 2.5-year-old *Populus trichocarpa*, where it amounted to 160 ppm (Zielenkiewicz et al. 2016). The concentration of zinc in wood biomass after SE and LHW processes increased together with the increase in process temperature and residential time, from about 10% to about 30%.

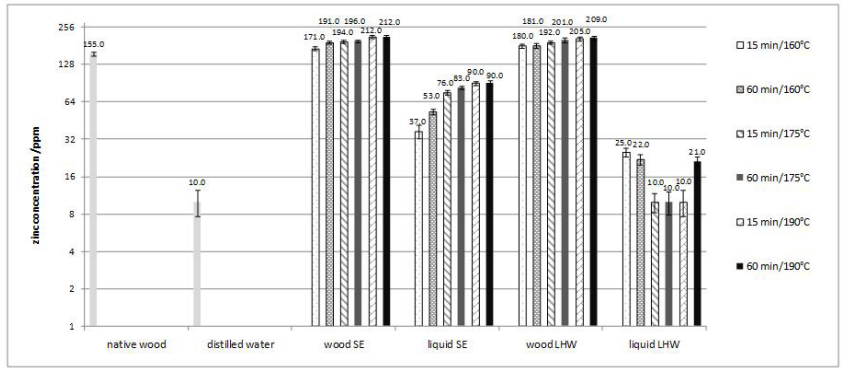

Fig. 5: Zinc concentration in native wood of a 5-year-old Populus trichocarpa, in wood after high temperature pretreatments (SE and LHW) with different residential times (15 and 60 min), in distilled water and in liquid fraction obtained after above pretreatments.

According to Zielenkiewicz et al. (2016), the wood biomass of a 2.5 year-old *Populus trichocarpa* subjected to steam explosion at the temperature of 130°C, with residential time of 15 min, the concentration of zinc increased two-fold comparing to its concentration in native wood; while after the process at 160°C it did not change; and it increased by 20% after the steam explosion process at 190°C. On the other hand, the concentration of zinc in the liquid fraction, generated as a result of pretreatment of wood biomass of a 5-year-old *Populus trichocarpa* both with SE and LHW, changed irregularly together with the increase in process temperatures and residential time during which the heating temperature was maintained.

On the basis of data presented in Fig. 6, we can conclude that the average concentration of iron in the wood of a 5-year-old *Populus trichocarpa* was low and amounted to 54.0 ppm. The iron average concentration in wood biomass after pretreatment processes (SE and LHW) at the temperatures of 160°C, 175°C and 190°C, with residential times of 15 and 60 minutes, grew from about 24 to 28 times, comparing to the iron average concentration in native wood. On the other hand, the average concentration of iron in the liquid fraction, generated as a result of pretreatment of wood biomass of a 5-year-old *Populus trichocarpa* both with SE and LHW, was low, as in distilled water, between 16.0 ppm and 40.0 ppm. On the basis of the presented data, it can be concluded that during the SE and LHW pretreatment processes, wood biomass absorbed the iron that passed from the pretreatment equipment to the solution due to high temperatures. The data obtained are in line with the findings of Zielenkiewicz et al. (2016), suggesting that the wood biomass of a 2.5 year-old *Populus trichocarpa* subjected to steam explosion at the temperatures of 130°C, 160°C and 190°C, without maintaining the heating temperature, contained a 43-times and 24-times higher iron concentration than the native wood.

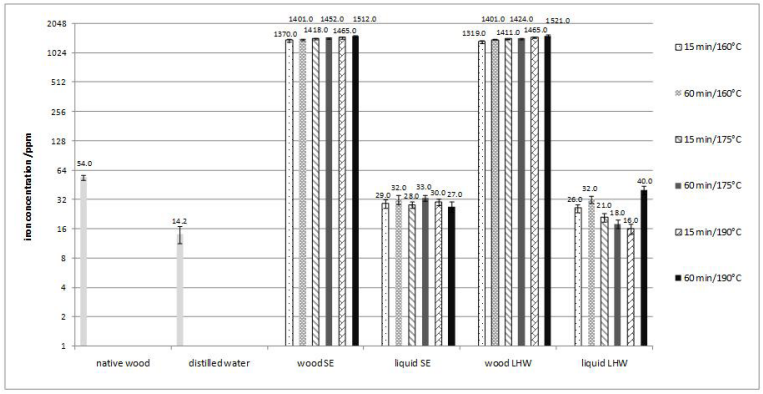

Fig. 6: Iron concentration in native wood of a 5-year-old Populus trichocarpa, in wood after high temperature pretreatments (SE and LHW) with different residential times (15 and 60 min), in distilled water and in liquid fraction obtained after above pretreatments.

According to Roberge (1999), an increase in the content of metallic elements in wood biomass is caused by the corrosion process of the equipment used for pretreatment by high temperature hydrolysis and steam explosion and the contact of steel with substances released from wood biomass during these processes. The raw lignocellulosic biomass is prone to absorb heavy metals (Kord and Kord 2011).

Out of all the tested elements that can inhibit the bioethanol production process (chromium, nickel, copper and iron), the biggest variations happened in case of the concentration of iron

in wood biomass, both after SE and LHW, independently of the process temperature and its residential time.

On the other hand, the average concentration of iron in the liquid fraction generated during the SE and LHW pretreatment processes of a 5-year-old *Populus trichocarpa*, with residential times of 15 and 60 min, was low and fell in the range between 16.0 ppm and 40.0 ppm.

CONCLUSIONS

The average concentration of all the tested elements that can inhibit the bioethanol production process (chromium, nickel, copper and iron) was quite low in native wood and ranged between 10.0 ppm and 54.0 ppm. The average concentration of manganese and zinc in the native wood was higher, at the level of 118.0 ppm and 155.0 ppm, respectively.

The concentration of iron in wood biomass of the 5-year-old *Populus trichocarpa* after pretreatment processes of SE and LHW at the temperatures of 160°C, 175°C and 190°C, with residential times of 15 and 60 min, increased from about 24 to 28 times, comparing to its average concentration in native wood. This means that during the pretreatment process, wood biomass absorbed iron that passed from the pretreatment equipment to the solution due to high process temperatures. The iron is an element considered to be a potential inhibitor in bioethanol production technology. The average concentrations of the tested elements: chromium, nickel, copper, zinc, manganese and iron, in the liquid fraction obtained during the pretreatment of wood biomass of a 5-year-old *Populus trichocarpa* in SE and LHW processes, with residential times of 15 and 60 min, were low and fell in the range between 10.0 ppm and 90.0 ppm.

ACKNOWLEDGMENTS

This work was financed by a research project from the National Centre for Research and Development, which was "Intelligent systems for breeding and cultivation of wheat, maize, and poplar for optimized biomass production, biofuels, and modified wood" (BIOSTRATEG2/298241/10/NCBR/2016). Poplar material used in presented work was obtained in Welcome 2008/1 project of the Foundation for Polish Science given to Prof. Stanisław Karpiński.

REFERENCES

1. Akimkulova, A., Zhou, Y., Zhao, X., Liu, D., 2016: Improving the enzymatic hydrolysis of dilute acid pretreated wheat straw by metal ion blocking of non-productive cellulase adsorption on lignin. Bioresource Technology 208: 110-116.
2. Alvira, P., Tomás-Pejó, E., Ballesteros, M., Negro, M.J., 2010: Pretreatment technologies for an efficient bioethanol production process based on enzymatic hydrolysis: A review. Bioresource Technology 101(13): 4851-4861.
3. Antczak, A., Marchwicka, M., Szadkowski, J., Drożdżek, M., Gawron, J., Radomski, A., Zawadzki, J., 2018: Sugars yield obtained after acid and enzymatic hydrolysis of fast-growing poplar wood species. BioResources 13(4): 8629-8645.
4. Antczak, A., Spyszewska, N., Michałuszko, A., Kłosińska, T., Archanowicz, E., 2014: Acid hydrolysis of poplar wood (*Populus* sp.). Przemysł Chemiczny 93(8): 1428-1431.

5. Antczak, A., Świerkosz, R., Szeniawski, M., Marchwicka, M., Akus-Szylberg, F., Przybysz, P., Zawadzki, J., 2019: The comparison of acid and enzymatic hydrolysis of pulp obtained from poplar wood (*Populus* sp.) by the Kraft method. Drewno 62(203): 53-66.
6. Chandel, A.K., Silvério da Silva, S., Singh, O.V., 2013: Detoxification of lignocellulose hydrolysate: biochemical and metabolic engineering toward white biotechnology. Bioenergy Research 6(1): 388-401.
7. Garcia-Aparicio, M.P., Ballesteros, J., Gonzalez, A., 2006: Effect of inhibitors released during steam explosion pretreatment of barley straw on enzymatic hydrolysis. Applied Microbiology and Biotechnology 129(1-3): 278-288.
8. Harju, L., Lill, J.O., Saarela, K.E., Heselius, S.J., Hernberg, F.J., Lindroos, A., 1997: Analysis of trace elements in trunk wood by thick-target PIXE using dry ashing for preconcentration. Fresenius Journal of Analytical Chemistry 358(4): 523-528.
9. Horn, S.J., Nguyen, Q.D., Westereng, B., Nilsen, P.J., Eijsink, N.G.H., 2011: Screening of steam explosion conditions for glucose production from non-impregnated wheat straw. Biomass and Bioenergy 35(12): 4879-4886.
10. Jönsson, L.J., Alrikssonn, B., Nivebrannt, N.O., 2013: Bioconversion of lignocellulose: inhibitors and detoxification. Biotechnology for Biofuels 6(1): 16-25.
11. Klinke, H.B., Ahring, B.K., Schmidt, A.S., Thomsen, A.B., 2002: Characterization of degradation products from alkaline wet oxidation of wheat straw. Bioresource Technology 82(1): 15-26.
12. Kord, B., Kord, B., 2011: Heavy metal levels in pine (*Pinus eldarica* Medw.) tree barks as indicators of atmospheric pollution. BioResources 6(2): 927-935.
13. Kumar, R., Wyman, C.E., 2009: Effects of cellulase and xylanase enzymes on the deconstruction of solids from pretreatment of poplar by leading technologies. Biotechnology Progress 25(2): 302-314.
14. Liu, H., Zhu, J.Y., 2010: Eliminating inhibition of enzymatic hydrolysis by lignosulfonate in unwashed sulfite-pretreated aspen using metal salts. Bioresource Technology 101(23): 9120-9127.
15. Mansfield, S.D., Mooney, C., Saddler, J.N.N., 1999: Substrate and enzyme characteristics that limit cellulose hydrolysis. Biotechnology Progress 15(5): 804-816.
16. Martin, C., Thomsen, M.H., Hauggaard-Nielsen, H., Thomsen, A.B., 2008: Wet oxidation pretreatment, enzymatic hydrolysis and simultaneous saccharification and fermentation of clover-ryegrass mixture. Bioresource Technology 99(18): 8777-8782.
17. Palmqvist, E., Hahn-Hägerdal, B., 2000a: Fermentation of lignocellulosic hydrolysates. I: Inhibition and detoxification. Bioresource Technology 74(1): 17-24.
18. Palmqvist, E., Hahn-Hägerdal, B., 2000b: Fermentation of lignocellulosic hydrolysates. II: Inhibitors and mechanisms of inhibition. Bioresource Technology 74(1): 25-33.
19. Palonen, H., Thomsen, A.B., Tenkanen, M., Schmidt, A.S., Viikari, L., 2004: Evaluation of wet oxidation pretreatment for enzymatic hydrolysis of sapwood. Applied Biochemistry and Biotechnology 117(1): 1-17.
20. PN-EN 1652, 1999: Copper and copper alloys - Plates, metal sheets, strips and discs of the general purpose.
21. PN-EN 10088-1, 2014-12: Corrosion resistant steels - Part 1: List of corrosion resistant steels.
22. Roberge, P.R., 1999: Handbook of corrosion engineering. McGraw-Hill Press. London, 309 pp.

23. Studer, M.H., Brethauer, S., De Martini, J.D., McKenzie, H.L., Wyman, C.E., 2011: Co-hydrolysis of hydrothermal and dilute acid pretreated populus slurries to support development of a high-throughput pretreatment system. Biotechnology for Biofuels 4(1): 19-28.
24. Tomás-Pejó, E., Alvira, P., Ballesteros, M., Negro, M.J., 2011: Pretreatment technologies for lignocellulose to bioethanol conversion. Elsevier Inc., Amsterdam, Pp 149-176.
25. Warzee, M., Ruston, W.R., de Dorlodot, P., Hennaut, J., Berge, J.Ph., 1966: Corrosion of stainless in high temperature water and steam. European Atomic Energy Community-EURATOM: 1-22.
26. Zielenkiewicz, T., Zawadzki, J., Radomski, A., 2012: XRF spectrometer calibration for copper determination in wood. X-Ray Spectrometry 41(6): 471-473.
27. Zielenkiewicz, T., Szadkowski, J., Drożdżek, M., Zielenkiewicz, A., Kłosińska, T., Antczak, A., Zawadzki, J., Gawron, J., 2016: Application of X-ray fluorescence technique for determination of heavy metals uptake by different species of poplar. Drewno 59(197): 113-126.

Donata Krutul, Jan Szadkowski, Andrzej Antczak*, Michał Drożdżek,
Andrzej Radomski, Janusz Zawadzki
Warsaw University of Life Sciences
Institute of Wood Sciences and Furniture
Nowoursynowska 159
02-776 Warsaw
Poland
*Corresponding author: andrzej_antczak@sggw.edu.pl

Stanisław Karpiński
Warsaw University of Life Sciences
Institute of Biology
Nowoursynowska 159
02-776 Warsaw
Poland

WOOD RESEARCH
66 (1): 2021
49-56
doi.org/10.37763/wr.1336-4561/66.1.4956

STUDY ON THE STRUCTURE AND PROPERTIES OF POLY(3-HYDROXYBUTYRATE-CO-4-HYDROXYBUTYRATE)/ RUBBER WOOD FIBER COMPOSITES MODIFIED WITH TITANATE COUPLING AGENT

Dongna Li, Jianing Li
Chinese Academy of Tropical Agricultural Sciences
China

Xiaojun Ma
Tianjin University of Science and Technology
China

(Received May 2020)

ABSTRACT

In this study, the biodegradable composites were prepared from rubber wood fibers (*Hevea brasiliensis*) and biopolymer poly(3-hydroxybutyrate-co-4-hydroxybutyrate) (P34HB) via hot pressing process, using the titanate as the coupling agent. The morphological, chemical structure, mechanical properties and water absorption (WA) of the composites were characterized by scanning electron microscopy (SEM), Fourier transform infrared spectroscopy (FTIR), mechanical properties and WA analysis. Results showed that a new absorption peak of Ti-O-C was formed due to the addition of titanate, indicating that it was successfully grafted on the surface of wood fibers. In addition, the mechanical properties of the composites first increased and then decreased with the increasing of the titanate content. The obvious improvement of WA of composites was attributed to the inclusion of P34HB by titanate modified wood fiber. Moreover, it was also found that the optimal condition of the titanate coupling agent content was 1 wt%.

KEYWORDS: Wood flour, P34HB, titanate, structure, mechanical properties.

INTRODUCTION

Currently, due to the shortage of raw materials and environmental problems caused by traditional petroleum-based polymers, biodegradable polymers with biocompatibility and

sustainability have been paid more and more attention, of which poly (3-hydroxybutyrate-co-4-hydroxybutyrate) (P34HB), derived from polyhydroxyalkanoates (PHAs) product, exhibits numerous qualities such as lower crystallinity, higher elasticity and toughness, which is considered as the most promising representative of eco-friendly polymers. However, the poor crystallization rate, mechanical properties, narrow thermal processing window and high cost of P34HB impede its large-scale commercial application.

Compared with synthetic fibers, wood fibers possess many potential advantages, including wide source, degradability, heat filling, low cost and excellent physical and mechanical properties (Zhang et al. 2010, Chen et al. 2017, Joffre et al. 2017, Panaitescu et al. 2020). Some studies showed that the addition of plant fibers to biopolymer matrix can improve the mechanical strength of composite materials, make up for the defects of biopolymer matrix, and reduce the manufacturing cost of composite materials (Torres-Telloa et al. 2017, Kellersztein et al. 2019). However, wood fiber is hydrophilic and incompatible with the hydrophobic biopolymer such as P34HB (Han et al. 2012, An and Ma 2017). It was found that the addition of coupling agent to modify the raw materials was one of the most effective methods to improve the interfacial compatibility. The two-phase structure of the coupling agent can enhance the compatibility between two different materials and improve the properties of the composites. The molecular formula of titanate coupling agent is R-O-Ti-$(OR')_n$, in which the pro inorganic end RO- is bonded with the hydroxyl -OH on the surface of wood fiber, and at the other end, the pro organic -OR can be bound with the organic body to achieve bridging effect and improve the interfacial compatibility between wood fibers and P34HB.

In this paper, rubber wood fibers (*Hevea brasiliensis*) were used to enhance the biopolymer poly(3-hydroxybutyrate-co-4-hydroxybutyrate) (P34HB), and titanate was used as the coupling agent, to prepare P34HB/T/WF composites. The effects of different contents of titanate (0.5 wt%, 1 wt%, 2 wt%, 4 wt%, 8 wt%) on the cross-section morphology, chemical structure, mechanical properties and water absorption (WA) of the composites were investigated by various experimental characterization methods.

MATERIAL AND METHODS

Rubber wood (80~100 mesh) used in this study was provided by Lichang Wood Industry Co., Ltd (Linying, Henan). P34HB powder was provided by Tianjin Guoyun Bio-Materials Co., Ltd. Prior to use, wood flour was dried in an oven at 103˚C for 12 h and P34HB was dried under vacuum at 80˚C for 6 h. All other chemicals in the study were reagent grade and they were used without further purification.

0.5 wt%, 1 wt%, 2 wt%, 4 wt%, 8 wt% of titanate coupling agent was added into 90 wt% aqueous alcohol solution, and then a small amount of dioctyl phthalate (DOP) was added into the mixed solution. Finally, the mixture was sprayed on wood flour for modification treatment. After the ethanol in the wood flour volatilized completely, the modified wood flour was dried at 103˚C for 6 h, and then cooled to room temperature and sealed for standby.

The modified wood flour and P34HB with a total mass of 150 g were weighed (mass ratio of 1:1) and put into a high-speed mixer to blend at 1420 r.min-1 for 4 min. Subsequently, the mixtures were evenly spread over a 250 × 250 × 2 mm molds, and thermoformed with a pressure of 17 t at 170˚C for 10 min. After hot pressing, the molds were removed into a flat vulcanizer with a pressure of 1 MPa for cold pressing of 3 min. Finally, the P34HB/T/WF composites were obtained by removing samples from the molds.

Cross-section microstructure of the composites was examined by the scanning electron microscopy (JSM-IT300LV, JEOL, Japan) with an applied voltage of 30 kV. The sample was sprayed with gold before observation. Fourier transform infrared spectroscopy (FTIR) was taken on a ThermoFisher Scientific iS5 instrument (Thermo, USA) in the resolution of 4 cm^{-1} and scanning time of 32 s. The mechanical properties of P34HB/T/WF composites were tested by Instron 3369 universal testing machine (Instron, USA) according to GB/T 1040-2006 and GB/T 9341-2008. Five samples were measured and the average values and standard deviation were reported.

According to the relevant provisions of GB/T 1034-2008, after the sample was cut into a size of 60 × 60 × 2 mm, it was dried in a vacuum drying oven at 50°C for 24 h, and then cooled to room temperature. At this time, the weight of the sample was recorded as m_1. Immerse the sample in container containing distilled water for 24 h, then take out and wipe the water on the surface of the sample with filter paper, and weigh again and record as m_2. The WA of each sample was calculated using the following formula:

$$WA = (m_2 - m_1)/m_1 \times 100\% \quad (1)$$

For each sample, three replicates were performed and the mean and standard deviation were reported.

RESULTS AND DISCUSSION

Fig. 1 shows the cross-section of P34HB/T/WF composites with different titanate coupling agent contents. As shown in Fig. 1a, the cross-section of the composites prepared by unmodified wood fiber exhibited high roughness, obvious fiber pull-out phenomenon and clear interface gaps (Han et al. 2012, Singh et al. 2008). It was mainly attributed to the poor compatibility and interfacial adhesion between unmodified wood fiber and P34HB, resulting in incomplete morphology (Aydemir et al. 2015, Barczewski et al. 2018).

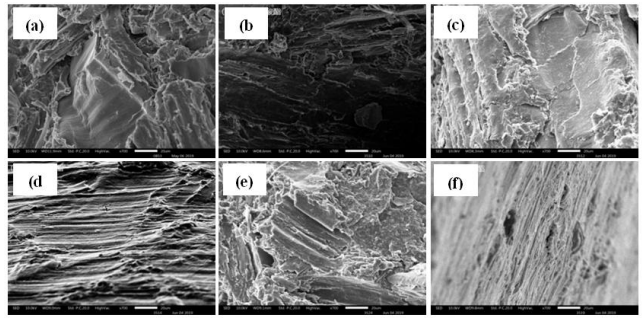

Fig. 1: The impact cross-section SEM image of P34HB/T/WF composites with different titanate contents. (a) 0 wt% titanate; (b) 0.5 wt% titanate; (c) 1 wt% titanate; (d) 2 wt% titanate; (e) 4 wt% titanate; (f) 8 wt% titanate.

After adding titanate coupling agent, the adhesion between wood fiber and P34HB matrix was improved, and the orientation was significantly enhanced, so that the wood fiber was evenly

dispersed in P34HB matrix without obvious gaps, forming a continuous homogeneous phase, as shown in Fig. 1b and c. When the titanate coupling agent content was more than 1 wt%, the cross-section structure of composites became uneven (Fig. 1d-f), the wood fiber presented fracture, and the holes were also increased, which indicated that the excessive titanate coupling agent covering the surface of wood fiber limited the role of "bridge". As a result, the compatibility between wood fiber and P34HB matrix was greatly weakened as the excessive titanate was added.

Fig. 2 shows FTIR spectra of P34HB/T/WF composites with different titanate coupling agent contents. The band at 3400 cm^{-1} as stretching vibration of the intermolecular hydrogen bond O-H, which was significantly broader in the curve of 2 wt% titanate content, indicating that new intermolecular hydrogen bonds were formed.

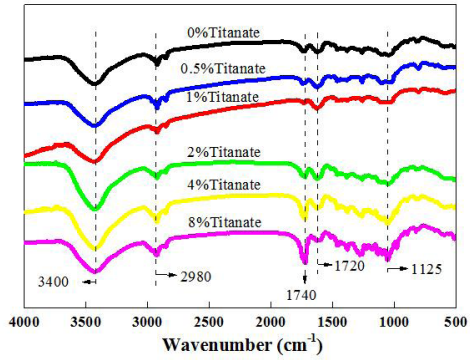

Fig. 2: FTIR spectra of P34HB/T/WF composites with different titanate contents.

When the titanate content was more than 2 wt%, the intensity of O-H vibration peak gradually decreased. The 2980 cm^{-1} band was the characteristic peak of the stretching vibrations of methyl -CH3, which was provided by wood fiber. The adsorption peaks at 1720 and 1740 cm^{-1} represented the stretching vibration of C=O in the fully crystallized and semi-crystallized states of P34HB molecular chain, respectively (Liu et al. 2016, Prado et al. 2019). With the increase of titanate content, the intensity of peaks at 1720 cm^{-1} increased first and then decreased, while the intensity change of peaks at 1740 cm^{-1} was reversed, indicating that the properties of the composite had changed because of adding the titanate. At the same time, the absorption peak at 1125 cm^{-1} exhibited more and more sharper due to the formation of Ti-O-C bond. It further revealed that the titanate could act as a bridge between the surfaces of wood fiber and P34HB, promoting the interfacial compatibility of the composites (Jin et al. 2019).

Fig. 3 represents the relationship between the tensile and flexural properties and the titanate contents of P34HB/T/WF composites.

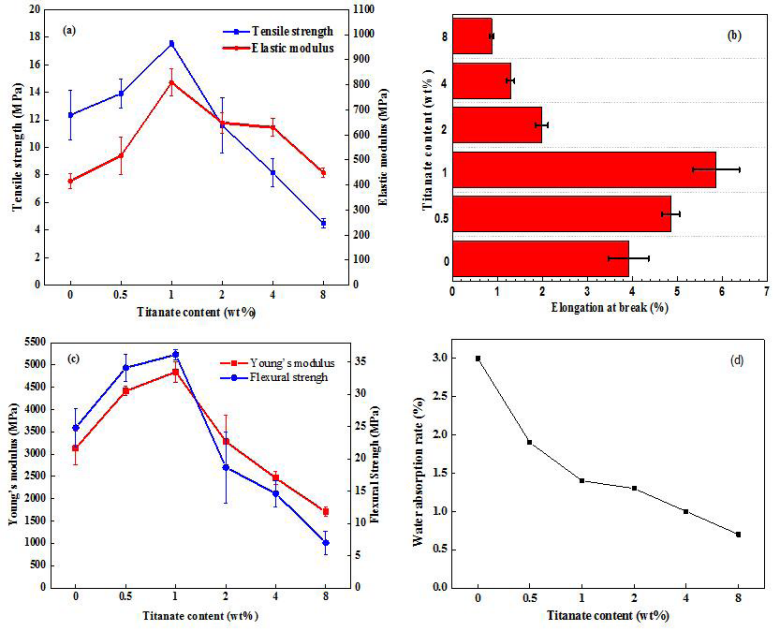

Fig. 3: Tensile properties and Water absorption: (a) tensile strength and elastic modulus, (b) elongation at break, (c) Young's modulus and flexural strength of P34HB/T/WF composites, (d) water absorption of P34HB/T/WF composites.

It can be seen from Fig. 3a-c that with the increase of titanate content, the mechanical and flexural properties of the composites first increased and then decreased. When the titanate content was 1 wt%, the mechanical properties of P34HB/T/WF composites reached the maximum values (tensile strength of 17.51 MPa, elastic modulus of 808.14 MPa, elongation at break of 5.86%, flexural strength of 36.14 MPa and Young's modulus of 4845.67 MPa), indicating that excessive titanate content had a negative role in the compatibility of wood fiber and P34HB. The increase of the mechanical properties of the composites was firstly attributed to the combination of alkoxy group (R-O-) in the titanate coupling agent with hydroxyl group on the surface of wood fiber through chemical bond to improve their compatibility. Meanwhile, the ester plasticizer DOP promoted the crosslinking of titanate, wood fiber and P34HB, which can effectively absorb the external force for composites (Liu et al. 2019, Hu et al. 2020, Pupure et al. 2020). In addition, due to the interaction between the molecular structure of titanate coupling agent and P34HB polymer, there was the closer bonding between composite substrates, improving the compatibility with P34HB, and finally resulting in the mechanical strength of the composites increasing (Gao et al. 2016, Nikpour and Rodrigue 2016). When excess titanate was added (more than 1 wt%), the monolayers formed between wood fiber and P34HB was destroyed because of self-agglomeration, resulting to form stress layer and uneven interface (Febrianto et al. 2017, Maslowski et al. 2018). Moreover, the redundant coupling agent molecules not involving in the reaction weakened the binding ability of wood fiber and biopolymer P34HB, and finally reduced the mechanical properties of composites (Jiang et al. 2019, Kuciel et al. 2020).

Fig. 3d shows the WA change curve of P34HB/T/WF composites with different titanate contents, WA of the unmodified composite was 3%. With the increase of titanate coupling agent content from 0.5 to 8 wt%, the WA decreased from 1.9 to 0.7%. The smaller the WA of the composites, the better the water resistance (Xu et al. 2016a, 2016b, Liu et al. 2019). In the process of hydrolysis reaction between alkoxy group of titanate coupling agent and hydroxyl group of wood fiber, Ti was connected to the surface of wood fiber through oxygen bridge, forming molecular layer of coupling agent. On the other hand, titanate coupling agent improved the interfacial compatibility between wood fiber and P34HB, enhancing the hydrophobic P34HB coating on the surface of wood fiber, which were beneficial to reduce the WA of the composites.

CONCLUSIONS

In this study, P34HB/T/WF composites were successfully prepared by using the titanate as the coupling agent to increase the interfacial adhesion. A new absorption peak of Ti-O-C was found by FTIR spectra, which indicated that titanate was successfully grafted on the surface of wood fiber to achieve an ideal modification effect. When the titanate content increased, the mechanical properties of the composites first increased and then decreased. The tensile and flexural properties reached the maximum values when the content of titanate was 1 wt%, including tensile strength of 17.51 MPa, elastic modulus of 808.14 MPa, elongation at break of 5.86%, flexural strength of 36.14 MPa and Young's modulus of 4845.67 MPa. The obvious improvement of WA of the composites was attributed to the inclusion of P34HB by titanate modified wood fiber. There was a positive correlation between the water resistance of the composites and titanate content, and the optimal value of WA was 0.7%. According to the comprehensive analysis, it was also found that the optimal condition of the titanate coupling agent content was 1 wt%.

ACKNOWLEDGMENTS

This research has been financially supported by Opening Project Fund of Key Laboratory of Rubber Biology and Genetic Resource Utilization, Ministry of Agriculture/ State Key Laboratory Breeding Base of Cultivation & Physiology for Tropical Crops/ Danzhou Investigation & Experiment Station of Tropical Crops, Ministry of Agriculture (RRI-KLOF202001), and Science Foundation of Tianjin Municipal Education Commission (2019ZD039).

REFERENCES

1. An, S.N., Ma, X.J., 2017: Properties and structure of poly(3-hydroxybutyrate-co-4-hydroxybutyrate)/wood fiber biodegradable composites modified with maleic anhydride. Industrial Crops and Products 109: 882-888.
2. Aydemir, D., Kiziltas, A., Gunduz, G., Han, Y., Gardner, D.J., 2015: Natural fillers-filled styrene maleic anhydride copolymer composites. Wood Research 60(1): 167-174.
3. Barczewski, M., Matykiewicz, D., Piasecki, A., Szostak, M., 2018: Polyethylene green composites modified with post-agricultural waste filler: thermo-mechanical and damping properties. Composite Interfaces 25(4): 287-299.

4. Chen, L., Han, J.Q., Huang, R.Z., Xu, X.W., Wu, Q.L., 2017: Thermal decomposition properties of recycled tire rubber filled wood/high density polyethylene composites. Wood Research 62(5): 701-714.
5. Febrianto, F., Hidayat, W., Wistara, I.N.J., Park, S.H., Jang, J.H., Lee, S.H., Teramoto, Y., Kondo, T., Kim, N.H., 2017: Influence of impact modifier-coupling agent combination on mechanical properties of wood flour-reinforced polypropylene composite. Journal of the Faculty of Agriculture Kyushu University 62(2): 445-450.
6. Gao, X., Li, Q.D., Cheng, W.L., Han, G.P., Xuan, L.H., 2016: Optimization of high temperature and pressurized steam modified wood fibers for high-density polyethylene matrix composites using the orthogonal design method. Materials 9(10): 847.
7. Han, L.J., Han, C.Y., Cao, W.L., Wang, X.M., Bian, J.J., Dong, L.S., 2012: Preparation and characterization of biodegradable poly(3-hydroxybutyrate-co-4-hydroxybutyrate)/ silica nanocomposites. Polymer Engineering and Science 10: 250-258.
8. Hu, W., Zhang, Y.M., Qi, Y.X., Wang, H.B., Liu, B.Y., Zhao, Q., Zhang, J., Duan, J., Zhang, L., Sun, Z., Liu, B., 2020: Improved mechanical properties and flame retardancy of wood/ PLA all-degradable biocomposites with novel lignin-based flame retardant and TGIC. Macromolecular Materials and Engineering 1900840.
9. Joffre, T., Segerholm, K., Persson, C., Bardage, S.L., Hendriks, C.L.L., Isaksson, P., 2017: Characterization of interfacial stress transfer ability in acetylation- treated wood fibre composites using X-ray microtomography. Industrial Crops and Products 95: 43-49.
10. Jiang, J., Mei, C.T., Pan, M.Z., Lu, F., 2019: Effects of hybridization and interface modification on mechanical properties of wood flour/polymer composites reinforced by glass fibers. Polymer Composites 40(9): 3601-3610.
11. Jin, X., Zhang, X.L., Xu, C., Nie, S.J., 2019: Effect of bamboo fibers with different coupling agents on the properties of poly(hydroxybutyrate-co-valerate) biocomposites. Journal of Applied Polymer Science 136(20): 47533.
12. Kellersztein, I., Shani, U., Zilber, I., Dotan, A., 2019: Sustainable composites from agricultural waste: The use of steam explosion and surface modification to potentialize the use of wheat straw fibers for wood plastic composite industry. Polymer Composites 40: 53-61.
13. Kuciel, S., Mazur, K., Hebda, M., 2020: The influence of wood and basalt fibres on mechanical, thermal and hydrothermal properties of PLA composites. Journal of Polymers and the Environment 28(4): 1204-1215.
14. Liu, Y.N., Guo, L.M., Wang, W.H., Sun, Y.N., Wang, H.G., 2019: Modifying wood veneer with silane coupling agent for decorating wood fiber/high-density polyethylene composite. Construction and Building Materials 224: 691-699.
15. Liu, H., Wang, J., Gong, C.L., Cheng, F., Wang, G.J., Wen, S., Zheng, G., 2016: Morphology and mechanical properties of PVC/straw-fiber coated with liquid nitrile-butadiene rubber composites. Journal of Applied Polymer Science 133(43): 44119.
16. Liu, M.H., Peng, L.M., Fan, Z.Q., Wang, D., 2019: Sound insulation and mechanical properties of wood damping composites. Wood Research 64(4): 743-758.
17. Maslowski, M., Miedzianowska, J., Strzelec, K., 2018: Influence of peroxide modifications on the properties of cereal straw and natural rubber composites. Cellulose 25(8): 4711-4728.
18. Nikpour, N., Rodrigue, D., 2016: Effect of coupling agent and ground tire rubber content on the properties of natural fiber polymer composites. International Polymer Processing 31(4): 463-471.

19. Panaitescu, D.M., Nicolae, C.A., Gabor, A.R., Trusca, R., 2020: Thermal and mechanical properties of poly(3-hydroxybutyrate) reinforced with cellulose fibers from wood waste. Industrial Crops and Products 145: 112071.
20. Prado, N.S., da Silva, I.S.V., de Morais, L.C., Pasquini, D., Otaguro, H., 2019: Effects of surface modifications of kraft wood pulp cellulose fibres on improving the mechanical properties of cellulose fibre/latex composites. Journal of Polymers and the Environment 27(11): 2445-2453.
21. Pupure, L., Varna, J., Joffe, R., Berthold, F., Miettinen, A., 2020: Mechanical properties of natural fiber composites produced using dynamic sheet former. Wood Material Science and Engineering 15(2): 76-86.
22. Singh, S., Mohanty, A.K., Sugie, T., Takai, Y., Hamada, H., 2008: Renewable resource based biocomposites from natural fiber and polyhydroxybutyrate-co-valerate (PHBV) bioplastic. Composites Part A: Applied Science and Manufacturing 39(5): 875-886.
23. Torres-Telloa, E.V., Robledo-Ortízb, J.R., González-Garcíab, Y., Pérez-Fonsecaa, A.A., Jasso-Gastinela, C.F., Mendizábalc, E., 2017: Effect of agave fiber content in the thermal and mechanical properties of green composites based on polyhydroxybutyrate or poly(hydroxybutyrate-co-hydroxyvalerate). Industrial Crops and Products 99: 117-125.
24. Xu, K.M., Tu, D.Y., Chen, T.A., Zhong, T.H., Lu, J., 2016a: Effects of environmental-friendly modified rubber seed shell on the comprehensive properties of high density polyethylene/rubber seed shell composites. Industrial Crops and Products 91: 132-141.
25. Xu, K.M., Zheng, Z.F., Huang, S.Y., Chen, T.A., Tang, Z.J., 2016b: Influence of glycidyl methacrylate grafting on the mechanical, water absorption, and thermal properties of recycled high-density polyethylene/rubber seed shell particle composites. Bioresources 11(1): 2617-2628.
26. Zhang, Y.C., Wu, H.Y., Qiu, Y.P., 2010: Morphology and properties of hybrid composites based on polypropylene/polylactic acid blend and bamboo fiber. Bioresource Technology 101: 7944-7950.

Dongna Li, Jianing Li
Chinese Academy of Tropical Agricultural Sciences
Rubber Research Institute
Ministry of Agriculture Key Laboratory of Biology and Genetic Resource
Utilization of Rubber Tree
State Key Laboratory Breeding Base of Cultivation and Physiology For Tropical
Crops
Danzhou 571700
China

Xiaojun Ma*
Tianjin University of Science and Technology
College of Light Industry Science and Engineering
Tianjin 300222
China
*Corresponding author: mxj75@tust.edu.cn

WOOD RESEARCH
66 (1): 2021
57-70
doi.org/10.37763/wr.1336-4561/66.1.5770

ANTIOXIDANT ACTIVITY OF *SWIETENIA MACROPHYLLA* KING BARK EXTRACTS

Masendra, Brandon Aristo Verick Purba, Ganis Lukmandaru
Universitas Gadjah Mada
Indonesia

(Received March 2020)

ABSTRACT

This study investigated the antioxidant activity from the methanol (MeOH) soluble extract of the inner and outer bark of *Swietenia macrophylla*. The MeOH soluble extracts were fractionated into ethyl acetate (EtOAc) soluble and insoluble. The antioxidant activity was conducted by DPPH (1,1-diphenyl-2-picrylhydrazyl) method and the phenolic compounds were detected by GC-MS. The levels of total phenolic content of soluble and insoluble fraction of EtOAc of outer bark were higher than in inner bark, while total flavonoid content showed opposite results. The crude methanol extract and its EtOAc soluble fraction of outer bark showed a higher level of antioxidant activity. The GC-MS analysis detected higher levels of fatty acids and alcohols of 87.12% than phenolic compounds of 12.17% in the inner bark, while the outer bark showed the opposite pattern with phenolic compounds of 82.65% than fatty acids of 8.43%. A strong correlation was demonstrated between total phenolic content and antioxidant activity.

KEYWORDS: *Swietenia macrophylla*, bark extractives, phenols, flavonoid, phytomedicines.

INTRODUCTION

Bark is the outermost part of a plant stem which acts as a protective layer against external forces such as wind, snow, and various disease-causing organisms. Anatomically, it consists of periderm in its outer part, and parenchyma on the inner part (Rosell et al. 2014). The outer and inner part of bark can be distinguished by its cells, function, and properties. The outer bark part of a tree, referred to botanically as the rhytidome, consists of dead tissues, fats, and suberins. Meanwhile, the inner part of bark mostly contains living cells and is referred to as the phloem. The inner bark also serves as storage for nutrients such as sugars and fatty acids (Morris et al. 2016, Masendra et al. 2018).

The protective functions of bark are often associated with bioactive compounds from secondary metabolites, mainly from tannins or polyphenols. The bioactivities shown by these compounds have been regarded as potential material for traditional medicine and for use by

pharmaceutical industries (Ogawa and Yazaki 2018, Elansary et al. 2019). One well-known utilization of bark can be found in the standardized Pycnogenol® from the species of *Pinus pinaster,* which contains phenolics e.g. taxifolin, catechin, procyanidin, and phenolic acids and shows high antioxidant activity against reactive oxygen and nitrogen species (Iravani and Zolfaghari 2011).

Phenolic compounds have been referenced in many literatures for their ability to promote health and to prevent disease through their antioxidant, anti-inflammatory, anti-obesogenic, and other beneficial properties (Pérez-Jiménez et al. 2010, Singh et al. 2011, Wang et al. 2014, Cory et al. 2018). Eating foods that are rich in flavonoids has been shown to improve cardiovascular health and lower blood pressure (Rees et al. 2018). Furthermore, polyphenol type compounds have been known to act as an antioxidant, which is able to neutralize free radical compounds such as hydrogen peroxide (H_2O_2) that can cause damage to cells (Halliwell and Gutteridge 1999, Sroka and Cisowski 2003). The effectively of polyphenols to neutralize free radicals is diverse and affected mainly by their structure. For example, previous research by Sroka and Cisowski (2003) on phenolic acids found stronger antioxidant activity with compounds that had a higher number of hydroxyl groups, especially those with *ortho* and *para* positions of the hydroxyl substitution.

S. macrophylla is a species native to Central and South America, and has been introduced and planted for its wood in many tropical countries such as Indonesia (Brown et al. 2003). In Indonesia, this wood has been highly prized in the production of furniture materials due its physical, mechanical, anatomical, and electrical properties (Husein et al. 2014, Anoop et al. 2014). In Jepara, Central Java, Indonesia, the utilization of *S. macrophylla* wood does not include bark, which is regarded as a waste. Previous work on antioxidant activity of the whole bark of this species has been initiated by Falah et al. (2008). However, there is no information of extractives and their antioxidant activity from both inner and outer bark of *S. macrophylla*. In this study, the bark of *S. macrophylla* was separated into inner and outer bark, then each part was analyzed for total phenolic content, total flavonoid content, and antioxidant activity.

MATERIAL AND METHODS

Bark specimen

The bark of *S. macrophylla* was collected from a furniture industry, SRIKANDIRATU in Jepara, Indonesia. The diameter of log wood was in arrange of 40 cm and the tree age was > 20 years old. The bark sample was separated to inner and outer part with color of inner bark is light red and outer bark is dark red. The thickness of inner bark is 0.5-1 mm and outer bark is 1.5-3 mm. The bark sample was grinded to powder (60 - 80 mesh) before extraction.

Extraction

For the extraction, the sample of inner and outer bark (each 500 g) was extracted with *n*-hexane and MeOH for 6 h and in hot water for 3 h in a reflux apparatus. The MeOH soluble extracts were then fractionated by ethyl acetate (EtOAc). The EtOAc fractionation was conducted by extracting MeOH soluble extracts with EtOAc for 12 h in room temperature using magnetic stirrer.

Chemicals

Gallic acid (97.5%), quercetin (≥ 95%), DPPH, trimethylchlorosilane (TMCS) and N,O-bis(trimethylsilyl) acetamide (BSA) were purchased from Sigma-Aldrich (Germany) while phenol reagent (Folin-Ciocalteu), aluminium chloride, and sodium carbonate were purchased from Merck (Darmstadt, Germany).

Determination of total phenolic content (TPC)

To observe TPC, 2.5 ml of Folin-Ciocalteu reagent was mixed with 0.5 ml of ethanol solution of the sample. The reaction was left to sit for 2 min before adding the sodium carbonate (2 ml of 7.5% aqueous), then the solution was stood again for 30 min. The absorbance of sample was read at 765 nm with an Ultaviolet (UV)/ Visible spectrophotometer (model SP-3000 Nano, Optima, Tokyo, Japan) and the results were expressed as gallic acid equivalents (mg GAE/g based on dry extract weight). The standard curve was made in concentration of 100, 50, 25, and 12.5 $\mu g \cdot ml^{-1}$ solutions of gallic acid in MeOH ($y = 0.1097x - 0.002$; $R^2 = 0.9968$). The Folin-Ciocalteu method used based on a previous study (Diouf et al. 2009). TPC were performed as the mean ± standard deviation of three replications of measurement.

Determination of total flavonoid content (TFC)

The TFC assay was conducted as follows: to 2 ml of sample (1 $mg \cdot ml^{-1}$) was mixed with 2% of $AlCl_3.6H_2O$ solution (2 g in 100 ml MeOH). After 1 h incubation at 20°C, the sample absorbance was read at 415 nm with an Ultraviolet (UV)/ Visible spectrophotometer (model SP-3000 Nano, Optima, Tokyo, Japan) and the results were expressed in quercetin equivalents (mg QE/g extract) (Brighente et al. 2007). The quercetin solutions in MeOH with concentration of 31.25, 15.63, 7.81, and 3.91 $\mu g \cdot ml^{-1}$ were made to perform the TFC calibration ($y = 0.0246x + 0.0005$; $R^2 = 0.9994$). Each sample was conducted in three replications for TFC measurement.

Gas chromatography mass spectrometry (GC-MS) analysis

GC-mass spectrometry (GC-MS) data were collected with a GCMS-QP 2010 (Shimadzu, Japan). The 1 µl of sylillated sample was injected to GC-MS machine. The GC condition: Rtx-5MS capillary column (30 m x 0.25 mm I.D. and 0.25 µm; GL Sciences, Tokyo, Japan); column temperature from 100°C (1 min) to 320°C at 5 $°C \cdot min^{-1}$; injection temperature of 250°C; detection temperature of 320°C; acquisition mass range from of 50-800 amu using helium as the carrier gas. The mass spectrum of sample was compared to NIST library. The sylilation method was conducted by dissolving 2 mg of sample into TMCS (15 µl) and BSA (85 µl) (Wijayanto et al. 2015). After 1 h incubation, the sample was evaporated and the dry extract was dissolved in 1 ml of MeOH. Peak relative method was used for quantification of individual substances.

Determination of DPPH radicals scavenging activity

Antioxidant activity assay was conducted according to a previous study (Baba and Malik, 2014). Briefly, 0.1 ml extract in MeOH with different concentration (100-1000 ppm) was mixed and reacted with 3 ml of 0.1 mM DPPH. The reaction was left to sit for 30 min in a dark and chilled room, then the absorbance was read at 517 nm. The antioxidant activity was calculated by Eq. 1 as follows:

$$\text{DPPH scavenged (\%)} = 100 \times (Ao - A1)/ Ao \quad (1)$$

where: Ao is absorbance of blank, A1 is absorbance of sample.

The antioxidant value was also in units of IC_{50} (the concentration of sample that inhibits activity of 50%).

Statistical analysis

The effects of bark part and extract fractions were calculated by analysis of variance (ANOVA). A Tukey's HSD (honestly significant difference) test was used to show which group means differ. All statistics were performed with SPSS 10.0 software

RESULTS AND DISCUSSION

Extractive content

The inner and outer bark of *S. macrophylla* were extracted by *n*-hexane, MeOH, and hot water, successively. The n-hexane and MeOH extract of the inner bark were higher than that of the outer bark, but the hot water extract showed the opposite results (Arisandi et al. 2019a). In this study, the MeOH extracts from previous work were fractionated by EtOAc. In Fig. 1, the EtOAc soluble fraction of the inner and outer bark was at a lower level than EtOAc insoluble fraction. This indicates that the inner and outer bark of *S. macrophylla* have bigger insoluble polymers such as tannin. The presence of EtOAc insoluble fraction of inner and outer bark were 11.15% and 6.12%, respectively. Those values were quite similar to MeOH extract of inner and outer bark (12.05% and 6.27%). These outputs encourage that the high concentration of insoluble polymers/tannins in the bark of *S. macrophylla* could increase the utilization of forest products in the future.

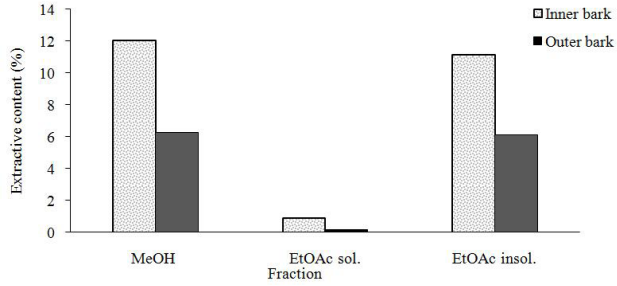

Fig. 1: Extractive content of S. macrophylla extraction; ethyl acetate soluble (EtOAc sol.) and ethyl acetate insoluble (EtOAc insol.)

Phenol contents

The results of TPC and TFC are shown in Fig. 2. ANOVA test showed significance in TPC and TFC in the interaction between bark and fraction (Tab. 1). The TPC values were significantly lower in the EtOAc soluble extract of inner bark. Meanwhile, insoluble fraction of both inner and outer bark showed significantly lower number of TFC compared to the soluble fractions. Furthermore, the soluble fraction of inner bark showed significantly higher values of TFC than outer bark.

Tab. 1: Two-way ANOVA for TPC and TFC value of S. macrophylla inner and outer bark.

Source of variation	df	p value	
		TPC	TFC
Bark (B)	1	<0.01**	<0.01**
Fraction (F)	2	<0.01**	<0.01**
B × F	2	0.03*	<0.01**
Error	12		
Total	18		

df: degrees of freedom;

at 5% level, n.s: not significant; *: p<0.05; **: p<0.01.

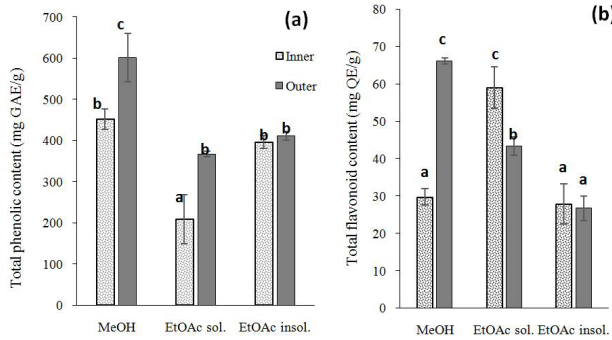

Fig. 2: The same letters are not statistically different at p < 0.05 by Tukeytest. " after sentence of "TPC (a) and TFC (b) inner and outer bark of S. macrophylla; EtOAc insoluble and solublefractions.

Phenolic compounds are secondary metabolites commonly found in plant parts. These compounds were known to act as a defense mechanism of plants against pathogens and insects as they have generally effective bioactivities that may prove to be beneficial to the tree, such as insect deterrent (Wafula et al. 2013) and anti-fungal bioactivities (Zabka and Pavela 2013, Popa 2015). Previous research on *Eucalyptus pellita* bark also found a significantly higher total phenolic content in its bark compared to its sapwood, with similar range of 368.4 to 632.5 mg GAE/g (Arisandi et al. 2019b). Thus, this higher amount of TPC in the outer bark might be explained as a defense mechanism of the tree. Moreover, the higher amount of TPC in the EtOAc insoluble extract indicates that the phenolic content of *S. macrophylla* bark is dominated by phenols with heavier molecular weight such as tannins. Previous research by Waheed et al. (2014) showed a higher amount of low molecular weight compounds of flavonoid and terpenoid groups in the EtOAc fraction of *Ballota limbata* extract. In TFC, the MeOH extract of outer bark showed a higher level than inner bark. On the contrary, TFC of the inner bark of EtOAc soluble and insoluble extract showed a higher concentration than outer bark extract.

GC-MS analysis

The GC-MS results in the bark of *S. macrophylla* showed that phenolics, fatty acids, and alcohols were abundant (Tab. 2). In the inner bark, the constituent mainly consisted of fatty acid (87.12%) i.e. pentadecanoic acid (29.78%). In the outer bark the constituent was dominated by phenolic compounds, such as catechol (58.04%), while in inner bark, resorcinol was the dominating phenolic compound (8.45%). The chromatogram of sample is displayed in Fig. 3.

Tab. 2: Constituents of EtOAc soluble extracts of S. macrophylla inner and outer bark.

Number	Ret. time (min)	Constituents	Sample (% of dried extract)		Similarity index (%)
			Inner bark	Outer bark	
		Phenolics	12.17	82.65	
1	10.4	Catechol	tr	58.04	96
2	11.4	Benzoic acid	tr	11.08	55
3	12.5	Resorcinol	8.45	2.79	94
4	13.9	4-Methylcatechol	tr	3.07	81
5	15.4	Syringol	tr	6.56	87

6	21.9	Antiarol	1.16	tr	81
7	23.9	4-Hydroxybenzyl alcohol	nd	1.11	55
8	25.9	Syringic acid	1.72	tr	87
9	30.4	2,3,4-Trimethoxycinnamic acid	0.84	tr	63
		Fatty acids and alcohols	87.12	8.43	
10	24.6	Myristic acid	0.77	nd	84
11	27.4	Palmitic acid, methyl ester	4.63	1.03	97
12	28.2	Pentadecanoic acid	29.78	7.4	94
13	28.6	10-Methyleicosane	0.89	nd	75
14	30.2	Linolelaidic acid, methyl ester	4.65	nd	96
15	30.3	9-Octadecenoic acid, methyl ester	2.95	nd	93
16	30.7	Methyl stearate	0.74	nd	87
17	31.0	11,14-Eicosadienoic acid, methyl ester	21.2	nd	88
18	31.2	cis-Vaccenic acid	18.01	tr	92
19	31.3	Stearic acid	3.5	nd	92

Note: (nd): not detected; (tr): trace.

Catechol (Fig. 4b) was detected as the major compound in the bark of *S. macrophylla*. The high concentration of catechol in the outer bark of *S. macrophylla* indicated that the presence of tannin with a catechol monomer. A previous work (Falah et al. 2008) isolated flavanols i.e., Swietema crophyllanin, catechin, and epicatechin from the bark of *S. macrophylla*. The chemical structure of catechin and epicatechin commonly have a catechol structure in their B ring (Fig. 5a).

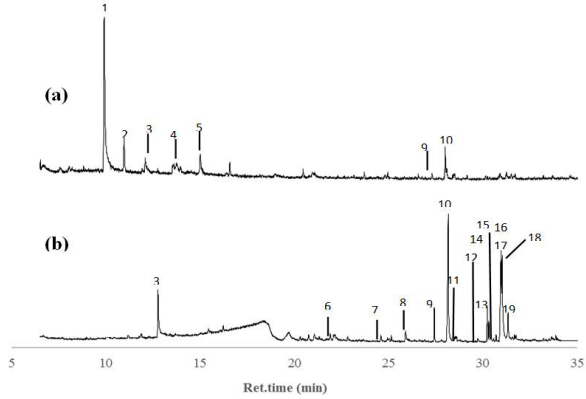

Fig. 3: Chromatogram GC-MS of outer (a) and inner (b) bark of EtOAc soluble extracts from S. macrophylla: 1. Catechol, 2. Benzoic acid, 3. Resorcinol, 4. 4-Methylcatechol, 5. Syringol, 6. Antiarol, 7. 4-Hydroxybenzyl alcohol, 8. Syringic acid, 9. 2,3,4-Trimethoxycinnamic acid, 10. Myristic acid, 11. Palmitic acid, methyl ester, 12. Pentadecanoic acid, 13. 10-Methyleicosane, 14. Linolelaidic acid, methyl ester, 15. 9-Octadecenoic acid, methyl ester, 16. Methyl stearate, 17. 11,14-Eicosadienoic acid, methyl ester, 18. cis-Vaccenic acid, and 19. Stearic acid.

In part of the inner bark, Tab. 2 and Fig. 3 show that fatty acids and alcohols dominated the composition of extractives. It has been suggested that this part has a role in nutrient transfer

and also as storage to save energy, such as sugars and fatty acids. This result is in agreement with previous studies (Morris et al. 2016, Masendra et al. 2018). In the case of phenolic compounds, the resorcinol in the inner bark part dominated the extractive constituents. In the structure of flavanols, the A ring has the structure of resorcinol (Fig. 5a). Thus, this fact also supports the presence of catechin or epicatechin as tannin monomers in the bark of *S. macrophylla*. The higher presence of resorcinol also suggests that the bark of *S. macrophylla* can be considered as a good source of resorcinol and catechol. This was in agreement with previous studies in the bark of *Pinus radiata* (Case et al. 2014, Pinto et al. 2018). The high concentration of resorcinol and catechol could possibly lead to the development of *S. macrophylla* bark for adhesives, pharmaceuticals, and leather industries.

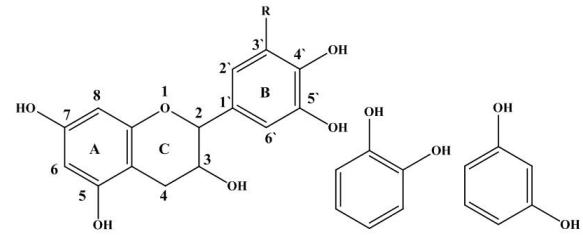

Fig. 4: Chemical structure of flavanols and their precursors.

Antioxidant activity

The results of antioxidant activity by IC_{50} of the bark are shown in Fig. 5. The results were compared with the crude MeOH extract antioxidant activity. The crude MeOH extract showed that outer bark had a higher antioxidant activity (a lower IC_{50} value) compared to inner bark. Furthermore, after fractionation, the soluble fraction of EtOAc of outer bark also showed the same pattern where levels of antioxidant activity were higher than inner bark. In the case of EtOAc insoluble, the result was different. The inner bark part showed a higher level of antioxidant properties. In this study, the ANOVA of the antioxidant activity showed a significant difference (Tab. 3).

Tab. 3: Two-way ANOVA for IC_{50} value of S. macrophylla inner and outer bark.

Source of variation	df	p value of DPPH IC_{50}
Bark (B)	1	0.03*
Fraction (F)	2	0.02*
B × F	2	<0.01**
Error	12	
Total	18	

df: degrees of freedom; at 5% level, n.s: not significant; * $p<0.05$; ** $p<0.01$.

Results showed that the antioxidant activity of the inner bark extract is mainly caused by the EtOAc insoluble fraction's compound. Furthermore, although without significant difference between values, the crude extract of the outer bark part showed stronger antioxidant activity than the fractionated parts. Synergism between natural compounds can be defined as an increased

effect, such as antioxidant activity, with the combination of those compounds Sonam and Guleria (2017). This synergism might explain why the crude extract of the outer bark showed a stronger activity. The finding of higher antioxidant activity levels in outer bark than in inner bark corroborates the ecological role of outer bark in protecting of the living tissue from damages or microorganisms attack (Wafula et al. 2013, Zabka and Pavela 2013, Popa 2015). In the opposite, the lower antioxidant activity in the crude extract of the inner bark part may be caused by the antagonistic effect between EtOAc soluble and insoluble fractions. A comparison with the standard of gallic acid and quercetin exhibited that the antioxidant in the samples were still at lower levels (Fig. 5).

The EtOAc soluble fraction of outer bark exhibited high levels of antioxidant activity (Fig. 5). This antioxidant activity might be caused by the high concentration of catechol. Catechol is a simple structured phenolic compound with two hydroxyl groups in an ortho position. Previous structure to activity relationship study has found better antioxidant activity from catechol compared to other simple phenols and anilines. Catechols have been shown as able to neutralize two peroxyl radicals (Valgimigli et al. 2008, Bendary et al. 2013). The ortho position of its hydroxyl groups was suspected as the reason for its effectivity in neutralizing DPPH radicals, where the lower bond dissociation energy makes it easier for catechol to lose its H atom. On the other hand, phenols with a meta position of hydroxyl group, such as resorcinol, showed a lower antioxidant activity (Bendary et al. 2013). In addition, catechol is known to be a degradation product of flavonoid compounds. Through bacterial degradation, catechin can be degraded into phloroglucinol carboxyl acid, protocatechuic acid, and catechol (Vasundevan and Mahadevan 1990, Arunachalam et al. 2003).

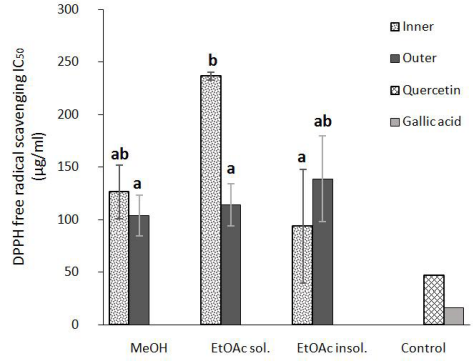

Fig. 5: Antioxidant activity of inner and outer bark S. macrophylla; MeOH crude, EtOAc insoluble, and EtOAc soluble fractions.

In the EtOAc soluble fraction of inner bark, the antioxidant levels were lower compared to other extracts. This may be due to the lower presence of phenolic compounds than fatty acids and alcohols. Additionally, the phenolic compound of resorcinol that dominated in this bark part may be less effective at inhibiting DPPH than catechol which was in a higher level in outer bark. However, as the catechol and resorcinol precursors were detected in the bark sample, this also suggests that the bark contains catechin or epicatechin as tannin monomers. Thus, it is reasonable that antioxidant levels of EtOAc insoluble fraction from inner bark was higher than other fractions.

Phenol contents and antioxidants activity correlation

Correlations between TPC, TFC, and antioxidant activity have been plotted in Figs. 6 and 7. The results showed positive correlations between TPC and DPPH scavenging activity in Fig. 6a (R^2= 0.6 and 0.7). Furthermore, a specific correlation was found in inner and outer barks as the TPC of inner bark and DPPH showed strong correlations in Fig. 6b (R^2 = 0.94 and 0.98). A low degree of correlation was measured in TPC of outer bark and DPPH in Fig. 6c (R^2 = 0.1 and 0.05).

In general, a sample with a high level of TPC gave a high level of DPPH. The correlation between total phenolic content and DPPH scavenging activity such in Fig. 6a and 6b was also found in previous works on *Punica granatum*, blackberries, *Thymus vulgaris*, and *Hyoscyamus gaagheri* (Eddebbagh et al. 2016, Guedes et al. 2017, Amamra et al. 2018, Hossain et al. 2019). Phenolic compounds are classified as its own group due to its benzene ring with hydroxyl group attached to it. Hydroxyl group in phenolic compounds is a good hydrogen donor, which can react and neutralize reactive oxygen such as DPPH (Pereira et al. 2009, Miguel-Chávez 2017). Thus, high concentration of phenolic compounds in an extract is often followed by a high antioxidant activity. In addition, the outer bark sample showed higher levels of TPC and catechol than inner bark. A significant correlation could not be found by analysis regression (Fig. 6c). This result was similar to a previous work on 13 citrus species peels and tissues (Ghasemi et al. 2009).

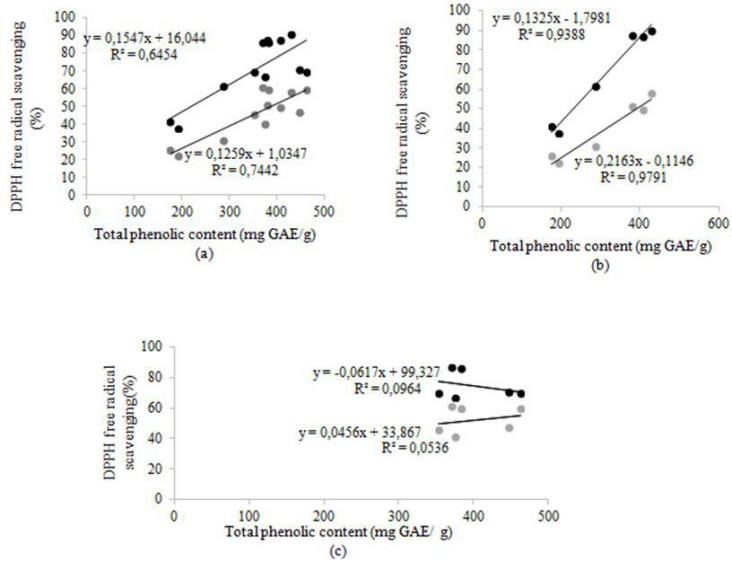

Fig. 6: Correlation between TPC and DPPH free radical scavenging activity in both outer and inner bark (a), inner bark only (b), and outer bark only (c); gray circle in 100 µg ·ml $^{-1}$ and black circle in 200 µg ·ml $^{-1}$ concentration.

The correlation also was observed between TFC and DPPH scavenging activity (Fig. 7). All correlations showed weak and negative relationships. In Fig. 7a, a negative correlation was demonstrated with R^2= 0.3 and 0.4. This suggests that TFC in the sample did not correspond with the DPPH levels. A strong negative correlation was calculated between TFC of inner

bark and DPPH (R^2= 0.6 and 0.7). This indicates that the flavonoid constituents in the inner bark sample do not relate to DPPH scavenging activity values. This could be due to the high concentration of fatty acids and alcohols and lower phenolic compounds in the inner bark part. In Fig. 7c, the TFC of the outer bark part was described. In 200 $\mu g \cdot ml^{-1}$ concentration of sample, the correlation was still negative even in low R^2 (0.1), while in 100 $\mu g \cdot ml^{-1}$ with low R^2 (0.05) value but the correlation was positive. In Fig. 7c, generally the sample with a high level of TFC also had a high level of DPPH radical scavenging activity, but it could not be explained with the correlation. These results agree with a previous study by Ghasemi et al. (2009) on 13 citrus species peels and tissues.

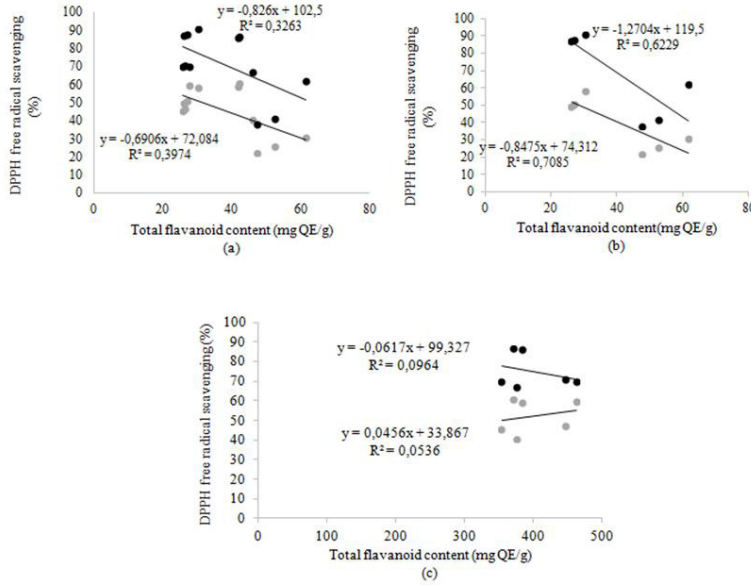

Fig. 7: Correlation between TFC and DPPH free radical scavenging activity correlation in both outer and inner bark (a), inner bark only (b), and outer bark only (c); gray circle in 100 µg/ ml and black circle in 200 µg/ ml concentration.

CONCLUSIONS

The phenol contents and antioxidant activity of MeOH soluble extract of *S. macrophylla* bark have been observed. The MeOH and EtOAc soluble extracts of outer bark showed higher antioxidant activity than the inner bark. The TPC measurement showed that outer bark had higher levels than inner bark. These findings suggest that the outer bark of *S. macrophylla* ecologically work as a protector of living tissues and natural antioxidant sources. With regard to TFC, only the MeOH crude extract showed higher values in the outer bark rather than the inner bark. The high antioxidant activity level was linearly related with GC-MS detection of phenolic compounds i.e. catechol and resorcinol in inner and outer bark sample. Correlation between phenol contents and antioxidant activity suggests that TPC strongly relates to antioxidant activity in the bark of *S. macrophylla*.

ACKNOWLEDGMENTS

We thank to SRIKANDIRATU, an industry of furniture in Jepara, Indonesia for the bark of *S. macrophylla*.

REFERENCES

1. Amamra, S., Cartea, M.E., Belhaddad, O.E., Soengas, P., Baghiani, A., Kaabi, I., Arrar L., 2018: Determination of total phenolics contents, antioxidant capacity of *Thymus vulgaris* extracts using electrochemical and spectrophotometric methods. International Journal of Electrochemical Science 13(8): 7882-7893.
2. Anoop, E.V., Jijeesh, C.M., Sindhumathi, C.R., Jayasree C.E., 2014: Wood physical, anatomical and mechanical properties of big leaf mahogany (*Swietenia macrophylla* Roxb) a potential exotic for South India. Research Journal of Agriculture and Forestry Sciences 2(8): 7-13.
3. Arisandi, R., Masendra, Purba, B.A.V., Wati, F.Z., Ihda, F.V., Sumantri, F., Lukmandaru, G., 2019: Lipophilic extractives of Mahogany (*Swietenia macrophylla* King) barks. Proceeding of 9th International Symposium of Indonesian Wood Research Society, Pp 92-102.
4. Arisandi, R., Marsoem, S.R., Lukmandaru, G., 2019: The contents of phenolics and cell wall component of *Eucalyptus pellita* F. Muell stemwood and bark. Wood Research 64(3): 411-422.
5. Arunachalam, M., Mohan, R.M., Mohanc, N., Mahadevand, A., 2003: Biodegradation of catechin. Proceedings of the Indian National Science Academy 69(4): 353-370.
6. Baba, S.A., Malik, S.A., 2015: Determination of total phenolic and flavonoid content, antimicrobial and antioxidant activity of a root extract of *Arisaema jacquemontii* Blume. Journal of Taibah University for Science 9(4): 449-454.
7. Bendary, E., Francis, R.R., Ali, H.M.G., Sarwat, M.I., El-Hady, S., 2013: Antioxidant and structure–activity relationships (SARs) of some phenolic and anilines compounds. Annals of Agricultural Science 58(2): 173-181.
8. Brighente, I.M.C., Dias, M., Verdi, L.G., Pizzolatti, M.G., 2007: Antioxidant activity and total phenolic content of some brazilian species. Pharmaceutical Biology 45(2): 156-61.
9. Brown, N., Jennings, S., Clements, T., 2003: The ecology, silviculture and biogeography of mahogany (*Swietenia macrophylla*): a critical review of evidence. Plant Ecology and Evolution System 6(1): 37-49.
10. Case, P.A., Bizama, C., Segur, C., Wheeler, M.C., Berg,A., DeSisto, W.J., 2014: Pyrolysis of pre-treated tannins obtained from radiata pine bark. Journal of Analytical and Applied Pyrolysis 107: 250-255.
11. Cory, H., Passarelli, S., Szeto, J., Tamez, M., Mattei, J., 2018: The role of polyphenols in human health and food systems: a mini-review. Frontiers in Nutrition 5(87): 1-9.
12. Diouf, P.N., Stevanovic, T., Cloutier, A., 2009: Antioxidant properties and polyphenol contents of trembling aspen bark extracts. Wood Science and Technology 43(5): 457-470.
13. Eddebbagh, M., Messaoudi, M., Abourriche, A., Berrada, M., Attaleb, M., Benbacer, L., Bennamara, A., 2016: Correlation of the cytotoxic and antioxidant activities of moroccan pomegranate (*Punica granatum*) with phenolic and flavonoid contents. Journal of Pharmacy and Pharmacology 68(4): 511-19.

14. Elansary, H.O., Szopa, A., Kubica, P., Ekiert, H., Mattar, M.A., Al-Yafrasi, M.A., El-Ansary, D.O., El-Abedin, T.K.Z., Yessoufou, K., 2019: Polyphenol profile and pharmaceutical potential of *Quercus* spp. bark extracts. Plants 8(11): 486.
15. Falah, S., Suzuki, T., Katayama, T., 2008: Chemical constituent from *Swietenia macrophylla* bark and their antioxidant activity. Pakistan Journal of Biological Sciences 11(16): 2007-2012.
16. Ghasemi, K., Ghasemi, Y., Ebrahimzadeh, M.A., 2009: Antioxidant activity, phenol and flavanoid contents of 13 citrus species peels and tissues. Pakistan Journal of Pharmaceutical Sciences 22(3): 277- 281.
17. Guedes, M.N.S., Pio, R., Maro, L.A.C., Lage, F.F., Abreu, M.P.D.A., Saczk, A.A., 2017: Antioxidant activity and total phenol content of blackberries cultivated in a highland tropical climate. Acta Scientiarum 39(1): 43- 48.
18. Halliwell, B., Gutteridge, J.N.C., 1999: Mechanism of damage of cellular targets by oxidative stress: lipid peroxidation. In: Free radicals in biology and medicine (ed. Halliwell B, Gutteridge JMC). Oxford University Press. Oxford, Pp. 284-313.
19. Hossain, M.A., Weli, A.M., Ahmed, S.H.J., 2019: Comparison of total phenols, flavonoids and antioxidant activity of various crude extracts of *Hyoscyamus gaagheri* traditionally used for treatment of epilepsy. Clinical Phytoscience 5(20): 1- 8.
20. Husein, I., Sadiyo, S., Nugroho, N., Wahyudi, I., Agustina, A., Komariah, R.N., Khabibi, J., Purba, C.Y.K., Ali, D., Iftor, M., Kahar,T.P., Wijayanto, A., Jamilah, M., 2014: Electrical properties of Indonesian hardwood, case study: *Acacia mangium*, *Swietenia macrophylla* and *Maesopsis eminii*. Wood Research 59(4): 695- 704.
21. Iravani, S., Zolfaghari, B., 2011: Pharmaceutical and nutraceutica effects of *Pinus pinaster* bark extract. Research in Pharmaceutical Sciences 6(1):1-11.
22. Masendra, Ashitani, T., Takahashi, K., Lukmandaru, G., 2018: Lipophilic extractives of the inner and outer barks from six different *Pinus* species grown in Indonesia. Journal of Forestry Research 29(5): 1329-36.
23. Miguel-Chávez, R.S., 2017: Phenolic antioxidant capacity: a review of the state of the art. In: Phenolic Compounds - Biological Activity (ed. Soto-Hernandez M, Palma-Tenango M, and Garcia-Mateos MR). IntechOpen, London, Pp 59-74.
24. Morris, H., Brodersen, C., Schwarze, F.W.M.R., Jansen S., 2016: The parenchyma of secondary xylem and its critical role in tree defense against fungal decay in relation to the CODIT model. Frontiers in Plant Science 7(1665): 1-18.
25. Ogawa, S., Yazaki, Y., 2018: Tannins from *Acacia mearnsii* De Wild. bark: tannin determination and biological activities. Molecules 23(4).
26. Pereira, D.M., Valentão, P., Pereira, J.A., Andrade, P.B., 2009: Phenolics: from chemistry to biology. Molecules 14(6): 2202-2211.
27. Pérez-Jiménez, J., Neveu, V., Vos, F., Scalber, A., 2010: Identification of the 100 richest dietary sources of polyphenols: an application of the phenol-explorer database. European Journal of Clinical Nutrition 64: 112–20.
28. Pinto, P., Romero, R., Carrie, M., Apelt, J., Segura, C., 2018: Fast pyrolysis of tannins from pine bark as a renewable sources of catechols. Journal of Analytical and Applied Pyrolysis 136: 69- 76.
29. Popa, V.I., 2015: Wood bark as valuable raw material for compounds with biological activity. Celuloză şi Hârtie 64(4): 1-14.
30. Rees, A., Dodd, G.F., Spencer, J., 2018: The effects of flavonoids on cardiovascular health: a review of human intervention trials and implications for cerebrovascular function. Nutrients 10(12): 1852.

31. Rosell, J.A., Gleason, S., Méndez-Alonzo, R., Chang, Y., Westoby, M., 2014: Bark functional ecology: evidence for tradeoffs, functional coordination, and environment producing bark diversity. New Phytologist 201(2): 486-497.
32. Singh, A., Holvoet, S., Mercenier, A., 2011: Dietary polyphenols in the prevention and treatment of allergic diseases. Clinical & Experimental Allergy 41(10): 1346-1359.
33. Sonam, K.S., Guleria, S., 2017: Synergistic antioxidant activity of natural products. Annals of Pharmacology and Pharmaceutics 2(8): 1-6.
34. Sroka, Z., Cisowski, W., 2003: Hydrogen peroxide scavenging, antioxidant, and anti-radical activity of some phenolic acids. Food and Chemical Toxicology 41: 753-758.
35. Valgimigli, L., Amorati, R., Fumo, M.G., Dilabio, G.A., Pedulli, G.F., Ingold, K.U., Pratt, D.A., 2008: The unusual reaction of semiquinone radicals with molecular oxygen. The Journal of Organic Chemistry 73(5): 1830-41.
36. Vasundevan, N., Mahadevan, A., 1990: Utilization of catechin by microorganism. Current Science 59(24): 1323-25.
37. Wafula, M.P, Hassanali, A., Swaleh, S., 2013: Phenolic and monoterpenoid mosquito repellent constituents of headspace vapors of *Conyza newii*. Journal of the Kenya Chemical Society 7(1): 7-10.
38. Waheed, I., Ahmad, M., Syed, N.H., Ashraf, R., 2014: Investigation of phytochemical and antioxidant properties of methanol extract and fractions of *Ballota limbata* (Lamiaceae). Indian Journal of Pharmaceutical Sciences 76(3): 251-256.
39. Wang, S., Moustaid-Moussa, N., Chen, L., Mo, H., Shastri, A., Su, R., 2014: Novel insights of dietary polyphenols and obesity. Journal of Nutritional Biochemistry 25(1): 1–18.
40. Wijayanto, A., Dumacay, S., Gerardin-Charbonnier, C., Sari, R.K., Syafii, W., Gerardin, P., 2015: Phenolic and lipophilic extractives in *Pinus merkusii* jungh. et de Vries knots and stemwood. Industrial Crops and Products 69: 466-471.
41. Zabka, M., Pavela, R., 2013: Antifungal efficacy of some natural phenolic compounds against significant pathogenic and toxinogenic filamentous fungi. Chemosphere 93(6): 1051-6.

Masendra, Brandon Aristo Verick Purba, Ganis Lukmandaru*
Universitas Gadjah Mada
Faculty of Forestry
Department of Forest Products Technology
Jl. Agro No. 1, Bulaksumur
55281 Yogyakarta
Indonesia
*Corresponding author: glukmandaru@ugm.ac.id

WOOD RESEARCH
66 (1): 2021
71-84
doi.org/10.37763/wr.1336-4561/66.1.7184

COMPARISON OF THERMAL TRANSFER AND INKJET PRINTING OF UHF RFID TAG ANTENNAS ON PAPER SUBSTRATES

Juraj Gigac, Mária Fišerová, Svetozár Hegyi
Pulp and Paper Research Institute Bratislava
Slovak Republic

(Received October 2020)

ABSTRACT

UHF RFID printed antennas on conventional and experimentally coated papers by thermal transfer and inkjet technique were not conductive due to high surface roughness. Reducing the surface roughness of paper and hence the electrical resistance of the antennas printed by thermal transfer and inkjet printing was achieved by coating and subsequent calendering process. Papers for thermal transfer and inkjet printed of aluminum and silver antennas were prepared by coating with top functional coating, whose main component was pigment - precipitated calcium carbonate with addition of polyvinyl alcohol, cationic polymer PDADMAC and glyoxal. The desired quality of inkjet-printed silver antennas was achieved by using coated paper with a polyvinyl alcohol barrier layer and a top functional hydrophilic layer. Silver nanoparticles of inkjet ink require a sintering process to obtain a conductive printed trace. The microstructure and thickness of antennas printed by thermal transfer and inkjet technique were compared. Thermal transfer printing created a more homogeneous antenna with greater sharpness of drawing compared to inkjet printing.

KEYWORDS: Paper, coating, calendering, thermal transfer printing, inkjet printing, RFID antenna, electrical resistance.

INTRODUCTION

RFID is a wireless identification technology to automatically identify and track physical objects or people by using radio frequency waves. This technology has several benefits over the conventional ways of identification, such as greater read range, faster data transfer, the ability to insert RFID tags into objects, the line-of-sight is not neccessary, and the ability to read a huge number of tags simultaneously (Want 2006). Passive UHF (Ultra High Frequency) RFID technology is beneficial in embedded applications as passive tags require minimal maintenance

because no battery replacement is required. The read ranges of passive UHF RFID systems are larger compared to other RFID frequencies (Dobkin 2013).

Printed antennas are usually applied to different plastic foils (Chin et al. 2012, Janeczek 2010, Betancourt and Castan 2013, Arazna et al. 2017). Recently, the popularity of RFID has increased significantly, particularly in relation to printing of antennas on paper substrates (Melampi et al. 2007, Tentzeris et al. 2007, Yang et al. 2007, Rida et al. 2009, Lakafosis et al. 2010, Jingtian et al. 2011, Zichner and Bauman 2011, Öhlund and Andersson 2012, Bollström and Toivakka 2013, Merilampi et al. 2014, He et al. 2016, Gigac et al. 2020). Modifications of paper substrates and printing processes are required in order to obtain working electronic devices. Coating and calendering processes can be used to modify the paper surface (Gigac et al. 2013, Stankovská et al. 2014). The paper surface is usually smoothed with a dispersion coating consisting of mineral pigments and organic binders. The smoothness of paper surface depends on composition of coatings, the number of coating layers and the final surface treatment. The surface properties of papers can be adjusted at the same time to achieve the desired functional properties, such as surface energy for print receptivity, water, oil and grease resistance, low vapor and gas permeability, and flame retardation. A number of techniques are available for printing electronics. These include well known and widely used methods inkjet and screen printing. They use an ink containing conductive particles or flakes typically metallic, which then requires sintering to achieve the maximum available conductivity. Thermal transfer printing use metal ribbons for printed electronics without the need of sintering step, which is esential in inkjet printing. The thickness of the metal in thermal transfer printing is relatively small (approximately 300 nm) compared to the metal thickness printed with the inkjet, which may be more than 1 μm (Kgwadi et al. 2014, Whyte et al. 2010).

Inkjet printing is a digital and non-contact technique that is almost free of chemical waste and doesn't require special facilities for its use. The possibility of using well known substrates like paper or polymer foils enables flexible, cheap and disposable device. It is ideal for fast prototyping and high throughput, low cost and improved environment-friendliness (Albrecht et al. 2016). The inks used for electronic printing are typically made of copper and/or silver nanoparticles due to their high electrical conductivity in an organic solvent and polymer coating (Dearden et al. 2004, Perelaer et al. 2006, Park et al. 2007). The polymer coating of the metal nanoparticles serves as stabilizer the dispersed particles in the ink to prevent them from coalescing, merging into larger aggregates, and clogging the print head nozzles in the inkjet printer. Printing of the conductive elements with metallic nanoparticle inks must be followed by an additional sintering step, usually achieved by heating to elevated temperature. Without sintering the printed trace of the metallic particles, nano-silver ink acts as an insulator in its as dried state. (Greer and Street 2007). The silver nanoparticle-based ink for printing of electronics has been developed, having a built-in sintering mechanism, which is triggered during drying of the printed pattern (Gouchko et al. 2011).

One digital printing technology that has not received much attention in the printed electronics arena is thermal transfer printing. Thermal transfer printing is a digital printing method in which material is applied to paper (or some other material) by melting a coating of ribbon so that it stays glued to the material on which the print is applied. It contrasts with direct thermal printing, where no ribbon is present in the process. Thermal transfer is a popular printing process particularly used for the printing of identification labels. It is the most widely used printing process in the world for the printing of high-quality barcodes. Thermal transfer printing contrasts with direct thermal printing where no tape is present in the process but a heat-sensitive substrate. Thermal transfer is preferable to direct thermal printing on heat-sensitive surfaces or when a longer life of the printed materials is desired. The thermal transfer ribbon

consists of a heat-resistant coating, a polyethylene terephthalate carrier film, a release layer, a vacuum metallized continuous layer and a thermoplastic tie layer. The carrier is a heat-resistant polyester film that has high tensile strength and, when thermally stabilized, transfers heat from the tips of the printer without excessive expansion. The release layer is prepared from waxy solids that are thermally softened during printing and which have a low cohesive strength. Because it is soft, it is disrupted by most subsequent operations, including printing or gluing. The metallized layer is a continuous conductor deposited on the release layer by vacuum deposition. The final layer is a thermoplastic adhesive that binds the metallized layer to the substrate when heated to form an image.

The aim of the work was to compare the influence of paper substrates, plastic foils, thermal transfer and inkjet printing as well as the design of UHF RFID antennas on their electrical resistance.

MATERIAL AND METHODS

Printing substrates

(1) *Paper TTP* – Thermal Transfer Paper Ultra 80 (Jujo Thermal), was calendered by two passes in a laboratory calender Kleinewefers at a linear load in the nip of 260 $kN \cdot m^{-1}$ and a metal roller temperature of 80°C.

(2) *Paper CFC* – Coated Folding Carton MB PRO FBB Bright, 185 gsm (Grafobal, Skalica, SK) was calendered by two passes in a laboratory calender Kleinewefers at a linear load in the nip of 260 $kN \cdot m^{-1}$ and a metal roller temperature of 80°C.

(3) *Paper EXP-PAP_1* – Base paper experimentally produced on pilot plant paper machine in Pulp and Paper Research Institute (Bratislava, SK) and sized into mass with 0.3% AKD (alkyl ketene dimer) was coated with a mixture of precipitated calcium carbonate pigment (100%), 30% polyvinyl alcohol (PVOH), 2.5% cationic polymer SMAI 1000 (styrene maleic anhydride imide). The coated paper was finally calendered by two passes in a laboratory calender Kleinewefers at a linear load in the nip of 260 $kN \cdot m^{-1}$ and a metal roller temperature of 80°C.

(4) *Paper EXP-PAP_2* – Base paper-Balance Pure Offset from 100% recycled fibres was coated with a mixture of precipitated calcium carbonate pigment (100%), 20% PVOH, 2.5% cationic polymer SMAI 1000. The coated paper was finally calendered by two passes in a laboratory calender Kleinewefers at a linear load in the nip of 260 $kN \cdot m^{-1}$ and a metal roller temperature of 80°C.

(5) *Paper EXP-PAP_3* - Base paper experimentally produced on pilot plant paper machine in Pulp and Paper Research Institute (Bratislava, SK) and sized into mass with 0.3% AKD (alkyl ketene dimer) was coated with a mixture of precipitated calcium carbonate pigment (100%), 30% PVOH, 2.5% cationic polymer PDADMAC (poly diallyldimethyl-ammonium chloride). The coated paper finally calendered by two passes in a laboratory calender Kleinewefers at a linear load in the nip of 260 $kN \cdot m^{-1}$ and a metal roller temperature of 80°C.

(6) *Paper EXP-PAP_4* - Base paper (Balance Pure Offset from 100% recycled fibres) was coated with a mixture of precipitated calcium carbonate pigment (100%), 30% PVOH, 2.5% cationic polymer PDADMAC. The coated paper was finally calendered by two passes in a laboratory calender Kleinewefers at a linear load in the nip of 260 $kN \cdot m^{-1}$ and a metal roller temperature of 80°C.

(7) *Barrier coated inkjet paper EXP-IJP_BC* – Base paper was coated with PVOH barrier coating and with top functional coating, whose basic component was an aqueous-isopropyl alcohol dispersion of a mixture of precipitated calcium carbonate pigment (100%), 30% PVOH,

2.5% cationic polymer PDADMAC. The coated paper was finally calendered by two passes in a laboratory calender Kleinewefers at a linear load in the nip of 260 kN·m^{-1} and a metal roller temperature of 80°C.

(8) PET (*polyethylene terephthalate*) *foil NOVELE* obtained from NovaCentrix was used as a reference substrate for printing UHF RFID antennas.

(9) PET labels from Acoding Company, SK.

Antennas design

UHF RFID antenna 1 - Type DogBone i, product of the Smartrac division of the company Avery Dennison, compatible with chip NXP UCODE G2iL / iM or Impinj Monza 5. *UHF RFID antenna 2* - Type undefined. *UHF RFID antenna 3* – Type AD-227m5 from the company Avery Dennison, compatible with chip Impinj Monza 5 (Fig. 1).

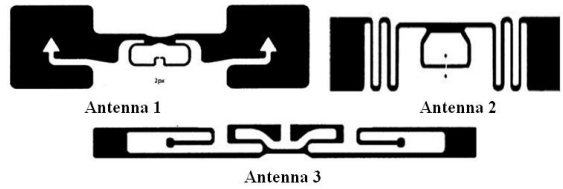

Fig. 1: Design of UHF RFID antennas.

Methods

Top functional coating of base papers for the preparation of (barrier-free) thermal transfer papers and inkjet papers was realized by laboratory knife coater (DOW Chemicals). Barrier coating of the base papers for the preparation of the barrier inkjet paper was realized by bar coating. Calendering of papers was performed by two passes in a laboratory calender Kleinewefers at a linear load in the nip of 260 kN·m^{-1} and a metal roller temperature of 80°C. Thermal transfer printing with conductive aluminum thermal transfer ribbon Metallograph® from companies SPF-Inc. and IIMAK in industrial printer SATO CL4NX with output of 3000-25000 antennas per hour (aluminum foil thickness 260 nm, thermal print head 305 dpi, substrate thickness up to 280 μm). Inkjet printing with conductive AgNPs ink Metalon JS-B25P from company NovaCentrix in the piezoelectric desktop printer EPSON Stylus 88+ (drop volume 3 μL, substrate thickness up to 110 μm). Sintering (curing) of inkjet-printed antennas was carried out at downforce of 75 kPa of the hot flat press heated to 130°C for 15 seconds.

Electrical resistance of the antennas was measured corner to corner using a multimeter UNIT-T, Model UT70B. The microstructure and thickness of the aluminum and silver antennas were determined by scanning electron microscopy (SEM) using a JEOL JSM 6610 microscope equipped with an EDS detector X-Max 50 mm^2 (Oxford Instruments Ltd.). Antenna samples were cut, ultrasonically cleaned and observed in a microscope at various magnifications. The surface of the samples was subjected to EDX analysis in an electron microscope at magnification 250x. Subsequently, all samples were glued vertically on the holder, and encapsuled into conductive potting mass. Samples were prepared metallographically – sanded and polished to the desired shape and surface. Subsequently they were rinsed in isopropyl alcohol, ultrasonically cleaned and thoroughly dried.

The distance between the ends of the UHF RFID antennas (in a place where the chip connects to the antenna) was measured at 50x magnification using a Leitz Wezler OP light microscope (Germany) and a Nicon Coolpix 4500 CCD camera (Japan).

RESULTS AND DISCUSSION

Paper has a rougher surface compared to a plastic foil, which is currently most frequently used as a substrate for printing UHF RFID antennas. Irregular surfaces and structural properties of conventional papers require higher ink consumption, which is achieved by conventional printing technique such as screen printing. In order to improve printability, research of label and packaging paper production technology is aimed at improving surface smoothness and absorption properties of paper. Thermal transfer and inkjet printing of antennas on uncalendered and calendered papers with surface roughness over 6%, expressed by optical variability of surface, provided only non-conductive antennas. The optical variability of paper surface was evaluated by the photoclinometric method (Kasajová and Gigac 2013, Gigac et al. 2013, 2014).

Electrical resistance of antennas

Fig. 2 compares the electrical resistance of three antenna designs (Fig. 1) printed by thermal transfer printing on calendered commercial and experimentally coated papers with antennas printed on PET label.

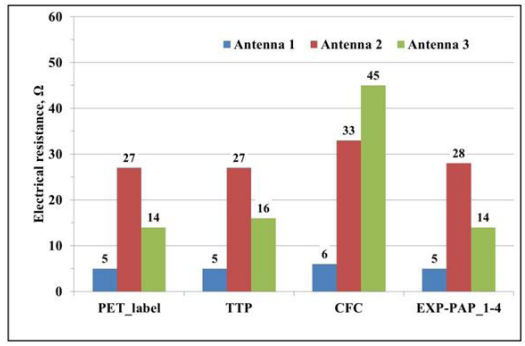

Fig. 2: Comparison of electrical resistance of antennas printed by thermal transfer printing on calendered commercial papers and calendered experimentally coated papers with antennas printed on PET label.

The design of antennas has a significant effect on their electrical resistance, which depends on the length of the antenna and is strongly influenced by the geometric dimensions of its narrowest part. Meander antenna 2 is the longest, so it has a higher electrical resistance compared to antennas 1 and 3.

The aim of paper coating and calendering was to improve its surface smoothness and the quality of UHF RFID antennas printed by the thermal transfer and inkjet printing. The electrical resistances of antennas printed with conductive Al ribbon by thermal transfer printing on calendered commercial paper (TTP) and calendered experimentally coated papers (EXP-PAP_1-4) were comparable to those of printed antennas on PET label.

The electrical resistances of antenna 2 and antenna 3 printed on calendered commercial paper (CFC) were about 6 Ω, respectively about 31 Ω higher than the resistances of the antennas printed on the PET label. The higher electrical resistance of the antennas printed on CFC paper was due to the higher surface roughness (6.2 %) compared to other papers (5.2- 5.8%) and PET labels. Surface roughness was evaluated by photoclinometric method as optical variability of surface (Gigac et al. 2020).

Calendered experimentally coated papers (EXP-PAP_1-4) prepared for thermal transfer printing of antennas were also printed by inkjet printing. Electrical resistances of antennas 1, 2 and 3 (Fig. 1) printed by both printing techniques are shown in Figs. 3-5. The electrical resistances of the UHF RFID antennas 1, 2, 3 printed by thermotransfer printing on all tested papers were lower compared to the inkjet printed antennas. The electrical resistance of antennas was significantly influenced by the antenna design, regardless of printing technique. Calendered experimentally coated papers EXP-PAP_3 and EXP-PAP_4 are suitable for printing antennas with both printing techniques.

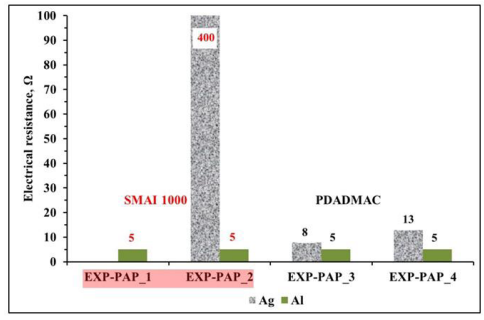

Fig. 3: Effect of cationic polymer in coatings of calendered experimentally coated papers on electrical resistance of Antenna 1 printed by thermal transfer (Al) and inkjet (Ag) printing (in coating of papers EXP-PAP_1 and EXP-PAP_2 was SMAI 1000 and of papers EXP-PAP_3 and EXP-PAP_4 was PDADMAC).

The antenna 1 printed by inkjet printing on these papers had electrical resistances 8 and 13 Ω (Fig. 3), the antenna 2 had electrical resistances 68 and 73 Ω (Fig. 4), and the antenna 3 (Fig. 5) had electrical resistances 24 and 25 Ω. Inkjet-printed antennas 1, 2, 3 on papers EXP-PAP_1 and EXP-PAP_2 were nonfunctional as they were nonconductive with high electrical resistance. A high electrical resistance of up to 400 Ω was measured on antenna 1 (Fig. 3). The only difference between the calendered experimentally coated papers was the type of cationic polymer used in preparation of the coating compositions and the type of base paper. The effect of the paper substrate on electrical resistance of the printed antennas on calendered experimentally coated papers was not detected.

We assume that the application of the cationic polymer SMAI 1000 in coatings of papers EXP-PAP_1 and EXP-PAP_2 caused the nonfunctioning of the inkjet printed antennas. A more suitable cationic polymer PDADMAC was used in the coatings of papers EXP-PAP_3 and EXP-PAP_4. For sintering the silver particles must be very close – touching. From a colloid perspective that is best if they are not flocculated. Perhaps the SMAI is causing flocculation – with the silver particles being separated so not close enough to sinter. With PDADMAC in the mix they are sintering.

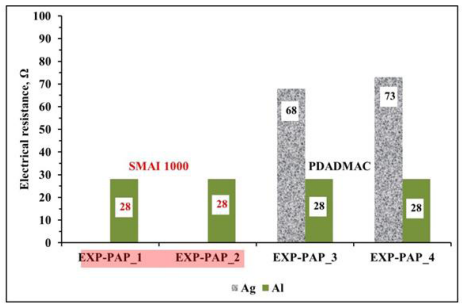

Fig. 4: Effect of cationic polymer in coatings of calendered experimentally coated papers on electrical resistance of Antenna 2 printed by thermal transfer (Al) and inkjet (Ag) printing (in coating of papers EXP-PAP_1 and EXP-PAP_2 was SMAI 1000 and of papers EXP-PAP_3 and EXP-PAP_4 was PDADMAC).

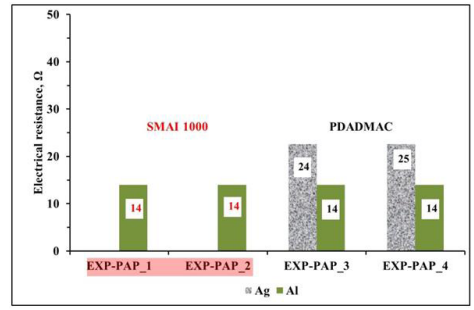

Fig. 5: Effect of cationic polymer in coatings of calendered experimentally coated papers on electrical resistance of Antenna 3 printed by thermal transfer (Al) and inkjet (Ag) printing (in coating of papers EXP-PAP_1 and EXP-PAP_2 was SMAI 1000 and of papers EXP-PAP_3 and EXP-PAP_4 was PDADMAC).

To produce a UHF RFID tag with a large reading range, high quality printed antenna with the lowest electrical resistance is required. Lower electrical resistance of aluminum antennas prepared by thermal transfer printing compared to silver antennas printed by inkjet printing on calendered experimentally coated papers EXP-PAP_3 and EXP-PAP_4 is in good agreement with the results of electrical resistances of antennas printed by thermal transfer and inkjet printing on plastic substrate THERMLfilm (Kgwardi et al. 2016). In this work, aluminum UHF RFID tags had lower electrical resistance, and their reading range was greater than of silver ones.

The desired quality of silver antennas was achieved using calendered experimentally paper with a top functional coating on a barrier coating of the base paper. The top functional coating was composed of a mixture of precipitated calcium carbonate (100%), PVOH (30%), cationic polymer (2.5%) and glyoxal (2%). Polyvinyl alcohol was used for the barrier coating.

Due to the presence of a barrier layer under the top functional coating in the calendered experimentally coated EXP-IJP_BC paper, the electrical resistance of antennas 1, 2 and 3 was reduced to the level of aluminum and silver antennas on the plastic substrate PET Novele. (Tab. 1).

Tab. 1: Comparison of electrical resistances of inkjet printed antennas on calendered experimentally papers and plastic substrate.

Paper	Description	Antenna 1 (Ω)	Antenna 2 (Ω)	Antenna 3 (Ω)
EXP-PAP_3	Barrier-free with calendered top coating	8	68	24
EXP-PAP_4	Barrier-free with calendered top coating	13	73	25
EXP-IJP_BC	Barrier with calendered - top coating	2.9-4.3	24-42	10.4-11.3
PET foil	NOVELE - Ag antenna	3.9-4.1	21-34	7.6-10.2
PET foil	NOVELE - Al antenna (Termal tranfer printing)	5	28	14

Characterization of antennas

Chemically etched aluminum antennas on plastic UHF RFID tags are shown in cross section using SEM microscopy in Fig. 6. The average thickness of the antennas was 10.12 μm (a), 16.48 μm (b) and 12.80 μm (c).

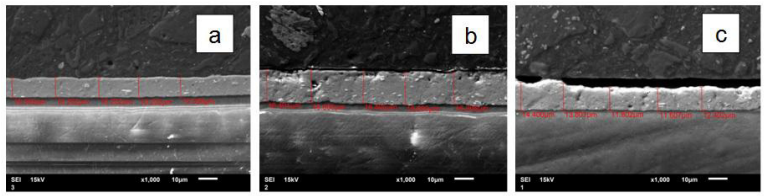

Fig. 6: SEM microstructure of chemically etched aluminum antennas on PET foil in cross section with the aluminum layer shown.

The thickness of the aluminum antenna printed by thermal transfer technique on PET foil (Fig. 7) was 260 nm, as well as on paper EXP-PAP_3 (Fig. 8), as it is given by the thickness of the aluminum layer on the Metallograph® ribbon.

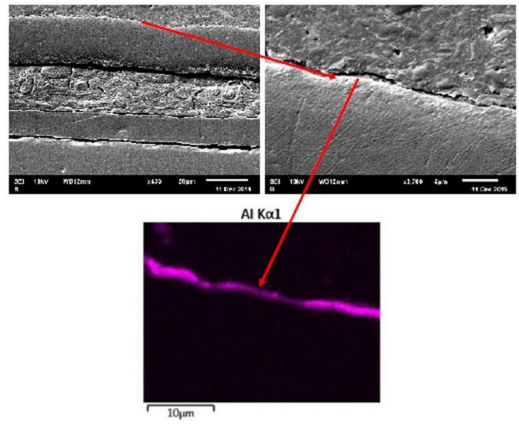

Fig. 7: SEM microstructure of an aluminum antenna printed by thermal transfer technique on PET foil in cross section with the aluminum layer shown by EDS mapping.

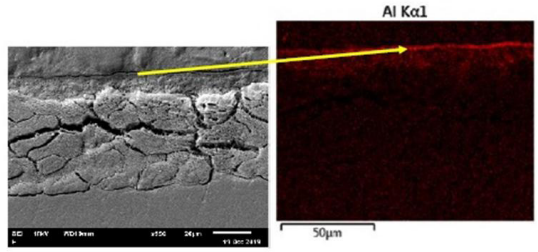

Fig. 8: SEM microstructure of an aluminum antenna printed by thermal transfer technique on paper EXP-PAP_3 in cross section with the aluminum layer shown by EDS mapping.

The average thickness of the silver antenna fabricated with inkjet printing technique on PET foil (Fig. 9) was 1.29 - 1.69 μm.

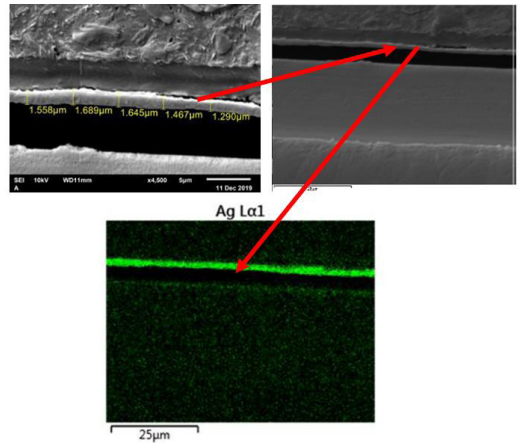

Fig. 9: SEM microstructure of a silver antenna printed by inkjet technique on PET foil in cross section with the silver layer shown by EDS mapping.

A comparison of thickness and material of the conductive film of the UHF RFID antenna according to the technique used is shown in Tab. 2. Compared to conventional printing techniques such as inkjet, screen, flexo and gravure printing, thermal transfer printing uses 130 times cheaper aluminum compared to silver and eliminates the sintering process of silver nanoparticles. The advantage of thermal transfer printing is also low aluminum consumption, as it is applied in thickness of 260 nm. The advantage of a greater thickness of the Ag and Cu conductive film in conventional printing methods and hot stamping is the good printability of substrates even with a rougher surface.

Tab. 2: Thickness and material of conductive film according to an antenna preparation technique.

Technique	Thickeness of conductive film (μm)	Antenna material
Screen printing	4-16	Ag
Flexo printing	1-2	Ag
Gravure	0.5-2.0	Ag
Inkjet printing	0.3-1.5	Ag
Thermal transfer printing	0.26	Al
Hot stamping (Taylor and Harrison 2017)	0.34	Cu
Chemical etching	10 and more	Al

In Tab. 2, in addition to printing techniques, there is also an etching technique which is currently used in the production of RFID tags. Aluminum antennas produced by chemical etching of the aluminum layer on a plastic foil have a thickness of 10-16 μm.

Details of UHF RFID antenna 1 printed by thermal transfer and inkjet printing on calendered experimentally coated paper and PET foil (Novele) were evaluated. The distance between the ends of the UHF RFID antenna at 50x magnification was measured using by light

microscop and a CCD camera. The gap between the ends of the antennas is the place where the chip is connected. Based on the measurement results in Fig. 10 it can be stated that distance between the ends of the dipole UHF RFID antenna was by 75-105 μm shorter achieved with inkjet printing (Ag nanoparticles) than with thermal transfer printing (Al ribbon). The gap size is adjusted by changing the print template for each printer. Thermal transfer printing is more homogeneous and has a sharper drawing.

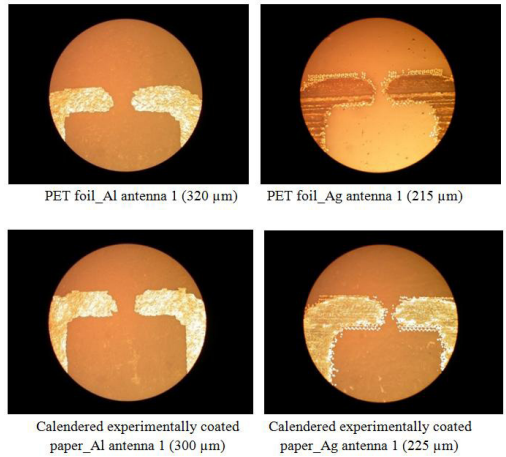

Fig. 10: Comparison of the distance between the ends of UHF RFID antenna 1 printed by thermal transfer (Al ribbon) and inkjet (Ag nanoparticles) printing on calendered experimentally coated paper and PET foil.

In Fig. 11 are SEM images of the aluminum layer and silver layers of UHF RFID antennas printed on the surface of the papers. The surfaces of aluminum and silver antennas differ significantly. The aluminum layer (a) is continuous, with little surface damage that may be related to the surface roughness of the paper. The sintered silver nanoparticles formed a porous layer (b) which reached a maximum of 65% of the conductivity of silver. In the case of a higher surface roughness of the paper, discontinuous layers (c) of silver were formed.

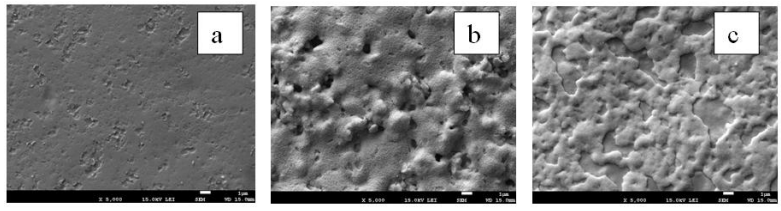

Fig. 11: SEM images of aluminum layer (a) and silver layers (b, c) of UHF RFID antennas printed on papers.

CONCLUSIONS

Paper substrates are more suitable for printing UHF RFID antennas than plastic substrates as they are recyclable and several times cheaper. However, printed antennas on conventional papers have higher electrical resistance due to the high surface roughness than those printed on plastic substrates.

Paper surfaces have been modified by coating and calendering processes to reduce surface roughness and electrical resistance of UHF RFID antennas printed by thermal transfer and inkjet printing. Composition of the top functional coating, the main component of which was pigment - precipitated calcium carbonate, and the calendering of the top coat had a positive effect on surface smoothness, electrical resistance and quality of UHF RFID antennas printed by thermal transfer and inkjet printing. Uncalendered papers and calendered papers with higher surface roughness, optical variability of surface over 6%, provided only non-conductive antennas. In the case of inkjet printing, in addition to the surface roughness of the paper, the correct choice of cationic polymer for the coating colour is also important.

Electrical resistance of UHF RFID antennas printed by thermal transfer printing on calendered experimentally coated papers was lower than inkjet printed antennas. The polyvinyl alcohol-based barrier coating improved the absorption and anchoring of the inkjet ink in the top functional coating. The electrical resistance of inkjet printed silver antennas was reduced by using experimentally coated paper with barrier coating on a base paper and with a top functional coating.

The process of calendering coated folding carton (CFC), to the extent necessary to reduce the surface roughness and make a conductive UHF RFID antenna by thermal transfer or inkjet printing, was not suitable as it unacceptably reduced the stiffness of this packaging material. The required stiffness of packaging materials with conductive antennas printed on rougher surfaces can be achieved by hot stamping with a copper layer 340 nm thick.

The advantage of thermal transfer printing UHF RFID antennas is the use of 130 times cheaper aluminum compared to silver used in inkjet printing. In addition, aluminum consumption is low because it is applied in thickness 260 nm, while in the case of inkjet printing, the thickness of the silver film was 1.3-1.7 μm. In addition, silver nanoparticles require a sintering process to create conductive antennas with low electrical resistance. Under optimal conditions, the silver nanoparticles formed a porous layer after sintering, which reached only 30-65% of the conductivity of silver.

Antennas printed by the thermal transfer technique were more homogeneous with greater sharpness of drawing than antennas printed by the inkjet technique.

Printed antennas on paper will be used for chip installation and communication quality evaluation of prepared UHF RFID tags.

ACKNOWLEDGMENT

This work was supported by Slovak Research and Development Agency under contract No. APVV-19-0029.

REFERENCES

1. Albrecht, A., Rivadeneyra, A., Salmerón, J., Abdellah, A., Lugli, P., 2016: Inkjet printing and photonic sintering of silver and copper oxide nanoparticles for ultra-low-cost conductive patterns. Journal of Materials Chemistry C(4): 3546–3554.
2. Arazna A., Janeczek, K., Futera, K., 2017: Mechanical and thermal reliability of conductive circuit injet printed on flexible substrates. Circuit World 43(1): 9-12.
3. Betancourt, D., Castan, J., 2013: Printed antenna on flexible low-cost PET substrate for UHF applications. Progress in Electromagnetics Research C 38: 129-140.
4. Bollström, R., Toivakka, M., 2013: Paper substrate for printed functionality. 15th Fundamental Research Symposium, Cambridge, September 2013, Pp. 945-966.
5. Dearden, A., Smith, P., Shin, D.Y., Reis, N., Derby, B., Paul O'Brien, P., 2004: A low curing temperature silver ink for use in ink-jet printing and subsequent production of conductive tracks. Macromolecular Rapid Communications 26(4): 315-318.
6. Dobkin, D., 2013: The RF in RFID: Passive UHF RFID in practice. Newnes, Elsevier, USA, second ed., 528 pp.
7. Gigac, J., Fišerová, M., Kováč, M., Stankovská M., 2020: Paper substrates for inkjet printing of UHF RFID antennas. Wood Reseaech 65(1): 25-36.
8. Gigac, J., Kasajová, M., Maholányiová, M., Stankovská, M., Letko, M., 2013: Prediction of surface structure of coated paper and of ink setting time by infrared spectroscopy. Nordic Pulp Paper Research Journal 28(2): 274-281.
9. Gigac, J., Kasajová, M., Stankovská, M., 2014: The influence of paper surface energy on multicolor offset print mottling. Tappi Journal 13(2): 55-64.
10. Greer, J.R., Street, R.A., 2007: Thermal cure effects on electrical performance of nanoparticle silver inks. Acta Materialia 55(18): 6345-6349.
11. Grouchko, M. Kamyshny, A., Mihailescu, C.F., Anghel, D.F., Magdassi, S., 2011: Conductive inks with a „built-in" mechanism that enables sintering at room temperature. ACS Nano 5(4): 3354-3359.
12. He, H., Sydänheimo, L., Virkki, J., Ukkonen, L., 2016: Experimental study on inkjet-printed passive UHF RFID tags on versatile paper-based substrates. International Journal of Antennas and Propagation, ID 9265159, 8 pp.
13. Chin, K.C., Tsai, C.H., Chang, L.C., Wei, C.L., Chen, W.T., Chen, C.S., Lai, S.J., 2012: Design of flexible RFID tag and rectifier circuit using low cost screen printing process. http://magazines007.com/pdf/RFIDdesign.pdf.
14. Janeczek, K., 2010: Performance of RFID tag antennas printed on flexible substrates. In: XII International PhD Workshop, Wisla, Poland, Pp 345-348.
15. Jingtian, X., Hailong, Z., Ye, T.T., 2011: Exploration of printing-friendly RFID antenna designs on paper substrates. In: 2011 IEEE International Conference on RFID, Pp 38-44.
16. Kavčič, U., Pivar, M., Dokič, M., Svetec, D.G., Pavlovič, L., Muck, T., 2014: UHF RFID tags with printed antennas on recycled papers and cardboards. Materials and Technology 48(2): 261-267.
17. Kasajová, M., Gigac, J., 2013: Comparison of print mottle and surface topography testing methods. Nordic Pulp & Paper Research Journal 28(3): 443-449.
18. Kgwadi, M., Vourch, C.J., Harrison, D.J., Drysdale, T.D., 2014: On-demand printing of antennas for TV white-space communications. In: 2014 Loughborough Antennas and Propagation Conference (LAPC), Loughborough, UK., Pp 553-556.

19. Kgwadi, M., Rizwan, M., Adhur Kutty, A., Virkki, J., Ukonen L., Drysdale, T.D., 2016: Performance comparison of inkjet and thermal transfer printed passive ultra-high-frequency radio-frequency identification tags. Antennas & Propagation 10(14): 1507-1514.
20. Lakafosis, V, Rida, A., Vyas, R., Li, Y., Nikolaou, S., Tentzeris, M.M., 2010: Progress towards the first wireless sensor networks consisting of inkjet-printed. Paper-based RFID-enabled sensor tags. In: Proceedings of the IEEE 98(9): 1601-1609.
21. Merilampi, S., Ukkonen, L., Sydanheimo, L., Ruuskanen, P., Kivikoski, M., 2007: Analysis of silver ink bow-tie RFID tag antennas printed on paper substrates. International Journal of Antennas and Propagation, 9 pp.
22. Merilampi, S. L., Virkki, J., Ukkonen, L, Sydänheimo, L., 2014: Testing the effects of temperature and humidity on printed passive UHF RFID tags on paper substrate. International Journal of Electronics 101(5): 711–730.
23. Öhlund, T., Andersson, M., 2012: Effect of paper on electrical conductivity and pattern definition for silver nanoparticle inkjet ink. In: Proceedings LOPE-C, Pp 115-119.
24. Park, B.K., Kim, D., Jeong, S., Moon, J., Kim, J.S., 2007: Direct writing of copper conductive patterns by ink-jet printing. Thin Solid Films 515: 7706-7711.
25. Perelaer, J., de Gans, B.J., Schubert, U.S., 2006: Ink-jet printing and microwave sintering of conductive silver tracks. Advanced Materials 18(16): 2101-2104.
26. Rida, A., Li, Y., Vyas, R., Tentzeris, M.M., 2009: Conductive inkjet-printed antennas on flexible low-cost paper-based substrates for RFID and WSN applications. IEEE Antennas and Propagation Magazine 51(3): 13-23.
27. Taylor, D.H., Harrison, D., 2017: High volume digital printing of flexible electronics with continuous copper and aluminum. LOPEC 2017, Munich.
28. Tentzeris, M.M., Yang, L., Rida, A., Traille, A., Vyas, R., Wu, T., 2007: Inkjet-printed RFID tags on paper-based substrates for UHF "cognitive intelligence" applications. In: IEEE International Symposium on Personal, Indoor and Mobile Radio Communications. Athens, Greece, Pp 1-4.
29. Want, R., 2006: An inroduction to RFID technology. IEEE Pervasive Computing 5(1): 25-33.
30. Whyte, G., Harrison, D., Cumming, D., Drysdale, T., 2010: Direct printing of flexible metallic millimetre-wave frequency selective surfaces. In: 2010 IEEE Antennas and Propagation Society International Symposium (APSURSI), Toronto, Canada, Pp 1-4.
31. Yang, L., Rida, A., Vyas, R., Tentzeris, M.M., 2007: RFID tag and RF structures on a paper substrate using inkjet-printing technology. IEEE Transactions on Microwave Theory and Techniques 55(12): 2894–2900.
32. Xi, J., Zhu, H., Ye, T.T. 2011: Exploration of printing-friendly RFID antennas designs on paper substrates. In: 2011 IEEE International Conference, Pp 38-44.
33. Zichner, R., Baumann, R.R., 2011: Communication quality of printed UHF RFID transponder antennas. LOPEC, Messe Frankfurt, Germany, Pp 361-363.

Juraj Gigac*, Mária Fišerová, Svetozár Hegyi
Pulp and Paper Research Institute
Dúbravská Cesta 14
841 04 Bratislava
Slovak Republic
*Corresponding author: gigac@vupc.sk

WOOD RESEARCH
66 (1): 2021
85-94
doi.org/10.37763/wr.1336-4561/66.1.8594

EFFECT OF SILICA ON ALKALINE BAGASSE CELLULOSE AND SOFTWOOD CELLULOSE

Samson Masulubanye Mohomane[1], Setumo Victor Motloung[2,3], Lehlohonolo Fortune Koao[4], Tshwafo Elias Motaung[3,5]

[1]University of Zululand, South Africa
[2] Nelson Mandela University, South Africa
[3]Sefako Makgatho Health Sciences University, South Africa
[4]University of The Free State, South Africa
[5]University of South Africa, South Africa

ABSTRACT

This study investigates the effect of silica on sugarcane bagasse (SCB) and softwood (SW) cellulose. Cellulose was extracted from raw SCB and SW chips using a three-step process, namely thermal pre-treatment, alkaline treatment and bleaching treatment. Alkali treated cellulose was then subjected to silica surface modification using the solvent exchange method. The effect of silica modification on SCB and SW cellulos was investigated using X-ray diffractions analysis (XRD), Fourier transform infrared (FTIR) spectroscopy and optical microscope (OPM) techniques. Both the FTIR and XRD results confirm successful extraction of cellulose from both raw fibers and addition of silane functional groups in the cellulose surface. XRD patterns of all samples revealed typical spectra for natural fibers corresponding to crystalline peaks of cellulose and undissolved amorphous hemicellulose respectively. SCB and SW showed similar increasing patterns of crystallinity with nanosilica surface modification. The surface morphology results showed that both SCB and SW cellulose modified with silica were swollen and displayed small particles agglomerating on the surface of the fibers. The solvent exchange method proved to be a successful method for modifying SCB and SW cellulose with nanosilica. It also proved to be cost-efficient and time-efficient.

KEYWORDS: Sugarcane bagasse, soft wood, cellulose, silica.

INTRODUCTION

There is a significant research interest in the application of natural fibers in the field of polymer composites due to their many advantages. Natural fibers are abundant, renewable, non-abrasive, non-toxic and biodegradable as compared to synthetic fibers. They also possess

outstanding mechanical properties with varying morphology and good surface properties (Sequeira et al. 2009, Jacob et al. 2005, Eichhorn et al. 2001, Sibuya et al. 2018). Amongst the natural fibers, sugarcane bagasse (SCB) is one of the major agricultural residues that have gained popularity lately and an exceptional fiber for composites reinforcement because of low modification cost and high quality composites attained. SCB is a versatile fibrous agricultural residue that is obtained after extraction of 'juice' from sugarcane, that can be can be converted to paper, feedstock, biofuel amongst others. It can also be used as an absolute substrate for microbial processes to produce electricity, chemicals, enzymes, and other valuable products. SCB contains about 40-50% cellulose, 25-30% of hemicellulose and about 20-25% of lignin content. It has been used for reinforcement for thermoplastics in the automotive, construction and food packaging industries (Loh et al. 2013, Mulinari et al. 2009, Ahmed et al. 2012).

Soft wood (SW) is one of the most used natural fibers in thermoplastic reinforcement. The main components in SW are cellulose, lignin and hemicellulose which account for 55%, 11% and 26% respectively. Wood elements employed in polymer composites vary in shape and can be used in combinations or alone. The shape and wood fiber size determine the properties of the final product such as surface chemistry. The strength of wood polymer composites depends on factors like chemical compositions, density, thickness, fiber content, and the type of bonding agent (if any). Softwood has applications in architectural woodwork, composite materials, construction and furniture fields (Terrett et al. 2019, Ashori, 2008). Cellulose is one of the highly abundant natural polymers found in earth. It can be extracted from several sources including bagasse, wood, cotton, pineapple leaves and sisal fibers amongst others. Structurally, it consist of D-anhydroglucopyranose units which are joined to form a linear molecular chain. Cellulose extraction is normally a three-step process, i.e. thermal pre-treatment, alkaline treatment and bleaching treatment. The alkalization step removes non-cellulosic components such as lignin, hemicellulose, waxes and pectin. The treatment increases the roughness of the fiber surface resulting in the improved adhesion between the fibre and the matrix (Zhao et al. 2013, Barra et al. 2006, Linganiso et al. 2019).

Silica (SiO_2) is mainly found as quartz in nature and in various living organisms. Silica as a filler is known for enhancing mechanical strength, thermal stability and transparency. It makes cellulose composites hydrophobic and resistant to structural deformation (Litschauer et al. 2011, Ha et al. 2019). Cellulose modification results in morphology changes and increases in hydroxyl groups. Hence, cellulose surface modification enhance surface tension, wettability, swelling, adhesion and compatibility with polymers (Ashori et al. 2008, Wei et al. 2015). The preparation of cellulose-silica composites can be achieved in various ways such as acid-catalyzed hydrolysis, sol-gel method or using precursors like tetraethoxysilane (TEOS) (Cerchiara et al. 2018, Maleki et al. 2014) amongst others. One of the cheap and simple methods of preparing cellulose-silica composites is the solvent exchange method, which substituted the need for surfactants when incorporating cellulose fibers into non-polar polymers. This method uses the percolating approach to prepare the cellulose surface for effective facial interaction with hydrophobic silica and allow the incorporation of composite formation without the use of catalysts and crosslinking agents. The cellulose fiber assembles to a three-dimensional template, then the percolating structure is then filled with nanosilica. Cellulose-silica composite normally takes days and energy to synthesize it. However, it only takes a few hours using the solvent exchange method because it is a one-step energy-efficient method. This method yields a composite with reduced moisture absorption, enhanced thermal properties and dimensionally stability (Rodríguez-Robledo et al. 2018). In a study by Barra et al. (2006), the treatment of sisal fiber with silica showed improvement in tensile strength, impact strength and tensile modulus. There are also changes in morphology and porosity of the cellulose-silica composite depending on the silica

content. Silica-based composites can be used to coat implants and medical products as biosensors, biocatalysts, and matrix for a controlled release of drugs (Hou et al. 2010, Xie et al. 2009). Due to their antifungal activity property, such composites can be used to avoid the growth of *Aspergillus Versicolor* which degrades paper artwork such as books, manuscripts, paintings, etc. (Rodríguez-Robledo et al. 2018, Cerchiara et al. 2018).

MATERIALS AND METHODS

Sugarcane bagasse was obtained from Tongaat Hullets sugar mill in Felixton, South Africa. Softwood (*Pinus patula*) chips was obtained from the nearby farm in Empangeni, South Africa. Silica (SiO_2), sodium hydroxide (NaOH), sodium chlorite ($NaClO_2$), glacial acetic acid (CH_3COOH), acetone (C_3H_6O), and ethanol (CH_3COOH) were purchased from Laboratory consumables, South Africa. All chemicals were used without further purification.

Thermal pre-treatment

SCB and SW feedstock were separately subjected to thermal pre-treatment. The feedstock was boiled with water for an hour on a hot plate. The mixture was removed from the hot plate and rinsed with distilled water. The process was repeated four times to ensure that impurities and any dirt trapped were effectively removed.

Alkaline treatment

The thermally pre-treated SCB and SW were treated with an alkaline solution (2% NaOH) prepared by dissolving 100 g NaOH in 5L distilled water. The mixture was boiled for an hour and rinsed with distilled water. The process was repeated four times.

Bleaching

The buffer solution was prepared by adding 54 g NaOH, 150 mL acetic acid, and distilled water in 2L volumetric flask. The solution of sodium chlorite (3.5%) was prepared by dissolving 70 g $NaIO_4$ salt in 2L distilled water. The buffer and sodium chlorite solution were mixed in 1:1 volume ratio before used. Alkali pre-treated fibers were boiled the solution for an hour before rinsed with distilled water. The same process was repeated four times.

Solvent exchange method

Firstly, water was added in droplets into cellulose fibers while stirring for 15 min to form a gel. The gel mixture was added to ethanol in 1:1 volume ratio and stirred for about an hour before acetone was added drop wise in a 1:2 volume acetone-water ratio. Stirring was continued for 3 hours more before nanosilica which was previously immersed in acetone was added. The mixture was further stirred for 10 min. Lastly, the mixture was sonicated for 20 min at an ultrasound bath of 40 kHz, maintaining the temperature below 40°C before the resultant product was dried at 60°C in an oven.

Characterization techniques

Optical microscope (OPM)

The powdered samples of cellulose and its silica composites were analysed using the Zeiss optical microscope. The morphology was captured using a digital system. A small amount of each sample was spread on a glass slide and stamped with a coverslip.

X-Ray diffraction analysis (XRD)

The samples were analysed using X-ray diffractometer (D8-Advance Bruker AXS GmbH) at room temperature (RT) with a monochromatic CuKα radiation source (λ = 0.1539 nm) in the step-scan mode with a 2θ angle ranging from 0° to 60° with a step of 0.04 and scanning time of 5.0 min.

Fourier transform infrared (FTIR) spectroscopy

The spectra of all samples were carried out on a Perkin-Elmer FTIR spectrophotometer using a standard ATR cell. The gauge was adjusted to 90 for sufficient contact. All samples were scanned over the wavenumber (450 - 4000 cm^{-1}).

RESULTS AND DISCUSSION

Spectral analysis

The FTIR spectra of SCB and SW celluloses as prepared are shown in Fig. 1. Both spectra showed the common peaks associated with cellulosic materials at 3336 cm^{-1} (OH-stretch), 2890 cm^{-1} (C-H asymmetric stretch), 1560 cm^{-1} (C=C) aromatic asymmetric stretch), 1031 cm^{-1} (C-O vibrations), and 560 cm^{-1} (C-OH out of plane) as reported in the literature (Maeda et al. 2006, Rodríguez-Robledo et al. 2018).

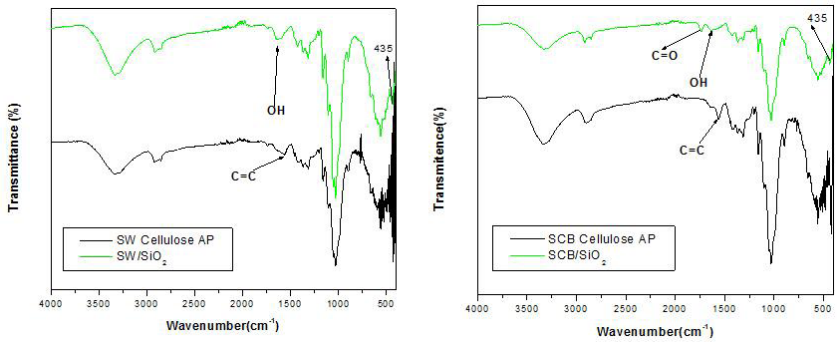

a) b)

Fig. 1: The FTIR spectra of a) SW cellulose and SW/SiO_2 b) SCB cellulose and SCB/SiO_2.

Moreover, the peaks linked to aromatic skeletal vibrations of lignin and hemicelluloses at 1241 cm^{-1} and 1722 cm^{-1} were reduced and are almost invisible. This might indicates the complete removal of lignin and hemicelluloses from SCB and SW. With the introduction of nanosilica in both SCB and SW celluloses, there are evident shifts in peak positions and intensities. The peaks at around 1315 cm^{-1} only appear in the prepared SCB and SW celluloses spectra corresponding with CH2 vibration functional groups (Jacob et al. 2005). The peak at 1367 cm^{-1} only appear in the modified SCB and SCW cellulose spectra. This peak correspond with C-H bending in the plane (Sibiya et al. 2018, Zhao et al. 2013, Linganiso et al. 2019) and could symbolise introduction of a new functional group resulting from silica modification. In addition, the peak at 435 cm^{-1} attributed to Si-O-Si bending only appears in modified cellulose which is evidence that nanosilica functional groups were added on the cellulose surface (Rodríguez-Robledo et al.

2018, Cerchiara et al. 2018, Maleki et al. 2014). The -OH from silanol absorbs around 1030 cm^{-1} and 3300 cm^{-1} might be the reason for bigger intensities observed in modified cellulose. These peaks are more pronounced in SW cellulose as compared to SCB cellulose. This may be due to the reduction in hydrogen bonding in cellulosic O–H groups, thereby increasing –OH concentration due to high energy of O–H bonds

X-Ray diffraction analysis

Fig. 2 is showing the diffractograms of SCB and SW celluloses as prepared and modified respectively. Both prepared and modified fibers display typical spectra for natural fibers with peaks around 16°, 23°, and 35° corresponding to amorphous cellulose I, crystalline cellulose II and undissolved amorphous hemicellulose respectively (Pothan et al. 2002, Xie et al. 2009). With the introduction of silica to SCB cellulose, there were minor changes in peaks positions observed and an increase in peak intensities. The minor peaks shift for SCB may be due to disorder caused by modification of fiber and might indicate an increase in the interplanar distance. The intensity increase could suggest that the nanosilica modification improved the crystallinity of SCB. The same trend was observed with SW cellulose.

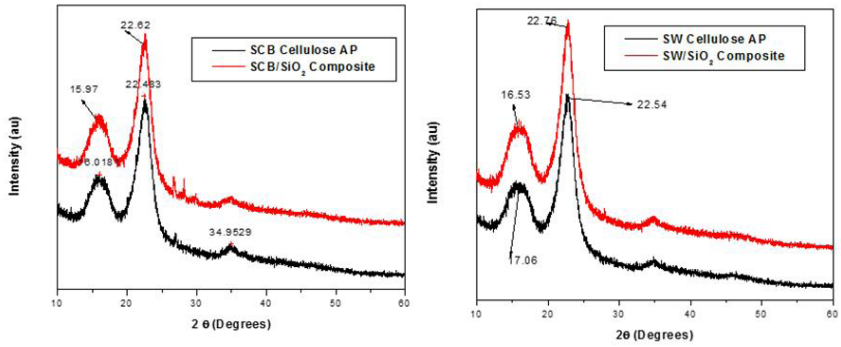

Fig. 2. The diffractograms of SCB cellulose, SCB/SiO_2, SW cellulose and SW/SiO_2.

Tab. 1: The crystalline indices and degree of crystallinity for unmodified and modified (SCB and SW) cellulose.

Sample	Peak height CI (%)	Deconvolution CI (%)
SW cellulose AP	42	63
SW/SiO_2	43	64
SCB cellulose AP	39	62
SCB/SiO_2	40	63

Tab. 1 showed the crystallinity index (CI) estimated using the deconvolution and peak height methods (Ciolacu et al. 2011, Johar et al. 2012, Kim et al. 2013). For both SCB and SW cellulose, there was an increase in crystallinity with the introduction of silica as expected. The differences in crystallinity index values for both SCB and SW might be due to differences in chemical compositions and exposure of cellulose after alkali treatment. It is clearly evident that the addition of nanosilica particles improves the crystallinity of both SCB and SW cellulose.

Optical microscope

The optical microscope images of unmodified and modified SCB and SW cellulose are displayed in Fig. 3. It could be seen that both SCB and SW unmodified fibers are thin and longer as compared with their modified counterparts. Both SCB/SiO_2 and SW/SiO_2 are swollen and display dusty small particles agglomerating on the surface of the fibers (see arrows). Similar results were also reported in modification of natural fibres (Mulinari et al. 2009, Maeda et al. 2006).

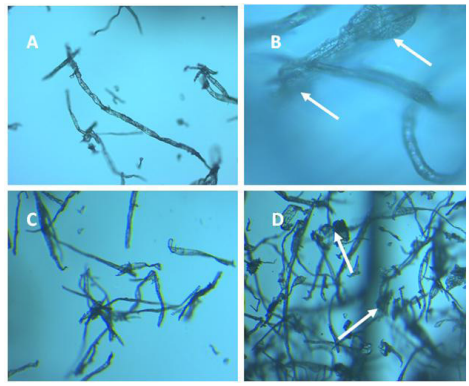

Fig. 3: The optical microscope images of: a) SCB Cellulose, b) SCB/SiO_2, c) SW Cellulose and d) SW/SiO_2 at 10 × 0.22 magnification.

According to Pothan et al. (2002), the swelling of the fiber leads to a transfer of the electrochemical double layer and the shear plane of the fiber to the electrolyte solution. Moreover, the fiber length for both SCB and SW were not affected by modification. In fact, the longer fibers (5 mm) have a property to allow high stress to be transferred to reinforcement and that contributes to its superior mechanical properties (Loh et al. 2013).

CONCLUSIONS

The study investigated the effect of silica on sugarcane bagasse (SCB) and softwood (SW) cellulose properties. FTIR and XRD results confirmed that cellulose was successfully extracted from SCB and SW using the alkali treatment. The surface modification of both SCB and SW cellulose were performed successfully using the solvent exchange method. FTIR analysis confirmed that silica functional groups were successfully added onto the surface of SCB and SW cellulose. There were evident shifts in peak positions and intensities with the introduction of silica. New peaks were detected at 1367 cm^{-1} and 435 cm^{-1} signaling that nanosilica functional groups were added on the cellulose surface. XRD patterns showed minor changes in peaks positions and an increase in peak intensities with the introduction of silica. There was also an increase in crystallinity index estimated using the deconvolution and peak-height method for both modified SW and SCB cellulose. The surface morphology displayed fiber swelling with introduction of silica, which has impact on mechanical properties of the fiber and the resultant composites. The solvent method proved to be cheap, simple and time efficient for use in cellulose modification.

REFERENCES

1. Ahmed, I.I., Gupta, A.K., 2012: Sugarcane bagasse gasification: Global reaction mechanism of syngas evolution. Applied Energy 91(1): 75-81.
2. Ashori, A., 2008: Wood–plastic composites as promising green-composites for automotive industries! Bioresource technology 99(11): 4661-4667.
3. Barra, G.M., Fredel, M.C., Qureshi, H.A., Taylor, A.W., Clemenceau, Jr.C., 2006: Properties of chemically treated natural amorphous silica fibers as polyurethane reinforcement. Polymer Composites 27(5): 582-590.
4. Cerchiara, T., Palermo, A.M., Esposito, G., Chidichimo, G., 2018: Effects of microwave heating for the conservation of paper artworks contaminated with *Aspergillus versicolor*. Cellulose 25(3): 2063-2074.
5. Ciolacu, D., Ciolacu, F., Popa, V.I., 2011: Amorphous cellulose-structure and characterization. Cellulose chemistry and technology 45(1): 13.
6. Demilecamps, A., Beauger, C., Hildenbrand, C., Rigacci, A., Budtova, T., 2015: Cellulose–silica aerogels. Carbohydrate Polymers 122: 293-300.
7. Eichhorn, S.J., Baillie, C.A., Zafeiropoulos, N., Mwaikambo, L.Y., Ansell, M.P., Dufresne, A., Entwistle, K.M., Herrera-Franco, P.J., Escamilla, G.C., Groom, L., Hughes, M., 2001: Current international research into cellulosic fibres and composites. Journal of materials Science 36(9): 2107-2131.
8. Ha, S.W., Weiss, D., Weitzmann, M.N., Beck Jr. G.R., 2019: Applications of silica-based nanomaterials in dental and skeletal biology. Nanobiomaterials in Clinical Dentistry Pp 77-112.
9. Hou, A., Yu, Y. and Chen, H., 2010: Uniform dispersion of silica nanoparticles on dyed cellulose surface by sol–gel method. Carbohydrate Polymers 79(3): 578-583.
10. Jacob, M., Joseph, S., Pothan, L.A., Thomas, S., 2005: A study of advances in characterization of interfaces and fiber surfaces in lignocellulosic fiber-reinforced composites. Composite Interfaces 12(1-2): 95-124.
11. Johar, N., Ahmad, I., Dufresne, A., 2012: Extraction, preparation and characterization of cellulose fibres and nanocrystals from rice husk. Industrial Crops and Products 37(1): 93-99.
12. Kim, S.H., Lee, C.M., Kafle, K., 2013: Characterization of crystalline cellulose in biomass: basic principles, applications, and limitations of XRD, NMR, IR, Raman, and SFG. Korean Journal of Chemical Engineering 30(12): 2127-2141.
13. Linganiso L.Z., Buthelezi T., Motaung T.E., 2019: A comparative study of sugarcane bagasse and soft wood. Wood Research 64: 273-280.
14. Litschauer, M., Neouze, M.A., Haimer, E., Henniges, U., Potthast, A., Rosenau, T., Liebner, F., 2011: Silica modified cellulosic aerogels. Cellulose 18(1): 143-149.
15. Loh, Y.R., Sujan, D., Rahman, M.E., Das, C.A., 2013: Sugarcane bagasse. The future composite material: A literature review. Resources, Conservation and Recycling 75: 14-22.
16. Maeda, H., Nakajima, M., Hagiwara, T., Sawaguchi, T., Yano, S., 2006: Bacterial cellulose/silica hybrid fabricated by mimicking biocomposites. Journal of materials science 41(17): 5646-5656.
17. Maleki, H., Durães, L., Portugal, A., 2014: An overview on silica aerogels synthesis and different mechanical reinforcing strategies. Journal of Non-Crystalline Solids 385: 55-74.
18. Mulinari, D.R., Voorwald, H.J., Cioffi, M.O.H., da Silva, M.L.C., Luz, S.M., 2009: Preparation and properties of HDPE/sugarcane bagasse cellulose composites obtained for thermokinetic mixer. Carbohydrate Polymers 75(2): 317-321.

19. Mulinari, D.R., Voorwald, H.J., Cioffi, M.O.H., Da Silva, M.L.C., da Cruz, T.G., Saron, C., 2009: Sugarcane bagasse cellulose/HDPE composites obtained by extrusion. Composites Science and Technology 69(2): 214-219.
20. Pothan, L.A., Bellman, C., Kailas, L., Thomas, S., 2002: Influence of chemical treatments on the electrokinetic properties of cellulose fibres. Journal of adhesion science and technology 16(2): 157-178.
21. Rodríguez-Robledo, M., González-Lozano, M., Ponce-Peña, P., Quintana Owen, P., Aguilar-González, M., Nieto-Castañeda, G., Bazán-Mora, E., López-Martínez, R., Ramírez-Galicia, G., Poisot, M., 2018: Cellulose-silica nanocomposites of high reinforcing content with fungi decay resistance by one-pot synthesis. Materials 11(4): 575.
22. Sibiya N.N., Mochane M.J., Motaung T.E., Linganiso L.Z., Hlangothi S.P., 2018: Morphology and properties of sugarcane bagasse cellulose- natural rubber composites. Wood Research 63: 821-832.
23. Sequeira, S., Evtuguin, D.V., Portugal, I., 2009: Preparation and properties of cellulose/silica hybrid composites. Polymer composites 30(9): 1275-1282.
24. Terrett, O.M., Lyczakowski, J.J., Yu, L., Iuga, D., Franks, W.T., Brown, S.P., Dupree, R., Dupree, P., 2019: Molecular architecture of softwood revealed by solid-state NMR. Nature communications 10(1): 1-11.
25. Wei, C., Zeng, M., Xiong, X., Liu, H., Luo, K., Liu, T., 2015: Friction properties of sisal fiber/nanosilica reinforced phenol formaldehyde composites. Polymer Composites 36(3): 433-438.
26. Xie, K., Yu, Y., Shi, Y., 2009: Synthesis and characterization of cellulose/silica hybrid materials with chemical crosslinking. Carbohydrate Polymers 78(4): 799-805.
27. Zhao, J., Zhang, W., Zhang, X., Zhang, X., Lu, C. and Deng, Y., 2013. Extraction of cellulose nanofibrils from dry softwood pulp using high shear homogenization. Carbohydrate Polymers 97(2): 695-702.

Samson Masulubanye Mohomane
University of Zululand (Kwadlangezwa Campus)
Department of Chemistry
Private Bag X1001, Kwadlangezwa 3886
Kwazulu Natal
South Africa

Setumo V. Motloung
Sefako Makgatho Health Sciences University
Department of Physics
P.O. Box 94, Medunsa 0204
South Africa
Mandela University
Department of Physics
P. O. Box 77000
Port Elizabeth 6031
South Africa

Lehlohonolo Koao
University of The Free State (Qwaqwa Campus)
Department of Physics
Private Bag X13, Phuthaditjhaba 9866
South Africa

Tshwafo E. Motaung*
Sefako Makgatho Health Sciences University
Department of Chemistry
P.O. Box 94, Medunsa 0204
South Africa
University of South Africa
Department of Chemisry
Po Box 392, Pretoria 0003
South Africa
*Corresponding author: motaungte@live.com

WOOD RESEARCH
66 (1): 2021
95-104
doi.org/10.37763/wr.1336-4561/66.1.95104

EFFECTS OF LIGHT THERMAL TREATMENTS ON THE COLOR, HYGROSCOPITY AND DIMENSIONAL STABILITY OF WOOD

Xin You Liu, Xin Wei Tu, Mihaela Liu
Nanjing Forestry University
China

(Received March 2020)

ABSTRACT

Ailanthus wood (*Ailanthus* desf.) was thermally treated at three different low temperatures (140, 160, 180˚C) for 2 and 4 h in order to investigate the effects on wood color, hygroscopity and dimensional stability. Results indicate that mass loss increased following the treatments, while equilibrium moisture content decreased from 11.86% to 9.88% for the 180˚C and 4 h treatment. Moreover, improvements in the dimension stability were observed for post-treatment samples. The thermal treatment induced color changes in the Ailanthus wood, with a significant reduction in the lightness, yet the redness and yellowness exhibited minimal changes. FITR spectra of the thermally treated wood suggest that the heat treatment resulted in the deacetylation of hemicellulose. These results help to conclude that thermal treating temperature under 160˚C can improve wood dimensional stability and maintain original color.

KEYWORDS: Thermal modification, Ailanthus wood, color change, dimensional stability.

INTRODUCTION

Wood is an essential renewable material, with an excellent strength to weight ratio, is easy to process, has excellent environmental characteristics and is widely used in construction engineering and interior design (He et al 2019, Percin et al. 2016). However, due to the dry shrinkage and wet swelling of wood, its use is often limited (Okon et al. 2017, Korkut and Hiziroglu 2014, Kasemsiri et al. 2012). Common methods of wood modification include impregnation resin, acetylation and high-temperature thermal treatments (Candan et al. 2013, Esteves et al. 2011, Esteves et al. 2007a, 2007b, 2008). In particular, high-temperature thermal treatment is an environmentally friendly modification method, which can degrade hemicellulose and lignin and reduce hydrophilic groups in wood. It can also increase the crystallization zone and crystallinity of cellulose, thus reducing wood hygroscopicity and improving the dimensional stability (Esteves and Pereira 2009).

The heat treatment of wood, also known as wood thermal modification, is defined by the European standard (CEN/TS 15679:2007) as follows: At a temperature higher than 160°C in a hypoxia environment, inducing changes in the cell wall composition and physical properties of the wood. The extent of the changes in wood properties during the thermal treatment is a function of the processing method, the wood species and, the initial moisture content of the wood, the ambient atmosphere and the treatment duration and temperature (Yildiz et al. 2006). Temperature has a greater impact on the thermal wood properties compared to the treatment time, and prolonging the treatment time does not result in the same effects as treating with a higher temperature (Korkut and Guller 2008). Compared with unmodified wood, thermal treated wood exhibits a lower EMC (equilibrium moisture content) (Santos et al. 2014, Zhou et al. 2013, Obataya et al. 2000) and smoother contact surfaces (Unsal and Ayrilmis 2005). The thermal treating of wood has been observed to lead to a darkening in color. For example, Esteves found that pine (*Pinus pinaster*) and eucalyptus (*Eucalypt globule*) wood became darker, with the lightness reduced by 50% following heat treatment with hot air or steam over a period of 2-24 h above 170°C (Esteves et al. 2007b). The dimensional stability of the wood often requires improvement while maintaining the original color. The color changes of thermal wood can be compensated via two techniques: thermally treating wood in a vacuum environment (Sivrikaya et al. 2019) and thermally treating under lower temperatures. In this study, the wood of Ailanthus (Ailanthus desf.) was treated at several temperatures of 140-180°C improvement while maintain hygroscopicity and dimensional stability were tested to explore a thermal treatment process that could improve the dimensional stability and maintain the original color.

MATERIAL AND METHODS

Sample preparation

Ailanthus (*Ailanthus* desf.), a white colored wood with a similar grain to white oak that is commonly cultivated in China, was sourced from Sichuan Province, China. The test specimens were prepared from sapwood with dimensions of 20 × 20 × 20 mm (length × width × thickness) and an initial moisture content of 70 ± 5% (according to the GB/T 1931–2009 standard) (Zhao et al. 2009). All specimens were dried at 103°C.

Thermal treatment

Thermal treatments were conducted in an oven at the temperatures of 140°C, 160°C and 180°C for 2 and 4 h. A control group of samples was left untreated (denoted as 20°C) and compared to the thermally modified samples.

Mass percentage loss (MPL)

The MPL was determined based on variations in the mass before and after the thermal treatment as follows:

$$MPL = \frac{m_0 - m_t}{m_0} \times 100\% \quad (1)$$

where: m_0 is the pre-treatment oven-dried weight of the specimen (g) and m_t denotes the post-treatment weight of the same specimen (g).

Wood dimensional stability estimations

Swelling tests were performed according to the GB/T 1931–2009 standard (Zhao et al. 2009). The treated and control groups were oven dried and subsequently stored in a climate controlled chamber at 20°C with 65% humidity in order to reach EMC. The dimensions and weights of the specimens were measured before and after conditioning. The swelling coefficient was calculated as follows (Zhao et al. 2009):

$$a = \frac{l_w - l_0}{l_0} \times 100\% \quad (2)$$

where: a is the swelling coefficient (radial, tangential or longitudinal), l_0 denotes the initial dimension of the specimen, and l_w represents the dimension after conditioning.

Moisture absorption (MA)

The process used to determine the MA is detailed as follows. The specimens were placed in a chamber with a constant temperature of 20°C and 65% humidity to reach the EMC according to the GB/T 1931–2009 standard (Zhao et al. 2009). Following conditioning in the climate chamber, the MA was calculated via Eq. (3):

$$MA = \frac{w_a - w_b}{w_b} \times 100\% \quad (3)$$

where: w_b (w_a) denotes the weight of the specimens before (after) conditioning in the climate chamber (g).

Color measurements

Pre- and post-treatment surface color measurements of all specimens on the tangential section were collected using an AvaSpec-USB2 spectrometer (Avante, Netherlands) equipped with an integrating AVA sphere with a diameter of 80 mm. Measurements were made using a D65 standard illuminant and a 10° standard observer. The reflectance percentage, collected at 10 nm intervals over the visible spectrum (400-700 nm) was converted into the CIELAB color system. The resultant pre- and post-treatment colour coordinates were lightness L* (from 0 for black to 100 for white), redness a* (from negative values for green to positive values for red on the green-red axis) and yellowness b* (from negative values for blue to positive values for yellow on the blue-yellow axis). Colour differences between treated and control samples were calculated based on Eq. (4):

$$\Delta E = \sqrt{\Delta L^{*2} + \Delta a^{*2} + \Delta b^{*2}} \quad (4)$$

where: ΔL*, Δa* and Δb* are the differences of the pre- and post-treatment values of L*, a* and b*, respectively. Low ΔE values correspond to a small colour difference.

Chemical structure analysis

ATR-IR spectra of the control and thermally modified wood milled samples were collected using a standard FTIR spectrometer (Tensor 27, Bruker, Germany) via direct transmittance at a resolution of 4 cm^{-1} for 32 scans across 700-4000 cm^{-1}. The alignment of the light equipment and the background spectra was performed before the measurements began. The spectra were averaged over 6 measurements for each treatment.

RESULTS AND DISCUSSION

Mass percentage loss

The MPL is a key indicator for the quality of thermally treated wood. In particular, it is a function of wood species, heating medium, temperature and treatment time (Esteves and Pereira 2009). Tab. 1 reports the mass loss of the treated samples. The results indicate that mass loss increased with temperature. More specifically, under the 180°C and 4 h heat treatment, the mass loss was observed as 2.437%, which is greater than the equivalent value for 140°C (1.432%). Moreover, the mass loss also increased with treatment duration. At 160°C, the mass loss was observed to be 1.395% and 1.734% under 2h and 4 h, respectively.

Tab. 1. Mass loss of the thermally treated wood.

Wood sp.	Treatment	Initial mass (g)	Mass loss (%)
Ailanthus	140°C, 2h	4.024	0.761 (0.071)
Ailanthus	140°C, 4h	4.139	1.432 (0.112)
Ailanthus	160°C, 2h	4.265	1.395 (0.094)
Ailanthus	160°C, 4h	4.035	1.734 (0.083)
Ailanthus	180°C, 2h	4.126	1.962 (0.132)
Ailanthus	180°C, 4h	4.135	2.437 (0.048)

*Values in parentheses indicate standard deviation.

Wood dimensional stability and moisture absorption

Wood dimensional stability has a significant influence on the quality and usage of wood products. The swelling coefficients in the tangential and radial directions are the most influential factors for wood dimensional stability estimations. Fig. 1 demonstrates the influence of the thermal treatments on wood dimensional stability.

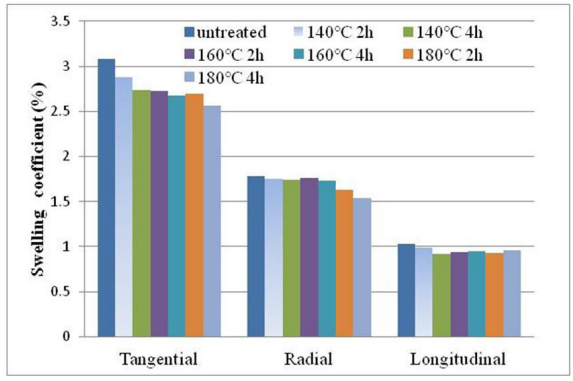

Fig. 1. Swelling coefficients in the tangential, radial and longitudinal directions for the treatment and control groups.

The average value of the swelling coefficient of the control group was 3.08%, 1.78% and 1.03% in the tangential, radial and longitudinal sections, respectively. Following the 180°C 4 h treatment and compared with the control group, the swelling coefficient decreased by 16.88% in

the tangential section, with a smaller reduction of 6.80% in the longitudinal section. Compared with the control group, all three swelling coefficient decreased with increasing treatment temperature and duration. The results demonstrate that the thermal treatments markedly decreased the wood swelling coefficients in the tangential and radial directions, with less of an impact on the wood swelling coefficients in the longitudinal direction. This may be attributed to the ease of shrinking and swelling of wood in the tangential and radial directions, with a greater stability in the longitudinal direction (Liu and Zhao 2012). The increase of wood dimensional stability via the thermal treatment is a result of the hydrophilic substances degradation induced by higher temperatures (Esteves and Pereira 2009).

Moisture absorption

Wood moisture content under the fiber saturation point (FSP) has been demonstrated to have a great impact on wood dimensional stability. To further investigate the effects of thermal treatment on wood dimensional stability, MA was recorded as an indicator for wood hygroscopicity. Tab. 2 reports the MA values for the specimens before and after conditioning in the climate chamber at a temperature of 20˚C with 65% humidity. The average mass of the untreated specimens pre- and post-conditioning varied from 4.036 to 4.507 g, with an MA of approximately 11.68%. Furthermore, the MA for the treated group was observed to decrease compared with the control group. Thus, the thermal treatments markedly decreased the MA ability of the wood samples, and can therefore be applied to increase wood dimensional stability.

Tab. 2. MA of untreated and thermally treated wood.

Wood sp.	Treatment	Pre-conditioning mass (g)	Post-conditioning mass (g)	MA (%)
Ailanthus	untreated	4.036	4.507	11.682
Ailanthus	140˚C, 2h	3.993	4.443	11.263
Ailanthus	140˚C, 4h	3.992	4.427	10.895
Ailanthus	160˚C, 2h	3.987	4.427	11.048
Ailanthus	160˚C, 4h	3.972	4.374	10.127
Ailanthus	180˚C, 2h	3.946	4.339	9.979
Ailanthus	180˚C, 4h	3.897	4.282	9.883

Post-treatment color changes

Ailanthus cultivated in China, used for furniture making, has white color. The values of the coordinates L *, a *, b * of untreated wood are 76.97, 5.96 and 27.48. ΔL* values were negative, indicating a darker color for the wood following the heat treatment via the reduced lightness due to higher temperatures during the heating process. The blackish hue increased for temperatures within 140-180˚C. For example, the lightness value (L*) decreased from 76.97 to 64.53 for the samples exposed to the 180˚C heat treatment for 4 h. However, for the same treatment duration under 140˚C, L* decreased from 77.20 to 75.88. Esteves et al. (2007b) observed a reduction in L* for transverse sections of pine by 9.4% and 28.4% for 2 h at 170 and 200˚C, respectively. The values of a* and b* slightly increased following the thermal treatment by 4.34 unit for Δa* and 5.42 unit for Δb* under the 180˚C 4 h treatment. Comparing the color change from these six thermal treatment processes, 140˚C (2 and 4 hours) and 160˚C(2 hours) can maintain original color better than other processes.

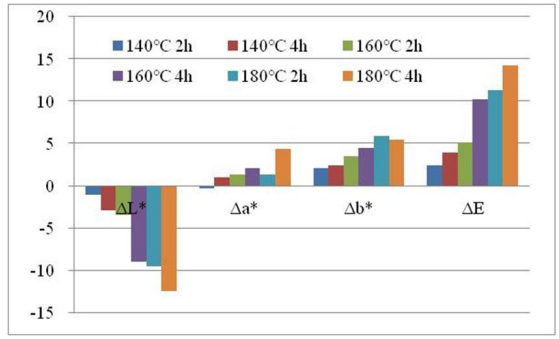

Fig. 2. Changes in L, a* and b* and the total color change (ΔE) for thermally treated samples.*

Chemical structure analysis

The dimensional stability of wood is directly linked to the hydroxyl (-OH) and other chemical contents, and can result in changes in, or the loss of, hydroxyl or other chemical groups that play key roles in the stability of wood (He et al. 2016, Jiang et al. 2015, Mitani and Barboutis 2014). FTIR spectroscopy is able to effectively measure variations in the chemical structure of samples resulting from different treatments (Basso et al. 2017, He et al. 2017, Chen et al. 2011). The FTIR spectra in the range of 800-1800 cm^{-1} for the treated samples at 140°C, 160°C and 180°C under 4 hours and the control group are displayed in Fig. 3.

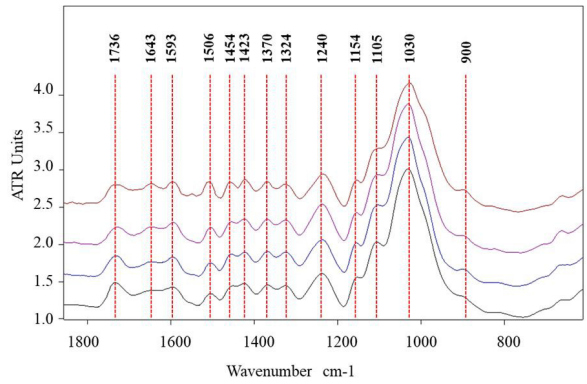

Fig. 2. Comparative FTIR spectra of untreated and thermal treated wood samples in the range of 800-1800 cm^{-1} (from bottom to top: untreated, 140°C, 160°C and 180°C).

To compare the spectra of the untreated and heat-treated samples, all spectra were normalized to the C-H aliphatic stretching peak at 2905 cm^{-1} (Kocaefe et al. 2008). Although the chemical structures of the thermally treated specimens were modified compared to the control, the changes were minimal. The band intensities at 1736 cm^{-1} were observed to decrease, corresponding to the stretching of the carbonyl groups of acetyls in hemicellulose (Chien et al. 2018). This indicates that the heat treatment resulted in the deacetylation of hemicellulose by the cleavage of the acetyl groups (Altgen et al. 2018a,b). The absorption band at 1643 cm^{-1} assigned to conjugated carbonyl groups, were observed to increase, especially after 180°C thermal

treatment 4 hours. This suggests that more conjugated/aromatic carbonyl groups were formed during thermal treatment. In addition, aromatic skeletal stretching bands in lignin were observed at 1593 cm^{-1}. The intensities of these bands increased with the heat treatment temperature. This is attributed to the increase of the relative percentage of lignin due to polysaccharide degradation, and in particular, hemicellulose degradation. An additional characteristical band for aromatic ring stretching appeared at approximately 1506 cm^{-1}, which also exhibited an increasing intensity with thermal temperatures. This can be explained by the thermal decomposition of the syringyl moiety of lignin. In addition, the band corresponding to C-O stretching at 1105 cm^{-1} appeared to be significant for the 180°C heat treatment. This may correspond to the formation of an ether linkage from the hydroxyl groups within hemicelluloses and lignin (Colom et al. 2003), or to the formation of new alcohols and esters (Kocaefe et al. 2008) during the heat treatment.

CONCLUSIONS

In the current study, wood from the Ailanthus tree genus was thermally modified at 140°C, 160°C and 180°C for 2 and 4 h. In particular, we investigated the mass loss, swelling coefficient, moisture absorption, color change and variations in FITR spectra of the treated wood compared to the control group. Following the thermal treatment, mass loss increased, while EMC was significantly reduced with increasing treatment temperature and duration. Furthermore, the dimension stability was improved with the thermal treatment. Changes in the color of the Ailanthus wood were induced by the thermal treatment, however changes in the redness and yellowness were limited. Permutations in the FITR spectra of the thermal treated wood compared to the control suggest that the heat treatment results in the deacetylation of hemicellulose. According to the results of color change and dimensional stability and moisture absorption, 160°C for 2 h can improve wood dimensional stability well and maintain original color.

ACKNOWLEDGMENTS

This work was supported by the Nanjing Forestry University Foundation for Basic Research (Grant No. 163104127) and the Priority Academic Program Development (PAPD) of Jiangsu Province, China.

REFERENCES

1. Altgen, M., Uimonen, T., Rautkari, L., 2018: The effect of de- and re-polymerization during heat-treatment on the mechanical behavior of Scots pine sapwood under quasi-static load. Polymer Degradation and Stability 147: 197-205.
2. Altgen, M., Willems, W., Hosseinpourpia, R., Rautkari, L., 2018: Hydroxyl accessibility and dimensional changes of Scots pine sapwood affected by alterations in the cell wall ultra structure during heat-treatment. Polymer Degradation and Stability 152: 244-252
3. Basso, M.C., Pizzi, A., Polesel Maris, J., Delmotte, L., Colin, B., Rogaume, Y., 2017: MALDI-TOF, 13C NMR and FTIR analysis of the cross-linking reaction of condensed tannins by triethyl phosphate. Industrial Crops and Products 95: 621–631.

4. Candan, Z., Korkut, S., Unsal, O., 2013: Effect of thermal modification by hot pressing on performance properties of paulownia wood boards. Industrial Crops and Products 45: 461–464.
5. CEN/TS15679, 2007: Thermal modified timber - definitions and characteristics.
6. Chen, W., Yu, H., Liu, Y., Chen, P., Zhang, M., Hai, Y., 2011. Individualization of cellulose nanofibers from wood using high-intensity ultrasonication combined with chemical pretreatments. Carbohydrate Polymers 83(4): 1804–1811.
7. Chien, Y., Yang, T., Hung, K., Li, C., Xu, J., Wu, J., 2018: Effects of heat treatment on the chemical compositions and thermal decomposition kinetics of Japanese cedar and beech wood. Polymer Degradation and Stability 158 : 220-227.
8. Chinese Standard: GB/T 1931, 2009: Method for determination of the moisture content of wood.
9. Colom, X., Carrillo, F., Nogues, F., Gaariga, P., 2003: Structural analysis of photo-degraded wood by means of FTIR spectroscopy. Polymer Degradation and Stability 80: 543-549.
10. Esteves, B., Domingos, I., Pereira, H., 2007a: Improvement of technological quality of eucalypt wood by heat treatment in air at 170-200°C. Forest products journal 57(1-2): 47-52.
11. Esteves, B., Marques, A.V., Domingos, I., Pereira, H., 2007b: Influence of steam heating on the properties of pine (*Pinus pinaster*) and eucalypt (*Eucalyptus globulus*) wood. Wood Science and Technology 41(3): 193-207.
12. Esteves, B., Graça, J., Pereira, H., 2008: Extractive composition and summative chemical analysis of thermally treated eucalypt wood. Holzforschung 62(3): 344-351.
13. Esteves, B., Pereira, H., 2009: Wood modification by heat treatment. A review. BioResources 4(1): 340-404.
14. Esteves, B., Videira, R., Pereira, H., 2011. Chemistry and ecotoxicity of heat-treated pine wood extractives. Wood Science and Technology 45(4): 661–676.
15. He, Z., Zhang, Y., Wang, Z., Zhao, Z., Yi, S., 2016: Reducing wood drying time by application of ultrasound pretreatment. Drying Technology 34: 1141–1146.
16. He, Z., Wang, Z., Zhao, Z., Yi, S., Mu, J., Wang, X., 2017: Influence of ultrasound pretreatment on wood physiochemical structure. Ultrasonics Sonochemistry 34: 136–141.
17. He, Z., Qian, J., Qu, L., Yan, N., Yi, S., 2019: Effects of tung oil treatment on wood hygroscopicity, dimensional stability and thermostability. Industrial Crops and Products 140: 111647.
18. Jiang, J., Li, J., Gao, Q., 2015. Effect of flame retardant treatment on dimensional stability and thermal degradation of wood. Construction and Building Materials 75: 74–81.
19. Kasemsiri, P., Hiziroglu, S., Rimdusit, S., 2012: Characterization of heat treated eastern red cedar (*Juniperus virginiana* L.). Journal of Materials Processing Technology 212(6): 1324–1330.
20. Kocaefe, D., S. Poncsak, Y. Boluk, 2008: Effect of thermal treatment on the chemical composition and mechanical properties of birch and aspen. BioResources 3(2): 517-537.
21. Korkut, D.S., Guller, B., 2008: The effects of heat treatment on physical properties and surface roughness of red-bud maple (*Acer trautvetteri* Medw.) wood. Bioresource Technology 99(8): 2846-2851
22. Korkut, D., Hiziroglu, S., 2014: Experimental test of heat treatment effect on physical properties of red oak (Quercus falcate michx.) and southern pine (*Pinus taeda* L.). Materials 7(11): 7314-7323.
23. Liu, Y.X., Zhao, G.J., 2012: Wood Science. China Forestry Press, Beijing Pp 125-134.

24. Mitani, A., Barboutis, I., 2014: Changes caused by heat treatment in colour and dimensional stability of beech (*Fagus sylvatica* L.) wood. Drvna Industrija 65: 225-232.
25. Obataya, E., Tanaka, F., Norimoto, M., Tomito, B., 2000: Hygroscopicity of heat-treated wood 1. Effects of after treatments on the hygroscopicity of heat-treated wood. Journal of the Japan Wood Research Society 46(2): 77-87.
26. Okon, K.E., Lin, F., Chen, Y., Huang, B., 2017: Effect of silicone oil heat treatment on the chemical composition, cellulose crystalline structure and contact angle of Chinese parasol wood. Carbohydrate Polymers 164: 179–185.
27. Percin, O., Perker, H., Atilgan, A., 2016: The effect of heat treatment of the some physical and mechanical properties of beech (*Fagus orientalis* Lipsky) wood. Wood Research 61(3): 443-456.
28. Santos, D.V.B.D., Mouora, L.F.D., Brito, J.O., 2014: Effect of heat treatment on color, weight loss, specific gravity and equilibrium moisture content of two low market valued tropical wood. Wood Research 59(2): 253-264.
29. Sivrikaya, H., Tesařová, D., Jeřábková, E. , Can, A., 2019: Color change and emission of volatile organic compounds from Scots pine exposed to heat and vacuum-heat treatment. Journal of Building Engineering 26: 100918.
30. Unsal, O., Ayrilmis, N., 2005: Variations in compression strength and surface roughness of heat-treated Turkish river red gum (*Eucalyptus camaldulensis*) wood. Journal of Wood Science 51(4): 405-409.
31. Yildiz, S., Gezer, E.D., Yildiz, U.C., 2006: Mechanical and chemical behavior of spruce wood modified by heat. Building and Environment 41(12): 1762-1766.
32. Zhou, Q.F., Tu, D.Y., Liao, L., Guo, Q., 2013: Variation of equilibrium moisture content of heat-treated *Couratari oblongifolia, Fraxinus excelsior* and *Quercus rubra* wood. BioResoures 8(1): 182-188.

Xin You Liu*, Xin Wei Tu, Mihaela Liu
Nanjing Forestry University
[1.]Co-Innovation Center of Efficient Processing and Utilization of Forest Resources
[2.]College of Furnishing And Industrial Design
[3.]Academy of Chinese Ecological Progress and Forestry Studies
Longpan No.159, Nanjing 210037
Nanjing
China
*Corresponding author: liu.xinyou@njfu.edu.cn

WOOD RESEARCH
66 (1): 2021
105-116
doi.org/10.37763/wr.1336-4561/66.1.105116

CROSS-CORRELATION OF COLOR AND ACIDITY OF WET BEECH WOOD IN THE PROCESS OF THERMAL TREATMENT WITH SATURATED STEAM

Ladislav Dzurenda, Michal Dudiak
Technical University in Zvolen
Slovakia

(Received June 2020)

ABSTRACT

The paper presents changes in the color and acidity of *Fagus sylvatica* L. in the process of heat treatment of wood with saturated water steam in the temperature range t = 105 – 135°C during τ = 3 to 12 hours. The light white-gray color of beech wood with a yellow tint changes on the pale pink, red-brown to a brown-red color in the heat treatment process. The color changes of beech wood expressed in the form of the total color difference are in the range of values ΔE^* = 1.97 – 26.85. Due to the hydrolysis of hemicelluloses, the acidity changes in the process of thermal treatment of wet beech wood. Decrease in acidity of beech wood in the range of temperatures t = 105 – 135 °C and time τ = 3 – 12 hours is in the range of pH values = 4.9 to 3.4. The dependence of the total color difference ΔE^* on the change in acidity of beech wood is described by the polynomial of function II. degree. The above knowledge is a suitable tool for evaluating the degree of change in beech wood color in the technological process based on the change in pH of wood.

KEYWORDS: Wood, *Fagus sylvatica* L, acidity, color difference, thermal treatment, saturated water steam.

INTRODUCTION

Wood placed in the environment of hot water, saturated water steam or saturated humid air is heated and its physical, mechanical as well as chemical properties change. Thermal treatment of wood, besides physical and mechanical changes applied in the process of manufacturing veneers, plywood, bentwood furniture or pressed wood are accompanied with the changes in chemical properties and color of wood (Kollmann and Cote 1968, Sergovskij and Rasev 1987, Trebula 1986, Tolvaj et al. 2010, Dzurenda and Orlowski 2011, Dzurenda 2013, Baranski et al. 2017, Sikora et al. 2018). In the past, color changes when wood becoming darker during the steaming

process were used to remove the undesirable color differences between light colored sapwood and dark colored heartwood or to eliminate wood stain colors as a result of mould. In recent times, research into thermally modified wood has been focused on the issue of the color change of specific wood species into more or less bright hues or wood imitation of domestic or exotic tree species (Molnar and Tolvaj 2002, Tolvaj et al. 2009, Dzurenda 2014, 2018a,b,c, Barcik et al. 2015, Baranski et al. 2017).

Free water in the lumens of wood cells is a dilute aqueous solution of sugars, organic acids and salts of calcium, magnesium, potassium, sodium, which are transported by the root system to the living tree (Čudinov 1968, Blažej et al. 1975, Zevenhoven 2001, Pňakovič and Dzurenda 2015). The value of the acidity of the aqueous solution in deciduous wood, in the range of pH values 5.5 – 4.8 (Sandermann and Rothkamm 1956, Solár 2014, Geffert et al. 2019).

The effect of thermal on wet wood is also initiated by chemical changes in wood. The first chemical reactions include partial hydrolysis of hemicelluloses and extraction of water-soluble substances (Fengel and Wegener 1984, Bučko 1995, Solár 2004, Sundqvist et al. 2006, Samešová et al. 2018). Depending on the temperature and duration of action of the hydrolysis products, which are acetic acid and formic acid, degradation of polysaccharides occurs. During the thermal treatment of wood, dehydration of pentoses to 2-furaldehyde well as oxidation of carbohydrates also occur. New chromophoric groups begin to form in lignin, causing the wood to change color (Fengel and Wegener 1984, Bučko 1995, Hon and Shiraishi 2001, Solár 2004, Sundqvist et al. 2006, Geffert et al. 2019).

The aim of the work is to determine the changes in acidity of beech wood in the technological process of wood color modification with saturated water steam in the temperature range t = 105-135°C during 12 hours and to determine the dependence of the total color change of beech wood (ΔE^*) in CIE L* a* b* on the pH value of beech wood obtained by the heat treatment process.

MATERIAL AND METHODS

Material

The wood of *Fagus sylvatica* L. in the form of blanks with dimensions: thickness of 40 mm, width of 90 mm, and length of 750 mm in 260 pieces was divided into 13 groups of 20 pieces in one group. The initial moisture content of wet beech wood was in the range of values w = 54.7 to 58.2%. Group 1 blanks were not thermally treated. The other blanks were divided into 12 groups of 20 pieces each and thermally treated with saturated water steam at t = 105°C, t = 125°C and t = 135°C for 3, 6, 9 and 12 h. Thermal treatment of beech wood with saturated water steam was carried out in a pressure autoclave APDZ 240 (Himmasch AD, Haskovo, Bulgaria) installed in the company Sundermann s.r.o., Banská Štiavnica (Slovakia).

Methods

The conditions of thermal treatment of beech wood with saturated water steam with indicating the sampling time intervals during the thermal treatment v are shown in Fig. 1.

The thermal process of beech wood color modification was performed in an APDZ 240 autoclave (Himmasch AD, Haskovo, Bulgaria) at a higher saturated water steam pressure than atmospheric pressure. Saturated water steam temperatures in individual color adjustment modes are given in Tab. 1.

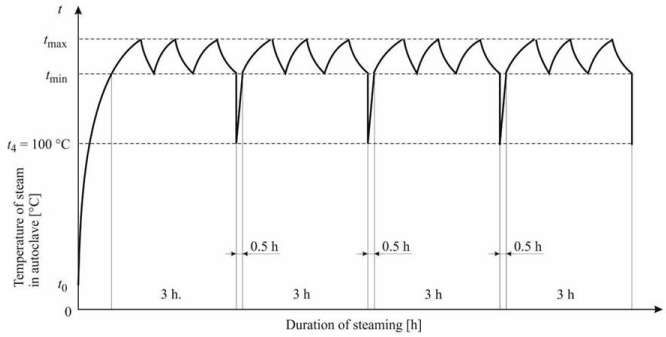

Fig. 1: Mode of color modification of beech wood with saturated water steam.

The temperatures t_{max} and t_{min} are the temperature intervals at which saturated water steam is fed into the autoclave to carry out the technological process. Temperature t_4 is the temperature of the saturated water steam in the autoclave after the water steam pressure in the autoclave has been reduced to atmospheric pressure to allow safe opening of the pressure equipment and sampling after the time thermal treatment 3, 6, 9, and 12 h.

Tab. 1: Modes of color modification of beech wood with saturated water steam.

Temperature of saturated water steam	t_{min}	t_{max}	t_4	Length of time wood is exposed to color modification			
Mode I	102.5	107.5	100	τ_1 = 3 h	τ_2 = 6 (+0.5[a]) h	τ_3 = 9 (+1.0[a]) h	τ_4 = 12 (+1.5[a]) h
Mode II	122.5	127.5	100				
Mode III	132.5	137.5	100				

Note: a time for taking out the specimens.

The moisture content and pH of the wet thermally treated wood were determined by taking samples from the autoclave and cooling the wood to ambient temperature. The moisture content of wet beech wood above the fiber saturation point (BNV) was determined by the gravimetric method according to the standard STN EN 13183-1 (2003).

The pH of wet beech wood was measured using a pH-meter SI 600 with a Lance FET + H puncture probe (Sentron, Roden, Netherlands). A hole with a diameter of 12 mm was created using an accu drill (DeWalt DCD791NT, Germany). Drilling sawdust was pressed into the hole and the LanceFET + H sensor head (Geffert et al. 2019) was inserted into the wet sawdust. After about 60 seconds of stabilization, the pH value was read on a SI 600 pH-meter (Sentron, Roden, Netherlands).

Color-modified beech wood with saturated water steam treatment technology is used as a material for the production of furniture, flooring or interior tiles in a dry state. For this reason, samples of uncooked and thermally treated beech wood were dried by a gentle drying regime to a final moisture content of w = 12 ± 0.5%. Subsequently, the surface of the dry blanks was machined on a FS 200 (BENET Trading, Kvasiny, Slovakia) milling machine.

The color of untreated and thermally treated beech wood in the CIE L* a* b* color space was determined using the Color Reader CR-10 (Konica Minolta, Japan). D65 light source with an

illuminated area of 8 mm was used. Color was evaluated based on changes in CIE L* a* b* color space on the coordinate of brightness L* the red color a*, the yellow color b* and the total color difference ΔE^*. The total color difference value is described by the Eq. 1.

$$\Delta E^* = \sqrt{\left(L_2^* - L_1^*\right)^2 + \left(a_2^* - a_1^*\right)^2 + \left(b_2^* - b_1^*\right)^2} \quad (1)$$

where: L^*_1, a^*_1, b^*_1 - values on the color space coordinates of the surface of dried milled thermally untreated beech wood.
L^*_2, a^*_2, b^*_2 - values on the color space coordinates of the surface of dried milled thermally treated beech wood.

Using the STATISTICA 12 program (V12.0 SP2, USA), graphical and mathematical dependences of pH = f *(t, τ)* and ΔE^* = f *(t, τ)* were determined from the measured data in the temperature range: t = 105 to 135°C and time τ = 3 to 12 h. The programmatic processing of the measured results partially eliminated the effect of measurement errors due to wood heterogeneity and a direct pH measurement method (Geffert et al. 2019).

RESULTS AND DISCUSSION

The light white-gray color with a yellow tinge of dry beech wood of uncooked beech wood was identified in the color space CIE L^* a^* b^* by the coordinates L^* = 76.6 ± 2.3; a^* = 6.9 ± 1.8; b^* = 19.8 ± 1.7. The values given are comparable to the values of color coordinates given for beech wood by the authors (Babiak et al. 2004, Dzurenda 2014, Meints et al. 2017).

In the heat treatment process, the light white-gray color changes to pale pink, red-brown to dark brown shades. The degree of coloring of beech wood by heat treatment with saturated steam is dependent on the temperature and duration of the technological process, as evidenced by Fig. 2.

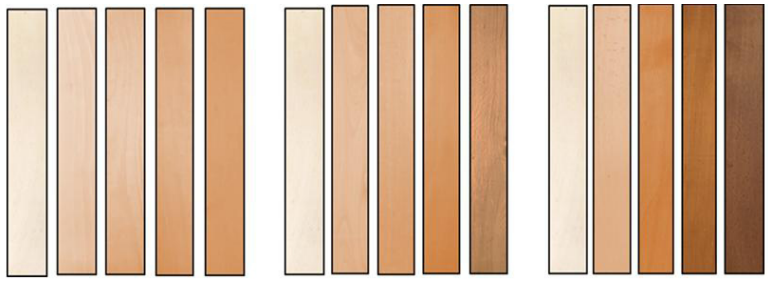

Fig. 2: Changes in the color of beech wood during thermal modification.

Information on changes in the color of beech wood during thermal treatment on the coordinate of brightness L^*, red color a^*, yellow color b^* and the total color difference ΔE^* is given in Tab. 2.

Tab. 2: Measured values on the coordinates L, a*, b* in the color space CIE L* a* b*, values of the total color difference ΔE* of beech wood during the process of thermal modification.*

Temperature of saturated water steam	Time of thermal modification of beech wood color			
	3 h	6 h	9 h	12 h
t_I = 105 ± 2.5°C	L* = 75.8 ± 0.9	L* = 70.5 ± 0.8	L* = 68.9 ± 1.0	L* = 67.4 ± 1.2
	a* = 8.5 ± 0.5	a* = 10.7 ± 0.4	a* = 10.5 ± 0.4	a* = 10.3 ± 0.6
	b* = 19.2 ± 0.4	b* = 20.2 ± 0.4	b* = 20.2 ± 0.5	b* = 19.5 ± 0.5
	ΔE* = 1.97	ΔE* = 7.25	ΔE* = 8.64	ΔE* = 9.84
t_{II} = 125 ± 2.5°C	L* = 70.5 ± 0.9	L* = 64.7 ± 1.2	L* = 62.9 ± 1.0	L* = 59.7 ± 0.9
	a* = 10.3 ± 0.4	a* = 11.9 ± 0.4	a* = 12.5 ± 0.4	a* = 12.2 ± 0.4
	b* = 19.8 ± 0.6	b* = 17.9 ± 0.5	b* = 18.5 ± 0.4	b* = 19.8 ± 0.3
	ΔE* = 7.03	ΔE* = 13.01	ΔE* = 14.80	ΔE* = 17.70
t_{III} = 135 ± 2.5°C	L* = 66.6 ± 0.6	L* = 60.7 ± 1.2	L* = 54.2 ± 0.8	L* = 50.4± 1.7
	a* = 11.6 ± 0.2	a* = 12.5 ± 0.5	a* = 12.5 ± 0.4	a* = 12.6 ± 0.4
	b* = 18.7 ± 0.3	b* = 19.4 ± 0.7	b* = 19.5 ± 0.6	b* = 18.8 ± 0.6
	ΔE* = 11.15	ΔE* = 16.89	ΔE* = 23.10	ΔE* = 26.85

From the difference of the values on the brightness coordinate L^* from the value L_0^* = 76.8 of thermally untreated beech wood and the values of L_4^* of thermally treated beech wood after 12 hours at individual temperatures of thermal treatment it follows that while at temperature t_I = 105 ± 2.5°C thermal treatment the brightness decreased by ΔL_4^* = - 9.4, so at thermal treatment with temperature t_{II} = 125 ± 2.5°C the brightness decreased by ΔL_4^* = - 17.1 and at temperature t_{III} = 135 ± 2.5°C the brightness decreased by up to ΔL_4^* = - 26.4. The decrease in the brightness of beech wood with an increase in temperature is not directly proportional. At higher temperatures of the heat treatment process, the decrease in brightness is greater and the darkening of beech wood is more pronounced.

A decrease in values of the coordinate of lightness L^* of thermally treated wood is in line with reports of wood darkening in the processes such as wood steaming (Varga and Van der Zee 2008, Tolvaj et al. 2009, 2010), Dzurenda 2014, 2018b,c, Hajdarski and Deliiski 2016, Banski and Dudiak 2019), or drying in warm humid air or high temperature wood drying in a superheated steam environment (Klement and Marko 2009, Dzurenda and Deliiski 2012a,b, Baranski et al. 2017).

Changes in the chromatic coordinate of red color a* have an increasing tendency. The value of the red color of native wood a_0^* = 6.9 increases during 12 hours in a thermal process with the temperature of saturated water steam t_I = 105 ± 2.5°C to the value a_4^* = 10.3 and at the temperature of water steam t_{III} = 135 ± 2.5°C to a_4^* = 12.6. The magnitudes of the changes on the red coordinate a^* are significantly smaller compared to the changes on the luminance coordinate L^*. The analysis of the influence of the parameters: temperature and duration of the technological process shows that with increasing temperature the values on the red coordinate a^* increase. The largest increase in the values of Δa* manifested by reddening of beech wood is in the first 6 hours of the technological process, a similar statement is given by the authors Banski and Dudiak (2019).

On the coordinate yellow color b^*, the changes are slight and contradictory, oscillating in a tolerance of ± 1.6 around the value b^* = 18.1. They point to the formation of less stable compounds with absorption of the electromagnetic radiation spectrum with a yellow wavelength

of 560 nm. Said compounds react with water or extraction products to form further thermal decomposition products with lower or zero absorption of the yellow wavelength electromagnetic radiation spectrum.

Color changes in beech wood during the thermal treatment, in addition to identification by means of values L^*, a^*, b^* in the color space CIE $L^* a^* b^*$, are aptly characterized by the parameter - the total color difference ΔE^*. The dependence of the change of the total color difference ΔE^* on the temperature t and time τ of beech wood during heat treatment of wood at saturated water steam temperatures in the range from t = 105 to 135°C and time τ = 3 – 12 h., is shown in the form of a 3D diagram in Fig. 3 and is mathematically described by Eq. 2.

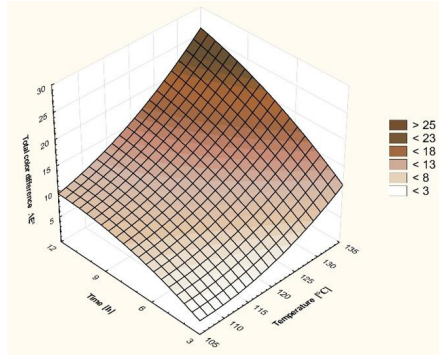

Fig. 3: Correlation of the ΔE^* value of beech wood and the temperature of saturated water steam t and the time τ.

The dependence of the total color difference of beech wood on the temperature of saturated water steam t and time τ is described by the equation in the form:

$$\Delta E^* = 128.919 - 2.384 \cdot t - 1.008 \cdot \tau + 0.108 \cdot t^2 + 0.029 \cdot t \cdot \tau - 0.085 \cdot \tau^2 \quad (2)$$

where: t - temperature of the saturated water steam °C,
τ - time wood is exposed to color modification in hours.

Under the influence of heat, in the process of thermal treatment of wet beech wood, the processes of hydrolysis of hemicelluloses take place, which are reflected in the change of acidity of beech wood. Measured values of moisture w and acidity pH of beech wood before the heat treatment process and during heat treatment of beech wood in the technological process measured at time 3, 6, 9 and 12 h. are listed in Tab. 3

Tab. 3: Average values of moisture content and acidity of beech wood in the process of heat treatment of wood.

Temperature of saturated water steam	Time of thermal modification of beech wood									
	0 h		3 h		6 h		9 h		12 h	
	w (%)	*pH*	*w (%)*	*pH*	*w (%)*	*pH*	*w (%)*	*pH*	*w (%)*	*pH*
t_I = 105 ± 2.5°C	56.9	5.1	49.6	4.9	49.2	4.7	49.5	4.6	48.9	4.4
t_{II} = 125 ± 2.5°C	55.8	5.2	44.3	4.3	44.9	4.0	45.2	3.9	44.7	3.8
t_{III} = 135 ± 2.5°C	56.5	5.1	46.5	3.8	45.8	3.7	46.0	3.5	44.3	3.4

The moisture values of the thermally treated beech wood after cooling to ambient temperature were lower than the moisture of the wood before the thermal treatment. Reduction of beech wood moisture content by Δw = 6.9 to 12.6% is caused by evaporation of water from wood to saturated water steam in autoclave during cooling to temperature t = 100°C before sampling from autoclave and vaporization of water from wood to atmosphere during cooling of wood to ambient air temperature. The source of heat for evaporation and vaporization of water from wood is the heat accumulated during the heating of the wood to the required technological temperature (Dzurenda and Deliiski 2000, Dzurenda 2018d).

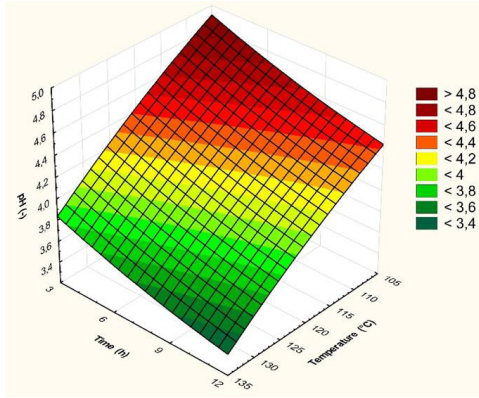

Fig. 4: Correlation of the pH value of wet beech wood and the temperature of saturated water steam t and the time τ.

Changes in the acidity of beech wood in the heat treatment process are a confirmation of the known knowledge about the decrease in the pH of wet wood (Bučko 1995, Sundqvist et al. 2006, Samešova et al. 2018, Geffert et al. 2019). From experimentally measured pH values of beech wood during heat treatment of wood with saturated steam in the range of temperatures from t = 105 to 135°C and time τ = 3 – 12 h, a graphical dependence of the change in acidity on temperature and time was determined in the form of a 3D diagram (Fig. 4).

Changes in the acidity values of wet beech wood at the temperature of saturated water steam in the range of values t = 105 – 135°C and time τ = 3 – 12 hours are given by a mathematical equation in the form:

$$pH = 5.0217 + 0.0236 \cdot t - 0.1021 \cdot \tau - 0.00022 \cdot t^2 + 0.0002 \cdot t \cdot \tau + 0.0019 \cdot \tau^2 \quad (3)$$

where: t – temperature of the saturated water steam °C,
τ – time wood is exposed to color modification in hours.

The course of changes in the total color difference ΔE^* on the acidity of wet beech wood in the process of thermal treatment in the temperature range t = 105 – 135°C and the time of the technological process τ = 3 – 12 h. is shown in Fig. 5.

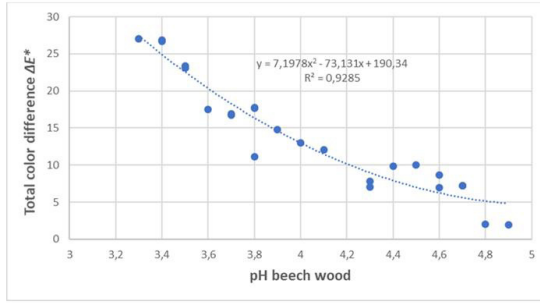

Fig. 5: Dependence on the total color difference of beech wood ΔE on the acidity value of beech wood pH in the heat treatment process.*

The dependence of the total color difference of beech wood on the value of acidity is mathematically described by the function:

$$\Delta E^* = 7.1978 \cdot (pH)^2 - 73.131 \cdot (pH) + 190.34 \quad (4)$$

where: pH - acidity value of wet beech wood.

A similar dependence of the total color difference of wood on the pH value of wet thermally treated beech wood is presented in the work Dzurenda et al. (2020).

It can be seen from the resulting dependence that the color of the heat-treated beech wood acquires darker shades due to the temperature of the saturated water steam and the modification time. The pH values of wet thermally treated wood, depending on the temperature of the saturated steam and the time of treatment decrease, i.e. they have a more acidic pH, which can be clearly seen in the given dependence the darker the shade the lower (more acidic) pH. The dependence of the total color difference ΔE^* on the change in the acidity of beech wood in the thermal process is a suitable tool for evaluating the achieved color change based on the pH of beech wood in the technological process.

CONCLUSIONS

(1) The paper presents the results of color change and acidity of *Fagus sylvatica* L. wood in the process of heat treatment of wood with saturated water steam at temperatures: t_I = 105 ± 2.5°C, t_{II} = 125 ± 2.5°C and t_{III} = 135 ± 2.5°C for τ = 12 hours.

(2) The color of beech wood changes from a light white-gray color with a yellow to pale pink, red-brown to a brown-red color in the heat treatment process. The magnitude of color changes is mathematically described by the equation $\Delta E^* = 128.919 - 2.384 \cdot t - 1.008 \cdot \tau + 0.108 \cdot t^2 + 0.029 \cdot t \cdot \tau - 0.085 \cdot \tau^2$.

(3) The rate of change of acidity from pH = 5.1 to pH = 3.4 in the process of thermal modification of beech wood color at temperature t time τ is described by the equation: $pH = 5.0217 + 0.0236 \cdot t - 0.1021 \cdot \tau - 0.00022 \cdot t^2 + 0.0002 \cdot t \cdot \tau + 0.0019 \cdot \tau^2$.

(4) The dependence of the total color change ΔE^* of beech wood on the acidity of thermally treated wood in the range of values pH = 4.9 - 3.4 is described by the equation: $\Delta E^* = 7.1978 \cdot (pH)^2 - 73.131 \cdot (pH) + 190.34$.

ACKNOWLEDGMENTS

This experimental research was prepared within the grant project: APVV-17-0456 "Termická modifikácia dreva sýtou vodnou parou za účelom cielenej a stabilnej zmeny farby drevnej hmoty" as the result of work of authors and the considerable assistance of the APVV agency.

REFERENCES

1. Babiak, M., Kubovský, I., Mamoňová, M., 2004: Farebný priestor vybraných domácich drevín (Color space of selected domestic trees). In: Interaction of wood with various forms of energy, 3rd International Scientific Symposium, Zvolen, Pp. 113-117.
2. Banski, A., Dudiak, M., 2019: Dependence of color on the time and temperature of saturated water steam in the process of thermal modification of beech wood. In: AIP 38th Meeting of Departments of Fluid Mechanics and Thermodynamics, 2118: 030003.
3. Barański, J., Klement, I., Vilkovská, T., Konôpka, A., 2017: High temperature drying process of beech wood (*Fagus sylvatica* L.) with different zones of sapwood and red false heartwood. BioResources 12(1): 1861-1870.
4. Barcik, Š., Gašparík, M., Razumov, E.Y., 2015: Effect of thermal modification on the colour changes of oak wood. Wood Research 60(3): 385-396.
5. Blažej, A., Šutý, L., Košík, M., Krkoška, P., Golis, E., 1975: Chémia dreva (Chemistry of wood). ALFA, Bratislava, 221 pp.
6. Bučko, J., 1995: Hydrolýzne procesy (Hydrolysis processes). Technical University in Zvolen, Zvolen, 116 pp.
7. Čudinov, B.S., Stepanov, V.L., 1968: Phasenzusammensetzung der Wasser in gefrorenem Holz. In: Holztechnologie 9(1): 14-18.
8. Dzurenda, L., Deliiski, N., 2000: Analysis of moisture content changes in beech wood in the steaming process with saturated water steam. Wood Research 45(4): 1-8.
9. Dzurenda, L., Orlowski K., 2011: The effect of thermal modification of ash wood on granularity and homogeneity of sawdust in the sawing process on a sash gang saw PRW 15-M in view of its technological usefulness. Drewno 54(186): 27-37.
10. Dzurenda, L., Deliiski N., 2012a: Convective drying of beech lumber without color changes of wood. Drvna industrija 63(2): 95-103.
11. Dzurenda, L., Deliiski N., 2012b: Sušenie bukového reziva v komorových sušiarňach režimami zachovávajúcimi pôvodnú farbu dreva (Drying of beech timber in chamber drying kilns by regimes preserving the original colour of wood). Acta facultatis xylologiae Zvolen 54(1): 33-42.
12. Dzurenda, L., 2013: Modification of wood colour of *Fagus sylvatica* L. to a brown-pink shade caused by thermal treatment. Wood research 58(3): 475-482.
13. Dzurenda, L., 2014: Colouring of beech wood during thermal treatment using saturated water steams. Acta facultatis xylologiae Zvolen 56(1): 13 – 22.
14. Dzurenda, L., 2018a: The shades of color of *Quercus robur* L. wood obtained through the processes of thermal treatment with saturated water vapor. BioResouces 13(1): 1525-1533.
15. Dzurenda, L., 2018b: Hues of *Acer platanoides* L. resulting from processes of thermal treatment with saturated steam. Drewno 61(202): 165-176.
16. Dzurenda, L., 2018c: Colour modification of *Robinia pseudoacacia* L. during the processes of heat treatment with saturated water steam. Acta Facultatis Xylologiae Zvolen 60(1): 61-70.

17. Dzurenda, L., 2018d: The effect of moisture content of Black locust wood on the heating in the saturated water steam during the process of colour modification. In: MATEC Web of Conferences 168(181): 06004.
18. Dzurenda, L., Geffert, A., Geffertová, J., Dudiak, M., 2020: Evaluation of the process thermal treatment of maple wood saturated water steam in terms of change of pH and color of wood. BioResources 15(2): 2550-2559.
19. Fengel, D., Wegener, G., 1984: Wood: chemistry, ultrastructure, reactions. Walter de Gruyter: Berlin, 613 pp.
20. Hadjiski, M., Deliiski, N., 2016: Advanced control of the wood thermal treatment processing. In: Cybernetics and Information Technologies. Bulgarian Academy of Sciences 16(2): 176-197.
21. Geffert, A., Geffertová, J., Dudiak, M., 2019: Direct method of measuring the pH value of wood. Forests 10(10): 852.
22. Klement, I., Marko, P., 2009: Colour changes of beech wood (*Fagus sylvatica* L.) during high temperature drying process. Wood Research 54(3): 45-54.
23. Kollmann, F., Côte, W.A., 1968: Principles of wood sciences and technology. Vol. 1. Solid Wood. Springer Verlag, Berlin, Germany, 592 pp.
24. Meints, T., Teischinger, A., Stingl, R., Hassmann, C., 2017: Wood colour of central European wood species: CIELAB characterisation and colour intensification. European Journal of Wood and Wood Products 75: 499-509.
25. Molnar, S., Tolvaj, L., 2002: Colour homogenisation of different wood species by steaming. In: Interaction of wood with various forms of energy. Pp 119-122, Technical University in Zvolen.
26. Pňakovič, Ľ., Dzurenda, L., 2015: Combustion characteristics of fallen fall leaves from ornamental trees in city and forest parks. BioResources 10(3): 5563-5572.
27. Samešová, D., Dzurenda, L., Jurkovič, P., 2018: Kontaminácia kondenzátu produktmi hydrolýzy a extrakcie z tepelného spracovania bukového a javorového dreva pri modifikácii farby dreva (Contamination of water by hydrolysis products and extraction from the thermal treatment of beech and maple timber during modification the color of wood). Chip and Chipless Woodworking Processes 11(1): 277–282.
28. Sanderman, W., Rothkamm, M., 1959: The determination of pH values of woods and their practical importance. Holz Roh- Werkstoff 17: 433-441.
29. Sikora, A., Kačík, F., Gaff, M., Vondrova, V., Bubeníkova, T., Kubovský, I., 2018: Impact of thermal modification on color and chemical changes of spruce and oak wood. Journal of Wood Science 64: 406–416.
30. Sundqvist, B., Karlsson, O., Westremark, U., 2006: Determination of formic-acid and acid concentrations formed during hydrothermal treatment of birch wood and its relation to color, strength and hardness. Wood Science and Technology 40(7): 549-561.
31. Sergovskij, P.S., Rasev, A.I., 1987: Gidrozermicheskaya obrobotka i konservironaniye drevesiny (Hydrothermal treatment and conservation of wood). Lesnaja promyslennost Moscow, Russia, 360 pp.
32. Solár, R., 2004: Chémia dreva (Wood chemistry). Technical University in Zvolen, Zvolen, Slovakia, 101 pp.
33. STN EN 13183-1, 2003: Moisture content of a piece of sawn timber. Part1: Determination by oven dry method.
34. Tolvaj, L., Nemeth, R., Varga, D., Molnar, S., 2009: Colour homogenisation of beech wood by steam treatment. Drewno 52(181): 5-17.

35. Tolvaj, L., Molnar, S., Nemeth, R., Varga, D., 2010: Color modification of Black locust depending on the steaming parameters. Wood Research 55(2): 81-88.
36. Trebula, P., 1986: Sušenie a hydrotermická úprava dreva (Drying and hydrothermal treatment of wood). Zvolen: TU Zvolen, 255 pp.
37. Varga, D., Van der Zee, M.E., 2008: Influence of steaming on selected wood properties of four hardwood species. Holz als Roh-und Werkstoff 66(1): 11-18.
38. Zevenhoven, M., 2001: Ash-forming matter in biomass fuels. Åbo Akademi University, Turku, Finland, 120 pp.

Ladislav Dzurenda*, Michal Dudiak
Technical University in Zvolen
Faculty of Wood Sciences and Technology
T.G. Masaryka 24
96001 Zvolen
Slovakia
*Corresponding author: dzurenda@tuzvo.sk

WOOD RESEARCH
66 (1): 2021
117-128
doi.org/10.37763/wr.1336-4561/66.1.117128

WOOD PROPERTIES COMPARATION OF *CEDRELA ODORATA* FROM TREES IN AGROFORESTRY AND IN PURE PLANTATION

Beatriz Segura-Elizondo, Róger Moya
Instituto Tecnológico de Costa Rica-Escuela de Ingeniería Forestañ
Escuela de Ingeniería Forestal
Costa Rica

(Received August 2020)

ABSTRACT

The aim of this work was to compare the general, physical, mechanical, chemical and energy properties of the wood from *Cedrela odorata* trees growing in two agroforestry condition (tree-agroforestry) with *Theobroma cacao* (9 and 10 years old), with a ten-year-old *C. odorata* tree growing in pure plantation (tree-plantation). The results showed that there growing in agroforestry presented higher heartwood diameter (6.7 to 7.6 cm) and heartwood (approx. 17%) and lower bark (12-13%) and sapwood (69-70%) percentages than trees in pure plantation. In addition, this tendency was observed through different heights of the tree. Moreover, wood from 9-tree-agroforestry presented highest specific gravity and volume shrinkage. Then wood from this growing condition presented highest strength in axial hardness and flexure relative, and extractives in cold water and ethanol-toluene. No differences were observed between the energy properties. In general, wood from trees in agroforestry present better properties than the trees growing in pure plantation. According with these results, the potential of agroforestry systems relative to pure plantations, as regards to differences in tree growth produced by crop fertilization, pruning and other management measures to which the agricultural crop is subjected, which can give the wood qualities different from those found at earlier ages.

KEYWORDS: Tropical wood, cedarwood, Spanish cedar, growing condition, farmer trees.

INTRODUCTION

Cedrela odorata Linneo belongs to the Meliaceae family. It is one of the most economically important species in America (Somarriba et al. 2013). It grows in natural forests of the life zones tropical wet forest, sub-tropical humid forest and tropical dry forest (Jaimez 2013). The quality of *C. odorata* wood is excellent and is used for light constructions, interior design, ship construction (decks and panelling) and general woodworks (Cordero 2004). On the other hand,

C. odorata has been planted in pure forest plantations for timber production (Jaimez 2013). However, the greatest potential observed so far is its good growth in association with other agricultural crops in agroforestry systems (Somarriba et al. 2014, Jaimez 2013). The tree species most used in agroforestry are those timbers presenting good size and shape, or those that provide a fresh environment to the plantation: *Cedrela odorata*, along with other species, has this potential (Somarriba et al. 2014).

Many tree species used in agroforestry have great potential for timber uses (Tscharntke et al. 2011). It has been pointed out that the intensive management in tree-crop associations propitiates an improvement of the wood properties compared to other growth conditions, such as pure plantations or natural forests (Tscharntke et al. 2011, Tenorio and Moya 2019). In addition, tree aging, frequent crop fertilization, as well as pruning application and the management to which the agricultural product is subjected in general, are factors that could give the wood different qualities from those of wood extracted from trees growing in natural forest or in pure forest plantations (Somarriba et al. 2014, Tenorio and Moya 2019, Kouakou et al. 2016). Wood production associated to agroforestry is an attractive economic activity in Costa Rica, as it complements other measures of optimization and diversification of farm products (Somarriba and Beer 2011). Several studies have shown the economic importance and growth of *C. odorata* planted in agroforestry (Somarriba and Beer 2011). The main studies conducted on *C. odorata* in agroforestry concentrate on silvicultural aspects (Tixier and Salazar-Dìaz 2019). Special interest has been shown in recent years on finding information about the quality of the wood of *C. odorata* in agroforestry (Tenorio and Moya 2019, Rigg-Aguilar and Moya 2018).

Specifically, Rigg-Aguilar and Moya (2019) studied the wood of trees of two varieties of *C. odorata* growing in an agroforestry, finding that some properties differed between both varieties regarding the percentages of bark and the volumetric shrinkage, moisture content (MC), green density, flexural MOR and MOE, longitudinal compression and tensile strength. In addition, Tenorio and Moya (2019) studied the properties of wood from trees from four agroforestry at different ages (7 to 11 years). These authors found that the analysed wood presented few differences between heights and ages. So far, the quality of wood from trees from agroforestry systems (tree-agroforestry) has not been compared to wood from pure plantations (tree-plantation) of *C. odorata*, in particular regarding physical, chemical, dasometric and mechanical properties. Therefore, more research was needed on this respect to determine the characteristics of wood under tree-agroforestry compared to wood under tree-plantation conditions. Hence, the objective of this work was to compare the dasometric, physical mechanical, chemical and energy properties of the wood from nine and ten year old tree-agroforestry of *C. odorata* with *T. cacao*, with a ten year old *C. odorata* tree-plantation.

MATERIAL AND METHODS

Study site and plantations

Trees from three different plantations were sampled: trees growing in nine- and ten-year-old agroforestry systems (9-tree-agroforestry) and (10-tree-agroforestry) combining *Cedrela odorata* and *Theobroma cacao* (cacao) and trees from a ten-year-old pure *C. odorata* plantation (10-tree-plantation). The plantations were located in Turrialba (9°58´02"N – 83°36´44"W), Costa Rica in two sites close to one another. The three plantations were planted with initial spacing of 3 x 3 m. Pruning and thinning began after two years and weed clearing was done two or three times a year, depending on weed growth. Ferns were planted in the pure plantation (10-tree-plantation) during the first year, and after that year, neither thinning nor weeding were applied.

Experimental design and sampling

Nine trees were randomly selected from each of the plantations of *C. odorata*. The sampled trees had a diameter similar to the average diameter of the plantation (Moya and Muñoz 2010), which was previously obtained by measuring the diameters of the established plots (Tab. 1). The cut trees had straight trunks, normal branching and no symptoms of diseases or pests. The commercial height was measured in these trees and represents the height when the diameter is 10 cm.

Tab. 1: Dasometric parameters of Cedrela odorata trees growing in an agroforestry system with Theobroma cacao and growing in pure plantation.

Ages	Density (trees·ha^{-1})	Total height (m)	Diameter breast height (cm)	Average growth rate (cm·years^{-1})
9-tree-agroforestry	1000	26.2	22.8	2.5
10-tree-agroforestry	720	28.0	23.9	2.4
10-tree-plantation	960	26.5	17.8	1.8

Sampling within the trees consisted of the extraction of cross-section discs and logs. In the case of the logs, two sections were obtained: one from the base to breast height diameter (DBH) and the other from the DBH to 25% of the commercial height. In the case of the cross-section discs, these were 3.0 cm thick and were cut at the base, at DBH, and at 25%, 50%, 75% and 100% of the commercial height.

Dasometric properties

For each cross section, tree diameter, bark (thickness and total area percentage), sapwood (thickness and total area percentage) and heartwood (diameter and total area percentage) were determined. Two perpendicular lines were drawn crossing the centre of each disc, one in the north-south direction and the other in east-west direction. Total diameter, diameter without bark and heartwood diameter were measured in both directions drawn on the disc. Bark thickness was calculated as difference between total diameter and diameter without bark and sapwood thickness as the difference between total diameter and heartwood diameter. The percentages of bark, sapwood and heartwood were calculated relative to the area of these sections and the total disc area.

Physical and mechanical properties

The physical properties determined were green density, specific gravity, green MC, volume and tangential and radial total shrinkage. These properties were determined in each disc from the trunk, for each percentage of commercial height (0%, DBH, 25%, 50%, 75%, 100%), except for the tangential and radial shrinkages, which were only determined for the DBH. A 3.0 cm-wide piece was cut from each cross section, pith included. The section was divided at the pith, obtaining two samples. To determine the radial and tangential shrinkage, two pieces (radial and tangential) were cut, with dimensions 2.5 x 2.5 x 10 cm. Green density is calculated by ratio of green weight/green volume, specify gravity, different shrinkage and MC according to ASTM D-143 (ASTM, 2014). The mechanical strengths determined were: static flexure, Janka hardness, compression parallel to the grain and shear strength parallel to the grain, following the ASTM D143-14 standards (ASTM, 2014). The logs obtained from the sampled trees were sawn and the pieces were dried to obtain 12% MC condition. For each one of the mechanical tests, 18 samples per age were prepared.

Chemical and energy properties

Three samples of each age were used for determination of following properties and the standards were: method T222 om-02 (Tappi 2002) for lignin content; Seifert (1960) for cellulose; the ASTM D1110-84 (ASTM 2013a) for extractives in water (hot and cold conditions); the ASTM D 1109-84 for sodium hydroxide (ASTM 2013b); ASTM D1107-96 for the ethanol-toluene solution (ASTM 2013c); ASTM D1108-96 (ASTM 2013d) for dichloromethane (ASTM 2013e); ASTM D1102-84 standard (ASTM 2013e) for ash content, ASTM D1762-84 (ASTM 2013f) for volatile content, respectively and ASTM D-5865 standard (ASTM 2013g) for determination of the calorific power. The CHNS vario El cube series 19171074 was utilized for determination of the contents of carbon (C), hydrogen (H), nitrogen (N) and sulphur (S).

Statistical analysis

A general statistical description (average and coefficient of variation) was applied for all wood properties. Then, an ANOVA (analysis of variance) was performed to determine the effect of different tree growth conditions (agroforestry and plantation). This analysis was applied only to the properties at DBH. Tukey multiple range test ($P<0.05$) was applied to test the significant differences between the physical, mechanical, dasometric and chemical properties. The statistical programs used were SAS and Info Stat.

RESULTS AND DISCUSSION

Dasometric properties

In relation to the dasometric properties at DBH, statistical differences were observed in general in all the parameters analyzed, with the exception of bark and sapwood thickness, for which there were no statistical differences (Tab. 2). Regarding the total diameter, 10-tree-plantation trees showed statistical differences with trees growing in agroforestry. In relation to bark, it was only found difference in bark percentage. With respect to sapwood percentage, trees in agroforestry systems did not show statistical differences between them, but statistic differences were observed relative to 10-tree-plantation. The diameter and percentage of heartwood was the highest in 9-tree-agroforestry.

Tab. 2: Comparison of the properties of different tree tissues at diameter at breast height of Cedrela odorata trees growing in agroforestry systems with Theobroma cacao and growing in pure plantation.

Type of tissue	Parameter	9-tree-agroforestry	10- tree-agroforestry	10- tree-plantation
Bark	Thickness (cm)	0.59^{A} (18.7)	0.56^{A} (22.2)	0.61^{A} (21.9)
	Percentage	13.85^{A} (19.9)	12.95^{B} (23.9)	15.00^{C} (12.1)
Sapwood	Thickness (cm)	4.60^{A} (28.9)	4.44^{A} (27.6)	4.55^{A} (22.0)
	Percentage	70.75^{AB} (7.4)	68.57^{A} (13.4)	72.96^{B} (5.7)
Heartwood	Diameter (cm)	6.69^{A} (36.9)	7.59^{B} (48.3)	5.56^{C} (37.5)
	Percentage	14.90^{A} (31.9)	17.97^{B} (49.4)	11.47^{A} (38.0)
Diameter at breast height		17.06^{A} (28.4)	17.59^{A} (30.9)	15.87^{B} (24.7)

Note: Different letters between ages and same wood property mean statistically different at 99%. The values between parentheses represent the coefficient of variation.

With regard to tree height variations, the thickness of the heartwood, sapwood and bark decreased from the base to the commercial height (Fig. 1a-c).

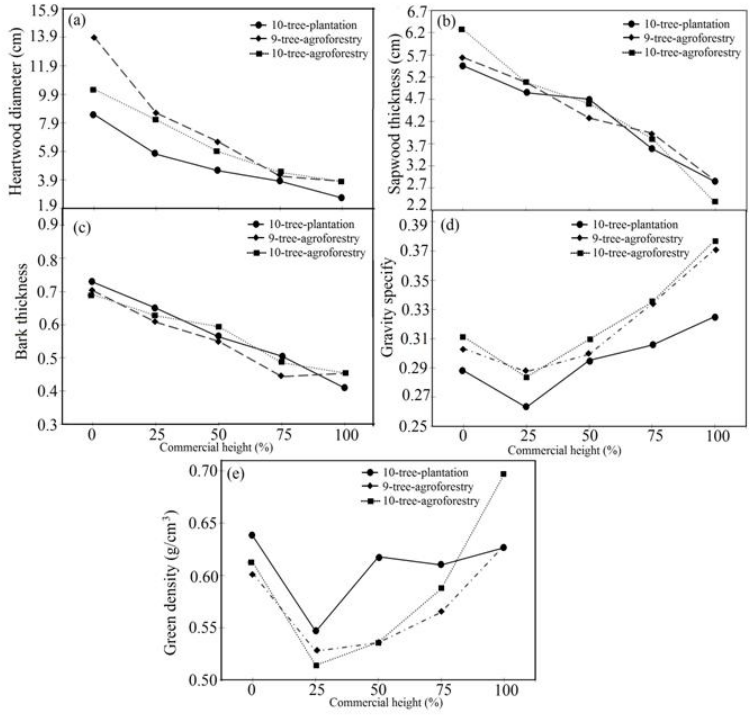

Fig. 1: Heartwood diameter (a), sapwood thickness (b), bark thickness (c), specific gravity, (d) and green density (e) in relation to commercial height of Cedrela odorata from trees growing in an agroforestry system with Theobroma cacao and growing in a pure plantation.

Concerning the differences in the two growth systems used (agroforestry systems and pure plantation), the heartwood diameter of agroforestry systems at any height is greater than in 10-tree-plantation (Fig. 1a). The 10-tree-plantation showed smaller diameter at all tree heights. In relation to sapwood and bark thickness (Fig. 1b,c), the three ages showed very similar thickness at different heights.

With respect to variations with the height of the tree (Tab. 3), it was found that the heartwood percentage of trees growing in agroforestry systems at any height was higher than heartwood percentage for trees growing in the 10-tree-plantation condition. Sapwood percentage and heartwood percentage behaved inversely: there was a lower sapwood percentage at all heights in trees growing agroforestry. Regarding the bark percentage, trees in 10-tree-plantation was higher than trees in agroforestry.

Tab. 3: Heartwood, sapwood and bark percentage of trees properties in different commercial height of Cedrela odorata from trees growing in agroforestry system with Theobroma cacao and growing in pure plantation.

Type of tissue	Commercial height (%)	9-tree-agroforestry	10- tree-agroforestry	10- tree-plantation
Heartwood (%)	0	17,91^{A} (22.7)	27.38^{B} (19.1)	16.50^{C} (14.6)
	25	17.02^{A} (7.2)	18.65^{A} (16.9)	11.41^{B} (9.8)
	50	12.76^{A} (9.6)	16.94^{B} (13.8)	8.93^{B} (15.0)
	75	11.61^{A} (12.6)	10.84^{A} (9.5)	9.19^{C} (19.0)
	100	15.42^{A} (14.3)	14.67^{A} (20.6)	7.49^{B} (11.5)
Sapwood (%)	0	70.88^{A} (9.0)	62.33^{B} (7.4)	69.88^{A} (9.6)
	25	69.81^{A} (20.4)	69.03^{A} (21.9)	72.87^{B} (21.0)
	50	72.49^{A} (21.6)	69.44^{B} (24.5)	76.05^{C} (23.6)
	75	73.45^{A} (16.5)	75.09^{B} (32.4)	73.83^{A} (22.2)
	100	65.19^{A} (13.0)	67.33^{B} (32.4)	74.28C (16.8)
Bark (%)	0	11.14^{A} (10.1)	10.25^{A} (10.3)	13.48^{B} (7.7)
	25	12.58^{A} (15.5)	11.83^{A} (17.3)	15.02^{B} (13.3)
	50	14.23^{A} (13.2)	13.13^{A} (20.7)	14.42^{A} (13.4)
	75	14.56^{A} (16.4)	13.45^{A} (20.9)	16.13^{A} (9.7)
	100	18.43^{A} (14.0)	17.04^{A} (35.5)	17.23^{A} (11.0)

Note: Different letters between ages and same wood property mean statistically different at 99%. The values in parentheses represent the coefficients of variation.

Leyva and Erguera (2014) and Rigg-Aguilar and Moya (2018) showed that the diameter values between 10 and 15 cm for this species in agroforestry systems, hence these values are within the range of values obtained in this study (Tab. 2). On other hands, Tenorio and Moya (2019) and Rigg-Aguilar and Moya (2018) reported similar dasometric properties of *C. odorata* trees than the results of this study.

Greater diameter is evident in 9-tree-agroforestry and 10-tree-agroforestry compared to 10-tree-plantation, at the different heights studied and at the DBH (Tabs. 2-4 and Fig. 1). Diameter growth of *C. odorata* trees, as for any other species, is greater when growing in agroforestry systems, compared to diameter growth in pure plantations. Frequent crop fertilization, in this case *T. cacao*, as well as the frequent application of pruning to handle the shade and in general the management to which the agricultural product is subjected in an agroforestry systems, provides better conditions for the growth of the tree than when growing under conditions of pure forest plantation (Jaimez 2013). In fact, trees growing in agroforestry systems require shorter rotations than pure plantations (Montagnini and Nair 2004, Kouakou et al. 2016). Therefore, the greater diameter growth results in differences in the dasometric characteristics of the tree, as occurred in the present study with heartwood and sapwood, although not in bark thickness (Tabs. 2-4, Fig. 1), which is related to tree growth (Taylor et al. 2002).

The heartwood diameter showed an increase with increasing tree diameter (Taylor et al. 2002), therefore, an increase in the heartwood percentage and a decrease in the sapwood percentage. This behaviour was evident in the trees of *C. odorata* of the present study, where the trees growing in agroforestry systems produce greater diameter development and heartwood percentage than trees growing in a pure plantation (Tabs 2 and 3, Fig. 1a). Heartwood formation results from the death of the parenchyma and accumulation of substances (extractives) in the inner

part of the tree, and is regulated by the physiological behavior of the enzymes in the sapwood, which in turn is regulated by growth conditions (Taylor et al. 2002). Knowledge about heartwood formation is scarce in tropical species (Taylor et al. 2002) and very limited for trees growing in fast growth tropical conditions (Moya et al. 2014). However, heartwood increase can be explained by the tree's need to increase the physiological processes of the enzymes in the sapwood in order to achieve the development observed in the trees in agroforestry systems conditions.

In relation to the bark, the greatest source of variation is within the species, tree age and height (Paine et al. 2010). This behavior is consistent with results found in *C. odorata* trees growing in agroforestry systems and pure plantations (Tabs. 2 and 4; Fig. 1c). According to Wilson and Witkowski (2003), bark variation during the first years of growth of the tree before flowering, is low. This is because it is unnecessary for the tree to invest heavily in creating a thick tissue, in contrast with bigger trees that need more protection for the various tissues and to produce elements for conduction. This physiological behaviour can also explain the little variation of the bark thickness in *C. odorata* growing in agroforestry systems compared to trees in pure plantation. However, due to greater diameter increase in 9-tree-agroforestry and 10-tree-agroforestry, the tree needs more protection all around its circumference, resulting in increased bark percentage in trees growing in agroforestry systems relative to pure plantations. This behavior is consistent with reports from Tenorio and Moya (2019) and Rigg-Aguilar and Moya (2018).

Physical and mechanical properties

There were statistical differences in all parameters analysed, in general, except for the green density, green moisture content and shrinkages (transversal, radial and volumetric) which showed no statistical differences between 10-tree-plantation, 9-tree-agroforestry and 10-tree-agroforestry conditions (Tab. 4). 9-tree-agroforestry and 10-tree-agroforestry conditions presented no statistical differences in specific gravity (SG), as opposed to 10-tree-plantation, which presented less SG. Regarding the variation of SG and green density with the tree height, it was found that these parameters decreased from the base up to 25% of the commercial height, and then increased up to 100% commercial height in the three conditions (Fig. 1e). In general, the SG was higher in 9-tree-agroforestry (Fig. 1d), but for green density was the highest in 10-tree-plantation condition (Fig. 1e).

The mechanical properties presented no statistical differences as regards to lateral and axial hardness, tangential and radial shear strength, compression parallel to the grain and tensile strength, for woods from 9-tree-agroforestry and 10-tree-agroforestry, as well as for trees growing in 10-tree-plantation condition. Flexure parameters (MOR and MOE) of trees from 9-tree-agroforestry and 10-tree-agroforestry conditions presented lower values than in trees from 10-tree-plantation.

Tenorio and Moya (2019) and Rigg-Aguilar and Moya (2018) reported SG, green density and their variation across of trunk and mechanical properties for Cedrela trees in pure plantation agree with those obtained in this study (Fig. 1e-f, Tabs. 3-4). In relation to mechanical properties, For *C. odorata*, some researchers reported higher mechanical properties. For example, 65.9 MPa resistance is reported for MOR (Bárcenas-Pazos et al. 2014) and 6700 MPa for MOE (Venson et al. 2008) in flexural test, with a lower MOR value obtained in this study.

The SG is a wood quality evaluation parameter that is related to many properties (Muller-Landau 2004), therefore, any change or difference in this parameter in trees growing in an agroforestry system or in a pure plantation, affects other important wood properties (Tixier and Salazar-Díaz 2019). Trees growing under 9-tree-agroforestry and 10-tree-agroforestry conditions showed higher SG than trees growing in the 10-tree-plantation condition (Tab. 4, Fig. 1d). The

growth rate of trees plays an important role in determining the SG (Suzuki 1999). In general, high growth rate in tropical trees is associated with low SG of wood (Suzuki 1999, Muller-Landau 2004), and low growth rate is associated with high SG of wood (Van Gelder et al. 2006). However, this behavior usually occurs in species with diffuse porosity (Zobel and Van Buijtenen 1989), but in annular or semi-annular species, as *C. odorata* the behavior is different. This behavior occurs because the region that presents ring porosity is relatively constant, while the region with diffuse porosity is proportional to the width of the ring, therefore, the wider rings contain more diffuse porosity region, resulting in a higher density (Zobel and Van Buijtenen 1989).

The differences in flexural MOR and MOE result from the direct relationship between SG and these parameters (Muller-Landau 2004). The highest value of SG in 9-tree-agroforestry and 10-tree-agroforestry conditions results in greater flexural MOR and MOE in trees under those growth conditions (Tabs. 2 and 4). In the case of extractives soluble in ethanol-toluene, differences were observed only between 9-tree-agroforestry and 10-tree-plantation. Extractives depend on the age of the heartwood formation; therefore, greater quantity can be found in older trees (Tenorio and Moya 2019). Although not every part of the tree was sampled (heartwood/sapwood) nor the age of formation of the heartwood was determined, it is likely that heartwood in trees in 10-year-old plantations contain more extractives than trees in 9-tear-old plantations.

Chemical properties

As for the chemical properties, significant differences were observed only in ethanol-toluene soluble compounds, where 9-tree-agroforestry condition differed from both 10-tree-agroforestry and 10-tree-plantation conditions. The condition 10-tree-agroforestry showed no statistical differences with 10-tree-plantation. Condition 9-tree-agroforestry had the highest statistical values for hot water-soluble compounds and the lowest value for ethanol-toluene soluble compounds (Tab. 4). The other chemical components (cellulose, lignin, dichloromethane soluble compounds, NaOH, hot water and amount of N, C and H) did not show statistical differences in the different plantations (Tab. 4).

Tab. 4: Averages of physical, mechanical and chemical properties of Cedrela odorata from trees growing in an agroforestry system with Theobroma cacao and growing in pure plantation.

Wood properties	Parameters	9-tree-agroforestry	10-tree-agroforestry	10- tree-plantation
Physical	Specific gravity	0.32^{A} (13.1)	0.31^{A} (13.4)	0.29^{B} (12.0)
	Green density ($g \cdot cm^{-3}$)	0.58^{A} (14.3)	0.57^{A} (13.6)	0.60^{A} (10.5)
	Green moisture content (%)	82.23^{A} (17.6)	83.09^{A} (27.6)	108.15^{A} (14.2)
	Volumetric shrinking (%)	8.97^{A} (15.0)	8.95^{A} (18.9)	9.54^{A} (19.1)
	Tangential shrinking (%)	4.25^{A} (10.7)	4.62^{A} (11.8)	5.01^{A} (19.7)
	Radial shrinking (%)	3.11^{A} (23.5)	2.80^{A} (16.2)	3.54^{A} (17.5)

Mechanical	Janka hardness	Lateral (N)	1418.3^{A} (18.8)	1458.0^{A} (21.8)	1283.0^{A} (27.2)
		Axial (N)	1704.5^{A} (17.9)	2002.2B (11.4)	1485.1^{A} (27.2)
	Shear	Tangential stress (MPa)	6.78^{A} (11.4)	6.77^{A} (11.2)	6.65^{A} (17.9)
		Radial stress (MPa)	6.10^{A} (15.0)	6.36^{A} (8.7)	6.34^{A} (14.4)
	Flexion	Module of rupture (MPa)	28.98^{A} (13.4)	30.23^{A} (11.7)	24.56^{B} (12.4)
		Module of elasticity (GPa)	4.07^{A} (12.3)	4.46^{A} (8.5)	3.70^{B} (11.9)
	Compression	Stress (MPa)	16.35^{A} (15.0)	17.19^{A} (21.3)	16.82^{A} (20.9)
	Tension	Stress (MPa)	41.30^{A} (32.3)	40.46^{A} (35.0)	49.44^{A} (38.4)
Chemical	Cellulose (%)		53.00^{A} (3.4)	52.50^{A} (1.6)	51.83^{A} (1.8)
	Lignin (%)		30.89^{A} (0.9)	30.72^{A} (2.6)	28.64^{A} (5.4)
	Extracts in dichloromethane (%)		3.33^{A} (37.4)	2.33^{A} (40.4)	1.67^{A} (56.6)
	Extracts in NaOH (%)		3.50^{A} (11.7)	3.50^{A} (35.0)	4.00^{A} (30.6)
	Extracts in hot water (%)		7.50^{A} (10.9)	5.00^{A} (21.6)	5.67^{A} (16.6)
	Extracts in cool water (%)		4.17^{A} (2.9)	4.17^{A} (15.0)	4.83^{A} (34.1)
	Extracts in ethanol-toluene (%)		7.33^{A} (12.7)	12.00^{B} (0.0)	11.33^{B} (8.3)
	Nitrogen (%)		0.15^{A} (0.1)	0.13^{A} (0.0)	0.18^{A} (0.0)
	Carbon (%)		45.58^{A} (0.7)	45.65^{A} (0.2)	45.69^{A} (1.0)
	Hydrogen (%)		6.34^{A} (0.3)	6.35^{A} (0.6)	6.36^{A} (1.0)

Note: Different letters between ages and same wood properties means statistically different at 99%. The values between parentheses represent the coefficients of variation.

Energy properties

According to the evaluation of the energy properties, the variables volatile percentage (Fig. 2a), ash (Fig. 2b) and calorific power (Fig. 2c) presented no significant differences between the three plantations analyzed.

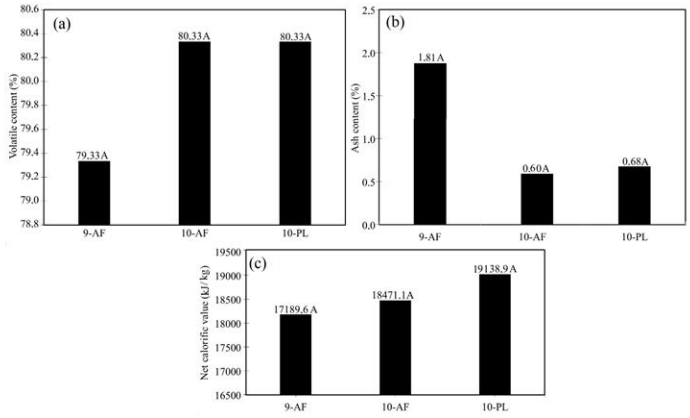

Fig. 2: Volatile and ash contents and net calorific value of Cedrela odorata from trees growing in agroforestry with Theobroma cacao and growing in pure plantation.

The general, physical, mechanical and chemical properties of wood from *C. odorata* trees growing in agroforestry systems with *T. cacao* present few differences with the properties of wood of trees from a pure plantation, except for some parameters. Specifically, trees in agroforestry systems feature greater diameter and greater heartwood diameter and higher heartwood percentage, lower sapwood and bark percentage, lower SG, greater modulus of rupture and modulus of elasticity and higher extractives in cold water and in ethanol-toluene solution (Tabs. 2-4 and Fig. 1). These differences can be explained relative to the growth rate characteristic of trees in agroforestry systems.

The parameters evaluated in this research showed the potential of agroforestry systems relative to pure plantations, as regards to differences in tree growth produced by crop fertilization (in this case cocoa), pruning and other management measures to which the agricultural crop is subjected, which can give the wood qualities different from those found at earlier ages. Apart from the increase in diameter, some other important properties, specifically, heartwood and SG that relate to durability and structural strength were improved in trees growing in agroforestry systems. This would imply that wood from trees from agroforestry conditions present better condition, i.e., is more valuable, than wood from pure plantations. This result found for wood of agroforestry systems and pure plantations contradicts the assertion of Kouakou et al. (2016), who indicate that wood extracted from agroforestry systems has a higher proportion of juvenile wood, lower mechanical resistance, inadequate drying behavior, low durability and a higher proportion of reaction wood (lower quality), conditions that were not found in *C. odorata* trees growing in agroforestry systems.

CONCLUSIONS

It was found that the dasometric properties of trees growing in agroforestry systems show differences with those of trees growing in pure plantations. There are differences in the total diameter, percentage of bark, percentage of sapwood, diameter and percentage of heartwood, physical and mechanical properties and chemical and energy are not affected. In general, trees wood from trees growing agroforestry system presented better properties than wood from trees under pure plantations. According with these results, the potential of agroforestry systems relative to pure plantations, as regards to differences in tree growth produced by crop fertilization (in this case cocoa), pruning and other management measures to which the agricultural crop is subjected, which can give the wood qualities different from those found at earlier ages. This would imply that wood from trees from agroforestry conditions present better condition, i.e., is more valuable, than wood from pure plantations.

ACKNOWLEDGMENTS

The authors are grateful for the support of the Vicerrectoría de Investigacion y Extensión of the Instituto Tecnológico de Costa Rica and also of Hacienda Azul S.A., whocontributed the materials for this research. The authors thank María Teresa Vargas L. for translating and editing to English.

REFERENCES

1. ASTM D134 (2014): Standard test method for small clear specimens of timber.
2. ASTM D1110 (2013a): Standard test methods for water solubility of wood.
3. ASTM D1109(2013b): Standard test method for 1% sodium hydroxide solubility of wood.
4. ASTM D1107-96 (2013): Standard test method for ethanol-toluene solubility of wood.
5. ASTM D1108-96 (2013d): Standard test method for dichloromethane soluble in wood.
6. ASTM D1102-84 (2013e): Standard test method for ash in wood.
7. ASTM D1762-84 (2013f): Standard test method for chemical analysis of wood charcoal.
8. ASTM D5865-11 (2013g): Standard test method for gross calorific value of coal and coke.
9. Bárcenas-Pazos, G.M., Ortega-Escalona, F., Ángeles-Álvarez, G., Ronzón-Pérez, P., 2014: Relación estructura-propiedades de la madera de angiospermas mexicanas (Structure-properties relationship of the wood of Mexican angiosperms). Ecosistemas y Recursos Agropecuarios 21(42): 45-55.
10. Cordero, J., 2004: Árboles de Centroamérica: un Manual para extensionistas (Trees of Central America: A manual for extension workers). Turrialba, CATIE, 1058 pp.
11. Jaimez, R.E., Araque, O., Guzmán, D., Mora, A., Espinoza W., Tezara, W., 2013: Agroforestry systems of timber species and cacao: survival and growth during the early stages. Journal of Agriculture and Rural Development in the Tropics and Subtropics 114(1): 1-11.
12. Kouakou, S.S., Marchal, R., Brancheriau, L., Guyot, A., Guibal, D., 2016: The quality of poplar wood from agroforestry: a comparison with forest plantation. In: Gosme M (ed) 3rd European agroforestry conference. Montpellier, France, Pp 274–276.
13. Leyva, R.R., Erguera, M.L.C., 2014: Cedar (*Cedrela odorata* L.) development in an agroforestry system in Yucatán, México. Revista Forestal Baracoa 33: 148-156.
14. Moya, R., Muñoz, F., 2010: Physical and mechanical properties of eight fast-growing plantation species in Costa Rica. Journal Tropical of Forest Science 22(3): 317-328.
15. Montagnini, F., Nair, P.K.R., 2004: Carbon sequestration: an underexploited environmental benefit of agroforestry systems. Agroforestry Systems 61(1-3): 281-295.
16. Moya, R., Bond, B., Quesada, H., 2014: A review of heartwood properties of Tectona grandis trees from fast- growth plantations. Wood Science Technology 48(2): 411-433.
17. Muller-Landau., H.C., 2004: Interspecific and inter-site variation in wood specific gravity of tropical trees. Biotropica 36(1): 20-32.
18. Paine, Ch., Stahl, C., Courtois, E., Patino, S., Sarmiento, C., Baroloto, Ch., 2010: Functional explanations for variation in bark thickness in tropical rain forest trees. Function Ecology 24: 1202-1210.
19. Rigg-Aguilar, P., Moya, R., 2018: Properties of wood from 7-year-old *Cedrela odorata* trees of two different populations growing in agroforestry systems with *Theobroma cacao*. Madera y Bosques 24(1):1-13.
20. Seifert, K., 1960: Zur frage der Cellulose-Schnellbestimmung nach der Acetylaceton-Methode. Das Papier 14: 104-106.
21. Somarriba, E., Suárez-Islas, A., Calero-Borge, W., Villota, A., Castillo, C., Vílchez, S., Deheuvels, O., Cerda, R. 2014: Cocoa–timber agroforestry systems: *Theobroma cacao–Cordia alliodora* in Central America. Agroforestry Systems 88(6): 1001-1019.
22. Somarriba, E., Beer, J., 2011: Productivity of *Theobroma cacao* agroforestry systems with timber or legume service shade trees. Agroforestry Systems 81: 109-121.

23. Somarriba, E., Cerda, R., Orozco, L., Dávila, M., Cifuentes, H., Astorga, T., Espinoza, C., 2013: Carbon stocks and cocoa yields in agroforestry systems of Central. America. Agriculture, Ecosystems and Environment 173: 46-57.
24. Suzuki, E. 1999: Diversity in specific gravity and water content of wood among Bornean tropical rainforest trees. Ecology Research 14(3): 211-224.
25. TAPPI, T222 om-02: Standard test for aci-insoluble lignin in wood and pulp (2002). Technical Association of Pulp and Paper Industry, Norcross (GA), 3pp.
26. Taylor, A.M., Gartner, B.L., Morrell, J.J., 2002: Heartwood formation and natural durability- a review. Wood Fiber Science 34(4): 587-611.
27. Tenorio, C., Moya, R., 2019: Evaluation of wood properties of four ages of *Cedrela odorata* trees growing in agroforestry systems with *Theobroma cacao* in Costa Rica. Agroforestry Systems 93(3): 973-988.
28. Tixier, P., Salazar-Díaz, R., 2019: Effect of plant diversity on income generated by agroforestry systems in Talamanca, Costa Rica. Agroforestry Systems 93(2): 571-580.
29. Tscharntke, T., Clough, Y., Bhagwat, S., Buchori, D., Faust, H., Hertel, D., Scherber, C., 2011: Multifunctional shade- tree management in tropical agroforestry lanscapes: a review. Journal Applied Ecology 48(3): 619-626.
30. Van Gelder, H.A., Poorter, L., Sterk, F.J., 2006: Wood mechanics, allometry and life-history variation in a tropical rain forest tree community. New Phycologist 171(2): 367-378.
31. Venson, I., Guzmán, J.S., Talavera, F.F., Richter, H.G., 2008: Biological, physical and mechanical wood properties of paraíso (Melia azedarach) from a roadside planting at Huaxtla, Jalisco, Mexico. Journal of Tropical Forest Science 20(1): 38-47.
32. Wilson, B.G., Witkowski, E.T.F., 2003: Seed banks, bark thickness and change in age and size structure (1978-1999) of the African savanna tree, Burhea africana. Plant Ecology 167: 151-162.
33. Zobel, B.J., Van Buijtenen, J.P., 1989: Wood variation: its causes and control. Springer Science & Business Media, New York, 890 pp.

Beatriz Segura-Elizondo, Róger Moya*
Escuela De Ingeniería Forestal
Instituto Tecnologico De Costa Rica
P.O. Box: 159-7050
Cartago
Costa Rica
*Corresponding author: rmoya@itcr.ac.cr

WOOD RESEARCH
66 (1): 2021
129-140
doi.org/10.37763/wr.1336-4561/66.1.129140

EFFECT OF HOT PRESSING MODIFICATION ON SURFACE PROPERTIES OF RUBBERWOOD (*HEVEA BRASILIENSIS*)

Zhipeng Zhu, Dengyun Tu, Ziwei Chen, Chuanfu Chen, Qiangfang Zhou
South China Agricultural University
China

(Received April 2020)

ABSTRACT

This research aims to investigate the effect of thermal modification by hot pressing on surface characteristics of rubberwood. For this purpose, rubberwood specimens were thermally modified by hot pressing in an open system at three different temperatures (170, 185, and 200°C) for two different durations (1.5 or 3 h). Based on the results, the values of chromatic aberration (ΔE), contact angle and glossiness increased, and roughness decreased with increasing temperature and enlarging duration further. Although the contact angle had increased, it was still less than 90°. This aesthetic surface of rubberwood could be retained by using transparent organic coatings. The thermally modified rubberwood with excellent performance could be used as a material for solid wood flooring, wallboard, and furniture applications.

KEYWORDS: Thermal modification, rubberwood, surface characteristics, compression ratio.

INTRODUCTION

Rubberwood (*Hevea brasiliensis*) is one of the most important wooden raw materials in South East Asia. The fundamental purpose of planting rubberwood is harvesting latex. Generally, the rubber trees will be probably felled when they are around 20 years due to a decrease in latex production. Thus, rubberwood is an important by-product resource and commonly used as industrial raw materials (Jiang et al. 2019). The rubber tree cultivated in Thailand is felled about 300 thousand hm^2 every year, and rubberwood exported to China accounts for 90% above (Cheng et al. 2017). Thus, it is one kind of sustainable development of artificial forest commodity material. Rubberwood, which features beautiful textures and excellent machining performance, is suitable for making wooden products such as furniture and solid wood flooring. However, rubberwood is extremely prone to mildew, moth, and decay, owing to a higher content of nutrients in the wood, about 8% of starch and free sugar (Jie et al. 2018, Li et al. 2012). Thermal modification is an effective method to enhance dimensional stability and biological durability, nowadays, without

the use of chemicals to improve the applied value of low nature wood (Cademartori et al. 2015). Therefore, it is necessary to conduct thermal modification to improve the quality of rubberwood and enhance its utilization value.

The thermal modification technology can also change the color of the wood surface. The wood surface is darkened after heat treatment. The color changes in the heat-treated wood surface were due to the degradation products from the hemicellulose and lignin. Previously research showed that the color of heat-treated wood was mainly affected by some factors, such as temperature, duration, wood species, and moisture content (Ding et al. 2017, Esteves et al. 2008, Yildiz et al. 2006, Yu et al. 2010). Generally, the surface color of heat-treated wood changed with the increase of heat treatment temperature and duration. The deep color is appealing to customers because it is similar to the rare wood, such as sandalwood and rosewood.

However, the mechanical strength of heat-treated wood typically reduced significantly by using traditional thermal modification techniques, due to the thermal degradation of the chemical components in the cell walls. The bending strength, modulus of elasticity, compression strength, and impact bending strength of rubberwood heat-treated at 230°C for 3 h decreased 63.74%, 41.22%, 26.16%, and 57.07%, respectively, compared with the control groups (Zhao et al. 2019). In general, the mechanical properties of heat-treated wood gradually decreased with the increase of the heat treatment temperature and duration. The primary factor leading the reduction of mechanical properties was the degradation of hemicellulose and parts of the amorphous cellulose (Cai et al. 2019, Korkut et al. 2015). Another study on poplar wood (*Populus tomentosa*), the wood was thermally treated at 195°C for 3 hours and then subjected to hot pressing at 160°C. The results showed that the surface hardness, modulus of elasticity, and modulus of rupture of treated wood increased by more than 30% (Du et al. 2013). This combined modification method can effectively compensate the loss of mechanical properties caused by heat treatment.

To improve the physical and mechanical properties of heat-treated rubberwood, the rubberwood could be compressed with a relatively low compression ratio, and then it was heat-treated under a pressure of about 1 MPa by hot pressing. The physical and mechanical properties of the thermally modified rubberwood were improved significantly due to the compression (Zhou et al. 2019). However, during the heat treatment process, the surface characteristics of rubberwood have changed evidently, which has a great influence on its practical applications. Thus, it is necessary to research this aspect. In this study, the effects of heat treatment temperature and duration on the surface characteristics of heat-treated rubberwood were investigated. The obtained results could be effectively guided the practical productions of the thermally modified rubberwood and realized its high value-added utilization.

MATERIALS AND METHODS

Wood material

Rubberwood (*Hevea brasiliensis*) was harvested from Thailand. Rubberwood samples used in this study, with the moisture content of 14% and air-dried densities of 0.72 $g \cdot m^{-3}$, were purchased from the wood market. Wood board samples, measuring 300 × 105 × 20 mm (longitudinal (L) ×tangential (T) × radial (R) direction), were prepared. Seven groups of samples (six for heat treatment by hot pressing and one for control) were prepared, and each group had 18 samples.

Thermal modification

The thermal treatment of rubberwood was performed with a laboratory-type single-opening hot press (BY302×2/15, Suzhou Xinxieli, China). Three different temperatures (170, 185, and

200°C) and two different durations (1.5, 3 h) were selected for the heat treatment of rubberwood. The heat treatment process was divided into four stages.

In the first phase, the upper and lower hot plates were heated to the target temperature (170, 185 and 200°C), then the samples were placed on the lower hot plate. To control the target thickness of heat-treated wood, two 18 mm thick metal plates were placed on the lower hot plate on both sides of the samples. The hot-press was closed so that the upper surface of the sample had contact with the upper hot plate. Until the core temperature of the samples reached the target temperature, the samples were compressed. In the second phase, the pressure increased to 14 MPa in 30 sec and kept 3 min, and the wood was compressed to target thickness (18 mm) by using a distance stop. The compression ratio of wood was 10%. In the third phase, the pressure decreased to 2 MPa, and the wood samples were heat-treated at the target temperature for 1.5 or 3 h. In the last phase, the hot plates were cooled down to room temperature by introducing the flowing water into the hot plates for 30 min under the pressure of 2 MPa, and then the wood samples were taken away from the hot-press.

In order to determine the surface properties of heat-treated rubberwood, the treated and control samples were cut into small clear samples with dimensions of 50 (L) × 50 (T) × 18 (R) mm. All the samples were conditioned at 20°C and 65% relative humidity for 2 months prior to further testing. Surface performance tests were conducted in a laboratory with 25°C and 60% relative humidity from August to November 2019.

Chromatic aberration

The color measurements were measured according to GB/T 3979 (2008). The changes in surface color of the heat-treated rubberwood samples were measured by automatic colorimeter (Model:SC-80C, Zhuhai Tian Chuang, China) with D65 illuminant and a 10° standard observer. Ten replicates were used for each group, and the average value was calculated.

The values of L*, a*, and b* of the samples were measured at five different locations on each. ΔE* was used to indicate the difference between the color of the treated samples and the color of the control in this study. It had embodied the greater difference between the measured object and the control color that ΔE* value was larger. And ΔE was calculated according to Eq. 1, and the average value was calculated:

$$\Delta E^* = \sqrt{(\Delta L^*)^2 + (\Delta a^*)^2 + (\Delta b^*)^2} \quad (1)$$

where: L* - the brightness ranging from black (0) to white (100), a* - the color coordinate from red (positive) to green (negative), b* - the color coordinate from yellow (positive) to blue (negative).

Contact Angle

The water contact angle of the wood surface was measured according to GB/T 30693 (2014). The water drop size was 4 μl. The datum after the water droplet contacts the wood surface for 15 s was recorded. Five replicates were used for each group, and the contact angles were measured at five different points of the same sample surface, and the average value was calculated.

Surface roughness

The stylus method was a well-accepted contact technique to evaluate the surface roughness of wood samples. Hence the surface roughness of the samples parallel to the fiber direction was measured by the stylus method according to DIN EN ISO 4287 (2009). The samples used for roughness tests were polished with 500 purpose sandpaper, and the values of the same measured

position were recorded before and after polishing. Five replicates were used for each group, and the surface roughness was measured at five different points of the same sample surface, and the average value was calculated. Three roughness parameters, including mean arithmetic deviation of profile (R_a) which is the average distance from the profile to the mean line over the length of assessment, mean peak-to-valley height (R_z), and maximum roughness (R_y) were used to evaluate surface roughness characteristics of the heat-treated wood samples.

Glossiness

Glossiness was a measure of the ability of a surface to reflect light. The surface glossiness of wood samples was measured using a gloss meter (KGZ-IC, Tianjin, China). The test angle was set at 60° according to ASTM standard D 2457-03 (Zhao et al. 2019). The samples for the glossiness tests were polished with 500 purpose sandpaper, and the values of the same measured position were recorded before and after polishing. Five replicates were used for each group, and the glossiness was measured at five different points of the same sample surface, and the average value was calculated. Measurements were carried out at two directions (Parallel to the fiber direction and perpendicular to the fiber direction). The glossiness of parallel to the fiber direction is denoted as GZL, and the glossiness of perpendicular to the fiber direction is denoted as GZT. The unit is GU.

For all parameters, multiple comparisons were first subjected to an analysis of variance (ANOVA), and significant differences between average values of control and treated samples were determined using Duncan's multiple range test at P value of 0.05.

RESULTS AND DISCUSSION

Chromatic aberration

The surface color of the heat-treated wood and control group are presented in Fig. 1. From Fig. 1, the surface color of heat-treated wood gradually deepened with the increase of heat treatment temperature. With the increase of treatment temperature, the surface color changed from beige to purplish brown. This color was a comfortable, warm tone that had attracted lots of people. Unlike the physical dyeing method, the distribution of the surface color was more uniform by using this thermal modification technique. Changes in color parameters of the untreated control group and the treatment group rubberwood are listed in Tab. 1.

Fig. 1: The color variation of the surface between untreated and thermal modified rubberwood.

Tab. 1: Color CIE Lab parameters and color difference between untreated and thermal modified rubberwood.

Temperature (°C)	Duration (h)	L*	a*	b*	ΔE*
-	0	76.16	7.69	20.36	/
170	1.5	62.89	11.32	24.31	14.31
170	3	58.46	12.46	22.73	18.48
185	1.5	56.60	12.78	21.82	20.26
185	3	52.06	14.35	20.58	25.00
200	1.5	41.78	15.04	15.69	35.47
200	3	37.44	14.93	13.33	40.01

As the heating temperature rose, lightness (L*) decreased steadily, and the longer duration, the more obvious the effect. The values of L* of heat-treated wood decreased by 50.84% compared with the untreated control group. The parameter a* increased slowly, and the parameter b* decreased slightly, indicating that the color of the heat-treated wood was changed to red and blue with the increase of temperature and duration. As the duration was the same, the ΔE* of the treatment group decreased obviously with the increase of treatment temperature. A similar trend was also noted by Sun et al. (2019).

Statistical analysis indicated that the P values of L* and b* with respect to treatment temperature and duration were both less than 0.05. Thus, both temperature and duration have significant effects on L* and b* values. After comparing the value of F, it is evident that treatment temperature is the most significant factor influencing L* and b*. The effect of temperature and duration on a* is not significant, while the effect on ΔE* is significant extremely. According to some previous studies, the main reason for the above results was that the thermal cracking reaction between cellulose and hemicellulose. A large number of hydroxyl groups were oxidized into carbonyl and carboxyl groups, thereby deepening the color of the wood. This was similar to the cause of color change in conventional heat-treated wood (Shukla et al. 2014, Srinivas et al. 2012). In addition, the change of wood extract content, especially phenols, caused by thermal modification was also an important factor affecting wood surface color (Esteves et al. 2008).

Contact angle

Fig. 2 presents the physical picture of the water contact angle of the control group and the treatment group. Fig. 3 shows the actual values of the water contact angle of each treatment group. The water contact angle of heat-treated wood increased with the increase of the treatment temperature and time. Statistical analysis indicated that treatment duration had significant effects on values of contact angle than temperature. Actually, during the heat treatment process, changes in physical and chemical occurred in the surface layers, which resulted in forming a modified surface with new characteristics (Li et al. 2011, Qin et al. 2019). During the heat treatment process, the porosity in the wood surface reduced significantly due to the surface densification, which resulted in the increase of the contact angle value of wood surface (Diouf et al. 2011, Unsal et al. 2005). In addition, the number of hydroxyl groups in the wood surface decreased notably because of the thermal degradation of the wood chemical components, which also resulted in the increase of the water contact angle.

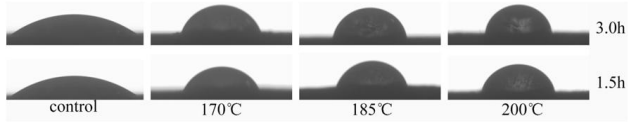

Fig. 2: The picture of water contact angle of the thermally modified rubberwood and untreated wood.

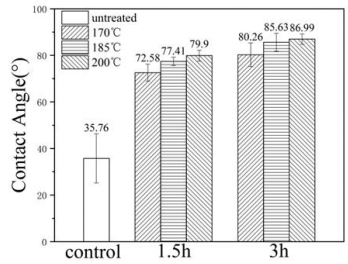

Fig. 3: The actual values of water contact angle of the thermally modified rubberwood and untreated wood.

Nonetheless, changes in the water contact angle of the treatment group was not obvious in this study. The contact angle of the samples heat-treated at 200°C for 3 h was 86.99°, still less than 90°. Because the contact angle value of the water droplet was lower than 90°, the wood surface exhibited hydrophilic property, resulting from the presence of hydroxyl groups in the heat-treated wood surface. In general, the hydrophilic surface was beneficial to make a good bond between the wood and coatings. The surface coatings need to wet, flow or penetrate into the cellular structure of wood to make a good bond between the wood and coatings. The results showed that the wettability of the specimens generally decreased with increasing treatment temperature. Although the effect on bonding strength between wood surface and coatings is small (Aleš et al. 2013).

Surface roughness

Changes in surface roughness parameters (R_a, R_z, and R_y) of the control group and the treatment group are presented in Fig. 4 (before sanding) and Fig. 5 (after sanding). As shown in Fig. 4, the untreated control group exhibited the highest surface roughness, while the lowest surface roughness was found in the specimens heat-treated at 200°C for 3 h. The parameter of R_z was measured to be 18.01 μm for the untreated control wood, while it was determined as 8.05 μm for the samples heat-treated at 200°C for 3 h (Fig. 4b). Similar results were found in the R_y value. The surface-densified wood specimens showed a glossy and smooth appearance after heat treatment processing. During the heat treatment process, the wood fibers in the surface layers were softened that some cell walls in the surface layers were plasticized and compressed, which improves the surface smoothness of the heat-treated wood (Ayrilmis et al. 2019).

In addition, significant changes in Ra was not observed among the treatment groups. The variation trend of the three parameters becomes clearer after sanding. As shown in Fig. 5, the values of three parameters decreased with increasing treatment temperature and time. When the wood was treated for three hours, the values of R_a and R_z were almost similar to the untreated control wood. It was distinctly that the three parameters of the treatment groups after sanding

were higher than those before sanding, especially the parameter R_z. With a compression ratio of only 10%, sanding may cause the densified layers in the wood surface to be destroyed. The results among treatment groups also showed that the value of higher temperature and shorter duration was roughly equal to that of lower temperature and longer duration. In consequence, the desired surface roughness may be obtained at a higher temperature but shorter duration, or at a lower temperature but longer duration. Statistical analysis indicated that treatment temperature was more significant than treatment time on surface roughness.

During the heat treatment process, surface densification reduced the porosity of the wood and made a glossy surface, which decreased the roughness of the wood surface. There was a negative correlation between the roughness and the compression ratio. Previously studies reported that surface roughness of heat-treated wood decreased with increasing treatment temperature and time (Aytin et al. 2015, Bekhta et al. 2014, Ratnasingam et al. 2012). This increase in smoothness or decrease in roughness was very important for many applications of solid wood. It is well known that the larger the surface roughness, the more coatings and adhesive is required. There should be enough coatings and adhesive to fill the valleys and form a continuous adhesive layer of equal thickness. Thus, further studies are needed to establish a correlation between surface roughness and coating material amount. To know which type of surface topography in terms of roughness parameters provides a higher bonding strength and fewer coatings, we might be able to choose appropriate parameters of surface roughness. It is also important to know if sanding is a necessary step.

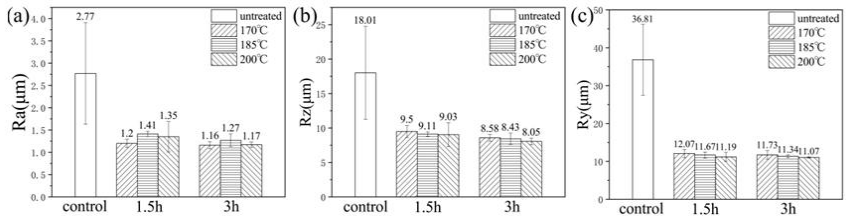

Fig. 4: Surface roughness of rubberwood (before sanding): (a) R_a, (b) R_z, and (c) R_y.

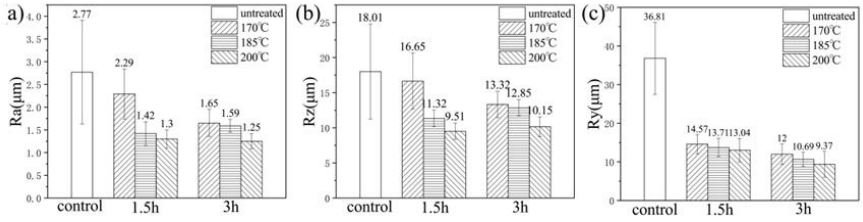

Fig. 5: Surface roughness of rubberwood (after sanding): (a) R_a, (b) R_z, and (c) R_y.

Glossiness

Changes in glossiness parameters (GZL and GZT) of the untreated control group and the treatment group are presented in Fig. 6 (before sanding) and Fig. 7 (after sanding). As shown in Fig. 6 and Fig. 7, the results show that the values of GZL and GZT increased with increasing treatment temperature and time no matter before or after sanding. The glossiness values of the treatment group were higher than those of the untreated control group. While the highest value

of glossiness is found in the specimens treated at the highest temperature (200°C) and the longest time (3 h). A typical finding for glossiness measurements for all specimens is that glossiness values, when measured along the grain, are higher than those measured across the grain. This can be explained by the anatomical structure on the surface of wood. The wood texture is parallel to the long axis of the cell. Then when the light ray enters along the grain, part of the light is refracted from inside the cell along the long axis of the cell, and the other is refracted along the outer wall of the cell. When light enters the vertical texture, the inner diameter of the cell is much smaller than its length. Thus the light is blocked by the inner wall of the cell (He et al. 2016).

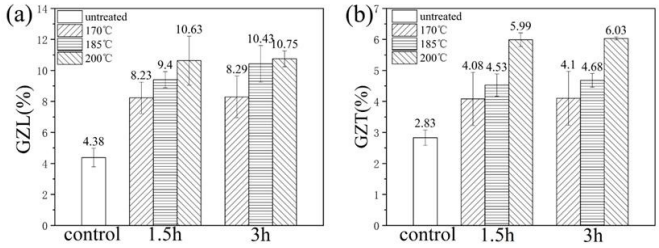

Fig. 6: Surface glossiness of rubberwood (before sanding): (a) GZL, and (b) GZT.

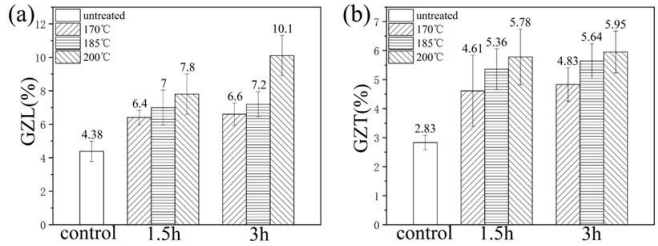

Fig. 7: Surface glossiness of rubberwood (after sanding): (a) GZL, and (b) GZT.

Other studies reported that the glossiness values of heat-treated wood specimens decreased with increasing treatment duration and temperature (Ahmet 2011). This can be explained that heat treatment was combined with wood densification in this study compared with previous studies where only wood heat treatment was applied. Wood compression was the main reason for improving the glossiness of the wood surface. The main reason for the increased glossiness of the wood surface was that the wood was compressed (Bekhta et al. 2014).

Obviously, the natural characteristics of wood have an influence on surface roughness and further on glossiness properties. Smaller roughness values correspond to higher gloss values. The reason is that the increasing roughness means more complex surfaces, and lead to the light scattering more irregular.

CONCLUSIONS

This study investigated the influences of heat treatment by hot pressing on the surface properties of rubberwood. The results showed that the values of contact angle and glossiness

increased slightly, and the color of wood changed darker significantly. The values of roughness decreased slightly with increasing heat treatment temperature and duration. The maximum value of roughness was obtained as the samples heat-treated at 200°C for 3 h. The heat-treated rubberwood with a warm tone is suitable for some applications. Further research is also needed to establish the quantitative relationships among color, roughness, glossiness and coatings of thermally modified wood.

ACKNOWLEDGEMENT

The authors are very grateful that this research was financially supported by the Guangdong government science and technology project (Grants No.2017A050501030) and the National Natural Science Foundation of China (Grant No. 31770601).

REFERENCES

1. Ahmet, A.M.D., Ergun, B., Hilmi, T., 2011: Colour and gloss changes of Socts pine after heat modification. Wood Research 56(3): 329-336.
2. Aleš, U., Kamke, F.A., Sernek, M., Pavlič, M., Kutnar, A., 2013: The wettability and bonding performance of densified VTC beech (*Fagus sylvatica* L.) and Norway spruce (*Picea abies* L. Karst.) bonded with phenol–formaldehyde adhesive and liquefied wood. European Journal of Wood and Wood Products 71(3): 371-379.
3. Ayrilmis, N., Kariz, M., Kwon, J.H., Kitek, K.M., 2019: Surface roughness and wettability of surface densified heat-treated Norway spruce (*Picea abies* L. Karst.). Drvna industrija 70(4): 377-382.
4. Aytin, A., Korkut, S., 2015: Effect of thermal treatment on the swelling and surface roughness of common alder and wych elm wood. Journal of Forestry Research 27(1): 225-229.
5. Bekhta, P., Proszyk, S., Krystofiak, T., Mamonova, M., Pinkowski, G., Lis, B., 2014: Effect of thermomechanical densification on surface roughness of wood veneers. Wood Material Science & Engineering 9(4): 233-245.
6. Bekhta, P., Proszyk, S., Lis, B., Krystofiak, T., 2014: Gloss of thermally densified alder (*Alnus glutinosa* Goertn.), beech (*Fagus sylvatica* L.), birch (*Betula verrucosa* Ehrh.), and pine (*Pinus sylvestris* L.) wood veneers. European Journal of Wood and Wood Products 72(6): 799-808.
7. Cademartori, P.H., Missio, A.L., Mattos, B.D., Gatto, D.A., 2015: Effect of thermal treatments on technological properties of wood from two *Eucalyptus species*. Anais Da Academia Brasilra De Ciências 87(1): 471-481.
8. Cai, S., Zhang, N., Li, K., Li, Y., Wang, X., 2019: Effect of pressurized hot water treatment on the mechanical properties, surface color, chemical composition and crystallinity of pine wood. Wood Research 64(3): 389-400.
9. Cheng, R., Chen, T., Luo, P., Luo, X., 2017: Effects of painting on color and gloss of modified rubberwood. Journal of Southwest Forestry University 37(4): 194-198.
10. Ding, T., Peng, W., Li, T., 2017: Mechanism of color change of heat-treated white ash wood by means of FT-IR and XPS analyses. Journal of Forestry Engineering 2(5): 25-30.

11. Diouf, P.N., Stevanovic, T., Cloutier, A., Fang, C.H., Blanchet, P., Koubaa, A., Mariotti, N., 2011: Effects of thermo-hygro-mechanical densification on the surface characteristics of trembling aspen and hybrid poplar wood veneers. Applied Surface Science 257(8): 3558-3564.
12. Du, C., Tu, D., Lao, Y., Yang, S., Zhen, F., 2013: The experiment on hot pressing process for thermally treated *Populus tomentosa* Carr. lumber. China Forestry Science and Technology 27(6): 105-107.
13. Esteves, B., Marques, A.V., Domingos, I., Pereira, H., 2008: Heat-induced colour changes of pine (*Pinus pinaster*) and eucalypt (*Eucalyptus globulus*) wood. Wood Science & Technology 42(5): 369-384.
14. He, T., Luo, J., 2016: Study on the color and luster of twenty species of rosewood. Journal of Forestry Engineering 1(2): 44-48.
15. Jiang, H., Lu, Q., Li, G., Li, M., Li, J., 2019: Research progress in thermal modification of rubber wood. Chinese Journal of Tropical Agriculture 39(4): 93-97.
16. Jie, G., Kim, J.S., Terziev, N., Cuccui, I., Daniel, G., 2018: Effect of thermal modification on the durability and decay patterns of hardwoods and softwoods exposed to soft rot fungi. International Biodeterioration & Biodegradation 127: 35-45.
17. Korkut, S., Aytin, A., 2015: Evaluation of physical and mechanical properties of wild cherry wood heat-treated using the thermowood process. Maderas. Ciencia y tecnología 17(1): 171-178.
18. Li, X., Cai, Z., Fu, F., Qiao, J., Liu, Y., Yuan, G., 2011: Effects of high temperature thermal treatment on color and wettability of *Pseudotsuga menziesii* wood. Journal of Central South University of Forestry & Technology 31(8): 178-182.
19. Li, X., Li, M., Qin, S., Li, J., Lin, W., 2012: Biological durability of heat-treated rubber wood. Scientia Silvae Sinicae 48(4): 108-112.
20. Qin, Z., Liao, M., Zhang, Y., Sun, J., 2019: Wood interface and surface wettability based on contact angle method. Journal of Beihua Univesity 20(2): 249-255.
21. Ratnasingam, J., Ioras, F., 2012: Finishing characteristics of heat treated and compressed Rubberwood. European Journal of Wood and Wood Products 71(1): 135-137.
22. Shukla, S.R., Sharma, S.K., 2014: Effect of high temperature processing under different environments on physical and surface properties of rubberwood (*Hevea brasiliensis*). Journal of the Indian Academy of Wood Science 11(2): 182-189.
23. Srinivas, K., Pandey, K.K., 2012: Effect of heat treatment on color changes, dimensional stability, and mechanical properties of wood. Journal of Wood Chemistry and Technology 32(4): 304-316.
24. Sun, B., Wang, Z., Liu, J., 2019: Study on color and surface chemical properties of *Eucalyptus Pellita* wood subjected to thermo-vacuum treatment. Wood Research 64(1): 01-12.
25. Unsal, O., Ayrilmis, N., 2005: Variations in compression strength and surface roughness of heat-treated Turkish river red gum (*Eucalyptus camaldulensis*) wood. Journal of Wood Science 51(4): 405-409.
26. Yildiz, S., Gezer, E.D., Yildiz, U.C., 2006: Mechanical and chemical behavior of spruce wood modified by heat. Building and Environment 41(12): 1762-1766.
27. Yu, L.L., Tang, Z.Z., Cao, J.Z., Yan, L., 2010: Properties of blue-stain Masson pine after compression and thermal modification. Advanced Materials Research 160-162: 1199-1204.
28. Zhao, X., Tu, D., Chen, C., Zhou, Q., 2019: Prediction of the mechanical properties of thermally-modified rubber wood on the basic of its surface characteristic. Wood Research 64(1): 25-34.

29. Zhou, Q., Chen, C., Zhao, X., Tu, D., Li, K., 2019: The effect of thermal modification by hot pressing on the some physical and mechanical properties in rubberwood (*Hevea brasiliensis*). Wood Research 64(2): 361-372.

Zhipeng Zhu, Dengyun Tu*, Ziwei Chen, Chuanfu Chen,
Qiangfang Zhou
South China Agricultural University
College of Materials and Energy
Guangzhou
China
*Corresponding author: tudengyun@scau.edu.cn

WOOD RESEARCH
66 (1): 2021
141-152
doi.org/10.37763/wr.1336-4561/66.1.141152

STUDY ON LAMB WAVE PROPAGATION CHARACTERISTICS ALONG THE GRAIN OF THIN WOOD SHEET

Minghua Wang, Ming Li, Tingting Deng, Saiyin Fang, Xiaosong Li, Fei Lai
Southwest Forestry University
China

(Received April 2020)

ABSTRACT

Through the time-frequency analysis of the propagation waveform of the acoustic emission (AE) signal propagating in the thin sheet of *Pinus sylvestris* var. mongolica, the propagation characteristics of the stress wave when propagating as a lamb wave was studied. An AE source was generated on the surface of the specimen, the discrete wavelet transform method was used to achieve AE signal de-noising and reconstruct the waveform of the AE signal. On this basis, the time difference positioning method was used to calculate the propagation velocity of lamb waves, and compared with the propagation characteristics of lamb waves in the metal specimen. The results show that the high-frequency mode of lamb waves attenuated sharply as they propagate in the thin wood sheet, indicating that the microstructure of wood has a significant low-pass characteristic for lamb waves. The average attenuation rates of lamb waves in metal and thin wood sheet were 87.1% and 75.7%, and the velocity was 4447.0 $m \cdot s^{-1}$ and 1186.3 $m \cdot s^{-1}$, respectively. This shows that AE signals can travel longer distances in the thin wood sheet, but the propagation velocity is significantly reduced.

KEYWORDS: Wood, acoustic emission, lamb wave, propagation characteristics, discrete wavelet transform.

INTRODUCTION

In thin plate members, stress waves propagate mainly in the form of lamb waves. Lamb wave is essentially a special form of stress waves formed by multiple couplings of longitudinal and transverse waves in a plate and have a strong ability to propagate, so they are mainly used for health monitoring of thin plate structures (Ai et al. 2012, Jiang et al. 2016). Using lamb waves to detect defects in plate-shaped structural parts has been one of the research hotspots in the field of active detection technology (Zhang et al. 2008, Wang et al. 2018).

Hou (2009) and Chen et al. (2011) used lamb waves to effectively identify the surface defects of aluminum plates. Chen et al. (2019) found that lamb wave images based on time inversion can intuitively reflect the damage location and defect shape of carbon fiber composite laminates. In order to achieve effective detection of near-field defects in aluminum thin plates, Zhang et al. (2019) proposed a method combining Green's function inversion theory with lamb wave array imaging. Gao et al. (2018) proposed a smooth Capon algorithm to estimate the exact path length of wave packets for the problem of low resolution of defect detection caused by lamb wave dispersion. Soleimanpour et al. (2016) studied the scattering behavior of lamb waves at cracks in aluminum plates and found that the scattering characteristics of A0 mode lamb waves are closely related to the size and direction of the notches. Han et al. (2015) proposed a time-frequency beam detection method based on lamb waves to achieve effective localization of structural defects in aluminum plates. For structural defect location, Yu et al. (2012) proposed a hyperbolic location algorithm. Lee et al. (2007a,b) used the amplitude attenuation and transmission time difference of lamb waves to characterize the degree of damage to the material structure and achieve defect localization. These studies have effectively promoted the development of AE technology based on stress wave analysis in the field of metal detection. In addition, the AE technology has also been applied to the study of damage detection of wood materials, such as the mechanical properties of wood under external load (Niemz et al. 2009, Krauss et al. 2011), classification and performance prediction of thermally modified wood (Nasir et al. 2019a, 2019b), identification defects of wood materials (Sun et al. 2008, 2013), etc. However, up to now, the research on lamb wave focuses more on isotropic materials such as aluminum plates, while the research on typical anisotropic materials such as wood, which is widely used, is relatively rare.

Wooden board is a common complex biomass material with the characteristics of both composite materials and porous materials, and its physical properties in all directions are significantly different (Zhao et al. 2011). Using the AE technique to study the propagation characteristics of lamb waves in specific directions on boards without damage defects and to investigate the effectiveness of the technique in this application will help to extend the application of the AE technique to active damage monitoring. In addition, this can lay a theoretical foundation for the future use of guided waves for defect detection in wooden boards. At present, the most common parameters used to characterize the structural changes of a plate using stress waves are time-frequency characteristics, AE wave velocity, AE energy, and so on. Therefore, this paper takes *Pinus sylvestris* sawn timber as the research object and explores the time-frequency characteristics and propagation law of lamb waves as they propagate along the grain direction of the wood. A 2-channel AE signal acquisition system based on NI high-speed acquisition equipment was used to obtain the original AE signal on the surface of the specimen, the discrete wavelet transform method and normalization process were used to reconstruct the AE signal waveform that was "submerged" in noise. Furthermore, according to the time-frequency characteristics of the reconstructed signal, the effect of the microstructure of the wood along the grain direction on the characteristics of the lamb wave signal was studied. Then used signal correlation analysis and time difference location methods to calculated the propagation velocity of lamb along the grain direction of the wood, and compared it with carbon steel of the same size to further studied the influence of wood microstructure on lamb wave propagation velocity and energy attenuation rate.

MATERIAL AND METHODS

Materials

In this paper, two sets of specimens were made using *Pinus sylvestris* sawn timber and Q235 carbon steel sheet respectively and tested independently. The size of both specimens was 580 × 55 × 4 mm. For carbon steel, the modified size refers to length, width and thickness respectively, and for wood it is axial, tangential and radial.

Based on NI USB-6336 high-speed acquisition card and Lab VIEW software to build a 2-channel AE signal acquisition platform, the maximum sampling frequency of each channel is 2 MHz. The existing research (Li et al. 2018, Shen et al. 2015) shows that the maximum frequency of AE signal of wood was approximately 200 kHz, in order to effectively collect the original AE signals with wide band distribution, the SR-150N single resonance AE sensor with a bandwidth of 22 kHz ~ 220 kHz was used. At the same time, a preamplifier with a gain of 40 dB was configured, and its response frequency is 10 kHz to 2 MHz. According to the Shannon sampling theorem, in order to restore the analog signal without distortion, the sampling frequency f_s and the maximum frequency f_{max} of the signal must satisfy $f_s \geq 2.f_{max}$, therefore, the sampling frequency of each channel was set to 500 kHz during the experiment.

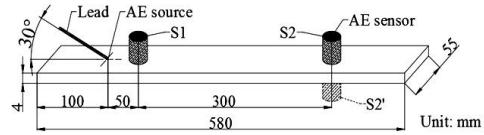

Fig. 1: AE sensor layout diagram.

Methods

An artificial AE source was generated by a pencil lead break at a position of 100 mm on the left end of the specimen. Sensors S1 and S2 were spaced 300 mm apart on the surface of the specimen. Among them, sensor S1 was placed 50 mm from the AE source (150 mm from the left end of the specimen), the sensor S2 adopted two arrangements of the same side (S2 of Fig. 1) and the opposite side (S2' of Fig. 1) with the sensor S1 to collected the AE signal on the surface of the specimen. In order to minimize the influence of the two sides of the specimen on the AE signal propagation, the AE source and the sensor were placed on the central axis in the width direction according to the above positions, as shown in Fig. 1. The experiment was divided into two groups, the first group was the *Pinus sylvestris* var. mongolica specimen and the second was the carbon steel metal plate specimen. The experimental operation refers to the American ASTM-E976 standard to ensure the consistency of the AE source during the experiment, that was, the 2H resin lead with a diameter of 0.5 mm was placed at an angle of 30° with the surface of the specimen, and it was broken at a distance of 2.5 mm from the contact point, to obtain original AE signals on the surfaces of both specimens. At the same time, in order to fully reduce the influence of the air medium on the experiment, high-temperature vacuum insulation silicone grease was filled between the specimen and the sensor. In addition, the sensor was fixed on the surface of the specimen with a rubber band.

The original AE signal contains a lot of noise signals. The discrete wavelet transform method has an excellent de-noising effect and time-frequency localization analysis ability, which can realize signal de-noising and reconstruct AE waveforms at the same time (Li et al. 2019, 2020). Therefore, this paper used the Daubechies wavelet as the discrete wavelet transform

basis function for the 5-level wavelet decomposition. In the original signal acquisition process, the sampling frequency f_s of each channel was 500 kHz, so the analysis frequency f_h of each channel was $f_h = f_s / 2 = 250$ kHz; after the 5-level wavelet decomposition, the frequency bands of the high-frequency detail signal of each level were (125 kHz, 250 kHz), (62.5 kHz, 125 kHz), (31.25 kHz, 62.5 kHz), (15.625 kHz, 31.25 kHz), (7.8125 kHz, 31.25 kHz), covering the entire measurement range of AE sensors.

The two-point time difference location and signal correlation analysis methods were used to calculate the propagation velocity of the AE signal. In the experiment, the two sensors were placed in a straight line at a fixed distance Δs = 300 mm. After measuring the time difference Δt that the reconstructed AE signal arrived at the two sensors using the cross-correlation function, the propagation velocity v of the AE signal on the surface of the specimen can be calculated according to the formula $v = \Delta s / \Delta t$. For two random signals $x(t)$ and $y(t)$, the cross-correlation function $R_{xy}(\tau)$ between them was defined as shown in Eq. 1:

$$R_{xy}(\tau) = \lim_{T \to \infty} \frac{1}{T} \int_0^T x(t) y(t+\tau) dt \quad (1)$$

The cross-correlation function can effectively reduce the influence of random factors in the AE signal. If $\tau = \tau 0$, the absolute value of the cross-correlation function is maximized, which means that after the random signal $y(t)$ was translated by τ_0 units on the time axis, the similarity with the random signal $x(t)$ reached the highest level. At this time, τ_0 was the time difference Δt when the AE signal reached the sensors S1 and S2.

RESULTS AND DISCUSSION

Characteristics of AE signals on the same side of the specimen

The AE source generated by artificially breaking the lead core was characterized by a significant signal mutation and a short duration, so the signal components that reflect the AE characteristics should appear in high-frequency detail part (Ju et al. 2018, 2019). According to the time-frequency characteristics of the signals of each level after decomposition, the detail signal of the second and third levels were selected to reconstruct the signal waveform. The waveform and spectrum of the reconstructed AE signal on the same side of the specimen as shown in Fig. 2.

In terms of time-domain waveform, in the *Pinus sylvestris* var. mongolica specimen (Fig. 2a), the signal amplitude of sensors S1 and S2 attenuates to a certain extent, which shows that the natural porous microstructure along the grain direction of wood has a certain obstruction on the AE beam. So the farther away from the AE source, the smaller the energy per unit area, and the lower the AE signal amplitude detected by the sensor. When the AE signal propagates in the thin plate specimen, the transverse and longitudinal waves were repeatedly reflected and overlapped to form a lamb wave, so the waveform appeared as a "wave packet", and the wave packet characteristic becomes more prominent as the propagation distance increases. Therefore, at the end of signal attenuation, the signal waveform detected by sensor S1 shows a small "wave packet" shape, and sensor S2 shows a large "wave packet" shape. In the carbon steel sheet specimen (Fig. 2c) the propagation medium of stress waves has a higher density, the internal friction of particles per unit area is much stronger than that of wood, and the energy consumption is larger, so AE signal not only has amplitude attenuation like that of wood but also shows the phenomenon that amplitude attenuation was more rapid and the degree of attenuation was larger.

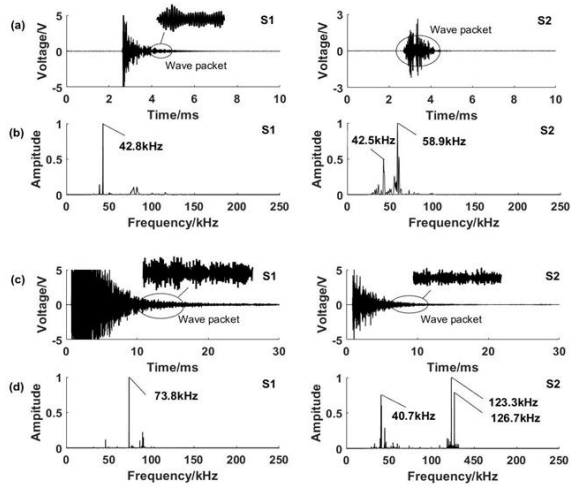

Fig. 2: Reconstructed signal waveform and spectrum on the same side of the specimen: (a) reconstructed signal waveform on the same side of Pinus sylvestris var. mongolica, (b) reconstructed signal spectrum on the same side of Pinus sylvestris var. mongolica, (c) reconstructed signal waveform on the same side of carbon steel, (d) reconstructed signal spectrum on the same side of carbon steel.

Comparing the time-domain waveform of the two materials (Fig. 2a,c), it was found that the "wave packets" of metal and wood were extremely different. The sensor S1 and S2 only show a small "wave packet" in the late stage of propagation attenuation when AE signal propagated in the metal plate, while the wave packet of the sensor S2 was more conspicuous than the sensor S1 when AE signal propagated in thin wood sheet. The reason is that the microstructure of wood is much more complex than that of metal, the interior of wood is full of cavities, the reflection of AE signal in it is relatively disordered, and there is also scattering caused by medium. Therefore, the formed lamb wave pattern is relatively complicated, and the signal waveform at different positions is greatly different. However, the metal's microstructure is relatively uniform, and the transverse and longitudinal wave have comparatively regular reflections, so there is no significant difference in the AE signal waveform between the two sensors except the amplitude attenuation caused by energy exchange.

Lamb wave is a special stress wave with multi-modal effects, and many different modes will be generated during the forward propagation. In the *Pinus sylvestris* var. mongolica specimen, the signal of the sensor S1 was distributed among a frequency band centered on 42.8 kHz, the sensor S2 had two distribution centers of 42.5 kH and 58.9 kHz, and the peak frequency was 58.9 kHz. Moreover, the spectral component of S2 was significantly more complicated than that of sensor S1. It means that the frequency of the main mode of the AE signal in the sensor S1 was 42.8 kHz, while in the sensor S2, the lamb wave undergoes a mode transition, and a variety of lamb waves of different modes were generated, and the frequencies of the main modes were 42.5 kH and 58.9 kHz. In the metal plate specimen, the central frequency of the main lamb wave mode in sensor S1 was 73.8 kHz, and there were other modes of lamb wave at a frequency band of 73.8 kHz as the distribution center. Similarly, the lamb wave's model changed during the propagation process, so the sensor S2 detected three lamb waves with different frequencies of 40.7 kHz, 123.3 kHz, and 126.7 kHz, respectively.

Comparing Fig. 2b and Fig. 2d, it can be seen that the degree of modal change of the lamb wave in the thin wood sheet was smaller than that of the metal, and only the middle and low-frequency lamb waves were generated during the propagation process. *Pinus sylvestris* var. mongolica is an anisotropic coniferous wood, and on the micro-scale, it is a porous material composed of hexagonal tracheids, which are mainly thin and long axial tracheids with striate holes in the longitudinal direction (Wittel et al. 2004). Such a microstructure makes it demonstrates a certain "selection" effect on the propagation band of lamb waves and is sensitive to high-frequency modal lamb waves. However, the microscopic composition of metal is relatively uniform, which has a small obstruction to the frequency band of lamb waves (in Fig. 2, the frequency band distribution of AE signal in the metal plate is wider than that in thin wood sheet). This "selection" effect determines that there were differences in the lamb wave's modal changes when the lamb wave propagates in wood and metal. In addition, the spectral composition is also related to the density of the material (Yang et al. 2007). The density of the metal plate is larger and the structure is regular. When the AE signal propagates in metal plate, the reflection of the stress wave is relatively regular in any direction. In addition to the anisotropy of the wood, which causes stress waves to be reflected more turbulently, there are also AE attenuation caused by changes in the medium. The difference in the form of stress wave propagation and the density of the medium also causes the difference in the spectral components.

Characteristics of AE signals on the opposite side of the specimen.

In order to further study the characteristics of the lamb wave, the discrete wavelet transform method was used to reconstruct the AE signal when the sensor was placed on the opposite side. The waveform and spectrum of the reconstructed AE signal were shown in Fig. 3.

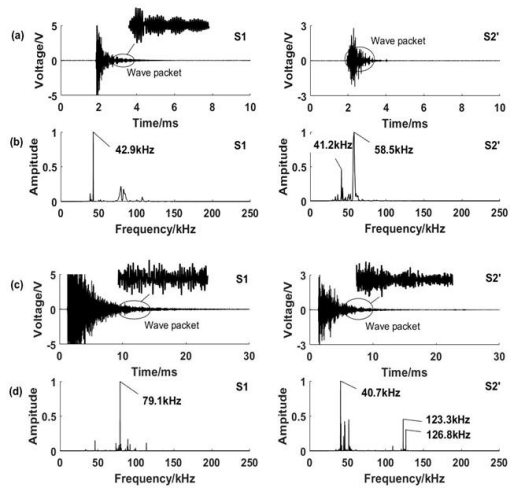

Fig. 3: Reconstructed signal waveform and spectrum on the opposite side of the specimen: (a) reconstructed signal waveform on the opposite side of Pinus sylvestris var. mongolica, (b) reconstructed signal spectrum on the opposite side of Pinus sylvestris var. mongolica, (c) reconstructed signal waveform on the opposite side of carbon steel, (d) reconstructed signal spectrum on the opposite side of carbon steel.

When the sensor was placed on the opposite side, due to the influence of the microstructure difference of the material itself, the AE signal has a larger energy loss in the metal plate, and the attenuation rates and the degree of the signal were more intense than those of the thin wood sheet. Moreover, the time-domain waveform of the signals collected by the two sensors in the metal plate has a certain similarity, but the time-domain waveform of the signals collected by the two sensors in the wood was tremendous differences. In the thin wood sheet (Fig. 3b), the frequency distribution center of the main mode of the lamb wave detected by the sensor S1 was 42.9 kHz. During the forward propagation process, the mode of the lamb wave has changed, resulting in the phenomenon that the lamb wave was distributed over the two frequency bands centered at 42.9 kHz and 58.59 kHz on the sensor S2'.As a result of the change of the Lamb mode in the metal plate (Fig. 3d), the center frequency of the main mode of the sensor S1 was 79.1 kHz, and the frequency centers of the three main modes of the sensor S2' were 40.7 kHz, 123.3 kHz, and 126.8 kHz. In addition, influenced by the physical characteristics of materials and the differences in reflected wave patterns, the frequency of the main lamb wave modes in thin wood sheet appeared in the low and medium frequency bands, and the mode change degree was smaller than that of metal.

Comparing with Fig. 2 and Fig. 3, it is not difficult to find a phenomenon: In the two samples, whether the sensor S2' was placed on the same side or on the opposite side of the specimen, there was no remarkable difference in the main mode of the lamb wave in the corresponding sensor. This is mainly because lamb wave is a two-dimensional body wave in nature, with small attenuation and long propagation distance compared with the three-dimensional body wave (Fan et al. 2011). Therefore, when the lamb waves propagate to the same location, their modes will not change obviously, no matter the upper side or lower side of the same position, the spectrum difference of the AE signal is small.

The propagation velocity of AE signals on the surface of the two specimens.

When calculating the propagation velocity and energy attenuation rate of AE signal, in order to minimize the effect of random errors on the experiment, 10 independent pencil lead broken tests were performed on the surface of the metal plate and the *Pinus sylvestris* var. mongolica specimen. Tab. 1 and Tab. 2 were the test results when the sensor was placed on the same side and the opposite side respectively.

Tab. 1: AE signal propagation velocity from S1 to S2.

Experiment number	***Pinus sylvestris* var.mongolica**			**Carbon steel**		
	Δt (us)	v (m·s^{-1})	η (%)	Δt (us)	v (m·s^{-1})	η (%)
1	276.0	1087.0	76.9	64.0	4687.5	84.8
2	292.0	1027.4	76.4	68.0	4411.8	87.8
3	224.0	1339.3	76.3	64.0	4687.5	83.6
4	210.0	1428.6	72.5	62.0	4838.7	89.8
5	224.0	1339.3	74.4	64.0	4687.5	79.2
6	276.0	1087.0	75.0	62.0	4838.7	84.6
7	224.0	1339.3	77.5	64.0	4687.5	88.5
8	274.0	1094.9	75.1	68.0	4411.8	84.0
9	250.0	1200.0	78.4	66.0	4545.5	83.9
10	276.0	1087.0	79.7	64.0	4687.5	85.4
Average value	252.6	1203.0	76.2	64.6	4648.4	85.2

Tab. 2: AE signal propagation velocity from S1 to S2'.

Experiment number	*Pinus sylvestris* var. mongolica			Carbon steel		
	Δt (us)	v (m·s^{-1})	η (%)	Δt (us)	v (m·s^{-1})	η (%)
1	290.0	1034.5	73.9	72.0	4166.7	85.0
2	234.0	1282.1	70.0	66.0	4545.5	90.2
3	288.0	1041.7	80.8	64.0	4687.5	87.5
4	232.0	1293.1	72.8	70.0	4285.7	84.2
5	234.0	1282.1	73.2	64.0	4687.5	90.7
6	234.0	1282.1	75.0	68.0	4411.8	82.8
7	288.0	1041.7	79.9	72.0	4166.7	84.6
8	234.0	1282.1	78.1	64.0	4687.5	86.2
9	288.0	1041.7	74.5	66.0	4545.5	89.8
10	234.0	1282.1	78.4	70.0	4285.7	89.6
Average value	255.6	1186.3	75.7	67.6	4447.0	87.1

In Tabs. 1 and 2: Δt - the time difference of propagation of the AE signal; v - the propagation velocity; η - the energy attenuation rate.

According to Tab. 1, when the sensors S1 and S2 were placed on the same side of the specimens, the average propagation velocity and the average energy attenuation rate of the AE signals along the texture direction of *Pinus sylvestris* var. mongolica are 1203.0 m·s^{-1} and 76.2% respectively, while in the metal sheet, the average propagation velocity of the AE signal is 4648.4 m·s^{-1}, and the average energy attenuation rate is 85.2%. The propagation velocity and energy attenuation of AE signals in the metal specimen was greater than those in the wood specimen. This is because the density of the metal plate is large and the number of particles per unit area is larger, so there is a large energy exchange between the lamb wave and the medium when it propagates in it, and only a large energy loss can be used to ensure the propagation velocity of the stress wave. In addition, the differences in the microstructure of the specimens also result in that the propagation mode of AE wave in the thin wood sheet was more intricate than that in the metal specimen, including lamb waves and a small part of scattering waves caused by complex internal boundaries. However, the AE wave in the metal plate is transmitted in the form of a purer lamb wave than the thin wood sheet. The difference in the AE waveform is also one of the reasons for the difference in the propagation velocity and energy attenuation of the AE signal in the two specimens.

When the sensor was placed on the opposite side of the specimens (Tab. 2), it was also due to the differences in the materials and the different AE waveform, the average propagation velocity and the average energy attenuation rate of the AE signal in the thin wood sheet are 1186.3 m·s^{-1} and 75.7% respectively, while in the metal sheet, the average propagation velocity of the AE signal is 4447.0 m·s^{-1}, and the average energy attenuation rate is 87.1%. Comparing with Tabs. 1 and 2, it can be seen that in the same specimen, no matter how the sensor was placed, there was no prominent difference in the propagation velocity and energy attenuation of signal. This also shows that the AE wave propagates forward in the form of lamb waves on the plate, so the same position of the same specimen, the signal's components, propagation velocity, and energy attenuation of the upper and lower sides of the specimens will not be greatly different.

CONCLUSIONS

This paper refers to the ASTM-E976 standard to generated an AE source, and studies the propagation characteristics of AE signals in two typical materials, and explores the differences in spectral characteristics and propagation velocity of lamb waves when it propagated in wood and metal. Preliminary explorations have shown that the AE technique based on lead core fracture is capable of being used to study the propagation characteristics of Lamb waves in wooden boards. Affected by the physical properties of the material, the propagation form of the AE signal is extremely complicated when it propagates in the thin wood sheet, which includes lamb waves and scattered waves caused by the discontinuous interface in the interior of the wood. So the time-domain waveform at different locations were significantly different. In the metal plate, the AE signal propagates in the form of lamb waves, so in addition to amplitude attenuation, the time-domain waveform at different locations have certain similarities.

The lamb waves will produce a variety of signal components in dissimilar modes during the propagation process, which results in the complexity of the signal's spectrum components and appear multiple distribution centers with an increase of the propagation distance. The interior structure of wood has a strong resistance to the high-frequency modes of lamb waves, and the reflection of stress waves in them is relatively chaotic. However, the metal plate has a uniform structure and has a small obstruction to each frequency band of the AE signal, and the boundary reflection is relatively regular. As a result, the lamb wave has a relatively small modal change in the thin wood sheet compared with the metal and only produces lamb waves at the low and middle frequency bands.

The crystals inside the metal plate are compactly arranged, and the vibration between particles in unit area is stronger than that of wood. Therefore, when Lamb propagates in it, it gets a higher propagation velocity in the form of higher energy consumption. However, the structure of the wood is relatively loose, and there are cavities and micro-discontinuous interfaces inside, which will cause some scattering of the stress wave. As a result, the lamb wave uses a lower energy consumption and a smaller propagation velocity to ensure that the signal can achieve a longer distance spread. Lamb wave is essentially a two-dimensional body wave and has a strong ability to propagate, so there is no predominant difference in signal components, propagation velocity, and energy attenuation between the upper and lower sides of the same material at the same location of the same specimen.

In this paper, the AE characteristics of the lamb wave propagating along the direction of the wood grain were initially explored. However, as a typical anisotropic material, wood has significant differences in mechanical properties in all directions. Therefore, using AE technology to further study the acoustic characteristics of wood in other directions has clear practical significance for the rational use of wood. Based on this study, the effect of wood anisotropy on AE signal propagation characteristics can be further explored in the future.

ACKNOWLEDGMENTS

The authors are grateful to the National Natural Science Foundation of China (NO: 31760182, NO: 31100424) and Department of Education of Yunnan Provincial (NO: 2017ZZX215, NO: 2020Y0376, NO: 2021J0156, NO: 2021J0158, NO: 2021Y224) for funding this research.

REFERENCES

1. Ai, C.A., Wang, X.Y., Liu,Y., 2012: Ultrasonic detection of lamb wave stimulation and modal analysis of thin steel plate structure. Noise and Vibration Control 32(1): 137-140.
2. Cao, X., Zeng, L., Lin, J., Hua, J.D., 2018: Improving the resolution for lamb wave testing via a smoothed Capon algorithm. Measurement science and Technology 29(4): 1-26.
3. Chen, J., Li, Z.H., Lin, L., Hou, Y.X., Ma, Q.J., 2011: Experiment investigations of lamb waves in an aluminum plate. Applied Acoustics 30(2): 98-104.
4. Chen, Y., Zhang, B.Y., Wu, X., Chen, G., Shi, W.Z., 2019: Air-coupled lamb waves imaging for impact damage of CFRP plates based on the time reversal damage index. Failure Analysis and Prevention 14(01): 5-11.
5. Fan, S.B., Yan, X.Q., Fu, M.F., Xie, Z.L., Yu, L., 2011: The research on locating method of acoustic emission source based on the dispersive characteristics of lamb wave in sheet. Chinese Journal of Solid Mechanics (S1): 283-287.
6. Han, J.H., Kim, Y.J., 2015: Time–frequency beam forming for nondestructive evaluations of plate using ultrasonic Lamb wave. Mechanical Systems & Signal Processing 54-55: 336-356.
7. Hou, Y.X., Chen, J., Lin, L., 2009: Mode identification and application for nondestructive evaluation of thin aluminum sheet by lamb waves. Nondestructive testing 31(7): 517-519.
8. Jiang, Y,D., Zhang, L.W., Yang, G.B., 2016: Load localization method for a metallic plate based on lamb wave. Nondestructive Testing 38(4): 26-30.
9. Ju, S., Li, X.C., Luo, T.F., Li, M., 2018: Characteristics of acoustic emission signals on the surface of Masson pine glulam with wavelet analysis method. Journal of Northeast Forestry University 46(08): 86-92.
10. Ju, S., Li, X.C., Luo, T.F., Li ,M., 2019: Anisotropic propagation of acoustic emission signal on surface of *Pinus massoniana* Lamb. glulam. China Forestry Science and Technology 4(2): 54-59.
11. Krauss, A., Kudela, J., 2011: Ulrasonic wave propagation and Young's modulus of elasticity along the grain of Scots pine wood (*Pinus sylvestris* L.) varying with distance from the pith. Wood Research 56(4): 479-488.
12. Lee, B.C., Staszewski, W.J., 2007a: Lamb wave propagation modelling for damage detection (I): two- dimensional analysis. Smart Materials and Structures 16(2): 249-259.
13. Lee, B.C., Staszewski, W.J., 2007b: Lamb wave propagation modelling for damage detection (II): Damage monitoring strategy. Smart Materials and Structures 16(2): 260-274.
14. Li, X.C., Ju, S., Luo, T.F., Li, M., 2019: Influence of adhesive layer at Masson pine glulam on acoustic emission signal propagation characteristics. Journal of Northwest Forestry University 34(3): 185-190.
15. Li, X.C., Ju, S., Luo, T.F., Li, M., 2020: Effect of moisture content on propagation characteristics of acoustic emission signal of *Pinus massoniana* Lamb. European Journal of Wood and Wood Products 78: 185-191.
16. Li, Y., Luo, T.F., Yu, S.S., Shen, L.J., Li, M., 2017: Signal propagation characteristics of acoustic emission and douglas fir glulam beams. Journal of Northwest Forestry University 32(5): 197-201.
17. Nasir, V., Nourian, S., Avramidis, S., Cool, J., 2019a: Stress wave evaluation for predicting the properties of thermally modified wood using neuro-fuzzy and neural network modeling. Holzforschung 73(9): 827–838.

18. Nasir, V., Nourian, S., Avramidis, S., Cool, J., 2019b: Stress wave evaluation by accelerometer and acoustic emission sensor for thermally modified wood classification using three types of neural networks. European Journal of Wood and Wood Products 77(1): 45-55.
19. Niemz, P., Brunner A.J., Walter O., 2009: Investigation of the mechanism of failure behaviour of wood based materials using acoustic emission analysis and image processing. Wood Research 54(2): 49-62.
20. Shen, K.N., Zhao, H.L., Ding, X.C., Li, M., 2015: Wavelet analysis of acoustic emission signal in wood damage and fracture process. Journal of Henan University of Science & Technology (Natural Science) 36(3): 33-37.
21. Soleimanpour, R., Ng, C.T., 2016: Scattering of the fundamental anti-symmetric lamb wave at through-thickness notches in isotropic plates. Journal of Civil Structural Health Monitoring 6(3): 447-459.
22. Sun, J.P., Wang, F.H., Zhu, X.D., 2008: Application of wavelet-neural network in defect location non-destructive testing of MDF. Chinese Journal of Scientific Instrument 29(5): 954-958.
23. Sun, J.P., Hu, Y.C., Wang, F.H., 2013: Study on quantitative nondestructive test of wood defects based on intelligent technology. Chinese Journal of Scientific Instrument 34(9): 1955-1960.
24. Wang, G.P., Shi, Z., Wu, M.L., Wei, M., 2018: Experimental study on damage identification of thin plate structure based on lamb wave. Internal Combustion Engine & Parts 255(03): 56-58.
25. Wittel, F.K., Dill-Langer, G., Kroplin, B.H., 2004: Modeling of damage evolution in soft-wood perpendicular to grain by means of a discrete element approach. Computational Materials Science 32(3): 594-603.
26. Yang, H.M., Wang, L.H., 2007: Nondestructive testing of wood hole defect by ultrasonic spectrum analysis. Journal of Northeast Forestry University 35(8): 30-32.
27. Yu, L., Cheng, L., Su, Z., 2012: Correlative sensor array and its applications to identification of damage in plate-like structures. Structural Control & Health Monitoring. 19(8): 650-671.
28. Zhang, H., Zhang, H,Y., Xu, M.Y., Fan, G.P., Zhu, F.W., Chai, X.D., 2019: Lamb waves topological imaging combining with Green's function retrieval theory to detect near filed defects in isotropic plates. Chinese Physics B 28(07): 290-296.
29. Zhang, H.P., Zhu, C.H., 2008: Study of propagational characteristics of lamb wave. Metrology & Measurement Technology 28(5): 5-9.
30. Zhao, R.J., Chen, X.B., Sun, J., Wang, X.Q., Fei, B.H., 2011: Study on the longitudinal tensile strength of the tracheids of soft wood. Journal of Anhui Agricultural University 38(4): 491-495.

Minghua Wang, Ming Li*, Tingting Deng, Xiaosong Li
Southwest Forestry University
School of Machinery and Transportation Engineering
Kunming 650224
China
*Corresponding author: swfu_lm@swfu.edu.cn

WOOD RESEARCH
66 (1): 2021
153-160

doi.org/10.37763/wr.1336-4561/66.1.153160

ANALYSIS OF CUTTING FORCE IN THE PROCESS OF CHIPLESS FELLING WOOD

Pavol Harvánek, Ján Kováč, Ján Melicherčík
Technical University in Zvolen
Slovak Republic

(Received June 2020)

ABSTRACT

This study compared the magnitude of the value of the cutting force using different tools with different thickness for different wood species with the same size. Measurements were made on wooden samples of spruce, aspen, and beech wood with dimensions 30 × 30 × 200 mm (w × d × h). The tearing machine pushed knives with dimension 150 × 100 mm and thicknesses of 4, 6, 8, and 10 mm with a 30° angle of cutting edge into the wood samples in a direction perpendicular to the fiber growth. Research shows that this angle of cutting edge is most effective for chipless cutting. The results were analysed by the Statistica 12 software. From the measurement results, for chipless wood felling is most preferred the 10 mm cutting knife thickness.

KEYWORDS: Chipless cutting, cutting force, tearing machine, transverse cutting, chipless felling wood.

INTRODUCTION

Wood chipless cutting is understood as a technological process by which a single-wedge knife operates to obtain a desired shape of the wood. Wood is split into smaller parts without the generation of waste in the form of chips (Koreň 1983). Chipless cutting in the forest harvesting process is mainly used by machines intended for tree delimbing (Hatton et al. 2015, Hatton et al. 2017). However, more often, chipless cutting of wood is used in chipless cutting heads in single-operation machines performing only the tree cutting. They are included in machine assemblies together with processors. These machine assemblies are able to further process sawn wood into chips for cellulose industry, oriented strand boards' production, but mainly for products of bioenergy because currently renewable energy sources are one of the most prevalent topics in the environmental industry (Jylha and Bregstorm 2016, Nathan and Hanzelka 2016, Stochlová et al. 2019).

Especially in older types of chipless cutting heads, a knife cutting device with one fixed and the other movable knife, or with two moving floating knives, can be used to maximize 25 cm log cutting (Kováč et al. 2017). Chipless cutting heads are used to cut logs up to 30 cm in diameter.

During the cutting process, hydraulic control gripping arms push the trunk into the cutting knife. The principle of a chipless cutting head is based on pushing the cutting wedge (cutting tool) into the trunk in a transverse direction to the fiber growth (Fig. 1). The longitudinal cutting is directly used for wood splitting (Minárik et Hricová 2015, Pichler et al. 2018, Wegener et Wegener 2013, Kováč et al. 2014)

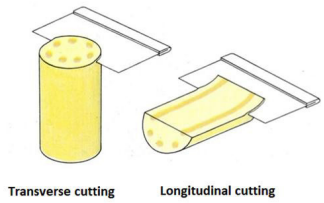

Fig. 1: Transverse cutting section.

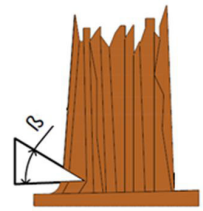

Fig. 2: Chipless cutting scheme β- cutting wedge angle.

Chipless wood cutting is defined as the penetration of the cutting tool into the wood in the direction perpendicular to the growth of the fibers. Chipless cutting of wood with a knife is based on the ability of wood to deform. The wood shows a relatively small deformation resistance when pushing the wedge into it. When pushing a cutting tool into the wood, the cutting edge interrupts the bonding between the fibers, leaving no waste chips and a cutting gap is equal to zero (Marko and Holík 2000). An illustration of a basic schematic of a chipless cutting by a single-action flat knife is shown in (Fig. 2).

MATERIAL AND METHODS

Measurements were conducted with a tearing machine Testometric M500-100CT operating with a force up to 100 kN, with cutting speed 50 mm·min^{-1} (Testometric Co., Ltd., Rochdale, England), an evaluation device (WinTestTM Analysis, Labor machine s.r.o, Opava, Czech Reublic), and a sample material from spruce (*Picea abies*), beech (*Fagus sylvatica*) and aspen wood (*Populus tremula*) from University Forestry Enterprise of Technical University in Zvolen, Slovakia. The results from the WinTest^{TM} software were processed in the Statistica 12 statistical software from TIBCO Software Inc., Palo Alto, CA, USA.

The tearing machine Testometric M500-100CT was equipped with a gripping tool. Cutting knives with different thickness were inserted into the gripping tool. The strength class 12.9 cylindrical head screws were used to fix cutting knives into the gripping tool. The gripping tool used for measurements is shown in (Fig. 3).

Steel 19 191 (STN 41 9191) or DIN C105W1 (Slavia Steel s.r.o, Rimavská Sobota, Slovakia) was used for cutting knives. Steel 19 191 is suitable for smaller-shaped cutting tools for wood, rubber, and plastics. The mechanical properties of steel are described in Tab. 1. Steel 19 191 is suitable for use in mowing machines but also for use in the cutting process due to high hardness and wear resistance (Falat et al. 2019, Kalincová et al. 2018, Ťavodová et al. 2106).

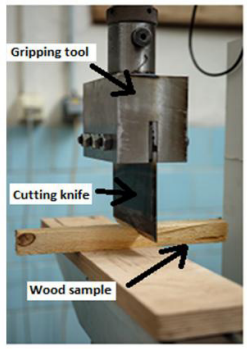

Fig. 3: Gripping tool for cutting knifes.

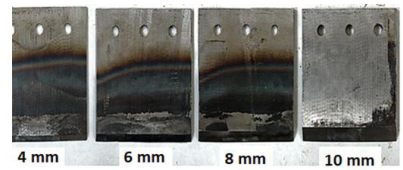

Fig. 4: Types of cutting knifes with different thickness.

Tab. 1: Mechanical properties of DIN C105W1 steel.

Parameter	Value	Units
Young's modulus	200000 to 200000	MPa
Tensile strength	650 to 880	MPa
Elongation	8 to 25	%
Fatigue	275 to 275	MPa
Yield strength	350 to 550	MPa

For this research, four knives were made. Cutting knives are flat, single acting knives with a thickness of s = 4, 6, 8, and 10 mm and a cutting edge angle β = 30°. According to Johansson (1996), Hirai et al. (1996), Marko (1996), this cutting edge angle is the most effective. The cutting edge of the cutting knife was quenched and tempered to the 56 HRC. The knives that were used for the experimental measurement are shown in (Fig. 4).

Measurements were made on wood samples from spruce wood, beech wood, and aspen wood with dimensions of 30 × 30 × 200 mm (w × d × h).

RESULTS

The criteria used for the analysis was the maximum force required to cut the wood sample in a direction perpendicular to the growth of the tree fibers. For each tree sample, a graph of 95% confidence interval for mean values of cutting force depending on knife thickness was produced separately where it was possible to separately observe the amount of cutting force for each cutting knife thickness. A similar measurement theory was used by Kováč et al. (2014), Kuvik et al. (2017, 2018) and Krilek et al. (2015). Fig. 5 shows the varying magnitude of the cutting force for the cutting knife with different thickness in spruce wood. The smallest cutting force occurred when the 4 mm thick cutting knife was used.

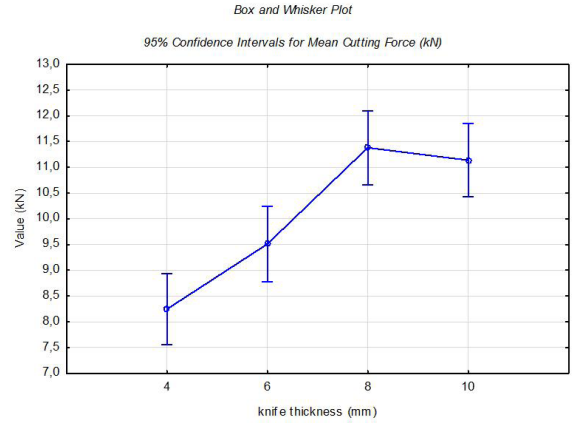

Fig. 5: Graph of 95% confidence intervals for mean values of cutting force depending on knife thickness for spruce wood.

However, at this thickness, the strength of the knife decreased, and use in practice would not meet the economical and safety requirements. The largest cutting force was achieved at an 8 mm thickness. The cutting force reduced for the cutting knife with 10 mm thickness compared to the 8 mm cutting knife. Based on these observations, it is advantageous to use a 10 mm-thick cutting knife for felling spruce wood due to the smaller cutting strength and greater knife strength.

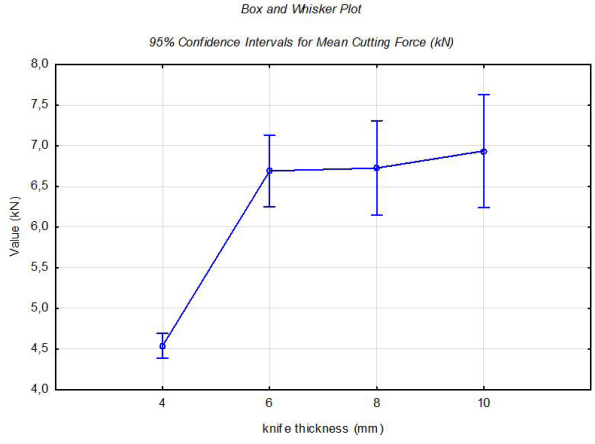

Fig. 6: Graph of 95% confidence intervals for mean values of cutting force depending on knife thickness for aspen wood.

It is evident from (Fig. 6) that the smallest cutting force was measured with the 4 mm knife, but it is interesting that there was not a large difference in the size of the cutting force between the cutting knives with 6 mm and 10 mm thickness. The difference between the 6 mm and 8 mm cutting knife was not statistically significant.

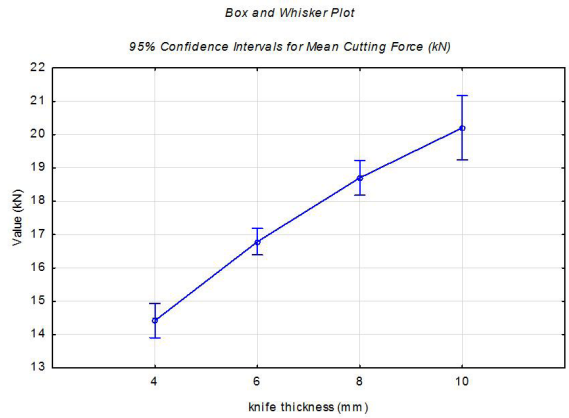

Fig. 7: Graph of 95% confidence intervals for mean values of cutting force depending on knife thickness for beech wood.

From (Fig. 7), the amount of cutting force for beech wood can be observed. The smallest cutting force was achieved using a 4 mm cutting knife. When using a 10 mm cutting knife, the maximum cutting force was achieved. It is preferable to incline to the cutting knife with a thickness of 10 mm despite a larger cutting force because of its increased resistance to damage. The research showed that the greatest cutting force was measured at a 10 mm-thick cutting knife, for this reason the use is inefficient in practice, but the strength of the cutting knife is best at a thickness of 10 mm. Therefore, from the perspective of the author, it is better to use a 10 mm cutting knife.

DISCUSSION

From the measurements according to (Fig. 8), it was found that the greatest forces were used to cut beech wood. These results are identical to that of Marko's (1996) study (Marko 1996). Furthermore, it was found that for a 10 mm knife, the beech and aspen samples increased the scattering of force value. Again, these results are similar to the study by (Marko 1996). Results from this study indicate that it is most advantageous to use a 10 mm thick cutting knife. The maximum cutting force for spruce wood was less with 10 mm knife than with the 8 mm knife. For the aspen samples, the difference in the cutting force was not significant for the 6 mm and 8 mm knife. Therefore, it is preferable to use the 10 mm cutting knife for its increased strength.

Based on a literature search Mikleš et al. (2012) say that the results of chipless cutting research showed that the cutting force when the knife penetrates into the wood initially increases linearly but then decreases to zero where the maximum cutting force corresponds to a knife penetration depth of 0.55 to 0.80 % diameter of the cut sample.

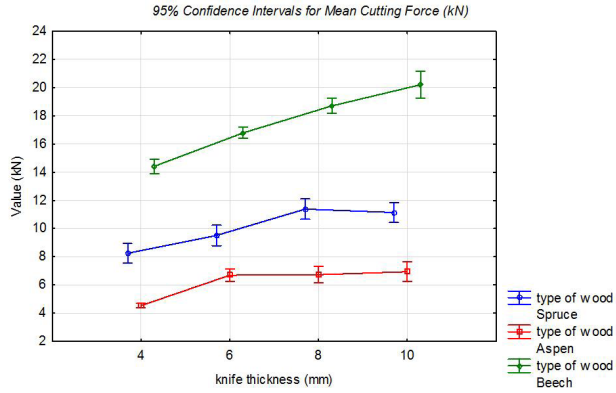

Fig. 8: Graphs of 95% confidence intervals for mean values of cutting force depending on knife thickness for spruce, beech and aspen wood.

However, this statement applies to wood samples of circular cross-section. In the case of our measurement, it was found that the maximum cutting force with 10 mm cutting knife for all samples was reached just before end of cutting the sample, which is also shown in Fig. 9. This statement is identical with the author (Melicherčík et al. 2020, Harvánek et al. 2019).

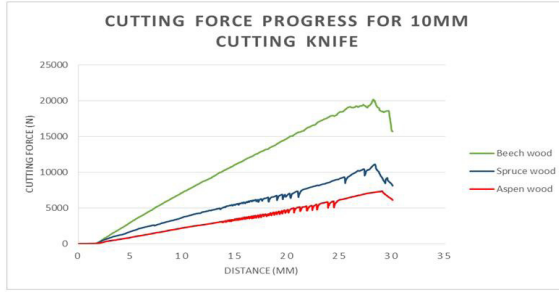

Fig. 9: Dependence of the cutting force on the distance of cutting knife.

CONCLUSIONS

Recently, when great emphasis is placed on the protection of the environment, the method of wood chipless cutting comes to the forefront. The purpose of this article was to determine the effect of the thickness of the cutting knife on the amount of cutting force required to cut the sample in a direction perpendicular to the fiber growth. Different wood samples of the same size were used for the experiment. From this analysis and experimental measurement, it has been shown that varying thickness of the cutting knife has a statistically significant effect on the size of the cutting force. The size of this cutting force is always different with the above-mentioned tree species. From the results of experimental measurement, it can be argued that for chipless wood cutting of spruce, beech or aspen It is best to use a 10 mm knife. The maximum cutting force for

spruce was 15.12 kN with 10 mm cutting knife compared to the 15.76 kN at 8 mm cutting knife. In case of aspen wood maximum cutting force was 11.39 kN for 10 mm knife thickness. In beech wood, the use of a 10 mm cutting knife is more advantageous mainly because of its strength, even if the cutting force is the highest.

ACKNOWLEDGEMENT

This article was created during the processing of the project VEGA no. 1/0642/18 "Analysis of the impact of structural parts of forestry mechanisms in the forest environment in terms of energy and ecology" and the project IPA 19/2020 “Research of the cutting mechanism of the cutting head in the area of chipless cutting of woody plants”.

REFERENCES

1. Falat, L., Džupon, M., Ťavodová, M., Hnilica, R., Ľuptáčiková, V., Čiripová, L., Homolová, V., Ďurišinová, K., 2019: Microstructure and abrasive wear resistance of various alloy hardfacings for application on heavy-duty chipper tools in forestry shredding and mulching operations. Materials 12(13): 1-16.
2. Harvánek, P., Kováč, J., 2019: Analysis of cutting forces in transverse cutting of spruce wood. In: Proceeding of XXI International conference of young scientists. Slovak University of Agriculture in Nitra, Faculty of Engineering, Pp 36-44.
3. Hatton, B., Bouzgarrou, J., Fauroux, V., Gagnol, V., Gogu, G., 2017: An approach for modelling harvester. Springer International Publishing AG, Pp 133-141.
4. Hatton, B., Pot, G., Bouzgarrou, B., Gagnol, V., and Gogu, G., 2015: Experimental determination of delimbing forces and deformations in hardwood harvesting. Croatian Journal of Forest Engineering 36(1): 43-53.
5. Hirai, T., Yoshida, S., Tsuchihashi, H., 1996:. Cutting performances of limbing knives of log harvesters. 1. Effect of wedge angles on cutting resistance of single-tapered knives. Journal of the Japan Wood Research Society 42(3): 258-263.
6. Johansson, J., 1996: Case studies on farm tractors as base machines for single-grip thinnings harvester heads. Forestry: An International Journal of Forest Research 69(3): 229–244.
7. Jylha, P., Bregstorm, D., 2016: Productivity of harvesting dense birch stands for bioenergy. Biomass and Bioenergy 88: 142-151.
8. Kalincová, D., Ťavodová, M., Jakubéczyová, D., 2018: Quality evaluation of the coatings and its influence on the wood machining tool wear. In Manufacturing Technology 18(4) : 578-584.
9. Koreň, J., 1983: Chipless wood cutting. Technical University in Zvolen, Slovakia, 105 pp.
10. Kováč, J., Krilek, J., Jobbágy, J., Dvořák, J., 2017: Technique and mechanization in forestry. Technical University in Zvolen, Slovakia, 354 pp.
11. Kováč, J., Krilek, J., Kučera, M., Barcík, S., 2014. The impact of design parameters of a horizontal wood splitter on splitting force. Drvna Industrija 65(4): 263-271.
12. Kováč, J., Krilek, J., Kučera, M., Barcík, Š., 2014: The impact of design parameters of a horizontal wood splitter on splitting force. Drvna industrija 65(4): 263-271.
13. Krilek, J., Kováč, J., Barcík, Š., Svoreň, J., Štefánek, M., Kuvik, T., 2015: The influence of chosen factors of a circular saw blade on the noise level in the process of cross cutting wood. Wood Research 61(3): 475-486.

14. Kuvik, T., Krilek, J., Kováč, J., 2018: Research of cutting mechanisms in cross-cutting of wood Technical University in Zvolen, Slovakia, 161 pp.
15. Kuvik. T., Krilek. J., Kováč. J., Štefánek. M., Dvořák. J., 2017: Impact of the selected factors on the cutting force when using a chainsaw. Wood Research 62(5): 807-814.
16. Marko, J., 1996. The issue of evaluation of cutting mechanisms for educational interventions. Technical University in Zvolen, Slovakia, 50 pp.
17. Marko, J., Holík, J., 2000: Theory of wood dividing. Technical University in Zvolen, Slovakia, 66 pp.
18. Melicherčík, J., Krilek, J., Harvánek, P., 2020: Simulation of stress and strain analysis on a delimbing knife with replaceable cutting edge. BioResources 15(2): 3799-3808.
19. Mikleš, J., Mikleš, M., 2012: Design of the chucking device logs of cutting mechanism cross-cutting line. In: Chip and Chipless Woodworking Processes 2012: 239-246.
20. Minarik, M., Hricova, J., 2015: Log splitter design and construction. Drvna Industrija 66(1): 11-16.
21. Nathan, C., Hanzelka, M., 2016. Productivity and costs of utilizing small-diameter stems in a biomass-only harvest. International Journal of Forest Engineering 27(1): 43-52.
22. Pichler, P., Leitner, M., Gruen, F., 2018: Evaluation of wood material models for the numerical assessment of cutting forces in chipping processes. In: Wood Science and Technology 52: 281-294.
23. Stochlová, P., Novotná, K., Costa, M., Rodrigues, A., 2019. Biomass production of poplar short rotation coppice over five and six rotations and its aptitude as a fuel. In: Biomass and Bioenergy 122: 183-192.
24. Ťavodová, M., Krilek, J., Perec, Andrzej - Kalincová, D., Kováč, J., 2016: Analysis of the wear of saw blade teeth and the proposal of methods of increasing their wear resistance. MM science journal 2016(05): 1287-1291.
25. Wegener, J., Wegener, T., 2013: Kinematics and geometry of helical chipping with cylindrical helical blades. Transactions of the ASABE 56(4): 1291-1297.

Pavol Harvánek*, Ján Kováč, Ján Melicherčík
Technical University in Zvolen
Faculty of Technology
Department of Environmental and Forestry Technology
Študentská 26
960 53 Zvolen
Slovak Republic
*Corresponding author: pavol.harvanek@gmail.com

WOOD RESEARCH
66 (1): 2021
161-170
doi.org/10.37763/wr.1336-4561/66.1.161169

SYNTHESIS AND CHARACTERIZATION OF RESOL TYPE PHENOL-FORMALDEHYDE RESIN IMPROVED BY SIO_2-NP

Günay Özbay
Aksaray University
Turkey

Erkan Sami Kokten
Karabuk University
Turkey

Ayhan Ozcifci
Aksaray University
Turkey

(Received February 2020)

ABSTRACT

In this work, resol type phenol–formaldehyde (RPF) resin was modified with silicon dioxide nanoparticles (SiO_2-Np). SiO_2-Np was added at varying ratios from 1 to 4 wt.% to improve the bonding performance of the RPF resins. The physical characteristics of the nano-modified RPF (nano-RPF) resins were examined. The effects of modification were studied by Fourier transform infrared spectroscopy (FT-IR) and thermogravimetric analysis (TGA). The results of FT-IR revealed that the nano-RPF resins were successfully produced by phenol, formaldehyde, and SiO_2-Np. The nano-RPF resins demonstrated high thermal stability at temperatures above 500°C. The adhesive performance of the nano-RPF resins was investigated under dry and wet conditions. The nano-RPF resins indicated better adhesive performance than unmodified RPF resin. The RPF resin could be improved by SiO_2-Np.

KEYWORDS: Adhesive performance, phenol–formaldehyde, silica nanoparticles, thermal stability.

INTRODUCTION

Phenol-formaldehyde pre-polymer (PF) resins are the major types of thermosetting polymers, which are widely used as an adhesive by the wood industry is because of its number of

advantages, such as high strength and extremely resistant to moisture of the cured resin (Kariž et al. 2009). PF resins are categorized into two main groups: resols or novolacs depending on the type of catalyst that are used in the production process of the resin. Resol type phenol-formaldehyde resins (RPF) are obtained by the polycondensation reaction of formaldehyde and phenol in a high-alkaline environment. The RPF resins have good thermal, chemical and mechanical properties (Viswanathan and Richardson 1985, Haupt and Sellers 1994, Schmidt 2005, Zhang and Sigman 2007, Riedlinger and Frazier 2008, Moubarik et al. 2009, Roslan et al. 2014, Kurt and Cavus 2011).

There are many studies on PF resin modification by different types of chemicals including boron carbide, boric acid, propylene carbonate, sodium carbonate, and potassium carbonate in order to improve adhesive performance (Gao et al. 1999, Park et al. 1999, Wang et al. 2010). Also, many different types of nano-chemicals such as nano-TiO_2, nano-SiO_2, nano-Fe_2O_3, nano-Al_2O_3, and nano-$CaCO_3$ particles were examined in order to enhance the thermal stability and/or the bond strength of thermosetting adhesives. It was pointed out that the use of nano-chemical could improve the adhesive properties (Cao et al. 2002, Bauer et al. 2006, Li et al. 2007, Shi et al. 2008, Wang et al. 2011). However, there is still a need for experimental studies involving the usage of the nano-chemicals in the polycondensation reaction of the RPF resins production and their applications in the wood products industry.

The purpose of this study is to use silicon dioxide nanoparticles (SiO_2-Np) in the RPF resin synthesis to enhance the adhesive performance of the nano-RPF resins. For this purpose, the effect of SiO_2-Np additives and loading ratio on the chemical and thermal characteristics of the resins were studied by FT-IR and TGA analysis respectively. Then, the bonding performance of laminated wood bonded with the nano-RPF resins was experimentally investigated under indoor/outdoor exposures.

MATERIALS AND METHODS

Materials

Phenol (liquid) and formaldehyde (at a concentration of 37%) were commercial products supplied by GENTAŞ, Turkey. Nano-SiO_2 with the particle size of about 20-30 nm and the density of 0.1-0.15 $g{\cdot}cm^{-3}$, was supplied by Sigma Aldrich. The beech (*Fagus orientalis* Lipsky) wood planks with a density of 0.670 $g{\cdot}cm^{-3}$ were used to evaluate the adhesive performance.

Synthesis of the nano-PF resins

The RPF resin syntheses were conducted in a laboratory glass reactor equipped with a condenser, a magnetic stirrer, and a thermometer. The reference resin was based on an unmodified RPF resin (Laboratory made RPF resin). The RPF resin synthesis procedure was as follows: The mixture of phenol and formaldehyde was fed into the reactor and, when the temperature of 60°C was reached, the catalyst, a 2/3 of total NaOH solution (50 wt.%), was added. The mixture was heated to 90°C and, it was followed that the resulting mixtures were heated at 90°C under stirring for 60 min. Then, it was cooled down to a temperature of 60°C. The second part of NaOH (50 wt.%) (1/3 of total NaOH weight solution) was added to adjust the pH to 11.0–12.0 into the reactor at this temperature. At end of the reaction, the mixture was allowed to cool to room temperature. The route for the synthesis of the nano-RPF resins was basically the same as RPF synthesis method. Before the synthesis, various amount of nano-SiO_2 was mixed uniformly with phenol and formaldehyde at room temperature. Loading of the SiO_2-Np in the formulations was variable; 1%, 2%, and 4%.

Characterization

Resol type phenolic resins are generally characterized for final viscosity, pH value, gel time, and solid content. A TES-1380 digital pH meter was employed for pH measurements. Viscosity measurements were carried out at a temperature of 25°C by using a Brookfield viscometer (model: Dv-IPrime). The resin solids content was measured in accordance with ASTM D 3529 (ASTM D3529M-97 2008).

The gel time of the resin was measured at 100°C. The test tube filled with 5 g of prepared the resin was immersed into boiling water and then, constant stirring was applied throughout the test. The elapsed time until the point when no further stirring was possible was defined as the gel time for the sample. The gel time of the resin was determined according to a procedure reported by Haupt and Sellers (1994). Infrared spectra were recorded an Alpha Fourier transform infrared spectrometer. IR spectra were obtained using a frequency range of 4000-400 cm^{-1} with a resolution of 4 cm^{-1} and 40 scans. Thermogravimetric analysis (TGA) was carried out on a HITACHI STA 7300 thermogravimetric analyzer at 5 °C/min under air atmosphere under the nitrogen atmosphere.

Preparation of wood samples and testing

The selected wood lamellas were obtained from beech wood planks with the dimensions of 5 × 50 × 500 mm in the radial, tangential and longitudinal directions, respectively. The lamellas were acclimatized at 20 ± 2°C and 65 ± 3% relative humidity in an acclimatization room. The resin was uniformly applied at the amount of about 180 $g \cdot m^{-2}$ manually by hand brush. Resin was applied on one lamella only. Two wood lamellas bonded with the RFP resin has assembled and hot-pressed under 1.6 MPa pressure at 130°C, for 10 min. The samples were acclimatized in a chamber having 65% relative humidity and temperature of 20°C and then cut into samples with the dimensions of 10 x 20 x 150 mm after the corresponding pre-treatment according to EN 12765 (2002). In bonding tests, 24 samples were evaluated for each group. During the test, the loading was applied centrally and in the plane of the bond. The loading was continued until a break at 2 $mm \cdot min^{-1}$. The bonding test was performed on a Zwick/Roell Z50 universal testing machine according to BS EN 205 (2003) standard. The following equation was used in order to calculate the tensile shear strength:

$$\sigma_y = F_{max}/A = F_{max}/l_2 \cdot b \quad (1)$$

where: σ_y is the tensile shear strength ($N \cdot mm^{-2}$), F_{max} is the applied maximum load (N), A is the bonding surface of sample (mm^2), l_2 is the length of the bonded surface (mm), and b is the width of the bonded surface (mm).

RESULTS AND DISCUSSION

Physical characterization

The physical characteristics of the nano-RPF resins are given in Tab. 1. In a comparison of nano-RPF resins with reference resin, the final pH value of the nano-PFR slightly decreases with increasing nano-SiO_2 content. As the amount of the nano-SiO_2 was increased from 1 wt.% to 4 wt.%, the pH value of the nano-RPF was decreased from 11.84 to 11.62. The decrement of the pH values could be attributed to the low pH value of the nano-SiO_2, which is below 3. The viscosity of nano-RPF resins was affected by SiO_2-Np content. As the SiO_2-Np content

increased, the viscosity values of nano-RPF resins also increased. The lowest viscosity with a value of 285 cPs was measured for the reference RPF resin, while the highest viscosity with a value of 315 cPs was determined for the 4 wt.% SiO_2-Np modified RPF resin. It can be explained that the high molecular weight of the nano-SiO_2 caused an increase in the viscosity of the resin. 4 wt.% SiO_2-Np modified RPF resin had the longest gel time when compared to the reference RPF resin. The solids contents of all the resins including reference RPF and nano-RPF resins were determined to be above 40 wt.%. The SiO_2-Np additive has slightly increased the solids content of the nano-RPF resins. The lowest solid content with a value of 42.84 wt.% was determined for the reference RPF resin, while the highest solid content with a value of 43.51 wt.% was measured for the 4 wt.% SiO_2-Np modified RPF resin (Tab. 1). As reported in the literature, the resin solid content is one of the most important characteristics of phenolic resin. The low solid content adhesive could be ejected out more water during the hot-press processing (Lin et al. 2014).

Tab. 1: Physical characteristics of the nano-PF resins.

Resin type	SiO_2-Np (wt.%)	pH (20°C)	Viscosity (25°C, cPs)	Solid content (%)	Gel time (100°C) (s)
Reference RPF	0	11.98	285	42.84	170
1% SiO_2-Np/RPF	1	11.84	301	43.17	173
2% SiO_2-Np/RPF	2	11.70	309	43.24	176
4% SiO_2-Np/RPF	4	11.62	315	43.51	188

Thermogravimetric analysis

The TGA analysis of the nano-RPF resins was evaluated in a large range of temperatures and it was considered as a measure of the thermal stability. Fig. 1 displays the TGA thermograms of the reference RPF resin and nano-RPF resins. It can be seen that the variations in the thermal stability of the SiO_2-Np modified RPF resin depend upon the temperatures and SiO_2-Np contents. The thermal degradation of these resins can be divided into three regions: 30°C to 120°C, 120°C to 300°C, and 300°C to 600°C. The first region occurred between 30°C and 120°C. This region is probably connected to the removal of the hydroxyl groups. Second region, between 120°C and 300°C, could be related to the terminal weak or strong OH groups. Nano-RPF resins were thermally stable up to 300°C. This thermal stabilization may be explained by new structures, which can be formed during resin synthesis. They are thermally stable until the whole polymer structure collapses (Lin et al. 2006). The weight loss occurs at temperatures between 300°C and 600°C and is caused by oxidative resin degradation. The thermal degradation of the reference RPF resin was higher than the nano-RPF resins. At temperatures below 300°C, nano-RPF resins showed higher thermal stability than reference RPF resin. RPF resin with 2% and 4% SiO_2-Np had higher thermal stability than RPF resin with 1% SiO_2-Np content. At temperatures higher than 300°C, the thermal stability of SiO_2-Np modified RPF resins was higher than that of the reference RPF resin. It can be said that the thermal stability of the RPF resin could be improved by SiO_2-Np. The similar findings, on the thermal stability of phenolic resins, were also reported by Burns and Orrell (1967), Chen et al. (2008), Wang et al. (2011), Bian et al. (2015) as well as Kokten et al. (2020).

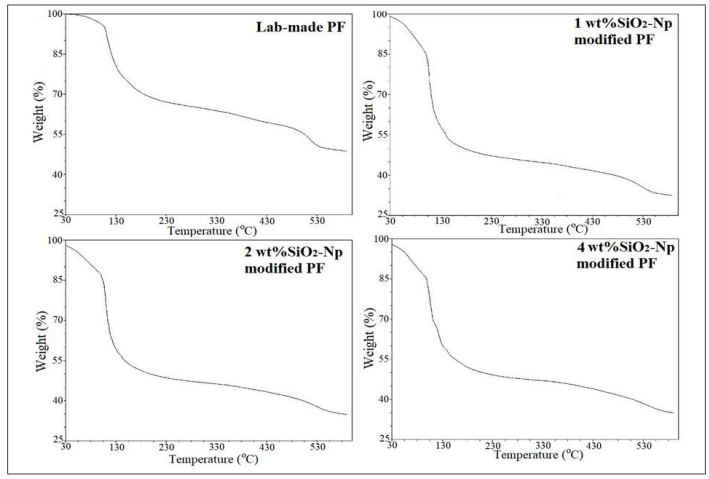

Fig. 1: TGA thermograms of the RPF resins modified by SiO_2-Np.

FT-IR spectroscopy

FT-IR analysis was used to confirm the modification of the RPF and determine the effect of SiO_2-Np on the chemical structure of the RPF resin. The results are shown in Fig. 2. The intense OH stretching band at 3450 cm^{-1} indicated that there are two different types of -OH group: phenolic and alcoholic. The peak shown in the range of 2900–2950 cm^{-1} indicated the symmetrical C-H stretch of CH2. The peaks at around 1700 and 1750 cm^{-1} assigned to the C=C stretching vibrations aromatic ring vibrations group, and also the peak at 1220-1250 cm^{-1} represented the C-O stretching in aromatic ring for all RPF resin. The stretching of C-O-C was found in all RPF resin at 850 cm^{-1}. The characteristic peaks of phenolic compounds were observed at about 1600, 1500, 1450, 1220, and 850 cm^{-1}, as reported in previous FT-IR studies on the PF resin (Liu et al. 2002, Chen et al. 2008, Wang et al. 2009, Zhao et al. 2013, Bobrowski and Grabowska 2015, Cui et al. 2017). New absorptions at 1650 cm^{-1} and 1680 cm^{-1} appeared to compare with the reference RPF resin, the absorptions of the RPF resin containing 4 wt.% SiO_2-Np at 1070–1090 cm^{-1}, representing the dissymmetry flexible vibration of linear Si–O–Si, is more obviously compared to that of the RPF resin containing 1 wt.% SiO_2-Np. The FT-IR results showed that the structures of nano-RPF and the reference RPF resins were similar. This similarity confirmed that nano-RPF resins were successfully synthesized with the SiO_2-Np, phenol, and formaldehyde under the alkali environment.

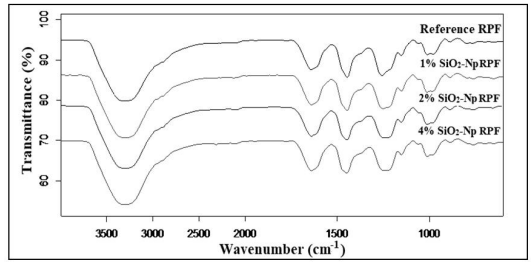

Fig. 2: FT-IR spectra of the nano-RPF resins.

Adhesive performance of the nano-RPF resins

The bond strength values of the specimens are presented in Tab. 2. The highest bond strength with a value of 11.87 N·mm^{-2} was found for the 2 wt.% SiO_2-Np-RPF specimens, followed by 1 wt.% SiO_2-Np-RPF specimens (10.92 N·mm^{-2}), reference RPF specimens (10.54 N·mm^{-2}), and 4 wt.% SiO_2-Np-RPF specimens (9.76 N·mm^{-2}) under dry conditions (pre-treatment 1). The specimens bonded with RPF resins modified by the SiO_2-Np with 1 wt.% and 2 wt.% exceeded standard requirements for the durability of class C1 (10 N·mm^{-2}) as defined by EN 12765 (EN 12765 2002). The bond strength values of the resins showed a significant drop under wet conditions, especially pre-treatments 3. The RPF resin containing 2 wt.% SiO_2-Np had the highest strength, while the RPF resin containing 4 wt.% SiO_2-Np reached lower bond strength values after the pre-treatment 2 and pre-treatment 3. However, for the pre-treatment 2 and pre-treatment 3, the RPF resins containing up to 4 wt.% SiO_2-Np satisfy the requirements for durability classes C2 (7 N·mm^{-2}) and C3 (4 N·mm^{-2}), respectively (Tab. 2). The bond strength test results demonstrated that the bonding performance of the RPF resin could be achieved with SiO_2-Np addition up to 2 wt.% in dry or wet conditions. Many studies stated that silica nanoparticles showed high strength, thermal stability, and chemical stability for polymer materials (Zhou et al. 2003, Sun et al. 2006, Yang et al. 2006, Qin et al. 2017, Zhang et al. 2018).

Tab. 2: The bond strength values of the SiO_2-Np modified RPF resins.

Type of PF resin	Pre-treatment 1 (C1>10)[a]	Pre-treatment 2 (C2>7)[a]	Pre-treatment 3 (C3>4)[a]
Reference RPF	10.54 (0.26)b	7.38 (0.21)	5.69 (0.39)
1% SiO_2-Np/RPF	10.92 (0.32)	7.44 (0.34)	6.03 (0.43)
2% SiO_2-Np/RPF	11.87 (0.48)	7.59 (0.31)	6.14 (0.35)
4% SiO_2-Np/RPF	9.76 (0.32)	6.58 (0.45)	5.27 (0.41)

[a]Minimum requirements of adhesive bond strength in N·mm^{-2} according to EN 12765 for each pre-treatment.
[b]The values in the parentheses are standard deviations.

CONCLUSIONS

The purpose of this study is to show usability of silicon dioxide nanoparticles (SiO_2-Np) in the RPF resin synthesis to enhance the adhesive performance of the nano-RPF resins. The effect of SiO_2-Np contains on the physical, chemical, and thermal characteristics of the resins were examined. The following conclusions can be outlined:

- The physical characteristics such as pH, viscosity, solid content and gel time of the nano-RPF resin were affected by SiO_2-Np content.
- The RPF resins modified by SiO_2-Np showed higher thermal stability than the reference RPF resin. The RPF resin with 2% and 4% SiO_2-Np had higher thermal stability than RPF resin with 1% SiO_2-Np content. The thermal stability of the RPF resin could be improved by SiO_2-Np.
- The results of the FT-IR spectrum showed that the nano-RPF had a similar FT-IR spectrum to the reference RPF resin. The molecular structure relationship demonstrated that nano-RPF resins were successfully synthesized with the SiO_2-Np, phenol, and formaldehyde under the alkali environment.
- The adhesive performance test results revealed that the bond strength of the RPF resin could be improved with SiO_2-Np addition up to 2 wt.%. Nano-based resins can be used in the production of wood adhesives.

ACKNOWLEDGMENTS

The authors would like to thanks the Aksaray University, Research Foundation (No. 2018-008) for the financial support that made this work possible. Thanks also to Research Assistant İlknur ULUDAG for the proofreading.

REFERENCES

1. ASTM D3529M-97, 2008: Standard test method for matrix solids content and matrix content of composite prepreg.
2. Bauer, F., Decker, U., Ernst, H., Findeisen, M., Langguth, H., Mehnert, R., Sauerland, V., Hinterwaldner, R., 2006: Functionalized inorganic/organic nanocomposites as new basic raw materials for adhesives and sealants. Part 2. International Journal of Adhesion and Adhesives 26(7): 567-570.
3. Bian, C., Wang, Y., Wang, S., Zhong, Y., Liu, Y., Jing, X., 2015: Influence of borate structure on the thermal stability of boron-containing phenolic resins: A DFT study. Polymer Degradation and Stability 119: 190–197.
4. Bobrowski, A., Grabowska, B., 2015: FTIR method in studies of the resol type phenol resin structure in the air atmosphere in some time intervals. Metallurgy and Foundry Engineering 41(3): 107.
5. BS EN 205, 2003: Adhesives. Wood adhesives for non-structural applications. Determination of tensile shear strength of lap joints.
6. Burns, R., Orrell, E.W., 1967: A thermal analytical study of phenol formaldehyde resins. Journal of Materials Science 2(1): 72-77.
7. Cao, Y.M., Sun, J., Yu, D.H., 2002: Preparation and properties of nano-Al_2O_3 particles/polyester/epoxy resin ternary composites. Journal of Applied Polymer Science 83(1): 70-77.
8. Chen, Y., Chen, Z., Xiao, S., Liu, H., 2008: A novel thermal degradation mechanism of phenol–formaldehyde type resins. Thermochimica Acta 476(1): 39-43.
9. Cui, Y., Hou, X., Wang, W., Chang, J., 2017: Synthesis and characterization of bio-oil phenol formaldehyde resin used to fabricate phenolic based materials. Materials (Basel), 10(6): 668.
10. EN 12765, 2002: Classification of thermosetting wood adhesives for non-structural applications.
11. Gao, J., Liu, Y., Yang, L., 1999: Thermal stability of boron-containing phenol formaldehyde resin. Polymer Degradation and Stability 63(1): 19-22.
12. Haupt, R.A., Sellers, T.J., 1994: Characterizations of phenol-formaldehyde resol resins. Industrial & Engineering Chemistry Research 33(3): 693-697.
13. Karіž, M., Jošt, M., Sernek, M., 2009: Curing of phenol-formaldehyde adhesive in boards of different thicknesses. Wood Research 54(2): 41-48.
14. Kokten, E.S., Özbay, G., Ayrilmis, N., 2020: Synthesis of biobased phenolic resins using catalytic pyrolysis oil and its effect on oriented strand board performance. The Journal of Adhesion 96(5): 475-489.
15. Kurt, R., Cavus, V., 2011: Manufacturing of parallel strand lumber (PSL) from rotary peeled hybrid poplar I-214 veneers with phenol formaldehyde and urea formaldehyde adhesives. Wood Research 56(1): 137-144.

16. Li, H., Zhang, Z., Ma, X., Hu, M., Wang, X., Fan, P., 2007: Synthesis and characterization of epoxy resin modified with nano-SiO_2 and γ-glycidoxypropyltrimethoxy silane. Surface and Coatings Technology 201(9-11): 5269–5272.
17. Lin, R., Fang, L., Li, X., Xi, Y., Zhang, S., Sun, P., 2006: Study on phenolic resins modified by copper nanoparticles. Polymer Journal 38(2): 178.
18. Lin, R., Sun, J., Yue, C., Wang, X., Tu, D., Gao, Z., 2014: Study on preparation and properties of phenol-formaldehyde-chinese fir liquefaction copolymer resin. Maderas Ciencia y Tecnologia 16(2): 159–174.
19. Liu, Y., Gao, J., Zhang, R., 2002: Thermal properties and stability of boron-containing phenol-formaldehyde resin formed from paraformaldehyde. Polymer Degradation and Stability 77(3): 495–501.
20. Moubarik, A., Pizzi, A., Allal, A., Charrier, F., Charrier, B., 2009: Cornstarch and tannin in phenol–formaldehyde resins for plywood production. Industrial Crops and Products 30(2): 188–193.
21. Park, B.D., Riedl, B., Hsu, E.W., Shields, J., 1999: Differential scanning calorimetry of phenol–formaldehyde resins cure-accelerated by carbonates. Polymer 40(7): 1689-1699.
22. Qin, W., Vautard, F., Askeland, P., Yu, J., Drzal, L.T., 2017: Incorporation of silicon dioxide nanoparticles at the carbon fiber-epoxy matrix interphase and its effect on composite mechanical properties. Polymer Composites 38(7): 1474–1482.
23. Riedlinger, D.A., Frazier, C.E., 2008: Morphological analysis of PF/pMDI hybrid wood adhesives. Journal of Adhesion Science and Technology 22(12): 1197–1208.
24. Roslan, R., Zakaria, S., Chia, C.H., Boehm, R., Laborie, M.P., 2014: Physico-mechanical properties of resol phenolic adhesives derived from liquefaction of oil palm empty fruit bunch fibres. Industrial Crops and Products 62: 119–124.
25. Schmidt, R.J., 2005: Industrial catalytic processes - phenol production. Applied Catalysis A: General 280(1): 89–103.
26. Shi, H., Liu, F., Yang, L., Han, E., 2008: Characterization of protective performance of epoxy reinforced with nanometer-sized TiO_2 and SiO_2. Progress in Organic Coatings 62(4): 359–368.
27. Sun, S., Li, C., Zhang, L., Du, H.L., Burnell-Gray, J.S., 2006: Effects of surface modification of fumed silica on interfacial structures and mechanical properties of poly (vinyl chloride) composites. European Polymer Journal 42(7): 1643-1652.
28. Viswanathan, T., Richardson, T., 1985: Thermosetting adhesive resins. Patent US4524164A.
29. Wang, J., Jiang, N., Jiang, H., 2010: Micro-structural evolution of phenol-formaldehyde resin modified by boron carbide at elevated temperatures. Materials Chemistry and Physics 120(1): 187–192.
30. Wang, M., Leitch, M., Xu, C.C., 2009: Synthesis of phenol–formaldehyde resol resins using organosolv pine lignins. European Polymer Journal 45(12): 3380–3388.
31. Wang, Z., Gu, Z., Hong, Y., Cheng, L., Li, Z., 2011: Bonding strength and water resistance of starch-based wood adhesive improved by silica nanoparticles. Carbohydrate Polymers 86(1): 72–76.
32. Yang, H., Zhang, Q., Guo, M., Wang, C., Du, R., Fu, Q., 2006: Study on the phase structures and toughening mechanism in PP/EPDM/SiO_2 ternary composites. Polymer 47(6): 2106-2115.
33. Zhang, Y., Sigman, M.S., 2007: Palladium (II)-catalyzed enantioselective aerobic dialkoxylation of 2-propenyl phenols: A pronounced effect of copper additives on enantioselectivity. Journal of the American Chemical Society 129(11): 3076-3077.

34. Zhang, Z., He, X., Wang, X., Rodrigues, A.M., Zhang, R., 2018: Reinforcement of the mechanical properties in nitrile rubber by adding graphene oxide/silicon dioxide hybrid nanoparticles. Journal of Applied Polymer Science 135(14): 46091.
35. Zhao, Y., Yan, N., Feng, M.W., 2013: Thermal degradation characteristics of phenol–formaldehyde resins derived from beetle infested pine barks. Thermochimica Acta 555: 46-52.
36. Zhou, S., Wu, L., Sun, J., Shen, W., 2003: Effect of nanosilica on the properties of polyester-based polyurethane. Journal of Applied Polymer Science 88(1): 189–193.

Günay Özbay
Aksaray University
Department of Industrial Engineering
68100 Aksaray
Turkey

Erkan Sami Kokten*
Karabuk University
Department of Industrial Engineering
78050 Karabuk
Turkey
*Corresponding author: erkansamikokten@karabuk.edu.tr

Ayhan Ozcifci
Aksaray University
Department of Industrial Engineering
68100 Aksaray
Turkey